Development of a Direct Metalisation Method for Micro-Engineering

Jack Hoy-Gig Ng

A dissertation submitted for the degree of Doctor of Philosophy

Heriot-Watt University

School of Engineering and Physical Sciences

November 2012

Abstract

This research concentrates on the establishment of a metalisation and micro-patterning technique that eliminates metal evaporation and/or photoresist molding procedures. The process design is chosen from the analysis of the broad field of direct metalisation techniques where novel photocatalysts or photoreducing agents are increasingly employed to create new processes.

The new photolithographic process in this study introduces two novel photoreducing agents for additive metal thin film fabrication: methoxy poly(ethylene glycol) and photosystem I. This work proves the concept of using light energy to directly reduce metal ions incorporated within an ion-exchanged polyimide substrate to produce metal thin films. The patterning step can be operated at atmospheric pressure, in a dry environment, using a coating of the photoreducing agent. This process offers a significant improvement to prior related work that relied on a water layer to enable the metalisation. Of particular importance for this process is the influence of light energy dose and heat treatment, which promote silver nanoparticles growth at the cost of degradation of the substrate polymer. The investigation was carried out thoroughly by laser writing experiments for a selected range of laser power and scan speed. To complement the phenomenon observed in the laser experiments, prolonged UV light exposure time and heat treatment experiments were carried out to confirm the hypothesis postulated in this thesis.

The morphology of the silver nanoparticles produced, the changes of the substrate surface and the adhesion of electroless plating were characterised. Results indicate that UV irradiation with the energy density required for reasonable production speed causes inevitable molecular damage to the polymer substrate. Photosystem I was found to be able to catalyse the production of visually similar silver thin film by light sources in the blue region. Using a similar light intensity, the exposure time was reduced by an order of magnitude whilst the degradation phenomenon observed during the UV process appears to be eradicated. With the fundamentals of the process established in this thesis, future optimization is suggested for the transition from a proof of concept to industrial implementation.

Dedication

To my parents

Your love and patience gave me the chance to find the limit of my life.

Acknowledgements

I would like to express my greatest gratitude to my principle supervisor Prof. Marc Desmulliez who provided me the opportunity and freedom to pursue this research. His insights, guidance and trust in my ability has allowed tremendous growth in my personal development. I would like to thank my second supervisor Prof. Duncan Hand who always pushed for impeccable research and helped me to focus on the big picture. Thanks also to Dr. David Hutt for serving as the external examiner of this thesis, and to Dr. Resham Dhariwal for being the internal examiner.

I would like to thank my many past and present colleagues within the Microsystems Engineering Centre for their advice, assistance and friendships, making our research group vibrant, fun and professional. Outside of our group, I would like to specially thank Dr. Aongus McCarthy and Dr. Himanshu Suyal at the Photon Counting group who shared the passion of my research and provided generous assistance in laser direct-writing. Thanks also goes to Dr. Tze Yang Hin from Loughborough University for his useful discussion and assistance in the characterisation of silver nanoparticles.

I would also like to acknowledge my best friend and ex-flatmate Dr. Norbert Lorenz who shared the good and bad times in and outside of the university.

Finally, I would also like to acknowledge the financial support of the Engineering and Physical Sciences Research Council (EPSRC).

Table of Contents

Chapter 7

Influence of UV energy and heat treatment time on substrate integrity

Chapter 8

Photosystem I as a photoreducing agent for the formation of thin metal film patterns

Chapter 9

Conclusions and future work

List of Tables and Figures

List of Publications by the Candidate

Patent:

1) **J. H.-G. Ng**, M. P. Y. Desmulliez, and D. E. G. Watson, "Additive metallisation process," U.S. Patent PCT/GB2012/000116

Journal publications:

1) **J. H.-G. Ng** and M. P. Y. Desmulliez,
"Current Trends in Resist-Free, Vapour-Free Deposition and Patterning of Metal Films,"
Materials Science and Engineering: R: Reports, in press.
2) **J. H.-G. Ng**, D. E. G. Watson, J. Sigwarth, A. McCarthy, K. A. Prior, D. P. Hand, W. Yu, R. W. Kay, C. Liu, and M. P. Y. Desmulliez,
"On the Use of Silver Nanoparticles for Direct Micropatterning on Polyimide Substrates,"
IEEE Trans. Nano., vol. 11, no. 1, pp. 139–147, 2012.
3) **J. H.-G. Ng**, M. P. Y. Desmulliez, M. Lamponi, B. G. Moffat, A. McCarthy, H. Suyal, A. C. Walker, K. A. Prior, and D. P. Hand,
"A direct-writing approach to the micro-patterning of copper onto polyimide,"
Circuit World, vol. 35, no. 2, pp. 3–17, 2009.
4) **J. H.-G. Ng**, M. P. Y. Desmulliez, K. A. Prior, and D. P. Hand,
"Ultra-violet direct patterning of metal on polyimide,"
Micro Nano Lett., vol. 3, no. 3, pp. 82–89, 2008.

Conference publications:

1) D. E. Watson, **J. H.-G. Ng**, and M. P. Y. Desmulliez,
"Additive photolithography based process for metal patterning using chemical reduction on surface modified polyimide,"
presented at the 18th European Microelectronics and Packaging Conference (EMPC), 2011, Brighton, UK, 2011, pp. 1–7.
2) D. E. Watson, **J. H.-G. Ng**, J. Sigwarth, J. Bates, and M. P. Y. Desmulliez,
"Silver nanocluster formation using UV radiation for direct metal patterning on polyimide,"
presented at the 3rd Electronic System-Integration Technology Conference (ESTC), 2010, Berlin, Germany, 2010, pp. 1–4.

3) **J. H.-G. Ng**, D. E. G. Watson, J. Sigwarth, A. McCarthy, H. Suyal, D. P. Hand, T. Y. Hin, and M. Desmulliez,
"An additive method for photopatterning of metals on flexible substrates," presented at the 36th International MATADOR Conference, Manchester, UK, 2010, pp. 389–392.
4) **J. H.-G. Ng**, M. P. Y. Desmulliez, A. McCarthy, H. Suyal, K. A. Prior, and D. P. Hand,
"UV direct-writing of metals on polyimide,"
presented at the Symposium on Design, Test, Integration and Packaging of MEMS/MOEMS (DTIP), 2008, Nice, France, pp. 360–363, 2008.
5) Marc P. Y. Desmulliez, Jens Kaufmann, **Jack Hoy-Gig Ng**, and Keith Sinclair,
"3D-Manufacturing Technologies for the Microelectronics Industry,"
presented at MicroTech 2008, Old Windsor, UK, Microelectronics International, Vol. 25 (3).
6) **J. H.-G. Ng**, M. Desmulliez, M. Lamponi, B. G. Moffat, A. C. Walker, A. McCarthy, H. Suyal, K. A. Prior, and D. P. Hand,
"UV direct-writing of metals on polyimide substrates,"
presented at the 2nd Electronics System-Integration Technology Conference (ESTC), 2008, Greenwich, UK, 2008, pp. 691–694.

Conference publications not related to this thesis:

7) **Jack Hoy-Gig Ng**, Robert T. Ssekitoleko, Hoang-Vu Nguyen, Knut E. Aasmundtveit, Christine E. M. Démoré, Sandy Cochran and Marc P.Y. Desmulliez,
"Low Temperature Bonding of Piezoelectric Single Crystal Materials for Miniaturized High Resolution Ultrasound Transducers,"
presented at the 4th Electronics System-Integration Technology Conference (ESTC), 2012, Amsterdam, The Netherland, in press.
8) **J. H.-G. Ng**, R. T. Ssekitoleko, D. Flynn, R. W. Kay, C. E. M. Démoré, S. Cochran, and M. P. Y. Desmulliez,
"Design, manufacturing and packaging of high frequency micro ultrasonic transducers for medical applications,"
presented at the IEEE 13th Electronics Packaging Technology Conference (EPTC), 2011, Singapore, 2011, pp. 93–98.

9) **J. H. G. Ng**, R. T. Ssekitoleko, D. Flynn, M. P. Y. Desmulliez, C. E. M. Démoré and S. Cochran,
"Design, manufacturing and packaging of a micro ultrasonic transducer for medical applications,"
presented at the 22nd Micromechanics and Micro systems Europe Workshop, Tønsberg, Norway, pp. 298-301, 2011.

10) Robert Ssekitoleko, Christine Demore, **Jack Hoy-Gig Ng**, David Flynn, Marc Desmulliez, Sandy Cochran,
"Design and Fabrication of PMN-PT Based High Frequency Ultrasound Imaging Devices Integrated into Medical Interventional Tools,"
presented at the IEEE International Ultrasonics Symposium 2011, Orlando, FL, USA. 2011

11) **J. H. Ng**, R. Ssekitoleko, D. Flynn, C. Démoré, M. P. Y. Desmulliez, and S. Cochran,
"Innovative Manufacturing and 3-Dimensional Packaging Methods of Ultrasonic Transducers for Medical Applications,"
presented at the 18th European Microelectronics and Packaging Conference (EMPC), Brighton, UK, in press, 2011.

12) **Jack Hoy-Gig Ng**, David Flynn, Yves Lacrotte, Marc P.Y. Desmulliez, Robert Ssekitoleko, Christine Démoré and Sandy Cochran,
"Progress towards the development of novel fabrication and assembly methods for the next generation of ultrasonic transducers"
presented at the 3rd Electronic System-Integration Technology Conference (ESTC), 2010, Berlin, Germany, 2010, pp. 1–4.

Chapter 1

Introduction

1.1 Motivation and objectives

Cross-disciplinary research at the crossroad between chemistry, physics and materials science is yielding new materials with exciting properties in electronic packaging, sensors and microelectromechanical systems (MEMS). These novel properties are utilized to create simpler and easier manufacturing processes, which accelerate the market adaptation of these new technologies and products where economical manufacturability is inevitably the limiting factor. Electronics and sensors systems that are more compact, thinner, and, at the same time, with higher functionalities are in high demand. The technology landscape is moving towards more complex, customised or personalised products that can be produced in low volume, as illustrated in the schematic diagram in Figure 1.1.

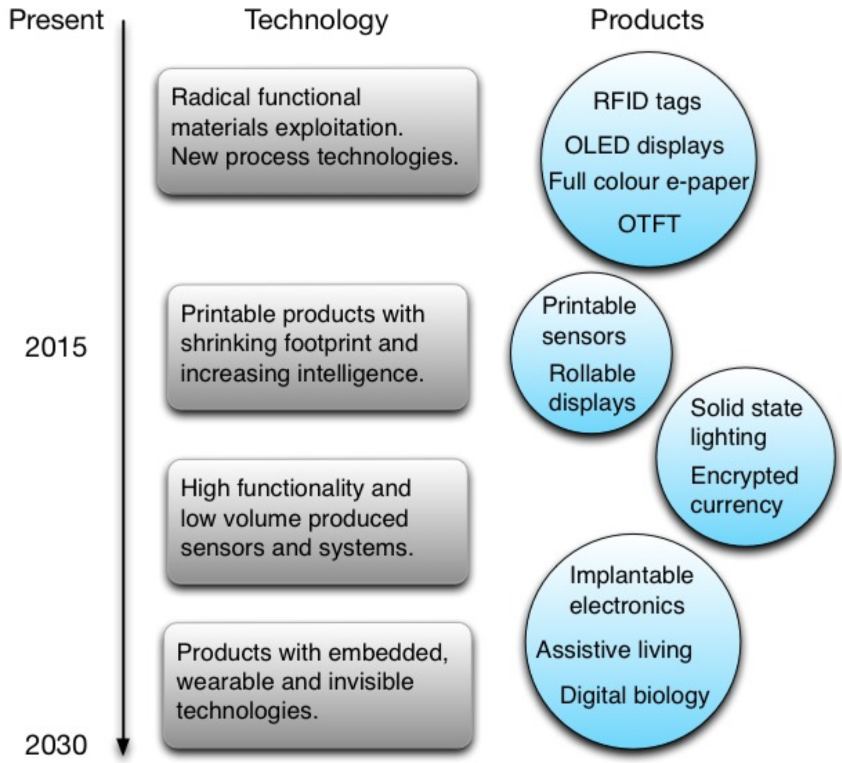

Figure 1.1: Schematic diagram of the technology landscape in electronics, sensors and systems.

This thesis aims to design, create and test a new additive manufacturing process from the bottom up with the added requirements that the process be low cost, flexible, and adaptable to mass manufacturing. In that respect, the field of electronic interconnection has been chosen. The bottleneck of electronic miniaturisation lies indeed in the interconnection between components for signals or power transmission within the package of the device [1]. Standard microfabrication technologies for conductor traces used for interconnection are usually subtractive. For this process a blanket layer of metal is first deposited onto a substrate, followed by a layer of photopatternable polymer, also known as photoresist which is used to mask off the metal for subsequent etching and / or plating to achieve the desired patterns of specified metal thickness. This kind of process is wasteful in nature because a large amount of valuable metal is removed from the blanket layer in order to obtain a pattern. The photoresist patterning process itself consists of a series of steps: application of the photoresist to the substrate, thermal curing, UV light exposure, dissolution of the unwanted photoresist. In addition, a master mask is required for the photopatterning of the photoresist. The mask itself can be costly to produce, and, in combination with the multi-step photoresist patterning process, production can only be economical with a large volume scale.

In order to alleviate some of the drawbacks of a subtractive process for creating metal interconnects, this thesis is devoted to the following objectives:

(i) To design a direct metalisation and micro-patterning process whereby metallic patterns are directly produced on the substrate in the areas where they are needed so that the photoresist patterning and metal etching process could be replaced.

(ii) To create a microfabrication process that substantially reduces time and costs by simplifying the number of process steps, equipment and materials required. This entails eliminating the use of toxic chemical reducing agents or harsh solvents, and the use of capital intensive or time consuming equipment such as high-end lasers, vacuum or inert gas chambers, and long heat treatment steps. The goal is to allow an economical small volume production of customizable designs or rapid prototyping to accelerate the iterations of product realization and improvements.

(iii) To develop scalability. The design of the microfabrication process is envisaged to be conveniently adaptable for small and large substrate areas ranging from several centimeters square, 3 inch wafer to A4 size sheets and beyond. The same process is intended to be flexible to accommodate serial manufacturing as well as reel-to-reel production. The choices in the use of any liquid immersion and coating techniques must be logistically compatible with the process flow.

1.2 Contribution to knowledge

A key challenge of this research was to introduce a radically new set of processing steps and new materials from outside the conventional protocols of electronics and microsystems fabrication in order to create a new light-directed patterning process that fulfils the objectives described above. The contribution to knowledge from this thesis is the construction of a new light-directed patterning process, whereby the concept of micro-patterning and direct metalisation is proven and the influential factors of each processing step are demonstrated. A significant improvement to other related processes is made by the use of two novel photo-reducing agents, methoxy poly(ethylene glycol) (MPEG) and photosystem I (PS-I), in the light-directed patterning where a dry coating allows the metalisation of thin films to take place in air and atmospheric pressure. Especially, the photoreduction rate is dramatically improved using PS-I with photons in the blue wavelength region, which has a lower photon energy than in the UV. This thesis demonstrates an understanding of the underlying fundamental mechanisms enabling the process, which include the surface modification of polyimide, the electron generation pathways and degradation of the substrate that interplay during photoreduction and post-processing. This thesis establishes a feasible and distinct light-directed patterning process and creates a clear direction for upscale manufacturing development.

1.3 Thesis layout

The layout and purpose of this thesis is presented schematically in Figure 1.2. Following this introductory Chapter, the remainder of the thesis is divided as follows.

<u>Design of process flow</u>

Chapter 2 presents the literature review on the wide range of techniques based on completely different principles with the same goal of direct metalisation and patterning without the use of evaporation or vacuum processing and photoresist materials. Drawing from this review, the criteria for the process design and the scheme of methodology chosen for this study concludes the Chapter.

Chapter 3 explains the fundamental mechanisms underlying each of the process steps. It explains in detail the surface modification of polyimide by hydrolysis and the ion-exchange theory, followed by a critical review of related metalisation and patterning processes. This Chapter also describes two novel photoreducing agents, MPEG and PS-I, as they are exploited for the first time for the metalisation of thin films.

<u>Experimental details</u>

Chapter 4 describes the preparation procedures of the silver ion-exchanged polyimide substrate, the MPEG preparation and coating, and the PS-I extraction from spinach leaves. This Chapter includes the Fourier Transform Infra-Red (FTIR) spectroscopy characterisation of the surface modified polyimide and the UV-visible (UV-vis) light absorption spectroscopy characterisation of the prepared MPEG and PS-I.

Chapter 5 first describes the exposure apparatus used in this thesis including three laser systems, a UV flood exposure system and two blue light emitting diodes (LED) sources. The scanning electron microscopy, elemental analysis and the mechanical profiling characterisation techniques are then described afterwards.

Implementation of process steps

Chapter 6 examines the photoreduction mechanisms through laser direct-writing experiments. Various regimes of laser power and scan rate parameters are described and assessed. Results indicate a diffusion limited process for the creation of a silver nanoparticles thin film. The impact of incident UV photon energy on the degradation of the substrate by UV photolysis is suggested.

Chapter 7 validates the hypothesis that the surface of the substrate is degraded through the photoreduction and the heat treatment steps. The loss of mechanical interlocking between the silver nanoparticles seed layer produced and the re-imidized polyimide substrate when subjected to electroless plating baths, leading to poor adhesion is investigated. High resolution scanning electron microscopy and polymer shrinkage characterisation is presented along with a concluding explanation of the degradation mechanisms.

Chapter 8 presents the decision to change the working wavelength of the photolithography in order to remedy the problems inherent in using a UV light source in the proposed process. This Chapter describes the innovation of using the natural dyes present in the leaves of plants to harvest visible light for effective electron generation and transfer. A proof of concept implementation is demonstrated.

Chapter 9 concludes this thesis by firstly highlighting the significance of the findings in this study and the milestones of research outcomes. Future work to optimise the photolithography process established in this thesis is suggested with a view to increase the technology readiness level of this technology for industrial implementation.

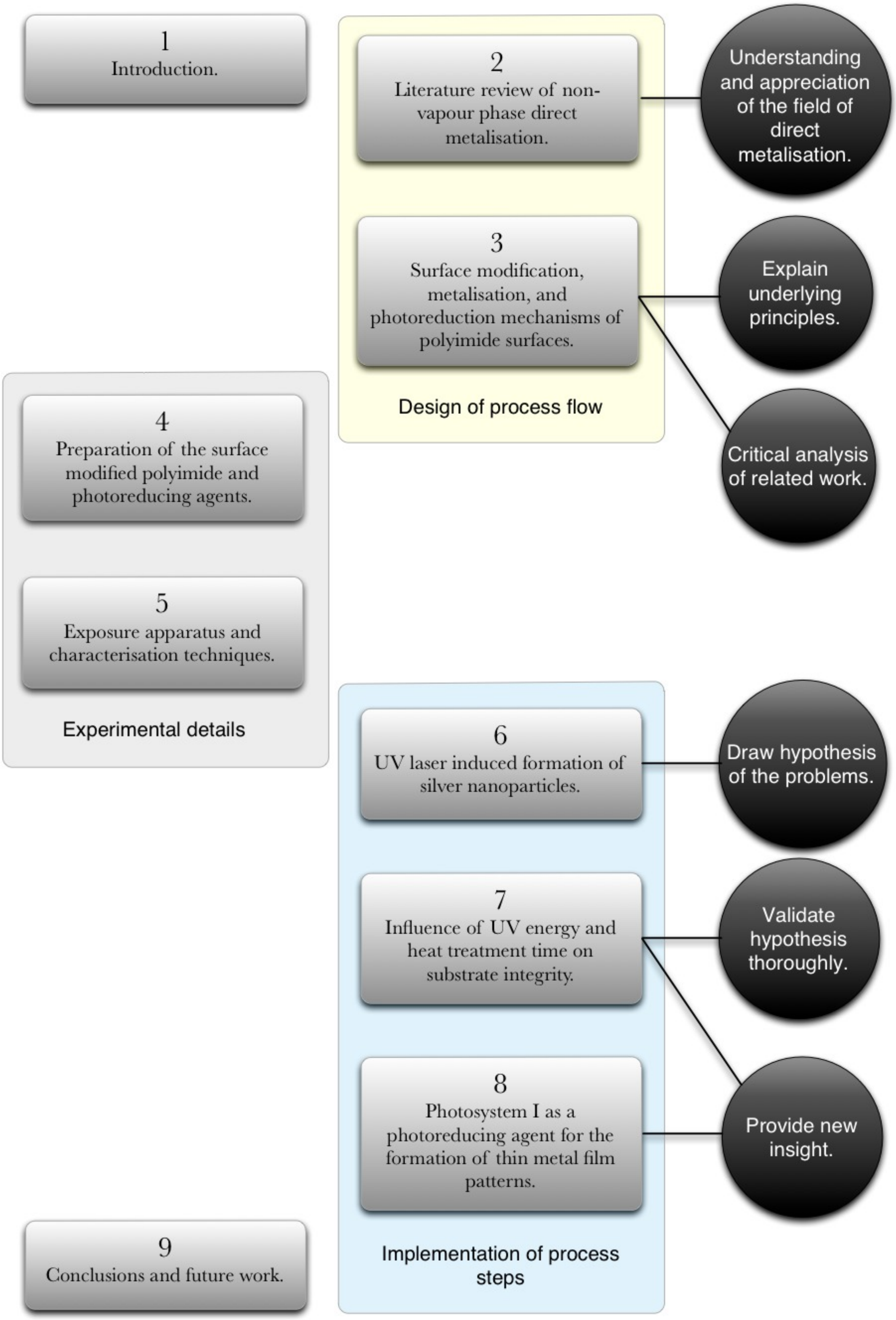

Figure 1.2: Layout of the thesis.

Chapter 2

Literature review of non-vapour phase direct metalisation

2.1. Introduction

In recent years, intensive research in the development of direct metalisation techniques on non-conducting or semiconducting substrates has emerged through the investigation of cross-disciplinary routes ranging from organic metal-complex chemistry, molecular self-assembly, polymer science, surface science, photochemistry, electrochemistry, laser optics, thermodynamics, fluid dynamics and semiconductor physics. These methods, classified as "direct" in contrast to the conventional photolithography-based processes, have in common two or more of the following characteristics:

(i) They do not use any evaporation techniques, or vapour phase chemical precursors, and, thereby, do not need vacuum chambers;

(ii) They do not use any photoresist materials and,

(iii) They do not require (photo)masks by virtue of their sequential laser writing or ink-jet printing process step.

The underlying mechanisms of these techniques can be divided into four main categories which are illustrated in the chart shown in Figure 2.1. Each category can be further subdivided into particular routes which have been supplemented with some supporting literature examples. The research undertaken in this thesis is a combination of two branches, namely “reduction of embedded metal ions” in surface modification for subsequent electroless deposition and “photo-reducing agent coating” in photocatalysis-mediated deposition. An overview of each of the four categories is given in Sections 2.2 to 2.5. The advantages of the two branches described above also being referred to as “direct writing”, are summarised together with the research direction of this thesis in Section 2.6.

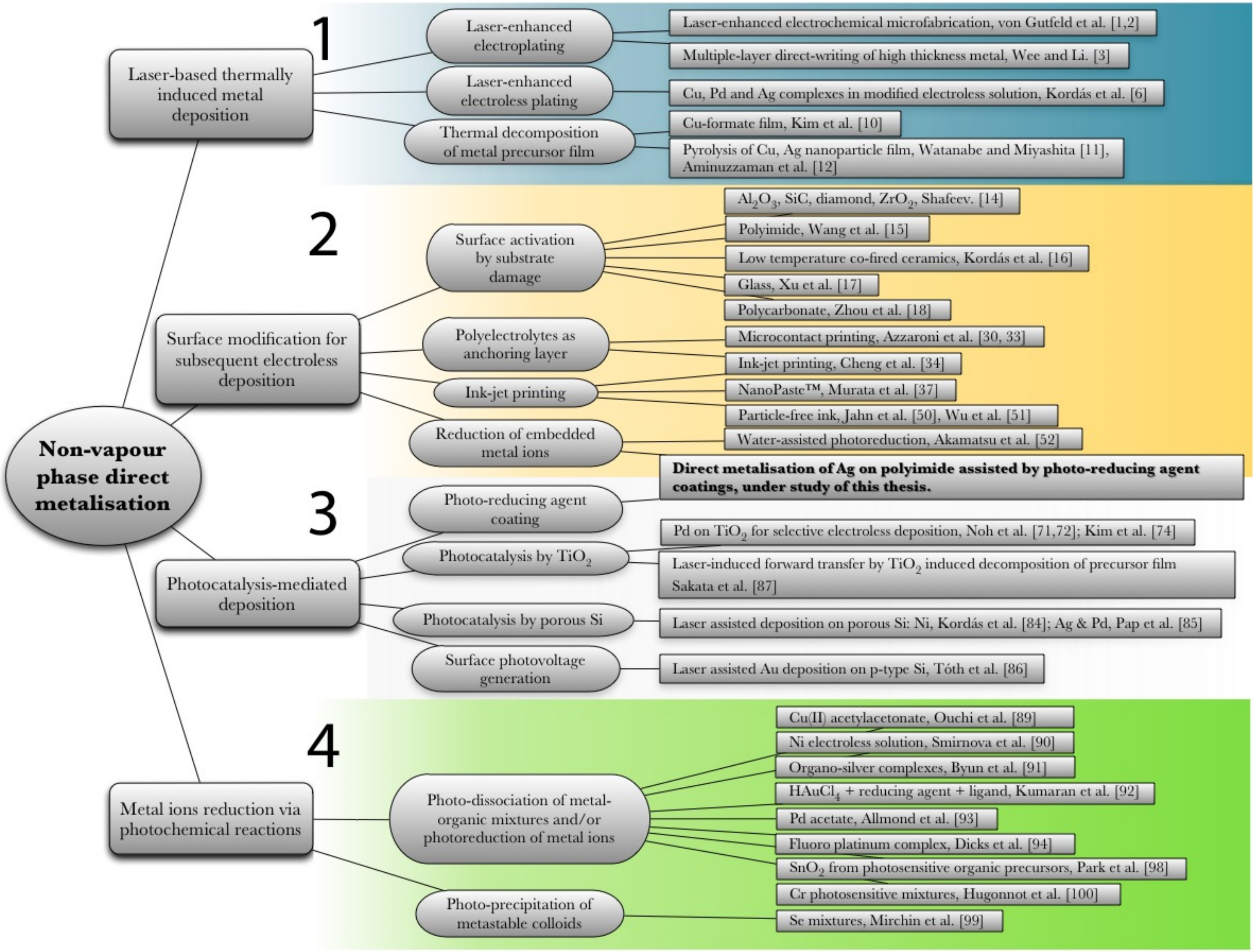

Figure 2.1: Chart of non-vapour phase direct metalisation techniques. All the methodologies reviewed can be classified into four main categories. Each route is referenced with literature examples. The direct metalisation on polyimide under study in this thesis is highlighted in bold.

2.2. Laser-based thermally induced metal deposition

This Section describes Route 1 as illustrated in the chart in Figure 2.1. A timeline of the development in metal deposition driven primarily and directly by heat is shown in Figure 2.2. This includes laser-enhanced electroplating and laser-enhanced electroless plating.

2.2.1. Laser-enhanced electroplating

Heat, amongst other influencing factors such as applied voltage and agitation of the electrolyte solution, can increase the plating rate of traditional electrolytic plating. In particular, the irradiation by a laser of a specific area generates localised heat that enables selectively enhanced electroplating. Investigation in this area began as far back as 1979 by IBM Research [2]. Figure 2.3 shows the apparatus set up in the 1980's of one of the pioneer direct writing experiments incorporating a laser in an electrolytic cell with anode and cathode electrodes together with a hydrostatic pressure jet to enhance rates of mass transport of the electrolyte [3]. A drawback of the laser-assisted electroplating method is that plating still proceeds, albeit at a slower growth rate, on the area of the electrode not exposed to laser irradiation. Moreover, laser irradiation through the electrolyte solution affects the resolution of the feature size, as the laser beam is subjected to diffraction through the liquid medium. Heat diffusion needs also to be taken into account for the resolution of the line width of the metal track achieved. Finally, the heat generated from a high-power or/and high-frequency pulsed laser beam can cause vigorous turbulence and bubbles in the liquid solution, making the process difficult to monitor.

In spite of these difficulties, research in laser-assisted electroplating continued. In 2005, Wee and Li [4] reported thickness of copper above 70 µm produced by multiple laser scanning at speed between 100 - 300 µm/s with line width in the region of a few hundred microns as shown in Figure 2.4. A recent report in 2012 [5] using a CW laser and a Nd:YAG laser with an electrolyte jet similar to the setup shown in Fig. 2.2 produced sparse unconnected copper particles, which is not suitable for electronic circuits manufacturing.

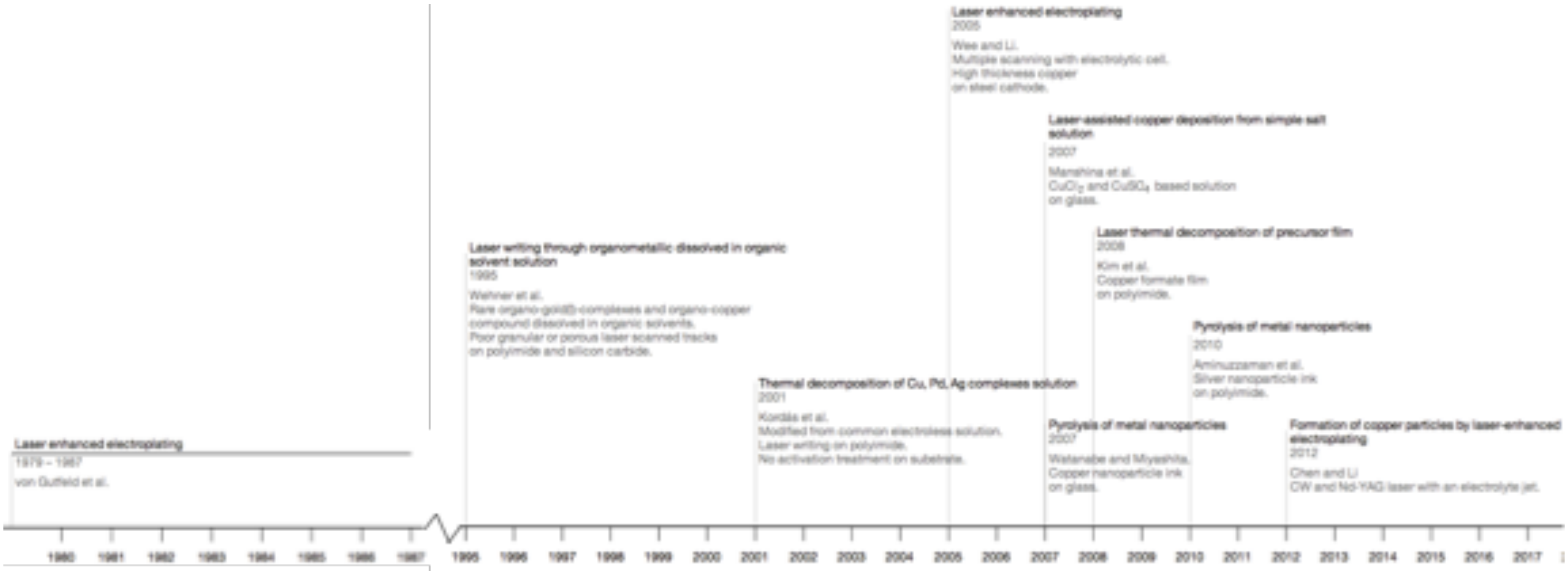

Figure 2.2: Timeline of the development of laser-enhanced electroplating and electroless plating.

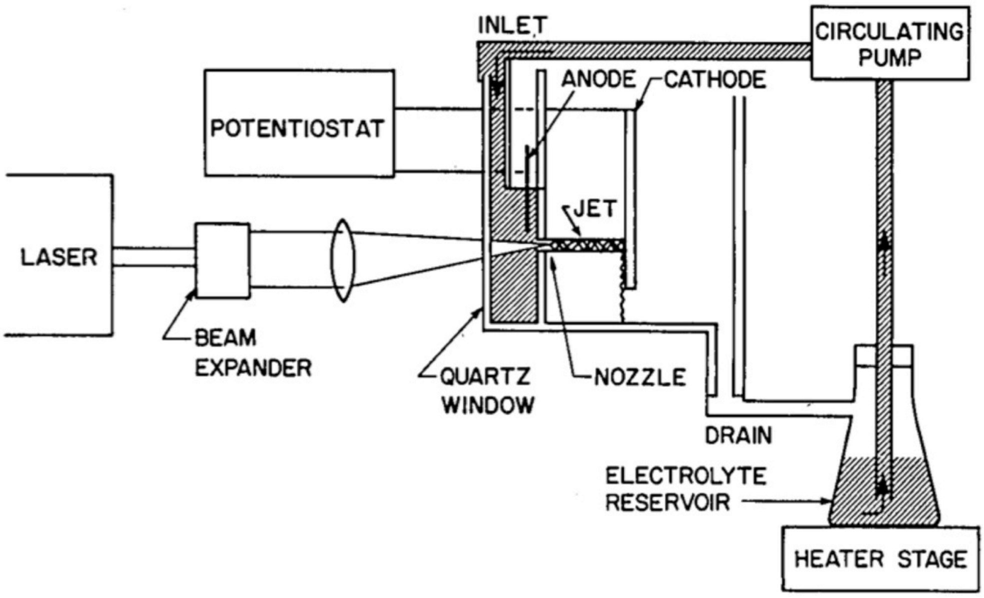

Figure 2.3: Diagram of a laser-jet cell for laser-enhanced jet plating [3].

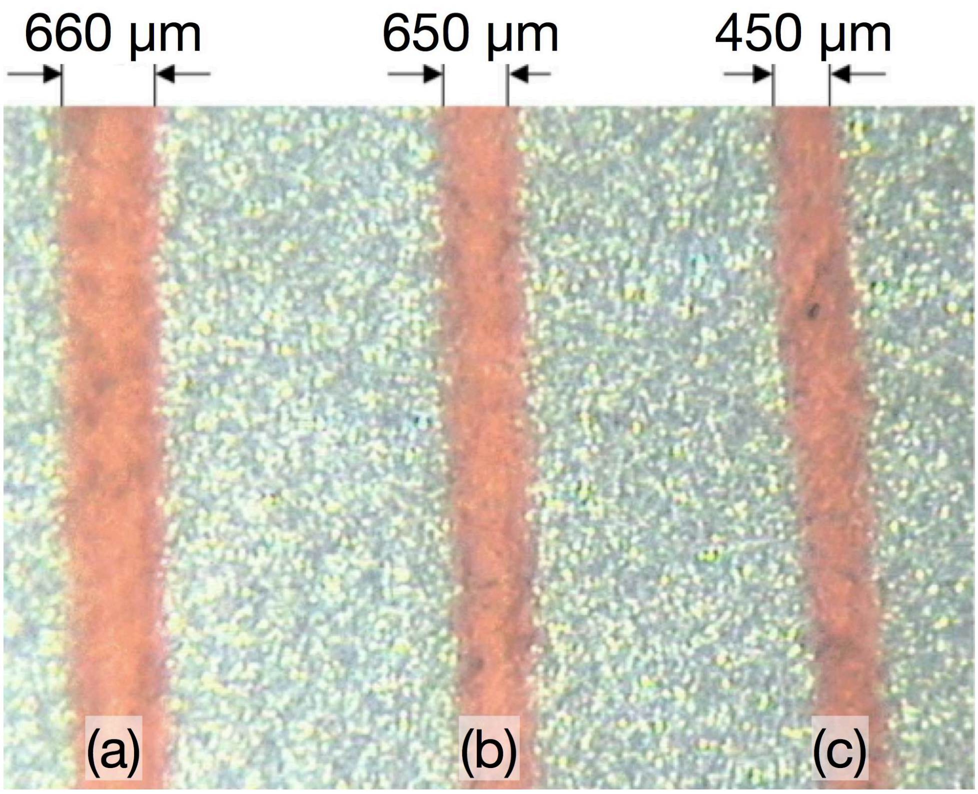

Figure 2.4: Copper deposition after 20 laser scans for each line with different scanning speeds: (a) 100 µm/s; (b) 200 µm/s; (c) 300 µm/s, with a laser power of 3.3 W [4].

2.2.2. Laser-enhanced electroless plating

In order to increase the selectivity of the metal deposition process, several metal-complex aqueous solutions have been employed as a replacement for conventional electrolytic plating baths from the late 1990's up to a few years ago [6-9]. The experimental set-up was also hugely simplified as shown in Figure 2.5, and did not require the use of anode and cathode electrodes or a potentiostat. This technique relies on the thermal decomposition of materials at the solution / substrate interface by the heat generated from the laser beam. One or a combination of the following mechanisms have been suggested [7]:

(i) The breaking of chemical bonds on the surface of the substrate e.g. polymer macromolecules on polyimide substrates. The randomly perturbed surface may provide electron transfer to metal complexes yielding metallic deposition.

(ii) The thermal decomposition of metal-complex compounds e.g. copper-tartrate complex forming a mixture of copper and copper oxide directly without chemical reduction.

(iii) The heating of the chemical solution which speeds up an electroless plating process with the presence of a reducing agent such as formaldehyde in the solution. Details of electroless deposition are described in Chapter 7.

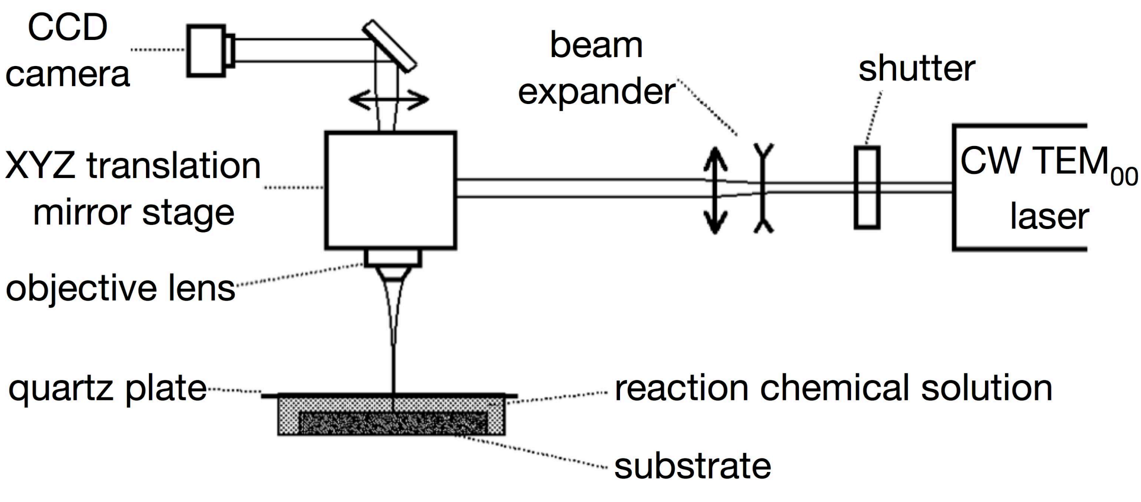

Figure 2.5: A simple solution-phase laser direct writing set-up [10].

In all cases, the resulting precipitation of metal particles / islands aggregates on the heated region of the substrate takes place. The morphology of the metal deposits achieved is generally uneven or discontinuous, despite the fine lateral resolution of the laser scanned tracks which are below 10 μm as demonstrated in Figure 2.6. This is due mostly to the use of a liquid phase precursor and the thermal conductivity of the system. Two different precursors are compared in Table 2.1. The laser scan speeds employed for these processes are generally slow, ranging from 10 up to a few hundred microns per second. Figure 2.6 (a) and (c) show palladium and silver metal particles, respectively, precipitated from the laser direct writing. Figure 2.6 (b) and (d) show electroless copper plated selectively onto the laser formed patterns shown in (a) and (c) in order to produce a thicker and more conductive metal layer. More on the electroless plating route for direct metalisation is introduced in the next section.

Table 2.1: Comparison of solution precursors in laser-assisted liquid phase deposition.

Solution processes	Power	Scan speed	Line width
Simple $CuCl_2$ and $CuSO_4$ based solution Manshina *el al*., 2007 [9]	10 - 400 mW CW Ar^+ laser 488 nm	10 µm/s	10 - 100 µm
Decomposition of Cu, Pd and Ag complex in modified electroless solution Kordás *el al*., 2001 [7]	10 - 300 mW, CW Ar^+ laser 488 nm	100 - 400 µm/s	6 - 60 µm

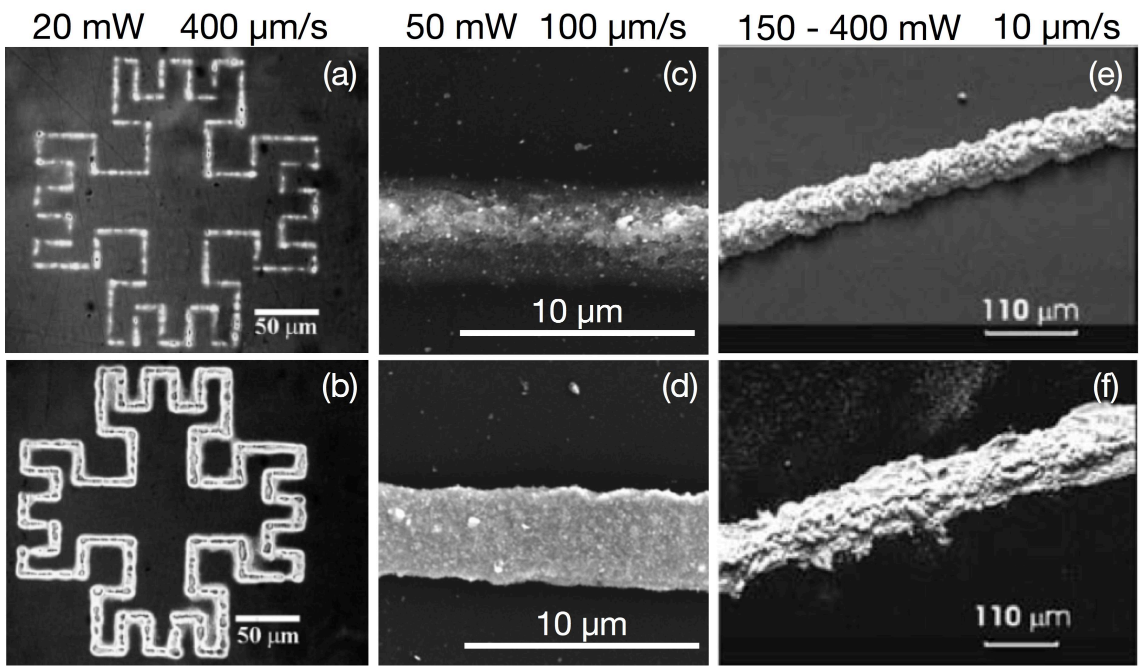

Figure 2.6: SEM images of micropatterns fabricated on polyimide substrates by a continuous-wave Ar^+ laser λ = 488 nm (a), P = 20 mW, at scan speed = 200 µm/s with 6 repeated multi-scans, through a coating solution containing 0.1 M $PdCl_2$, 1 M NH_3, 0.125 M NaOH; (b) 5 minutes of electroless copper plating on (a); (c) P = 50 mW, at scan speed = 100 µm/s through a coating solution containing 0.05 M $AgNO_3$, 2 M NH_3; (d) several minutes of electroless copper plating on (c) [7]; (e) and (f) P = 150 mW and 400 mW respectively, at scan speed = 10 µm/s, through a coating solution containing 0.1 M $CuCl_2$, 0.2 M KNa-tartrate (Rochelle salt), 0.125 M NaOH, 6 M HCOH (formaldehyde) [9].

2.2.3. Thermal decomposition of metal precursor films

More recently, solid/gel-like precursors have been coated as a thin film layer deposited on top of the target substrate [11]. A copper formate aqueous solution was coated and dried on a polyimide substrate surface. Sufficient thermal energy from a laser decomposes the copper formate into hydrogen, carbon dioxide and copper metal which is described by the following reaction:

$$Cu(HCOO)_2 \xrightarrow{thermal} Cu + H_2 + 2CO_2 \tag{2.1}$$

The Q-switched 355 nm wavelength diode pumped solid state (DPSS) laser in the experiments employed 20 ns pulses at 30.303 kHz with a focused spot size of 20 μm. The UV wavelength of the laser causes the breaking of chemical bonds in the polymer such as C-N and C=O bonds which renders the substrate hydrophilic and enhances adhesion to the top copper layer.

The optimal conditions for copper deposition are with a laser fluence of 150 mJ/cm^2 and a scan speed of 14.3 mm/s. This scan speed is not as slow as in the previous examples which are in the range of μm/s, but it is still far from the m/s velocity desired for mass scale production. Although the resolution of the features is better as the laser beam irradiates through a thin film layer instead of a liquid medium, the resultant line width was approximately 55 μm, three times as large as the spot size, as shown in Figure 2.7. The uniformity of shape of the deposits and its morphology still need to be improved. However a low resistivity of the copper trace, 1.07×10^{-6} Ω.m and a maximum thickness of 8.5 μm were reported. Therefore this method also has the advantage of not requiring subsequent electroless plating.

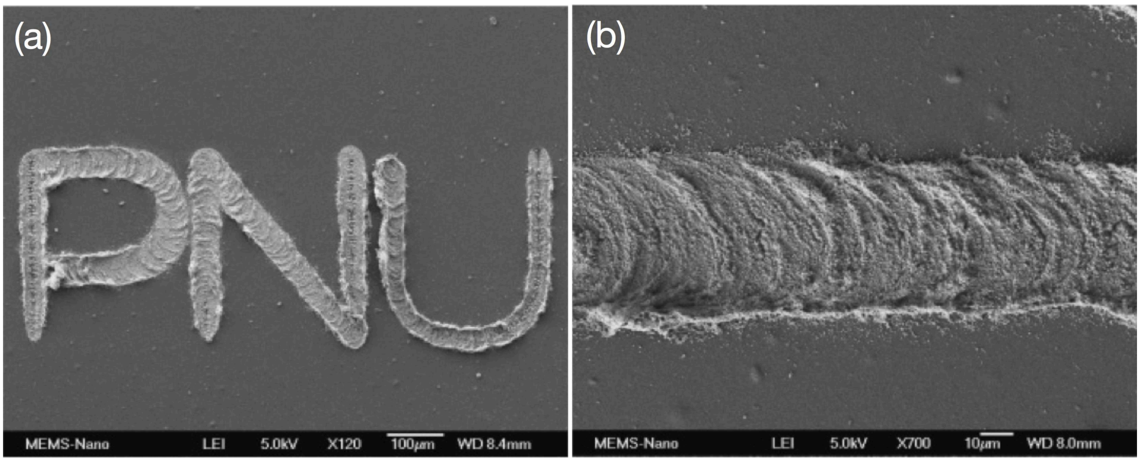

Figure 2.7: SEM images of the deposited copper layer on polyimide using a 355 nm nanosecond pulse laser: (a) patterned text with copper; (b) high magnification showing the morphology of the copper layer. [11]

Between 2007 and 2010, further research activities were conducted on the metal deposition induced by the thermal energy from a laser. The irregularity of thermally induced deposition is overcome by laser-induced pyrolysis of metal nanoparticles such as a copper nanoparticle ink [12] and a silver nanoparticle ink [13]. The metal nanoparticle inks exhibit a large reduction in melting temperature due to the thermodynamic size effect [14]. This low melting temperature minimises the spreading of the deposition process. Ultra-fine line width as low as 6 μm was achieved at the cost of a slow scan speed of 200 μm/s using a CW-Ar ion laser (λ = 488 nm) with power intensities between 1.2 - 3.0 kW/cm^2 as shown in Figure 2.8. Resistivity of the Ag microline was determined to be 4.1×10^{-6} Ω cm. The proprietary nanosilver ink material spin-coated on the substrate is washed away in the non exposed regions, which is rather wasteful.

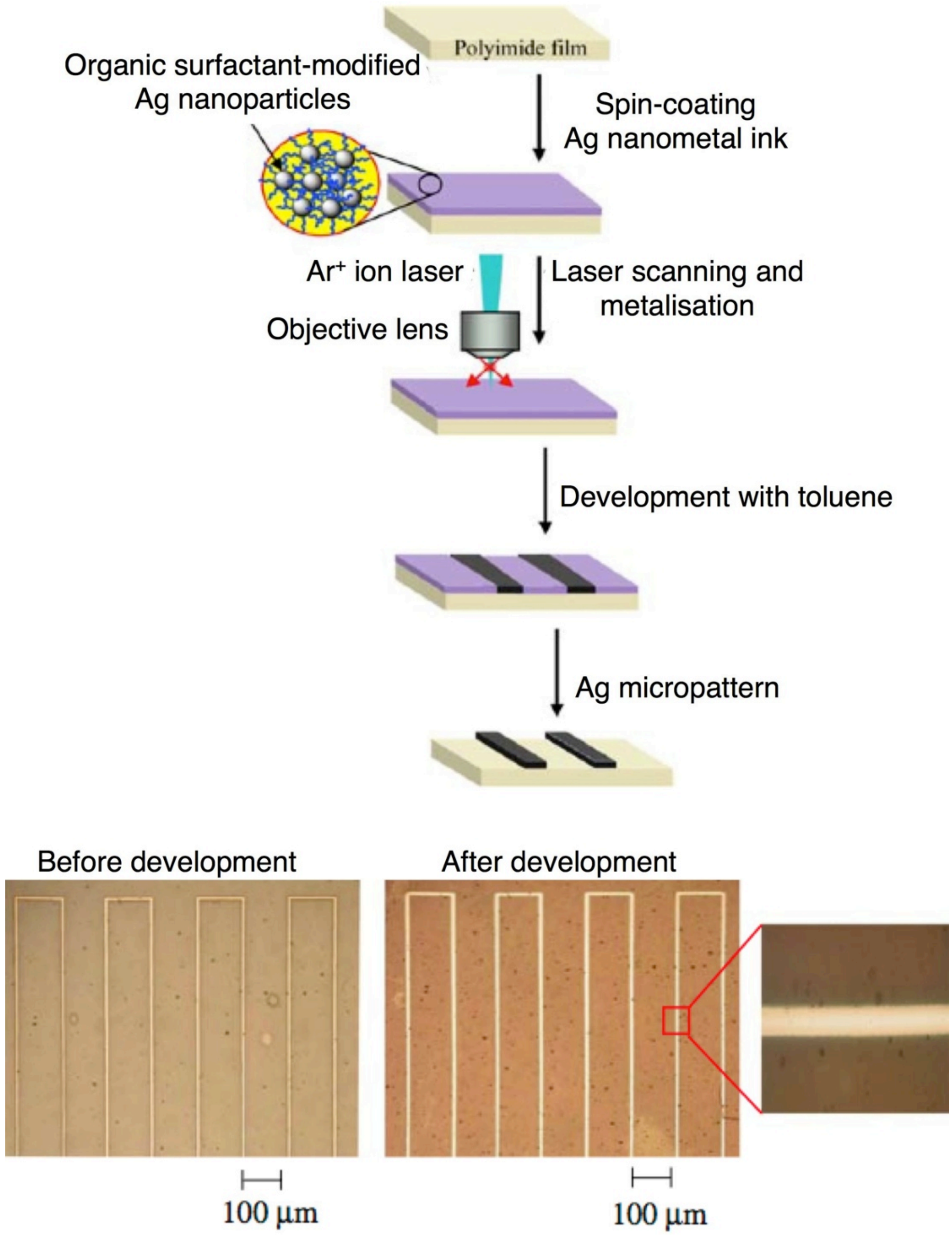

Figure 2.8: Fabrication of Ag micropatterns on a flexible polyimide film by pyrolitic laser direct-writing technique from a liquid-dispersed Ag nanoparticles precursor film [13].

2.3. Surface modification for subsequent electroless deposition

This Section describes Route 2 as illustrated in the flow chart in Figure 2.1. As the thermally induced deposition techniques produce irregular or oversized features, a more attractive approach is the use of non-thermal driven processes combined with electroless deposition to achieve a more uniform deposit. Electroless deposition is an isotropic process which is primarily driven by the release of free electrons generated by a mixture of chemical and electrochemical reactions within the plating bath. Detailed background information for the electroless deposition process is described in Chapter 7. A key feature of electroless deposition is that, unlike electrolytic deposition, no external voltage is applied to drive the deposition. Therefore the substrate does not need to be electrically conductive. However, suitable catalysts on the surface of the substrate are required to trigger the chemical reactions occurring during electroless deposition. The production of these active catalysts on the surface is referred to as activation and the triggering of the electroless deposition is known as initiation. Consequently, micro-patterning of metals on non-conducting surfaces can be accomplished by producing first of all patterns of active catalytic sites on the surface of the substrate, so that electroless deposition takes place selectively.

Researchers have demonstrated many surface modification techniques on various substrates that create microscale patterns of active catalytic surfaces for this route of metalisation. These techniques can be categorised as follows.

2.3.1. Surface activation by substrate damage

This is one of the pioneering efforts in creating active catalytic sites in order to initiate selective electroless deposition. The active sites result from open molecular bonds generated either by the removal of atoms such as hydrogen, oxygen or carbon from the molecular structure of the substrate, or by the re-deposition of charged species on top of the surface of the substrate generated by the rapid and high-temperature reactions during laser melting or ablation. Such processes have been carried out on Al_2O_3, SiC, diamond and ZrO_2 substrates [15], polyimide [16], and low-temperature co-fired ceramics (LTCC) [17]. Although this method is fast and easy to apply, the heat generated by the high-power lasers induces undesired machining of the substrate, such as that shown in the examples of LTCC in Figure 2.9, and limits the minimum feature size achievable due to heat diffusion.

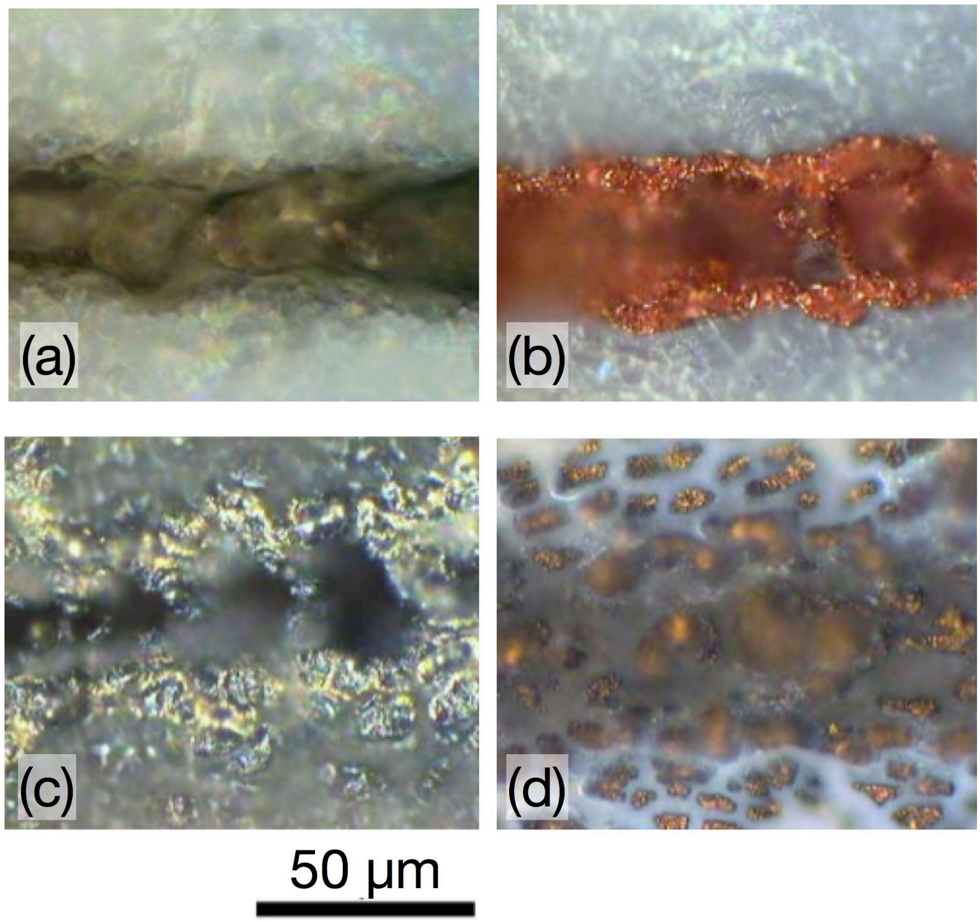

Figure 2.9: Laser-activated track on LTCC (a) using moderate laser power (f = 2 kHz, E = 0.35 mJ/pulse, v_{scan} = 2000 µm/s) and chemically deposited Cu thereon. (b) Deposition of copper takes place all over the treated area, both in the etched groove and along the line. In the case of higher pulse energies and slower scans (f = 1 kHz, E = 1 mJ/pulse, v_{scan} = 20 mm/s), deep grooves are formed and a larger volume of LTCC along the scan is annealed, yielding a rough and large activated surface area. Such surfaces are seen for (c) silver and (d) gold electroless plating. [17]

Ultra-fast pulsed laser such as a femtosecond laser has also been used recently to minimise the thermal effect on the substrates [18]. Silver atoms were produced inside the groove formed by the laser ablation on a glass surface coated with silver nitrate films. The silver atoms can serve as catalyst seeds for subsequent selective electroless copper plating. However the mechanisms involving material removal during ablation whilst retaining the silver atoms in the scanned areas are still under investigation. Figure 2.10 shows the ablated tracks plated with electroless copper; the tracks display lateral irregularities at both edges and small micro-cavities in the cross-section view of the filled groove. Use of a femtosecond laser represents a very large capital overhead for a manufacturing process in terms of equipment but also maintenance costs.

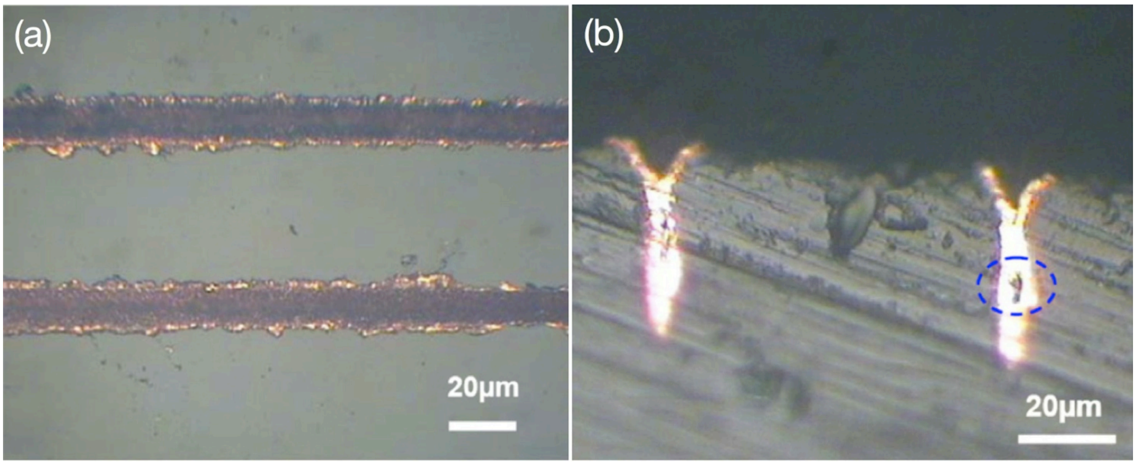

Figure 2.10: (a) Two electroless copper plated lines using silver atoms as seeds formed by femtosecond laser ablation (average power: 6 mW, 20 multiple scans); (b) cross-section view of (a) showing the electroless copper filled grooves with small embedded micro-cavities. [18]

Besides a high power laser, a low intensity UV light source can also cause photolytic damage to some polymer surfaces in order to produce active sites for metal ion anchoring and subsequent electroless plating. A polycarbonate sheet can be selectively activated by a low-pressure mercury lamp shining through a photomask in order to create active surface regions [19]. Carboxyl groups are generated by photochemical oxidation of the methyl groups in the exposed regions on which tin ions Sn^{2+} can be easily chemisorbed. Subsequently, silver ions can be adsorbed onto the Sn^{2+} ions through the reaction of $Sn^{2+} \rightarrow Sn^{4+} + Ag^{+}$. The prepared substrate containing the silver ion patterns is then immersed in a gold electroless bath containing formaldehyde. In this bath, the adsorbed Ag^{+} ions are reduced to Ag^{0} atoms which immediately catalyses the electroless gold plating process. A schematic diagram of the processing steps is shown in Figure 2.11.

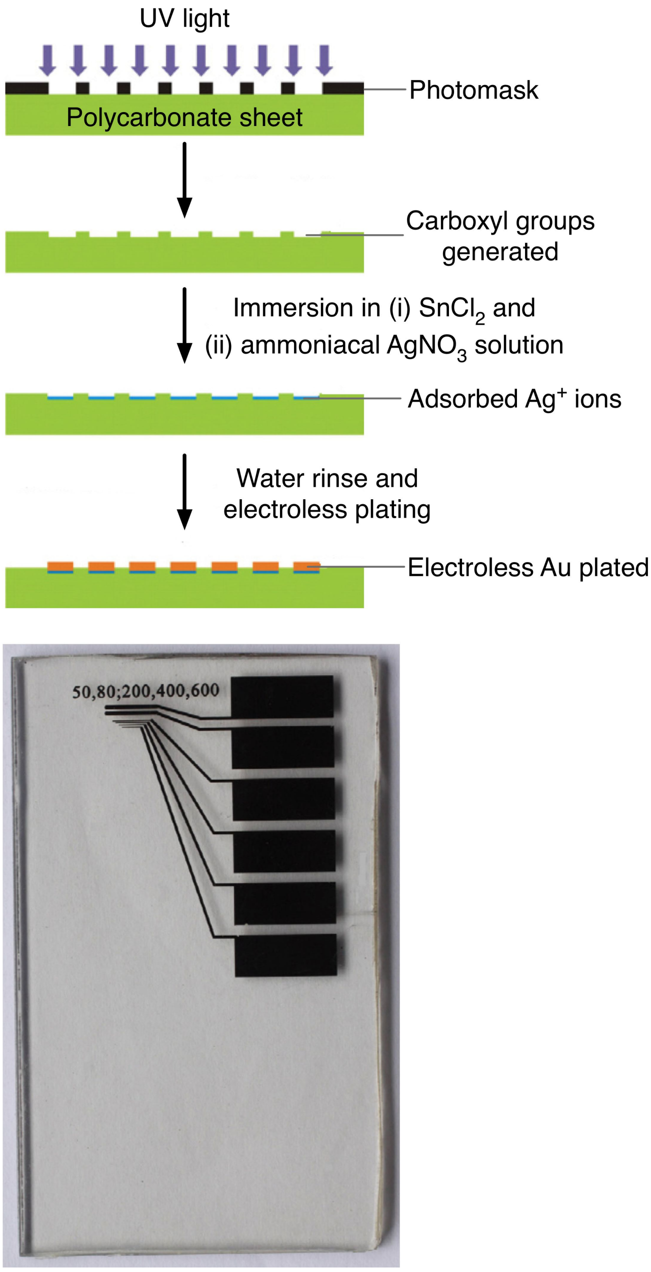

Figure 2.11: Schematic diagram of the processing steps for photolytic surface modification and photograph of electrodes electroless plated on polycarbonate. The width at the tips of the electrodes shown are 50, 80, 200, 400 and 600 μm. [19]

2.3.2. Polyelectrolytes as anchoring layers

Instead of inducing decomposition or ablation either on the metal precursors or on the substrate materials as described above, this type of surface modification technique aims to add and adhere materials onto the surface of the substrate by layer-by-layer assembly of polyelectrolytes [20]. A lot of groundbreaking research has taken place recently which highlights the emerging techniques and importance in polyelectrolyte multilayers [21]. Such techniques offer potential for “bottom up” nanoscale assembly applications. These methods mostly rely on the electrostatic attraction of oppositely charged polyelectrolyte molecules [22] although multilayer films fabricated from same-charge-carrying polymer have also been demonstrated [23]. Adsorption of a surface hydroxyl group -OH layer can create a slightly negatively charged surface on a substrate. Such an adsorption process can be achieved either by subjecting inorganic substrate materials such as glass to piranha cleaning (sulphuric-peroxide), or by exposing organic substrates like FR4 and polyimide to an ultra-violet (UV)/ozone treatment. This treatment is then followed by the immersion of the substrate into a solution of polyelectrolytes of opposite charge in an alternating manner as shown in Figure 2.12. Multilayers of polyelectrolytes with good adhesion properties to the substrate can thus be formed. This charged surface can be used as an adhesion layer for metal nanoparticles which can then serve as a catalyst for subsequent electroless plating (Figure 2.13) [24-27].

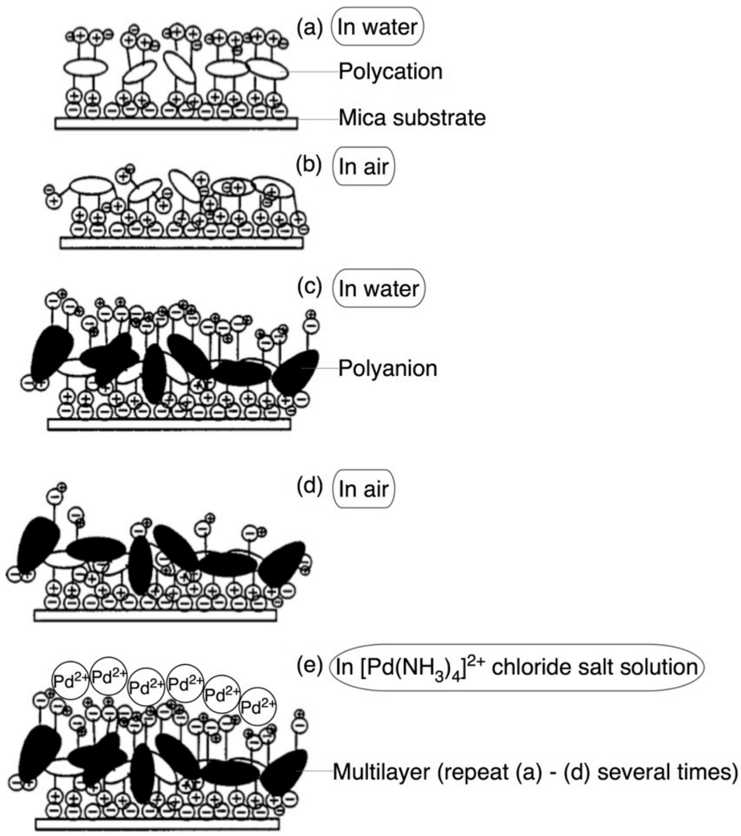

Figure 2.12: A schematic structure of the surface layer of polycation and polycation/polyanion films. The surface behaviour of the polyelectrolyte layer changes in aqueous solution and in air. Diagram modified from reference [28].

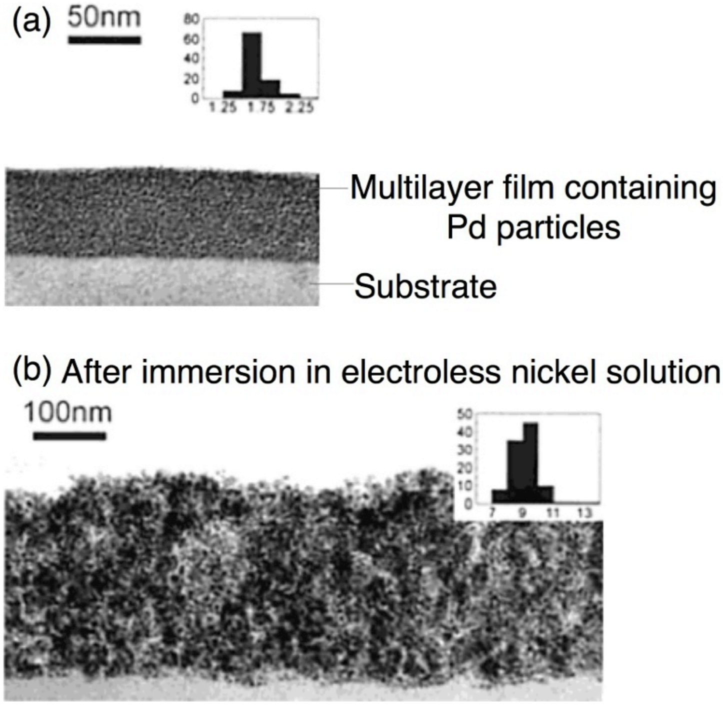

Figure 2.13: Cross-sectional TEM images of (a) multilayer film of polycation and polyanion containing in situ synthesized Pd particles (mean diameter = 1.7 nm); (b) after immersion in electroless nickel solution with 0.2 M NH_4OH for 16.5 hours (mean particle size = 9 nm) [24].

To enable the successful adhesion of the multilayers, the properties of the polyelectrolyte solution such as the type of interacting polyelectrolyte chains, the ratio of their lengths, and ionic strength and pH of the deposition solution needs to be finely tuned [29]. The multilayers usually require at least seven to ten layers of the self-assembled ultra-thin polyelectrolyte molecules to allow for good adhesion to the metal nanoparticles. This renders the process quite time-consuming. Methods for preparing multilayers have evolved to accelerate the coating process and to bring the technique out of the small-scale laboratory environment. For example, if the substrate is spun while immersed, the enhanced mass transport by convection then speeds up the deposition by an order of magnitude. This approach is referred to as hydrodynamic layer-by-layer methods. Sprayed films and other regimes of assembly methods have also been reported for preparing large areas or larger amounts of adsorbed materials requiring fewer layers [21].

To deposit polyelectrolyte selectively on a substrate, microcontact-printing via soft lithography using a polydimethylsiloxane (PDMS) master stamp have been used [30-32]. Typical procedures in microcontact printing can be found in the review [33] and from the literature by Azzaroni *et al* [34]. Figure 2.14 shows a schematic diagram of a strong covalent anchoring scheme by which a layer of polyelectrolyte is polymerised onto the first layer of initiator terminal group containing thiol and silane which is microcontact-printed onto the substrate. By utilising such polymerisation using 2-(methacryloyloxy)ethyl-trimethylammonium chloride (METAC), it provides a strong anchoring strength to the metal catalysts which are subsequently adsorbed to the polyelectrolyte layer without the need to repeat the coating of many layers of polyelectrolyte.

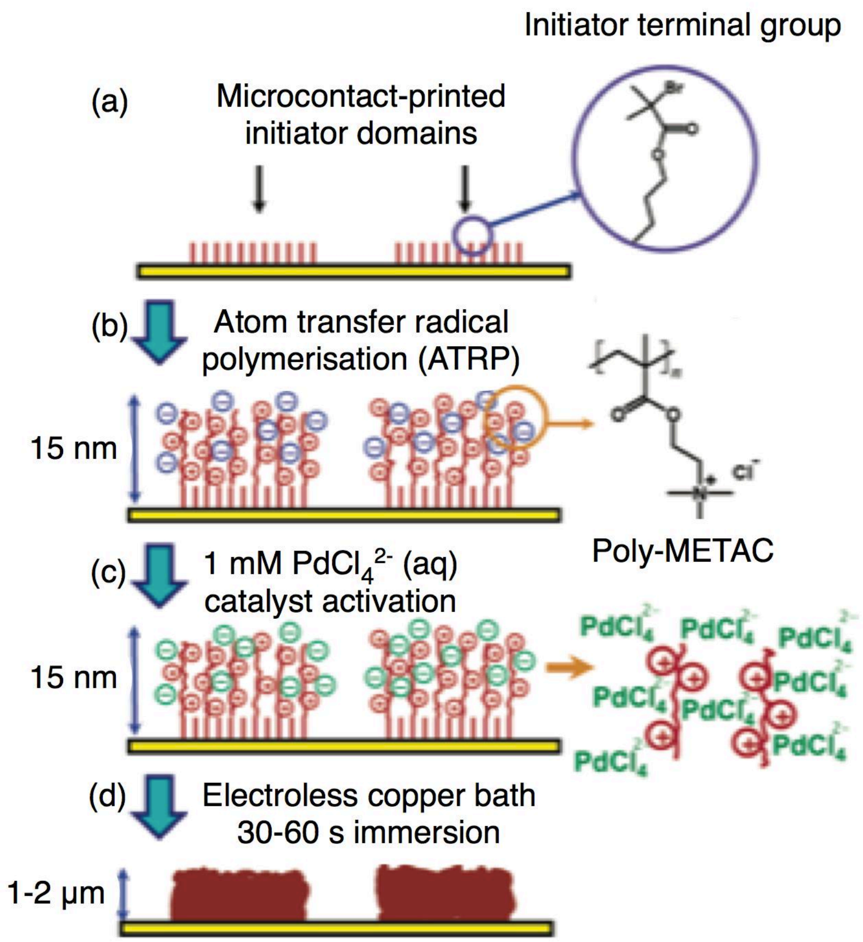

Figure 2.14: Schematic diagram of the processing steps in site-selective electroless metalisation using patterned polyelectrolyte brushes. (a) The initiator molecules are microcontact-printed on the substrate by a PDMS stamp; (b) atom transfer radical polymerisation of the polyelectrolyte brush layer takes place in an aqueous solution; (c) the cationic brushes are coordinated with the palladium catalyst; (d) standard electroless copper plating. [31]

High resolution line width and spacing can be achieved by microcontact-printing where the fine features on the PDMS stamp are fabricated by photolithography and subsequent molding and curing. The anchored polyelectrolyte layer and the palladium catalysts do not exhibit significant spreading behaviour. Figure 2.15 shows the well-defined copper microstructures fabricated by the scheme depicted in Figure 2.14.

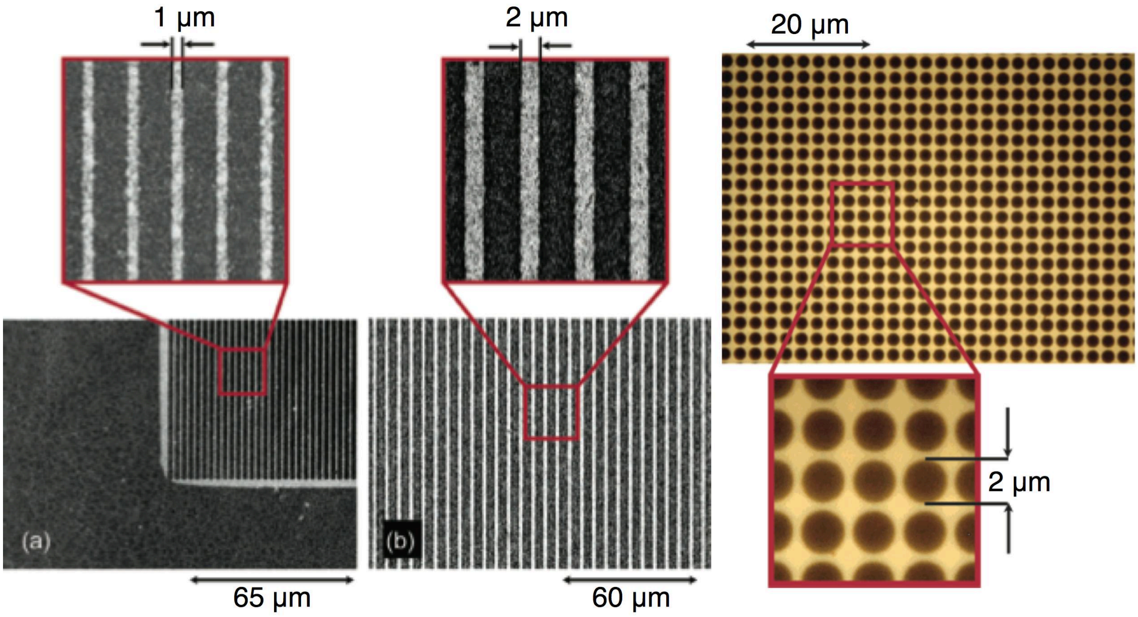

Figure 2.15: (Left) SEM images of electroless copper tracks deposited on patterned poly-METAC brushes grown on SiO_2/Si substrates: (a) 1 µm lines; (b) 2 µm lines. (Right) Optical micrograph of site-selective deposition of electroless copper dots 2 µm in diameter and ultra-fine spacing. [31]

Polyelectrolytes can also be patterned by ink-jet printing [35]. Alternative to the additive method, shorter chain molecules such as self assembled monolayer (SAM) can be ink-het printed and act as a masking resist for subtractive copper etching [36]. The branch of ink-jet printing deposition technology is described in the next Section.

Metal deposition via polyelectrolyte methods remains a rapidly expanding field of research and holds potentials for being implemented into a device production line and for fabrication of nano-scale feature resolution [26]. However, much research is still needed into the fundamental chemistry, the dynamics of polyelectrolytes and the choice of the charge-carrying-polymer systems.

2.3.3. Ink-jet printing

Ink-jet technology has become increasingly important during the past decade, particularly because of its popularity in low-cost desktop printers. An early report describes the use of a laboratory prepared platinum sol to replace the ink in a cartridge of a common desktop Hewlett-Packard printer with a resolution of 300 dpi for printing platinum catalyst directly onto polyethylene terephthalate (PET) transparency sheets for subsequent electroless metal deposition [37]. Since then, the trends in ink-jet printing technology have been to continuously enhance the printing quality and speed by:

(i) Reducing droplet size.

(ii) Increasing the number of channels per head.

(iii) Increasing ejection rates.

(iv) Reducing problems such as crosstalk between channels and satellite droplets.

Generally, the variation of the size of the drop size is about 5 - 10%. When combined with other factors such as uniformity of substrate properties, plating variation, operation deviation etc., the total blurring deviation of the line formed on the substrate is larger. The line width strongly depends on the drop size of the ink and is controlled by the orifice of the nozzle and the jetting energy. For example, the minimum volume size of droplet from a fine ink-jet head is roughly 2 pL that is 16 µm in diameter as a sphere. The drop, after landing on the substrate, will spread by a factor of 1.5 at the minimum, depending on the surface property of the substrate [35]. Particularly for printing on metal and glass surfaces, the spread factor is between 2 – 4 for aqueous fluids in most cases [38]. Development of ink-jet technologies different from piezo-drive or thermal-drive ink-jet systems was reported to produce super-fine droplet [38]. In addition, with the use of a proprietary paste of trade name NanoPaste™ (Harima Chemical Inc., Osaka, Japan) allowed the production of super-fine droplets measuring less than 1 µm in diameter, ultra-fine line width of about 3.6 µm and space of 1.4 µm on polyimide has been produced [38]. Figure 2.16 shows the fine patterns produced by this printing technology, however the technical details have not been released due to commercial confidentiality.

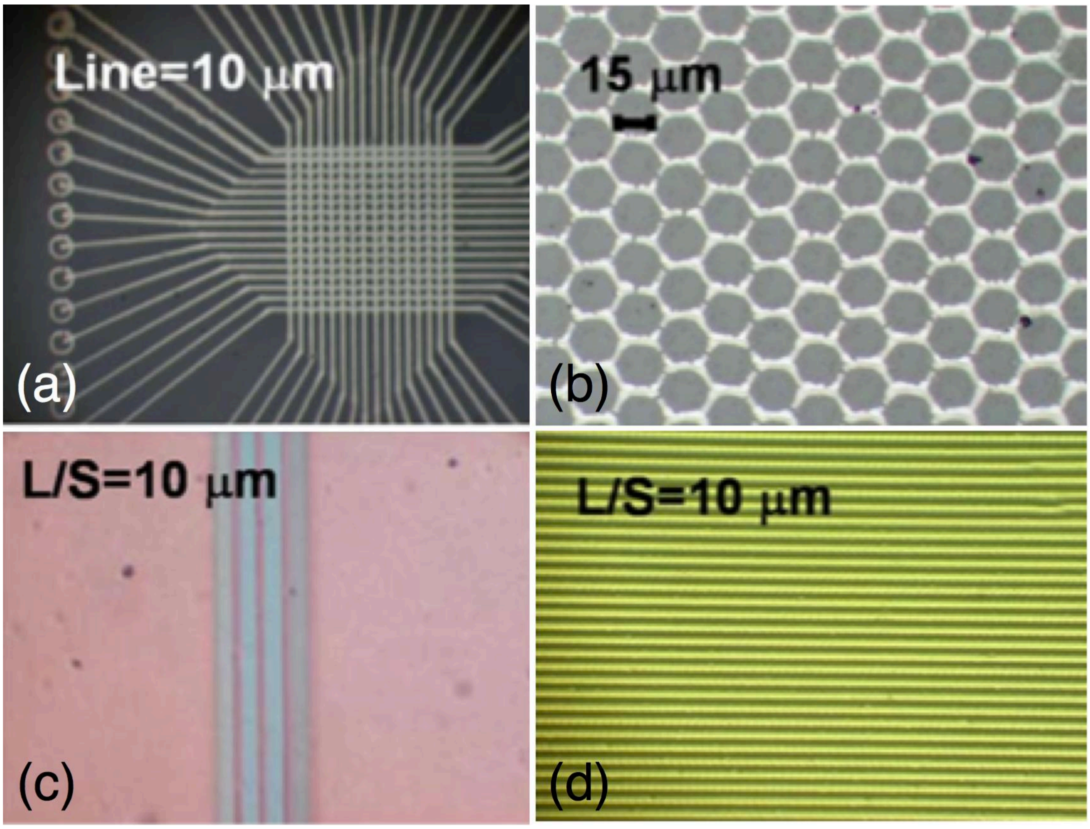

Figure 2.16: Optical micrographs of fine patterns using silver NanoPaste™. (a) Circuit pattern (line width 3 µm, 10 µm pitch at lattice area); (b) network of fine wires; (c) ultra-fine lines with line width about 3.6 µm and spacing of 1.4 µm; (d) array of lines with 10 µm line width and 20 µm pitch. [38]

Another way to reduce the droplet size is to convert the metal ink into an aerosol through the use of an atomizer. Applications of such aerosol jet printing metalisation have been reported where ultra-fine feature size and high speed and precision printing can be realised. Development in this area is fairly new and is beyond the scope of this thesis [39], [40].

Besides the problems of minimum ink droplet size, nozzle clogging, low metal density inks (typical solid fraction can be 20 wt% which corresponds to ~2 vol%), and directionality of the printed ink, a major challenge of a direct ink-jet nanoparticle process is the ink formulation. The inks must contain the appropriate precursors and a carrier compound, and may further contain various binders, dispersants, and adhesion promoters, depending on the nature of the precursor and the particular application. Ink composition is critical because it defines the process in which the ink is jetted, the adhesion to the substrate, the line resolution and its profile, and the electronic properties of the formed metal. Some recent reports using pre-manufactured metal nanoparticle ink showed that some printed silver tracks with line width of 40 μm have conductivity 13 - 23% of the bulk silver [41-43].

Another challenge is the requirement of a sintering post-process for the metal thin film to have a good electric property and adhesion to the substrate. Figure 2.17 illustrates the sintering process for typical metal nanoparticle inks. Usually, the sintering is carried out at a high temperature of 300°C or higher, which limits the range of substrates that can be used, particularly amongst the organic substrates used in flexible electronics. However, low temperature sintering processes for silver inks using microwave [44] and laser-assisted sintering [45], chemical conversion [46], electrical sintering [47], [48], and plasma treatment [49] have recently been explored. Figure 2.18 shows a cross-sectional image of a printed contact pad exhibiting a porous structure, indicating incomplete sintering.

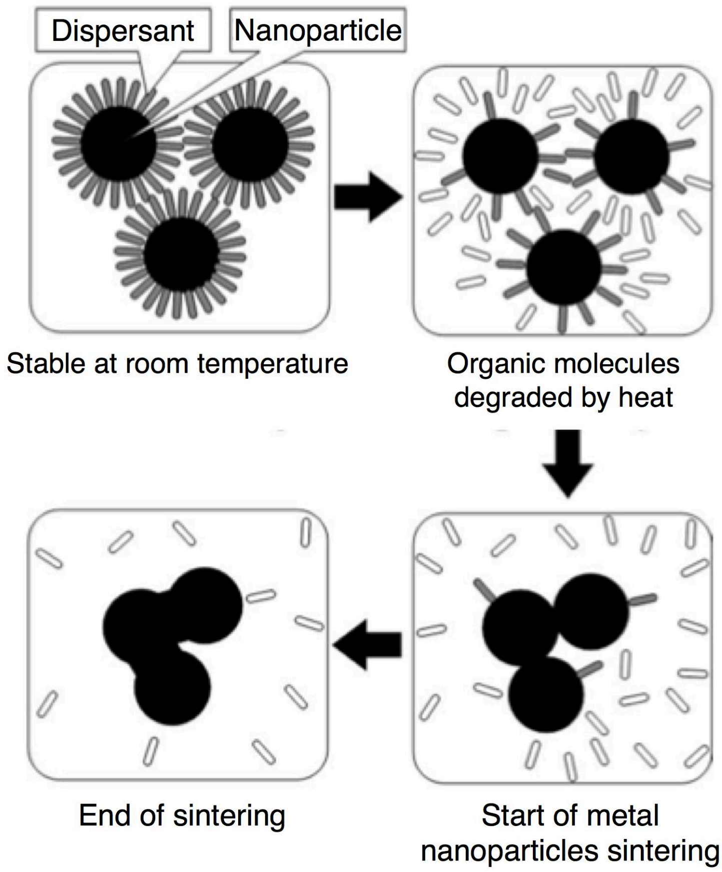

Figure 2.17: Schematic diagram of the sintering process for metal nanoparticle ink. Diagram modified from [38].

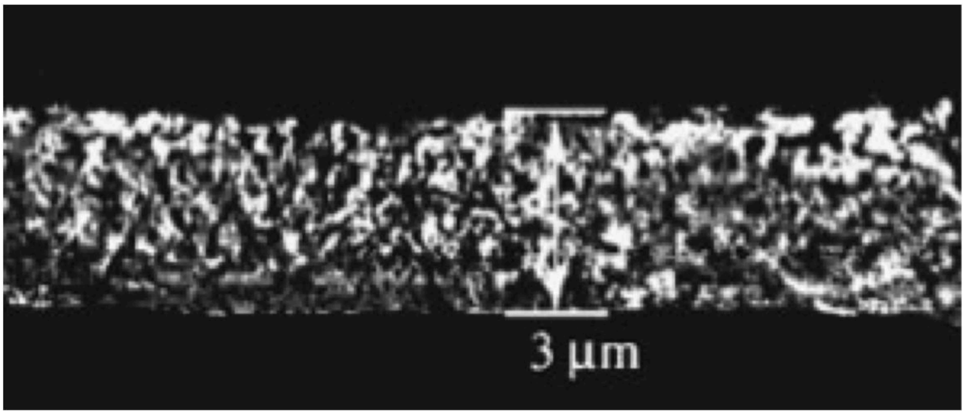

Figure 2.18: Cross-sectional SEM image of a contact pad created by printing silver nanoparticle suspension ink, sintering at 300°C for 15 minutes. The porous structure suggests incomplete sintering [50].

In a different approach [35], a flexible substrate is first treated by self-assembled polyelectrolytes to enhance its adhesion; this eliminates the binder content normally required in the ink-jet ink and, as a result, higher printing quality can be achieved. In addition, the ink has changed to a water-based catalyst ink which has dissolved metal ions such as palladium ions in order to avoid the sintering process needed for printing metal nanoparticles. A comparison between a conventional metal nanoparticle ink and a water-based ink containing dissolved metal ions is illustrated in Figure 2.19. When the water-based ink was dried, the palladium ions diffused into the monolayer of the self-assembled polyelectrolytes and adhered onto the substrate surface. The printed pattern of palladium ions serves as the catalyst for initiation of subsequent electroless deposition.

There is a continuing development in particle-free ink with metal ions dissolved in water or simple polymer solutions in order to eliminate the binder and dispersant in the ink composition [46], [51], [52]. Silver ions have been used in these studies and the printed patterns have been converted to metallic silver directly by reduction.

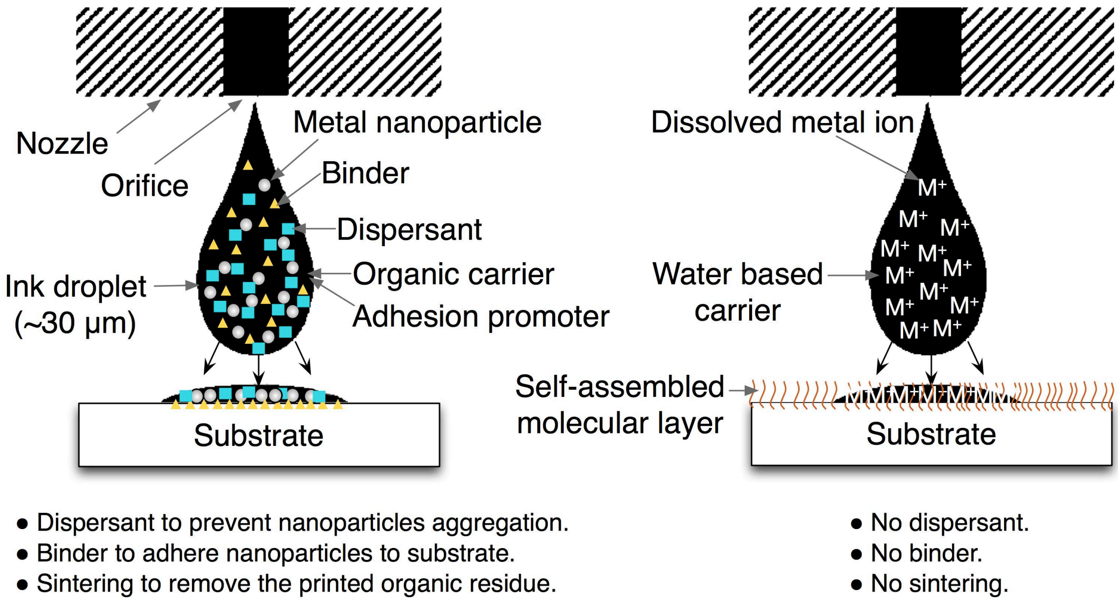

Figure 2.19: Comparison between a conventional metal nanoparticle ink and a water-based ink containing dissolved metal ions.

In summary, the printing ink formulation is very important in ink-jet printing technologies. Proprietary ink containing synthesised nanoparticles can be costly. In addition, the resolution of the printed feature size depends on a multitude of factors such as the drying mechanisms of the ink, the fluid dynamic relationship between the ink and the nozzle used, the interfacial properties between the printed nanoparticle catalytic layer and the subsequent electroless metal layer, the printed profile of the nanoparticle tracks which can lead to irregular and anisotropic growth of the electroless layer. Therefore, the resulting final metal deposit can have resistivity values several times bigger than that of its bulk metal counterpart [35].

2.3.4. Reduction of embedded metal ions

If the substrate already contains the "resource" for metalisation, i.e. the metal ions within itself, metal nanoparticles can be formed *in-situ* within the substrate. This minimises the difficulties arisen in the methods described so far inasmuch that:

(i) Requirements of anchoring mechanisms at the interface between the foreign metal layer and the substrate material are reduced. There is no need for thermal sintering to nucleate the foreign metal on the substrate, or for creating electronically active sites by breaking chemical bonds on the substrate material to adhere the foreign metals.

(ii) The removal of the carrier medium for the foreign metal material e.g. a solvent, an anion solution or an organic complex solution is omitted. Organic residues can affect conductivity of the metal deposit.

This is the route chosen in this thesis which focuses on the development of an additive metalisation process for incorporation of the metal source into the substrate. Metal ions can be incorporated into a thin layer of the surface of the polyimide substrate by ion-exchange in a simple metal salt solution after pretreatment by potassium hydroxide (KOH) hydrolysis [53]. The alkaline hydrolysis of polyimide and ion-exchange is described in Chapter 3.3. The central concept of this type of metalisation techniques is the following: mobile metal ions available on the surface of the substrate can be reduced to their zero-valent state by gaining electrons, resulting in a metallic layer. Whilst the direct electrical supply of electrons by external voltage is not an option for non-conducting substrates, the reduction of these metal ions can be achieved by electrons transferred from neighbouring molecules via either thermal, chemical or optical techniques. Figure 2.20 illustrates these three different schemes. The particular different reduction methods for metalisation of the embedded metal ions on polyimide substrate are summarised in Chapter 3.4.

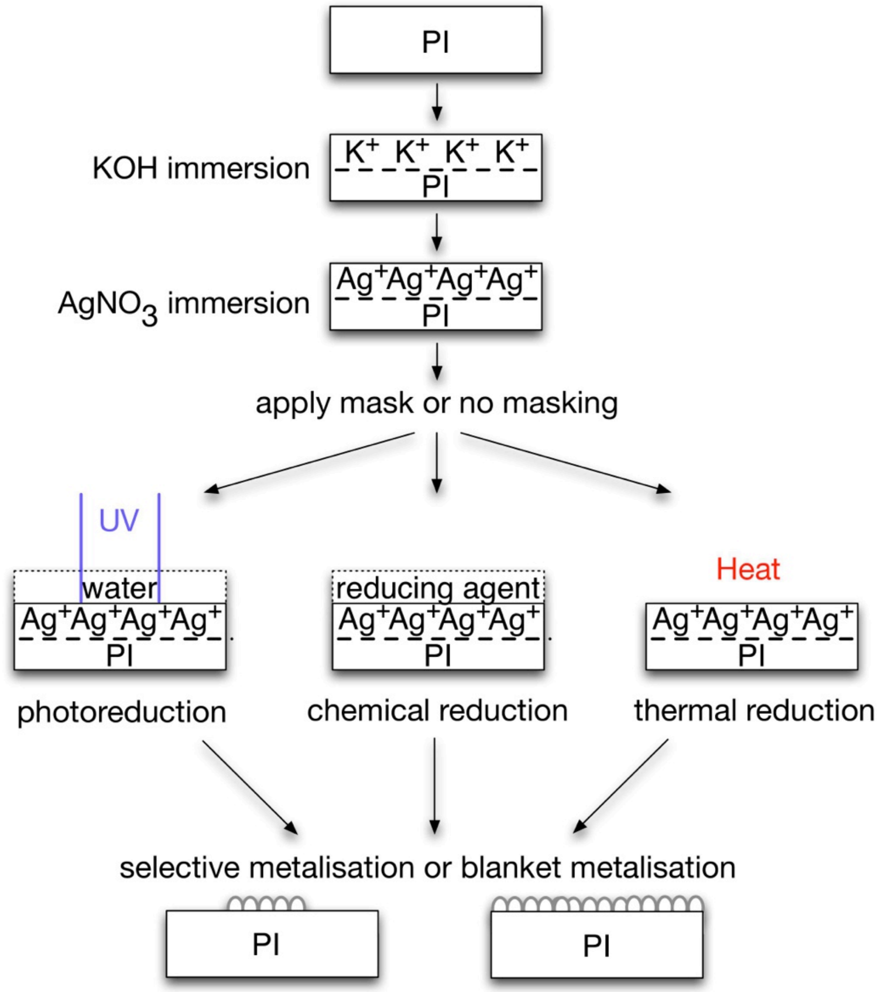

Figure 2.20: Schemes of metalisation of polyimide. The photoreduction route is described in this Section. Silver is used as an example. Some other metal ions are also possible for incorporation into the substrate. See Chapter 3 for literature examples of chemical and thermal reduction and incorporation of other types of metal ions.

Photoreduction is the chosen metalisation method in this thesis to reduce the embedded metal ions. An example of prior work by Akamatsu *et al* [53] uses a water layer to accelerate, i.e. catalyse, the photoreduction of silver metal ions incorporated into polyimide substrates (the photoreduction route in Figure 2.20). This route is attractive because it is a non-contact, light-directed, additive process where no heat treatment is involved in the patterning step. Excellent spatial resolution and temporal control is expected for such a room temperature process. The use of harmful strong chemical reducing agents is also avoided. Silver nanoparticles are formed *in situ* and well defined circuit features can be produced by UV exposure through a photomask as shown in Figure 2.21. However, the use of a liquid (water) coating in the process makes the handling of substrates inconvenient. There is therefore a need to search for a rigid solid coating that could serve the purpose of water in catalysing the photoreduction reactions. Such materials, referred to as photo-reducing agents, are introduced in Section 2.4.1 as part of the Route 3 category of this review.

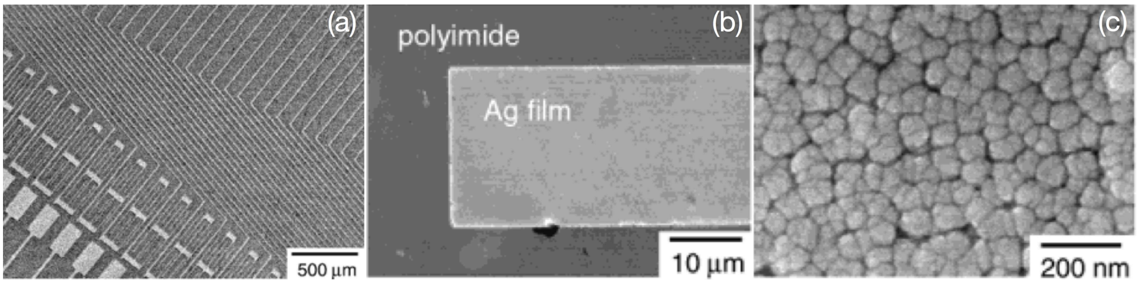

Figure 2.21: FEGSEM images of (a) silver circuit patterns formed by UV irradiation for 60 minutes through a photomask with a water layer coating, on a KOH modified, silver ion-exchanged polyimide substrate. (b) and (c) are higher magnifications of (a). [53]

2.4. Photocatalysis-mediated deposition

Route 3 as illustrated in the chart in Figure 2.1 represents the employment of materials with the ability of donating electrons or radicals upon light irradiation. Consequently, the transfer of the excited electrons or radicals reduces nearby metal ions to zero oxidation state, thereby resulting in aggregation of metal atoms to nanoparticles and eventually a layer of metal thin film. These types of reduction of metal ions can be broadly termed as "irradiation-assisted synthesis" while the materials assisting the liberation of electrons or radicals so that the reduction could occur are known as photocatalysts or photo-reducing agents. There are various compounds that can serve as a photo-reducing agent which can be either an organic or an inorganic compound. Each of these compounds involves tailored mechanisms of physics and chemistry in the release of electrons or radicals upon excitation by photon energy. This section introduces some examples from this relatively new field for metal deposition.

In Section 2.4.1, organic photo-reducing agents are introduced. Two novel organic compounds as photo-reducing agents for thin film metalisation have been discovered through the research in this thesis. These two materials can be used as a rigid solid coating on top of a metal ion-doped polyimide substrate as described in the last Section. The backgrounds and chemistry of these two different compounds, namely methoxy poly(ethylene glycol) (MPEG) and chlorophyll, are described in detail in Chapter 3. In Section 2.4.2, the photocatalysis by a semiconductor for metalisation is introduced.

2.4.1. Organic photo-reducing agents

A polymer material able to be excited by light to activate its reducing power would be an excellent alternative to the water film used in the catalysis for the photoreactions mentioned in Section 2.3.4. In the field of metal / inorganic nanoparticles synthesis research, photochemical synthesis has remained a relatively new topic until recently. Only a small emphasis on "radiation-assisted reduction" is presented in the two review articles published in 2002 [54] and 2004 [55] on the methodologies in preparing metal / inorganic nanoparticles mostly involving reduction of metal ions within a solution phase. Within this category, the majority of these early techniques employed deep UV irradiation or high energy γ-radiation for direct photolytic dissociation of water molecules to liberate radicals or electrons.

A timeline of the research in organic photo-reducing agents is shown in Figure 2.22. Except the work carried out in this thesis between 2007 and 2010 with MPEG and chlorophyll, all prior work employing organic photo-reducing agents describes the production of metal nanoparticles capped by polymer chains in a one-pot solution synthesis as shown in Figure 2.23. At the start of this decade, a popular surfactant polymer used for dispersing metal nanoparticles had a trade name called Triton X-100, chemically named as poly(oxyethylene)iso-octylphenyl ether, was used as a polymer photo-reducing agent for reduction of Au(III) ions in a simple chloroauric acid ($HAuCl_4$) [56]. It was reported that the surfactant polymer has a dual function of a stabiliser - dispersing and capping the metal nanoparticles in regular sizes, and reducing the Au(III) ions under irradiation of UV light at 254 nm wavelength. The irradiation took 25 minutes using a 15 W germicidal lamp at a 3 cm distance. Sparse gold nanoparticles in the reaction solution were produced as shown in the TEM image in Figure 2.24. Earlier efforts in using other popular simple polymers such as polyvinyl alcohol (PVA) and polyethylene glycol (PEG) to carry out similar experiments required up to 48 hours at 254 nm irradiation [57]. Metal nanoparticles were more commonly synthesised via a thermal reduction assisted by a widely used polymer poly(N-vinylpyrrolidone) (PVP) which activates its reducing power upon heat.

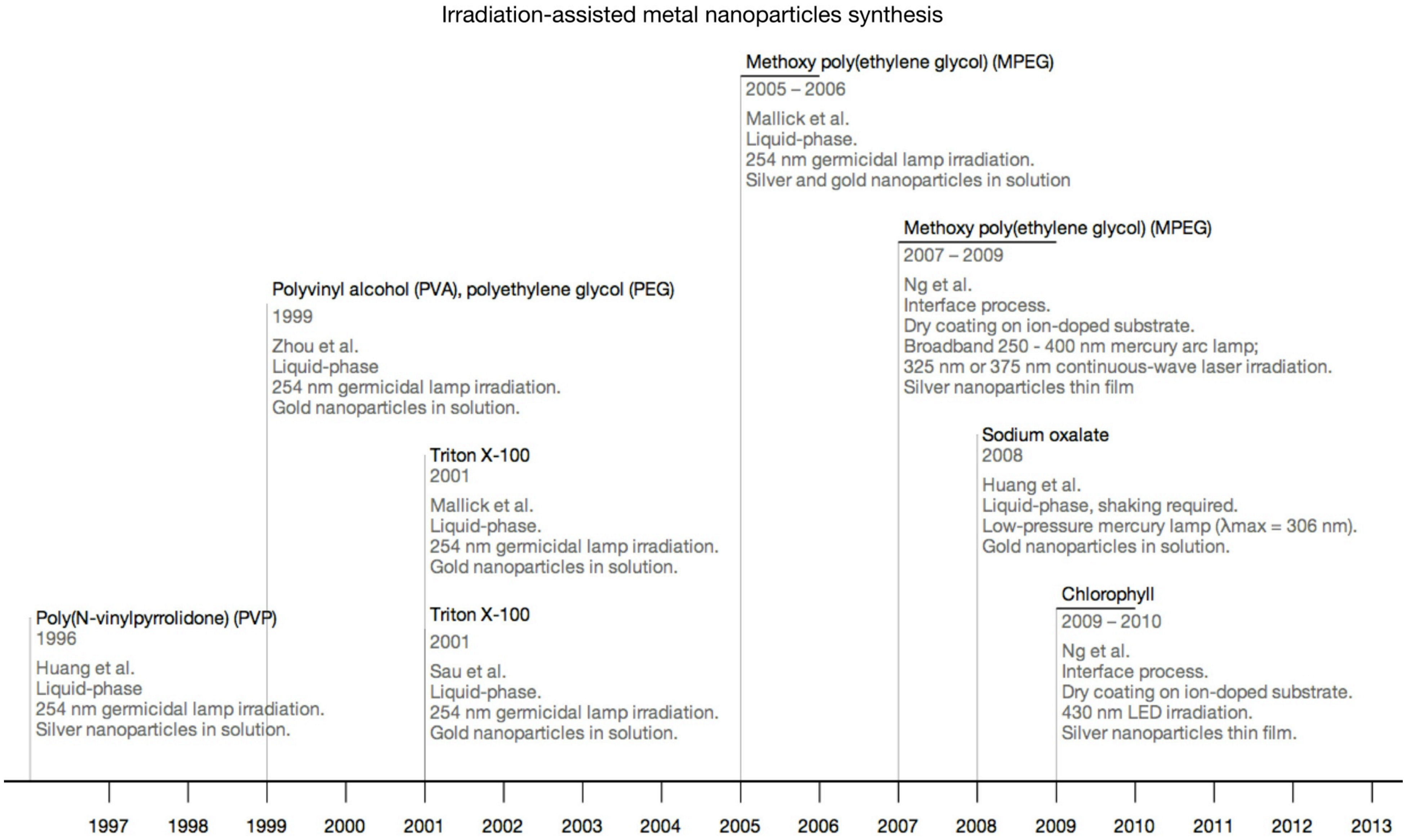

Figure 2.22: Timeline of publications describing some organic photo-reducing agents used for metal nanoparticles synthesis.

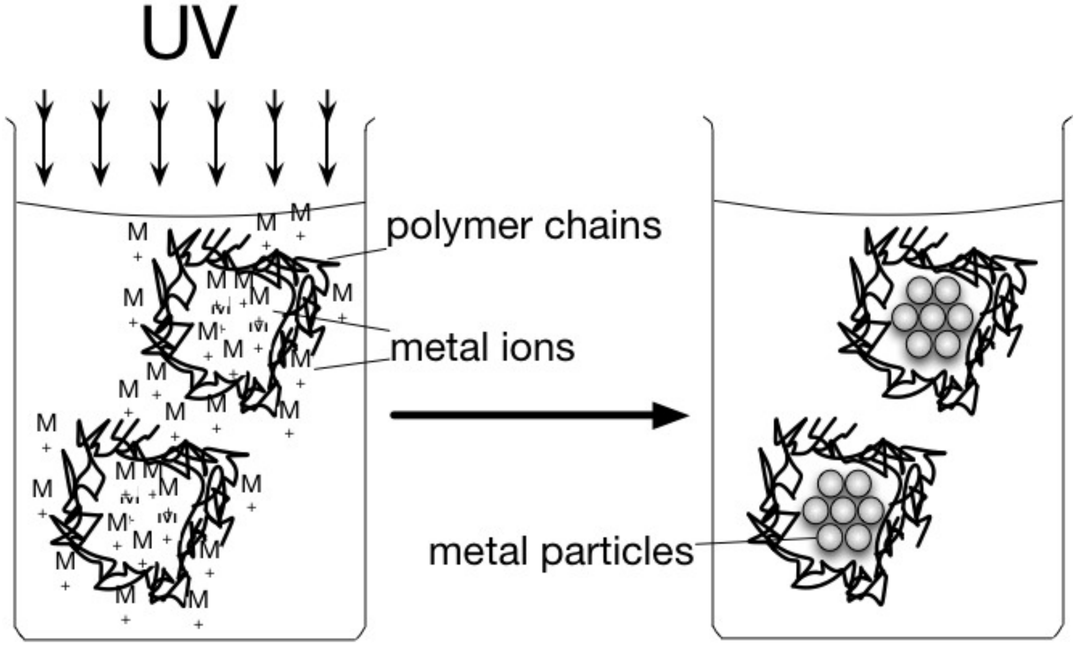

Figure 2.23: Schematic diagram of photoreduction of metal ions using a polymer as the reducing agent and the capping agent to form metal nanoparticles in a one-pot synthesis solution.

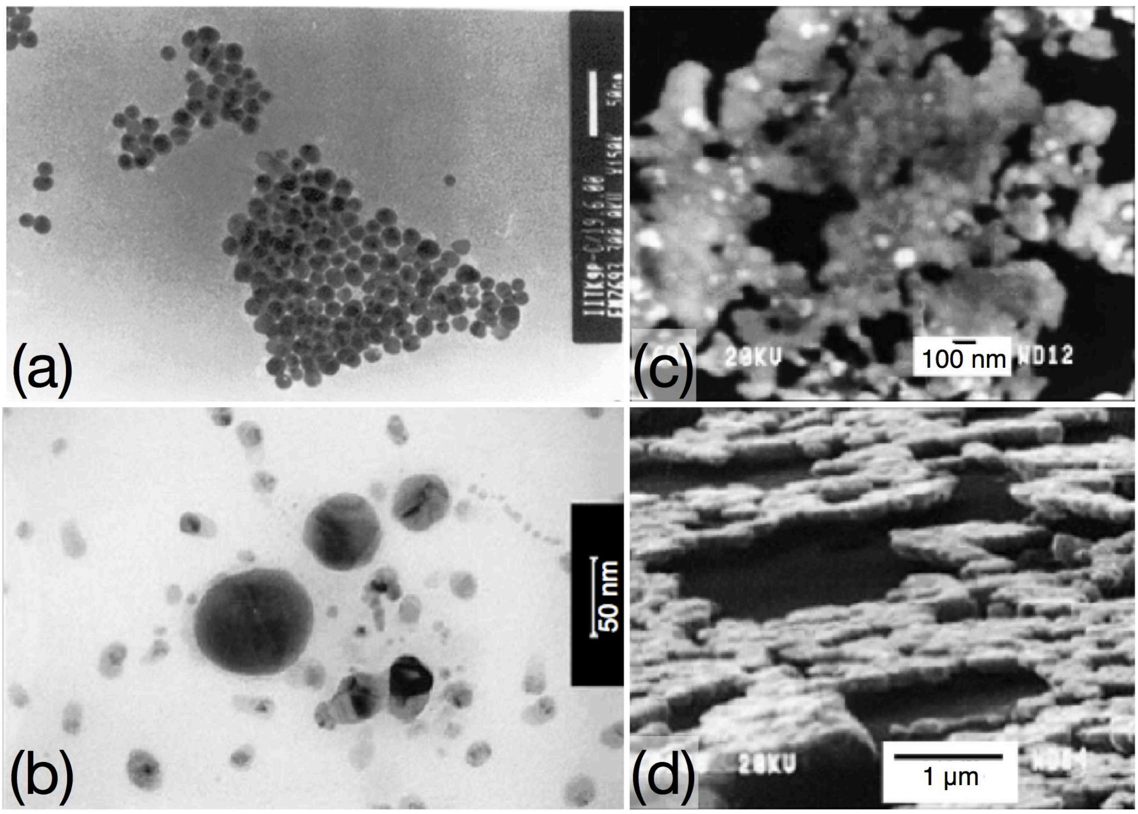

Figure 2.24: (a) TEM image of Au nanoparticles prepared from a $HAuCl_4$ and Triton X-100 aqueous solution after 25 minutes of UV irradiation [56]; (b)TEM image of the Ag nanoparticles after 3 minutes UV irradiation of $AgNO_3$ and MPEG solution mixture; (c) Secondary electron SEM images showing a planar view of the morphology of the silver film exhibiting metallic silver reflectivity after 30 minutes UV irradiation, and (d) a cross-sectional view of the film when it was tilted 80° to the horizontal. The film thickness is estimated to be ~0.2 µm [58].

Also in 2001, Mallick *et al* [59] reported the use of Triton X-100 for photoreduction of the chloroauric acid ($HAuCl_4$) solution; similar results were presented along with the chemical pathways of radicals liberation and explanation of the growth of metal nanoparticles. Between 2005 to 2006, the same group of researchers demonstrated the use of a novel photo-reducing agent methoxy poly(ethylene glycol) (MPEG) for photochemical reduction of Ag^+ and Au^{3+} ions from their salts, $AgNO_3$ and $HAuCl_4$ respectively, to metal nanoparticles in a one-pot aqueous solution [58], [60-63].

A later paper in 2008 [64] reported the use of sodium oxalate as an organic photo-reducing agent with the aim of shortening the UV irradiation time required using a 8 W, low-pressure mercury lamp (λ_{max} = 306 nm). Illumination times of 10 - 120 minutes generated different concentrations and properties of gold nanoparticles. However the reaction vial was required to be shaken at 200 rpm during the UV irradiation to assist the reactivity of the photoreduction, a procedure that is not possible in the proposed use of a standalone coating of polymer reducing-agent.

The fact that metal ions dissolved in the ternary reaction solution can be reduced to metal atoms directly in a simple UV irradiation experiment is encouraging for the proposed configuration where a polymer reducing agent is required to coat on top of a substrate containing free metal ions. Unlike the one-pot solution-phase process, the metal ions are in the vicinity of the polymer molecules which can readily act as the reducing agent within the solution as shown in Figure 2.25. The proposed interface reaction requires the liberated electrons or radicals to travel from the polymer coating across the polymer / substrate interface and reach the free metal ions within the substrate. More detailed discussions in this regard will follow in Chapter 3.

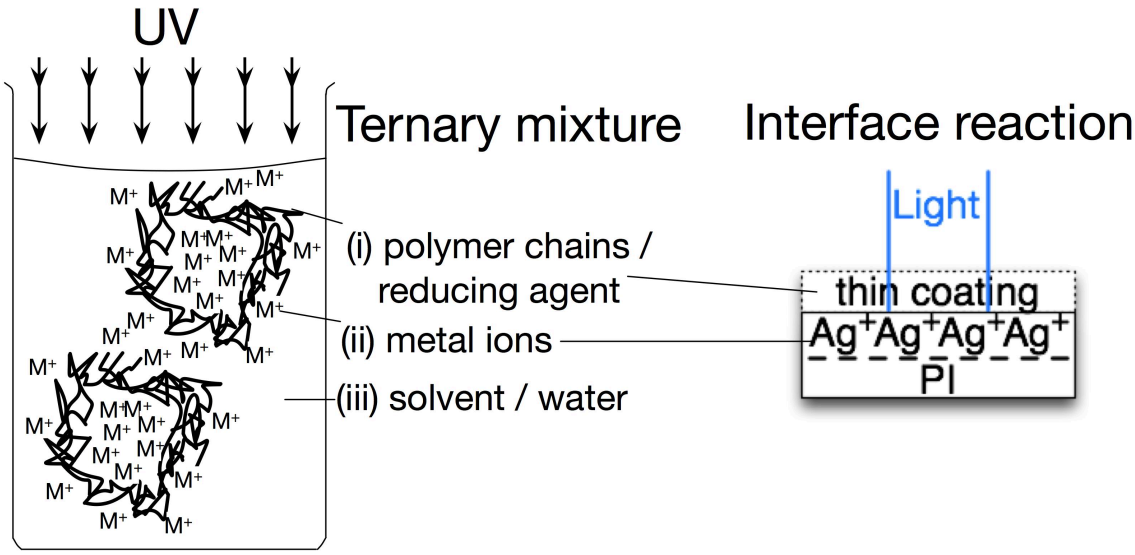

Figure 2.25: Schematic diagram of a ternary mixture and the interface reaction set up.

2.4.2. Photocatalysis by TiO_2 and Si

Semiconductor materials can also be photo-reducing agents for the liberation of electrons for metalisation. In the last Section, the organic photo-reducing agents are polymer chains which are either dissolved with the metal salts together in the same solution phase or served as a sacrificial coating. Here the solid semiconductor materials are often used as the substrate itself. Therefore the photoreduction process takes place *on top* of the surface of the semiconductor which makes the crystalline form critically important for the success of the photo-catalysed metalisation. These methods are also limited by the fabrication process of the semiconductor layer onto the target substrates.

Electron-hole pairs are created when the incident photon energy is larger than the bandgap energy of a semiconductor substrate. The utilisation of these photo-excited charge carriers for subsequent reactions is generally referred to as semiconductor photocatalysis. Some key factors that determine the success of metalisation by semiconductor photocatalysis include:

(i) Adsorption of free metal ions on to the surface of the semiconductor.
(ii) The lifetime of the photo-excited electrons.

(iii) The transfer rate of charge carriers within the semiconductor crystalline structure.

The basic mechanisms of semiconductor photocatalysis for metal deposition are depicted by the schematic diagram in Figure 2.26 below.

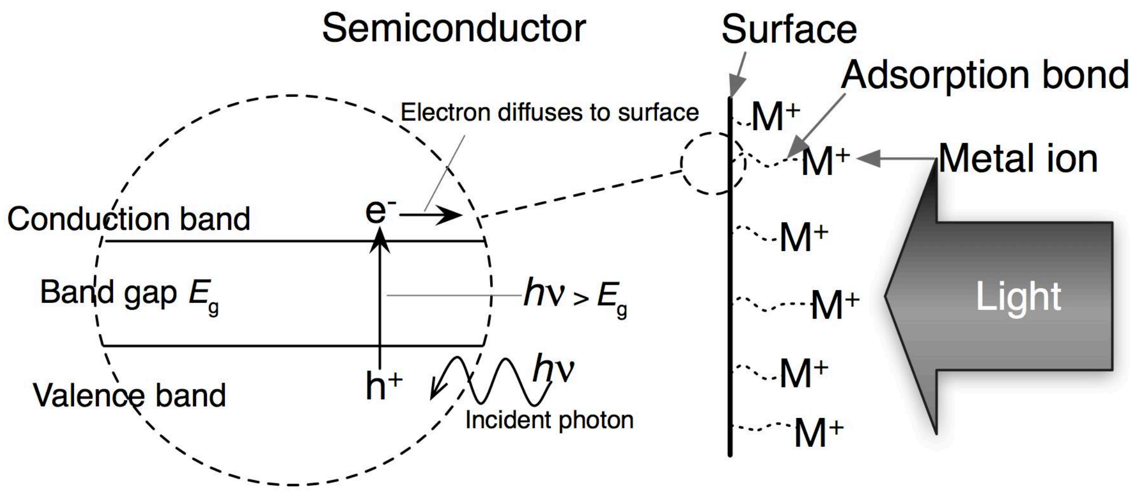

Figure 2.26: The basic mechanisms of semiconductor photocatalysis for metal deposition.

Metal oxide semiconductors, in particular, TiO_2 show the best photocatalytic efficiency in utilising the photo-excited charge carriers [65]. Electron traps and surface-trapped holes are produced at the semiconductor surface as molecular oxygen and hydroxyl groups and are easily adsorbed on TiO_2 surfaces [66]. These groups can suppress the recombination of the electron-hole pairs which take place within a nanosecond timescale. The fundamental physical mechanisms governing the interfacial electron transfer are non-trivial and much research work is still needed to understand the influence on the photocatalytic efficiency from doping [67], defects, energy band bending, epitaxial growth, adsorption and reaction of organic molecules, etc. [66]. Therefore a large body of literature in the preparation techniques of TiO_2 films can be found owing to the substantial research interests in their photocatalytic properties recently, largely driven by metalisation for microsystems and solar cells applications [68-70]. A recent review on the photocatalytic properties of TiO_2 nanoparticles can be found in reference [71].

The electronics manufacturer Samsung has heavily invested in the research of this metallisation approach using TiO_2 photocatalysts [72-77] and has filed many patents related to the applications of using such fabrication techniques in recent years [78-84]. An example from reference [73] describes a method where a uniform layer of amorphous TiO_2 is first deposited onto a glass substrate by spin-coating and baking of a thin film of *n*-butyl polytitanate (Tyzor® BTP, DuPont, 5% in 2-propanol) as shown in Figure 2.27. An additional layer of polyvinyl alcohol (PVA) is coated on top of the amorphous TiO_2 layer. The PVA film acts as a hole scavenger which suppresses the recombination of the excited electron with the positive hole, thereby prolonging the lifetime of the excited electron and enhancing the reduction reaction of the metal ion. A low power intensity UV lamp (4.5 mW/cm^2 at 314 nm) and a short exposure time of 15 s are used. The substrate is immersed in an aqueous solution of palladium salt for 1 minute to deposit palladium on the exposed areas of the TiO_2 surface. Line width broadening was observed depending upon several factors such as TiO_2 thickness, film baking temperature, and UV exposure energy. This phenomenon is considered to be caused by electron transfer on the TiO_2 layer. When the photomask with patterns of 10 μm line width is used, the line width of the subsequent electroless copper patterns is about 20 μm as the copper thickness reaches 3 μm. The copper films prepared by electroless plating or electroplating show resistivity of less than 3 μΩ cm.

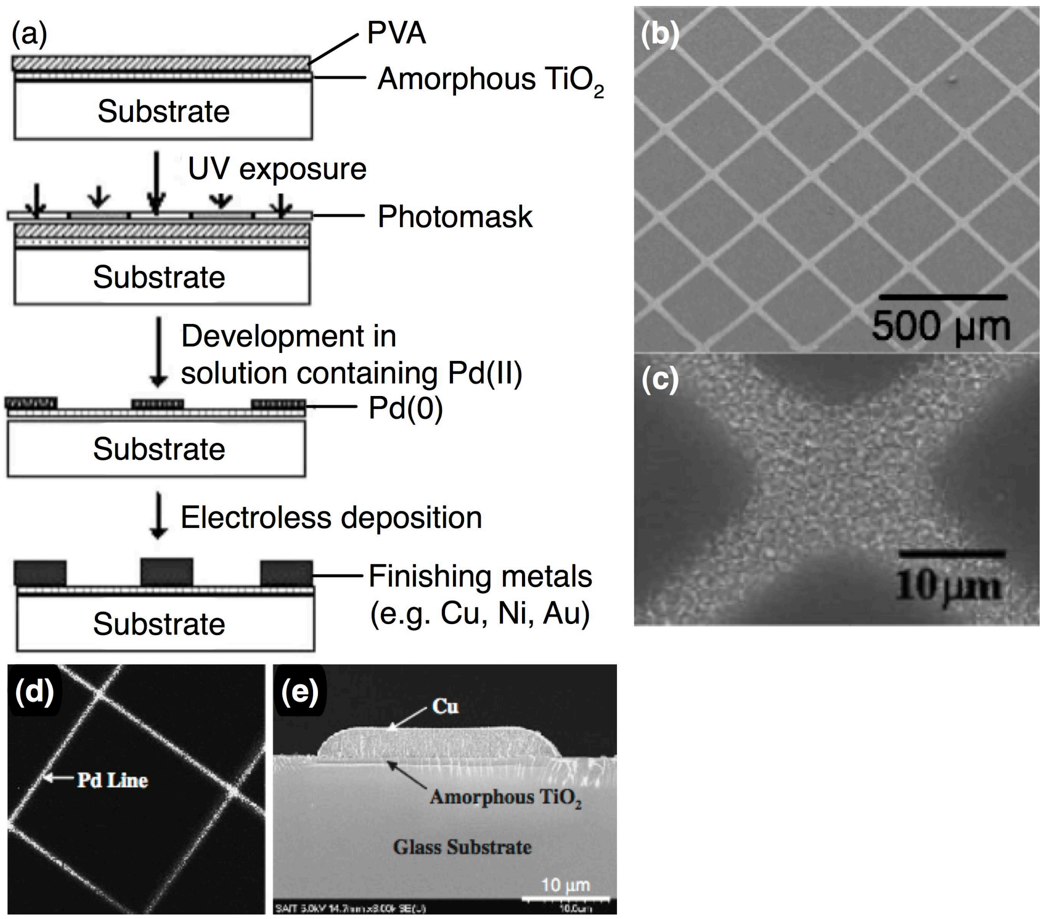

Figure 2.27: (a) Schematic steps of selective metalisation using a layer of TiO_2 as photocatalyst; (b) SEM image of Ni film electrolessly deposited on top of the patterned palladium; (c) carbon nanotubes immobilised onto the nickel film shown in (b); (d) TOF-SIMS image of the palladium metal patterns on the UV exposed areas; (e) SEM cross-sectional view of the substrate (d) after copper electroplating. [73], [75]

Besides TiO_2, porous silicon also displays similar photocatalytic deposition ability as demonstrated by Kordas *et al* [8], [85], [86] using Ni, Pd and Ag electroless solution and irradiation by a CW-Ar ion laser. Similar photocatalytic-mediated metal ion reduction has also been studied on p-type silicon [87].

The utilisation of photocatalysis can also extend to the decomposition of materials surrounding the semiconductor. Using a TiO_2-Au nanocomposite film, a laser-induced forward transfer (LIFT) process where metallic materials can be transferred to a substrate placed at a certain distance underneath the precursor film was achieved by a Nd:YAG laser [88]. Upon UV-laser irradiation from the backside of a UV-transparent support ribbon, part of the precursor material originally adhered to the ribbon is released from the ribbon and transferred onto the target substrate. A review of LIFT using a variety of UV-absorbent reagents and specific techniques was published recently [89].

2.5. Photochemical reduction of organometallic compounds

This Section describes Route 4 as illustrated in the chart in Figure 2.1. This category, still in its infancy, is attractive for three reasons:

(i) The patterning is directed by light only;

(ii) No intermediate layers of photocatalysts or polymers that assist adhesion, charge carrier suppression or masking are required; and

(iii) The final metal deposit is formed by the light (usually UV) energy alone; in other words, no subsequent electroless plating is required.

A carefully formulated chemical compound containing a metal core and organic ligands, known as organometallic compounds, undergoes a series of mechanisms triggered by irradiation of light (usually in the UV wavelength region) and resulting in the reduction of the metal core into a neutral metal atom. These mechanisms can include cleavage of the binding bonds to the metal core, formation of organic radicals and abstraction of hydrogen atoms from neighbouring molecules, etc.

Table 2.2: Selected examples of photochemical synthesis of the important metals used in microsystems.

Metal	Precursor / Method	Nanoparticles/Thin Film	Year	Reference
Copper	Copper(II) acetylacetonate, $(C_5H_7O_2)_2Cu$ - Laser irradiation of solution through quartz in a Pyrex vessel. - ArF laser at 193 nm, 30 mJ/cm^2 and KrF laser at 248 nm, 540 mJ/cm^2, 10 Hz. - 10-30 minutes irradiation. - No anneal.	Thin film. Can be discontinuous and uncontrollable. (See Figure 2.28)	2007	[90], [90]
Nickel	Electroless nickel plating solution - Solution irradiation through a quartz cell. - 365 nm mercury lamp, intensity = 10^{18} photon/cm^2/s, 40 s - 90 minutes irradiation. - Further catalytic plating under dark in fresh solution. - No anneal.	Thin film	2006	[91]
Silver	Organo-silver complexes - $(n\text{-}PrNH_2)Ag(NO_2)\cdot 0.5CH_3CN$ and 3 other similar precursors. - Excess amount of amine (*n*-propylamine) added drop by drop to a $AgNO_3$ in CH_3CN solution, under dark and in nitrogen atmosphere, 4 hours stirring of reaction mixture. - Spin-coat on glass, silicon, plastic substrates. - Broadband UV exposure for several minutes. Power unspecified. - Anneal at 200 - 350°C in vacuum.	Thin film. 5 - 10 µm tracks. (See Figure 2.29)	2005	[92]
Gold	Electroless gold plating solution - Solution spilled on glass substrate. - 365 nm mercury lamp, top illumination, 15 minutes. - No anneal.	Thin film	2006	[93]
Palladium	Palladium acetate, $Pd(CH_3COO)_2$ - Dissolved in chloroform and frozen as a solid target. - Excimer laser irradiation, λ = 248 nm, 5 Hz, 25 ns, fluence = 0.25 0.75 J/cm^2. - No anneal.	Nanoparticles. Mean diameter between 2-3 nm	2007	[94]
Platinum	Fluoro platinum complex, cis-$(C_3F_7)_2Pt(II)\text{-}C_8H_{12})$ - Evaporation of precursor onto substrate. - 260 nm exposure at 16.5 mW/cm^2 for 2 hours. - 3 stages anneal: (i) 70°C for 6 hours, (ii) 195°C for 4 hours, both in air, and (iii) 435°C in 40% hydrogen for 2-6 hours.	Thin film (See Figure 2.30)	2004	[95]

Some pioneering work in the photochemical decomposition of gold organometallic compound in the vapour phase for projection printing of high resolution micropatterns can be found in the 1980s [96]. Several reports have emerged in more recent years (Table 2.2) concerning the solution-phase formulation of specific photosensitive metal precursor compounds for the deposition of Cu [90], [97], Ni [91], Ag [92], Au [93], Pd [94], [98], Pt [95], SnO_2 [99], Se [100] and Cr [101]. For this type of process, highly specialised knowledge is required for each type of photochemical reaction which is related to each specific compound. Moreover, the synthesis of such compounds can be very time-consuming, or a very short wavelength light source is required for the photoreduction to take place [98]. The yield of metal production, its quality, density and conductivity versus time of irradiation, might not be very high. Some improved formulae required exposure time of several minutes [92], while the others [102-104] need a long time of light exposure from a few hours to hundreds of hours.

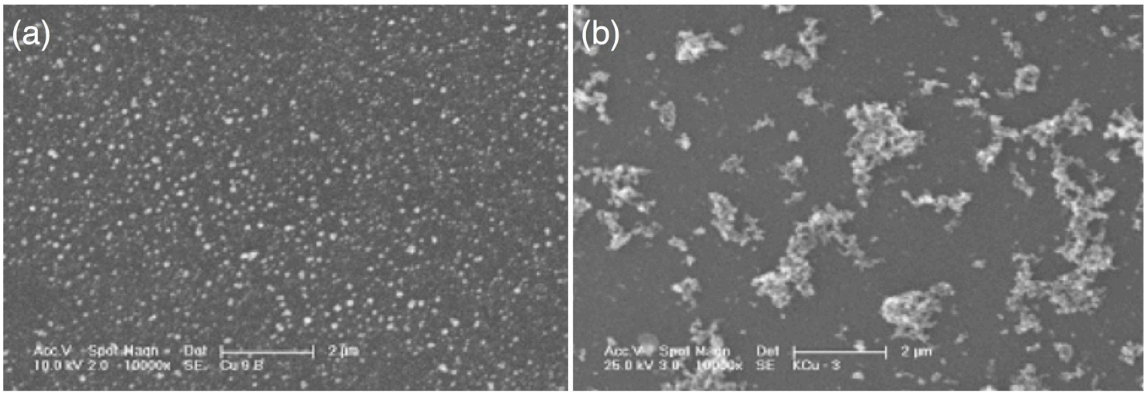

Figure 2.28: SEM images of copper films deposited: (a) with ArF laser on quartz window; (b) with KrF laser on the target glass plate. [90]

The photolytic decomposition of organometallic complexes and the nucleation or the precipitation of metal particles involves colloidal aggregation of particles. As a result, discontinuity or sparse density of copper nanoparticles in the deposited film (Figure 2.28) was found in the process [90]. Figure 2.29 shows continuous silver tracks with fine line width prepared by organo-silver complexes [92] where the subsequent anneal step did not induce any significant spreading as no heat is involved in the patterning step. Figure 2.30 shows some well defined platinum test structures fabricated by the platinum organometallic precursor method described in [95]. However this method requires long exposure time of 2 hours and extremely long 3-stage anneal processes which take up to 16 hours altogether to burn off the organic residues. However, the final metal deposit product can still contain high-resistivity residues of the organic metal precursor afterwards. The resistivity of the deposited thin film using optimum conditions was found to be $4.58 \times 10^{-6}\ \Omega$ m which is significantly higher than the reported resistivity of $1.06 \times 10^{-7}\ \Omega$ m.

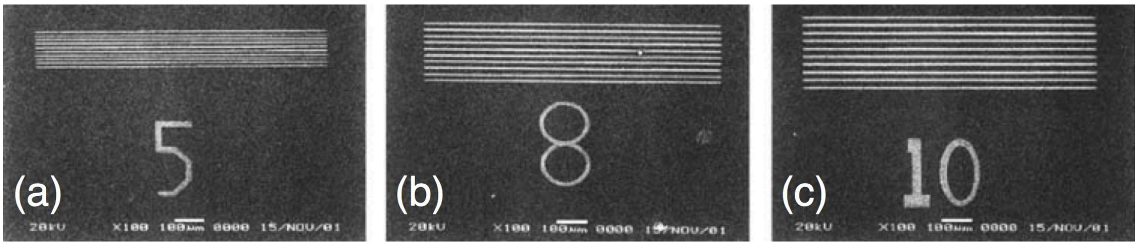

Figure 2.29: SEM images of photolithographic patterns of silver with 5, 8 and 10 μm tracks deposited on a glass substrate using the organometallic silver complex described in [92]. UV exposure time = 90 s.

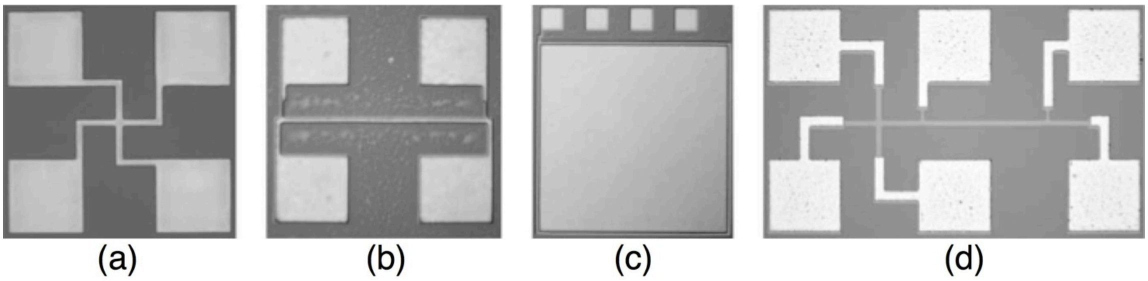

Figure 2.30: Test structures produced using the organometallic process: (a) Greek cross test structure with an arm width of 10 μm, (b) bridge resistor with a track width of 10 μm and a length of 350 μm, (c) platinum capacitor with an area of 1 mm, and (d) linewidth test structure with a width of 10 μm and a length of 200 μm. [95]

2.6. Criteria for the development of a direct-writing process

The ideal direct-writing process should be agile, time efficient and applicable to any substrate material. All the methods reviewed in this thesis do not involve any vapour phase processing and any metallic precursor or substrate preparation needed is fairly straightforward to carry out without requiring complex chemistry procedures, apart from the case of organometallic compound synthesis. Apart from the laser-enhanced electroplating and electroless plating processes, and some photochemical deposition from organometallic compounds where the light-directed patterning is carried out in liquid phase, the patterning step in the rest of the techniques in this review is all carried out in air atmosphere. All the techniques described here also do not require expensive overhead of equipment apart from the case of femtosecond laser processing.

The core methodology surrounding the development of a direct-writing process is to additively deposit first of all a thin layer of metal seed particles which is required to adhere to the substrate, and subsequently build a conductive metal layer on top of the nucleation sites usually by electroless plating or by repeat deposition of the thin metal layers by ink-jet printing or laser scanning. As cross-disciplinary research in engineering progresses, new deposition techniques start to utilise a combination of principles of processes categorised in this review. For example, ink-jet printing of polyelectrolytes for anchoring instead of printing metal nanoparticle ink. The scheme of deposition developed in this thesis combined several disciplines of techniques and is described in more detail in Section 2.6.1. Table 2.3 below summarises the key influencing factors in each of the processes reviewed with their listed advantages and drawbacks listed.

Table 2.3: Summary of the key influencing factors in each of the categories of processes reviewed.

	Key Factors	Advantages	Drawbacks
Laser enhanced electroplating	- Laser fluence - Applied voltage	- Parameters relatively easy to control	- Liquid phase process - Plating occurs in background
Laser enhanced electroless plating	- Laser fluence - Electroless mechanism response to heat	- No electrolytic cell requirement.	- Liquid phase process - Irregular deposits
Thermal decomposition of metal precursor film	- Laser fluence - Composition of the organic precursor - Sintering of metal nanoparticles	- Dry film process	- Thermal diffusion - Wasteful of pre-manufactured nanoparticle material
Surface activation by high power laser substrate damage	- Laser fluence - Absorption of the substrate material - Anchoring of catalyst seed - Electroless plating	- Easy means to activate a surface	- Irregularity of laser modified surface - Adhesion issue
Surface activation by photolytic substrate damage	- Photochemical chemistry of the substrate material - Anchoring of catalyst seed - Electroless plating	- Easy mean to activate a surface - No thermal effect	- Substrate specific - Two steps catalyst adsorption
Polyelectrolyte as anchoring layer	- Chemistry of polyelectrolytes - Surface treatment of substrate - Anchoring of catalyst seed - Electroless plating	- Strong adhesion strength - High resolution by microcontact-printing - No thermal effect	- Tailoring of polyelectrolytes assembly
Ink-jet printing	- Ink droplet size - Ink composition - Nozzle - Surface properties of substrate - Sintering - Electroless plating (not in all cases)	- Direct deposition of metal	- Mechanical design of jet systems - Proprietary ink formulation - Sintering - Printed metal conductivity level

	Key Factors	Advantages	Drawbacks
Reduction of embedded metal ions	- Chemical properties of substrate - Reduction methods (chemical, thermal or photo-initiated)	- Metal seed formed in situ within substrate - Ion-doped substrates can be used in a wide variety of reduction and patterning processes	- Substrate specific
Organic photo-reducing agents	- Choice of compounds - Reaction time	- Non-contact light-directed process - No thermal effect - Low cost - Can be purchased off the shelf	- Not usually used for thin film metalisation - No wide studies of compounds and mechanisms - Reaction can take a long time
Photocatalysis by semiconductors	- Semiconductor preparation - Quantum yield	- Non-contact light-directed process - No thermal effect	- Specific preparation of a semiconductor layer of TiO_2 or porous Si
Photochemical reduction of organometallic compounds	- Photochemistry of organometallic compounds	- Direct deposition of metal - Non-contact light-directed process - No thermal effect	- Tailoring of the compound - Chemical synthesis - Residues in the final metal deposit

Having considered each of these routes and their particular drawbacks, the direct-writing method on polyimide described in this thesis meets all of the criteria such as:

(i) An additive process, therefore waste materials are reduced compared to etching (subtractive) patterning processes.

(ii) Capability of patterning high-resolution feature size – line widths of a few microns could be achieved by a light-directed, non-contact patterning process in air atmosphere on flexible substrates.

(iii) Evaporation techniques and therefore vacuum chambers are not needed. This makes the handling of the substrates a lot easier. Moreover contour on 3-D substrates can potentially be directly patterned. Processing time is also reduced as there is no need for a vacuum.

(iv) Reduction of the overall number of processing steps and time, thereby allowing quicker turnover time which makes prototyping and small volume production economical.

(v) Complex, hazardous chemicals are avoided in substrate preparation and metal precursor synthesis. All materials required should be simple to prepare and either commercially available at a low cost or can be easily extracted from natural resources.

The research on this polyimide specific process would reduce the time and cost for manufacturing flexible circuits which is the fastest growing segment of the electronic circuit industry. Applications such as sensors, LED indicator and lighting arrays, heaters, medical devices, RFID, GSM and WLAN antennas, commonly require polyimide as the standard substrate material. Figure 2.31 illustrates a comparison between the proposed process design in this thesis and a state-of-the-art industrial inkjet additive manufacturing process for flexible circuits [105]. Besides the production cost and time, it is worth noting that the stated minimum line width of the industrial inkjet process is currently limited to 50 μm. Hence there exists a wide and important scope for research.

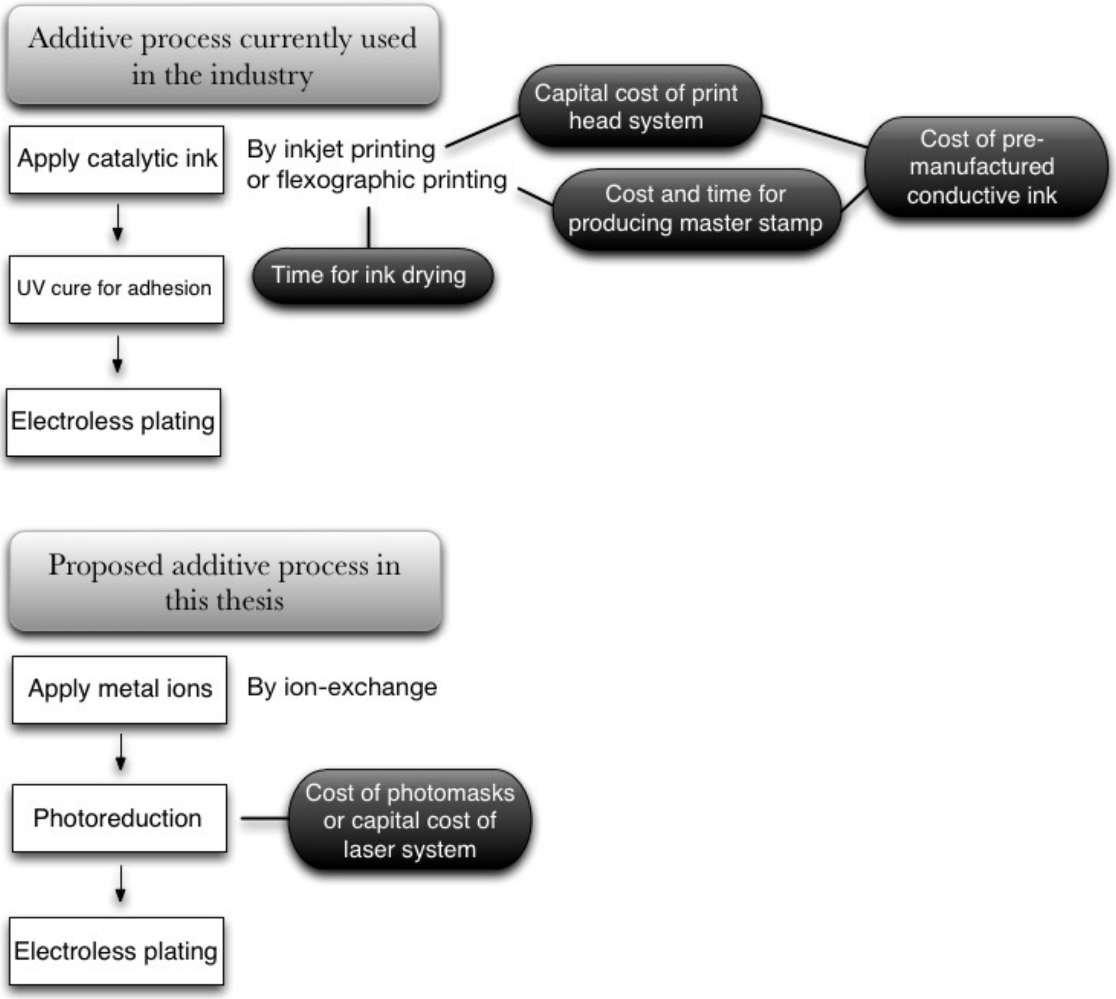

Figure 2.31: Comparison between the manufacturing methodology proposed in this thesis and an additive inkjet process currently used in the industry [105].

2.6.1. Description of the chosen metalisation scheme

The chosen direction of this research combines the advantages from a few different principles described in this literature review whilst minimising the shortcomings of each of the techniques. Each of the processing steps is described in Table 2.4 and the schematic diagram in Figure 2.32.

Table 2.4: Methods and reasons behind the chosen scheme of direct metalisation on polyimide.

Step	Method & Purpose	Beneficial Reason
(1) Apply metal source onto substrate	Ion-exchange on polyimide (i) Using KOH solution for surface alkaline hydrolysis modification. (ii) Using simple $AgNO_3$ aqueous solution as metal source.	Particles can be formed in situ from within substrate. Strong anchoring of metal seed.

Step	Method & Purpose	Beneficial Reason
(2) Apply photoreducing agent coating	Spin-coat as a dry film (i) MPEG in ethanol solution. (ii) Chlorophyll (extracted from spinach) in ethanol solution.	Ease of processing using dry film (i.e. no liquid or vapour phase reagents). Simple easy to use materials, no complex synthesis, low cost.
(3) Patterning and reduction of metal seed	UV or visible light exposure (i) Exposure time (ii) Patterning and reduction of metal ions in one single step	Reduction of metal ions instead of deposition of pre-formed metal particles. Non-contact, high resolution patterning, low power continuous UV or visible light instead of high power infrared or pulsed lasers. no thermal effect.
(4) Washing	Washing in dilute H_2SO_4 acid to remove the unreacted Ag^+ ions.	No solvent required to dissolve any material.
(5) Heat treatment	250°C for (i) Re-imidization, reforming the polyimide molecular structure from the cleaved imide rings. (ii) Silver particles sintering.	Two functions in one step: (i) recovery of the surface modified polymer substrate; (ii) sintering of Ag nanoparticles.
(6) Electroless plating	Electroless copper Electroless silver	Isotropic plating, good for plating small features, no voltage applied, higher thickness and conductivity level.

Figure 2.32 depicts the scheme of the direct metalisation on polyimide chosen for this body of research. Firstly, by alkaline surface modification of polyimide and ion-exchange (route 2 in Figure 2.1), metal ions are incorporated into the substrate easily without anchoring issues (short coming of self-assembly and laser machining surface modification). Processing steps are simplified as a seed catalyst layer does not need to be fabricated. It is instead formed *in situ* by photoreduction during the patterning step. The adhesion is thereby ensured by the mechanical interlocking of the polymer molecules and the metal aggregates. By a photochemical reduction mechanism (route 4 in Figure 2.1) no heat is generated (shortcoming of route 1 and some methods in route 2). As no heat is being required at the patterning step, a low-power UV or visible laser can be used to provide light energy solely for the reduction of metal ions, thus allowing fine resolution of feature size. With the use of a simple photoreducing agent (route 3 in

Figure 2.1) and with the metal ion source separated from it, complication of organometallic compounds are avoided (shortcoming of route 4).

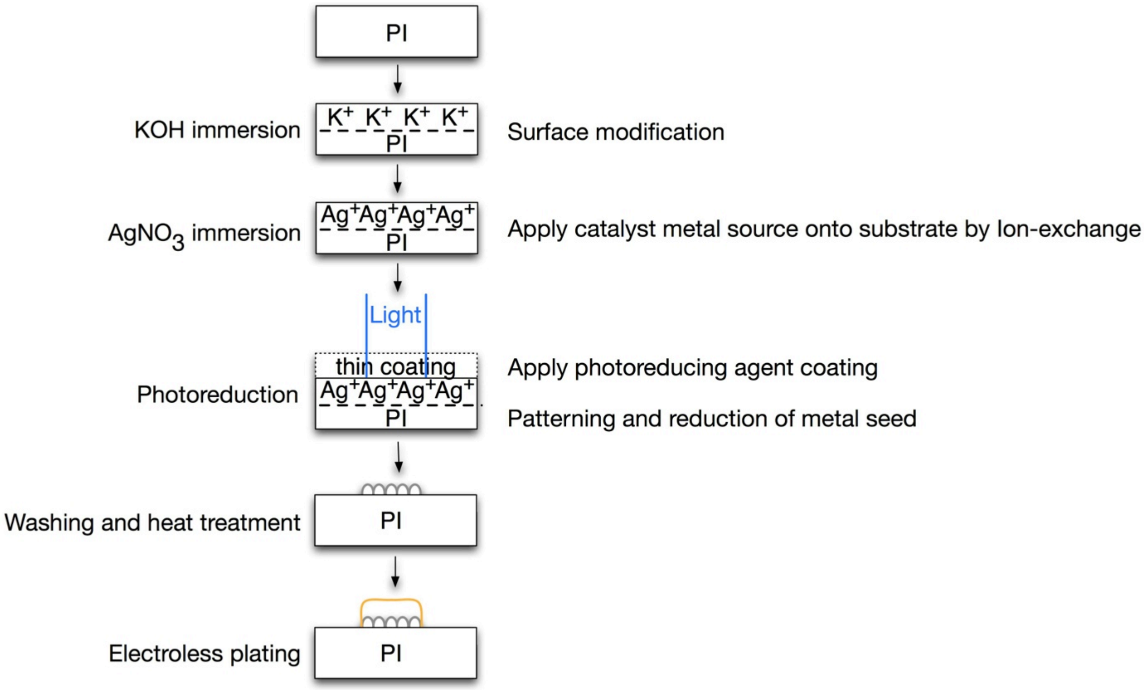

Figure 2.32: Scheme of direct metalisation on polyimide proposed in this thesis.

Chapter 3

Surface modification, metalisation, and photoreduction mechanisms of polyimide surfaces

3.1 Introduction

This Chapter introduces the background material necessary to understand the overall direct metalisation scheme as proposed in subsection 2.6.1. A quick depiction of these processes and material, and their explanation within this Chapter is shown in Figure 3.1. After an introduction on the material properties of polyimide in Section 3.2, the methods for surface modification of polyimide carried out throughout this thesis, namely alkaline hydrolysis and ion-exchange, are described in detail in Sections 3.3 and 3.4. The reduction methods for metal ions are introduced in Section 3.5. Some related research activities in the polyimide metalisation and patterning based on the ion-doping technique are discussed in Section 3.6. The backgrounds of the two new photoreducing agent materials for microfabrication of metals, MPEG and chlorophyll, are presented in Section 3.7 and 3.8. Figure 3.1 highlights the sections of this chapter describing the particular processing steps

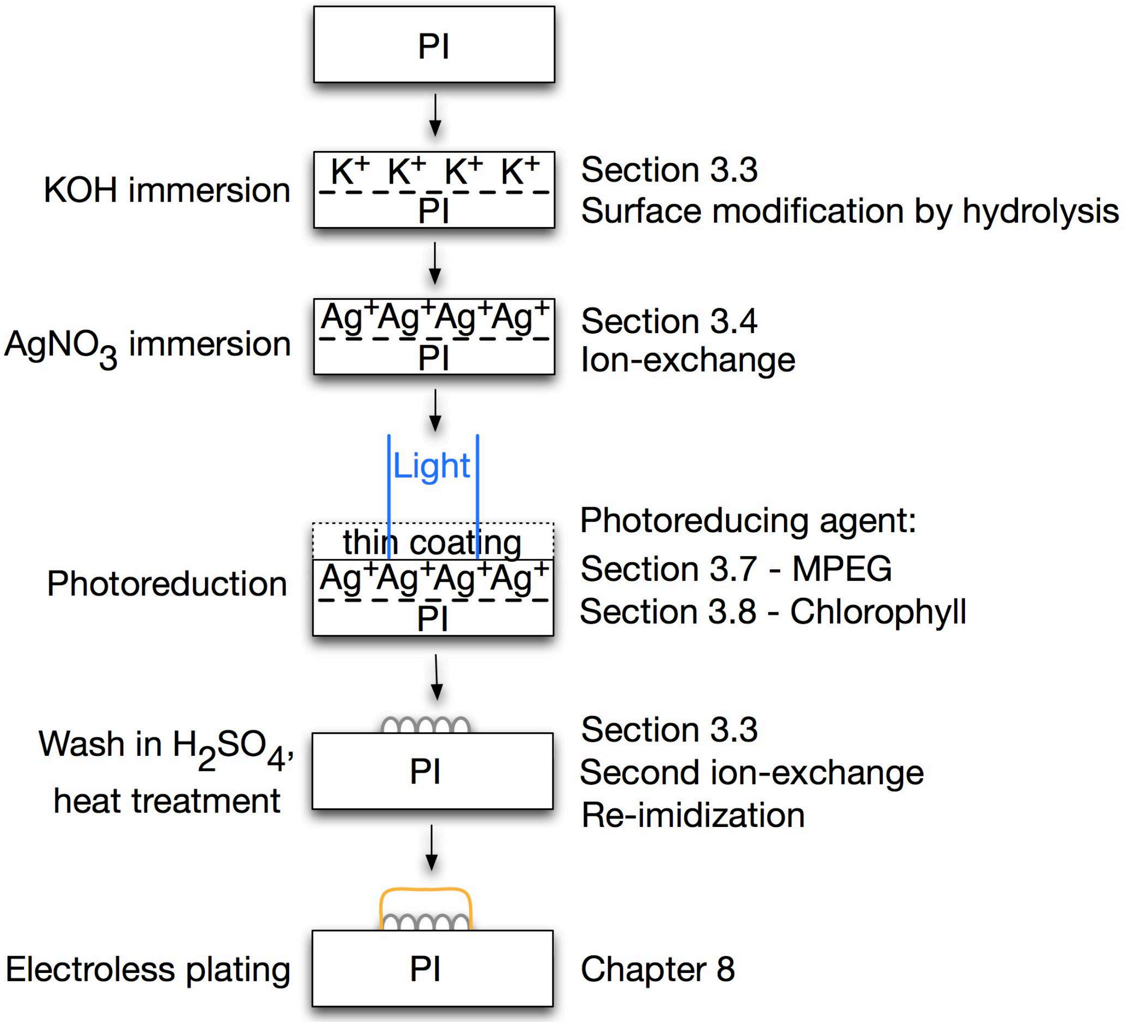

Figure 3.1: List of the background material for each of the processing steps in Chapter 3.

3.2 Polyimide

Polyimides are widely used in microsystems technology owing to their many desirable properties which include low dielectric constant (~3, compared to the value of 4.0 of the standard SiO_2 insulator), high mechanical strength, high resistance to solvent, heat(glass transition temperature ≈365 °C) and radiation, chemical inactivity as well as bio-compatibility. Although the drawback of polyimide is its higher cost compared to other types of flexible substrate materials such as poly(ethylene terephthalate) (PET) and poly(ethylene naphthalate) (PEN), in many specific environments when mechanical or thermal durability requirements, electrical insulation or radio frequency shielding are necessary, polyimide is the preferred if not the only choice of substrate materials. Nowadays, technology demands have integrated polyimide into many different industrial applications ranging from the fields of defence to medical devices. Some modern applications of polyimides are described in Section 3.2.2. There is a wide range of commercial polyimides available in different forms and with different properties to suit the fabrication flow or the operation of the final device. These different types of polyimides are introduced in Section 3.2.1.

The conventional route to metalisation and patterning on polyimide films is by subtractive methods. Either a roll of polyimide pre-laminated with a copper top layer is processed through a reel-to-reel production line (Figure 3.2) or a seed metal layer such as chrome or titanium is sputtered onto bare polyimide. Dry film photoresist can be laminated to the flexible polyimide films. Then photolithography steps of UV exposure, development and metal etching are performed to obtain the desired flexible circuits. The additive approach based on ion-exchange on the surface-modified polyimide in this thesis is drastically different from these standard industrial methods and the chemistry involved is described in the following sections in this chapter.

Figure 3.2: Reel-to-reel production equipment for flexible circuit manufacturing [106].

3.2.1 Chemical structures and types of polyimide

Kapton® is the trade name of the first commercially available polyimide film made by the Company DuPont in 1960. This product series has since remained a popular brand in the industry. Figure 3.3 shows a typical Kapton polyimide film sold as a roll. With the advancement of polymer technology, other types and brands of polyimide have also emerged, each offering unique properties for specific applications. Besides films, polyimides are also commercially available as a liquid with adjustable viscosity suitable for spin-coating or spraying or as powder for producing parts and shapes by sintering technologies such as hot compression molding or isostatic pressing (VTEC® polyimide from Richard Blaine International Inc.), or as paste for large scale wafer screen printing (HP-500 polyimide paste series by Hitachi Chemical Co.).

Figure 3.3: A 10 meter length, 515 mm width roll of Kapton® HN type 50 μm thickness polyimide film from DuPont.

There is also a wide variation of properties on offer by tailoring the chemical structure of the polyimides. All exhibit similar outstanding mechanical, chemical and thermal resistant properties, but they can also be customised for specific applications. For example, they can offer a high optical transmission range in the visible spectrum (Neopulim® by Mitsubishi Gas Chemical Company Inc., Japan); a fast curing time of a few minutes ; a high rigidity of similar strength as ceramic (VTEC™ by Richard Blaine International Inc., U.S.A.); a large elasticity as shown in Figure 3.4 or a low temperature cure type below 100°C. Polyimide are also available as sprayable or castable resins instead of standard film and can be both positive and negative types of photoresist (HD Microsystems from Cupertino, CA, U.S.A).

Figure 3.4: Stretchable elastic polyimide from ManTech International Corp. [107]

The chemistry of polyimides is in itself a vast area with a large variety of monomers available and several methodologies available for synthesis. The process for the most extensively developed PMDA-ODA Kapton® polyimide utilises the monomer pyromellitic dianhydride (PMDA) and 4,4'-oxydianiline (ODA) as illustrated in Figure 3.5 [108]. When the monomer PMDA is replaced by another monomer for instance 4,4'-oxydiphthalic anhydride (ODPA), ODPA-ODA polyimides can be synthesised with colourless and high optical transparency properties. The chemical structure of ODPA is shown in Figure 3.6 which contains the same end group as the PMDA at both ends of the monomer. The formation of the imide rings involves only the end groups of the monomer and is not affected by the particular arrangements of the aromatic structures at the centre. This thesis concerns the alkaline hydrolysis of polyimide which induces C-N bond cleavage at the imide rings as explained in Section 3.3. Therefore such a surface modification could be applied to all types of polyimides and is not affected by the type of monomer used for synthesis of the corresponding type of polyimide.

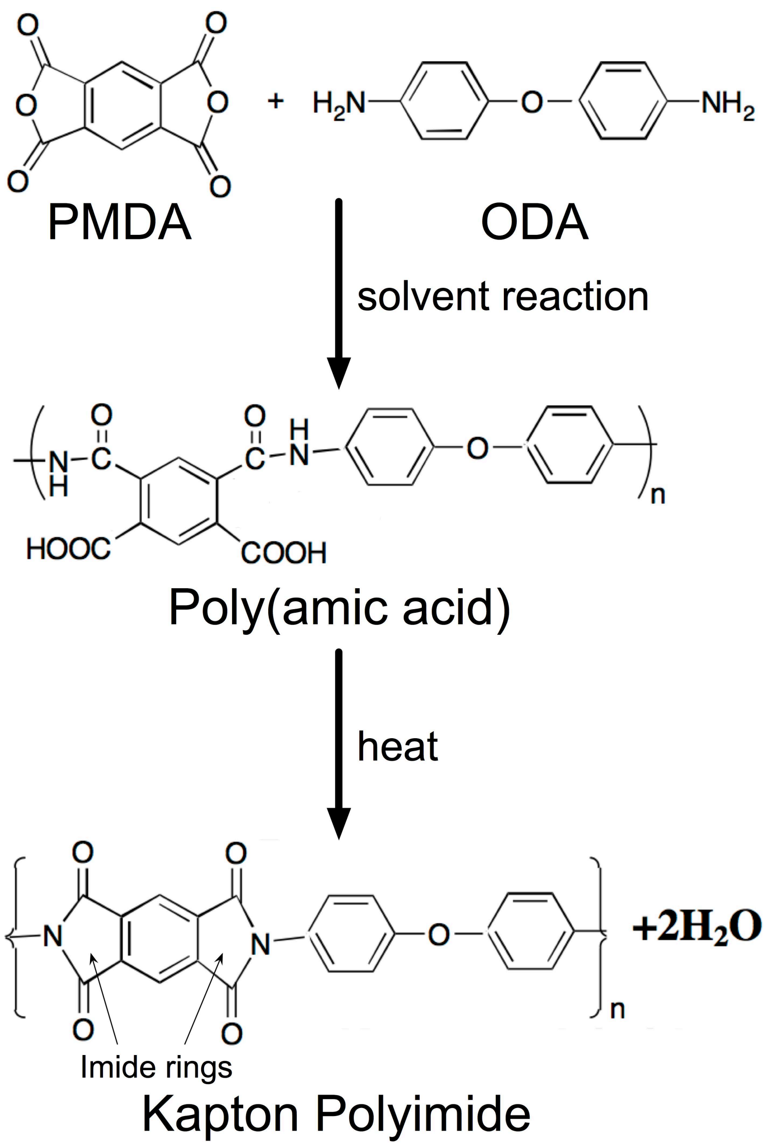

Figure 3.5: Reaction scheme for the preparation of Kapton® polyimide [108].

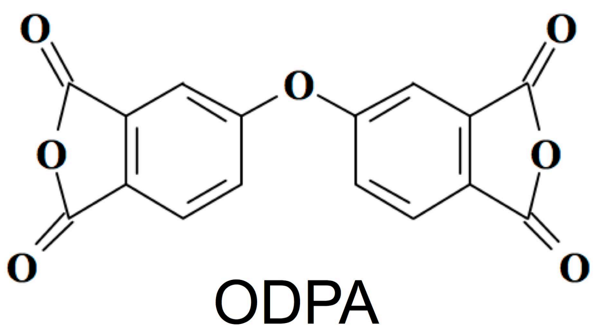

Figure 3.6: Chemical structure of the monomer 4,4'-oxydiphthalic anhydride (ODPA) [108].

3.3 Hydrolysis and re-imidization of polyimide

This Section describes the alkaline hydrolysis technique for incorporating metal ions into a surface-modified polyimide substrate. The surface modification of polyimide with KOH solution was first reported by researchers at IBM Research in 1990 [109]. The hydrolysis of a polyimide substrate can generate vacancies within the polymeric molecules which can be filled in by suitable positive ions. The ability to incorporate metal ions within a surface region of a polymer substrate without any intermediate anchoring molecules or treatment steps is very attractive for direct and selective metalisation. Inasmuch, this technique has become the starting procedure for research in direct metalisation of polyimide in a considerable number of reports that have appeared in the literature in the last decade. A review of these reports is presented in Section 3.5.

The KOH hydrolysis of polyimide results in a surface layer of potassium polyamate. The K^+ ions incorporated in this amorphous layer are then later exchanged with Ag^+ ions by an ion-exchange process. This section describes the chemical mechanisms of alkaline hydrolysis on polyimide and the recovery of the hydrolysed polymer back into the polyimide molecular structure, called re-imidization. The K^+/Ag^+ ion-exchange is described in the next Section.

3.3.1 Alkaline hydrolysis mechanisms

Polyimide hydrolysis is the opening of the imide ring structure in the polyimide molecule, as illustrated in Figure 3.7. The C-N bond cleavage is induced by an alkaline solution. A kinetic study of the early stages of polyimide hydrolysis is difficult because of the small amount of material being converted to polyamate on the polyimide surface. The mechanism and kinetics of alkaline hydrolysis of polyimide surface was proposed in 2000 [110]. The hydroxyl ions OH^- diffuse from the alkaline solution into the polyimide polymer phase. The nucleophilic attack of OH^- on a carbonyl carbon of the imide creates an equilibrium product, the intermediate anion (II) shown in Figure 3.7. Then the conversion (II) → (III) occurs through cleavage of a C−N bond with proton transfer from oxygen to nitrogen to create the ionizable functional groups, the carboxylic group COO^-. When the polyimide is completely hydrolysed, the resultant polyamate can be converted to the original precursor of polyimide, poly(amic acid) (PAA), upon neutralization.

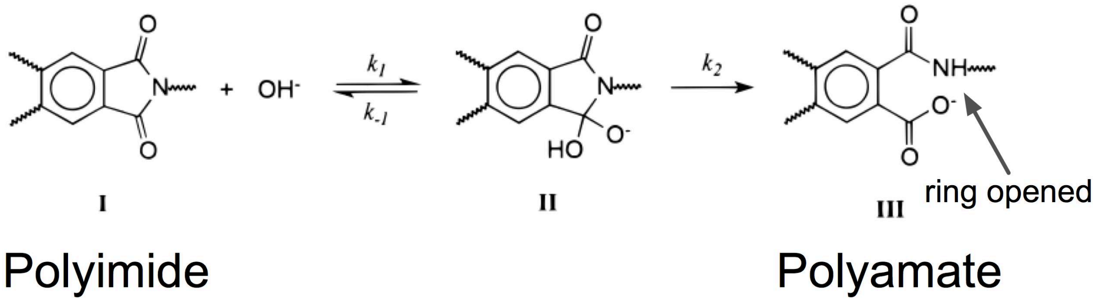

Figure 3.7: Opening of the imide ring by alkaline hydrolysis [110].

Under mild reaction conditions, the diffusion of reactant [OH^-] through the hydrolysed polyimide is the rate-determining step. A balance is established between hydrolysed material and underlying unmodified polyimide as the conversion from (I) → (III) proceeds in the direction from the substrate surface towards the bulk of the polyimide. In essence, the hydrolysed polyimide is a self-limiting layer that retards further diffusion of OH^- from the surface into the bulk and thus further hydrolysis.

The alkaline hydrolysis is an etching process because it involves dissolution of the broken macromolecules into the alkaline solution, in other words, the removal of material from the polymer substrate. The hydrolysed layer appears as a solvent-swollen, gel-like material when observed on a macroscopic scale during gross etching of PMDA-ODA polyimide. Mechanical agitation is often required to facilitate removal. However, depending on the chosen type and concentration of alkaline solution and reaction conditions such as temperature and agitation, a distinct layer of amorphous partially or completely hydrolysed polyimide can be produced with substantial adhesion to the unmodified polyimide underneath.

When potassium hydroxide (KOH) is used for the alkaline hydrolysis, the potassium ions from the solution can be electrostatically immobilised by the charge on the carboxylic group COO^-, therefore a thin layer of potassium polyamate is formed on the surface of a polyimide film [111].

3.4 Ion-exchange

Ion-exchange is probably the third most vital process in plant and animal life after photosynthesis and respiration. It occurs between the soil particles and growing plant roots to allow plants to obtain nutrients. Besides producing deionized water as a common commodity in laboratories nowadays, ion-exchange is important in blood analysis, drug purification, metal recovery and waste water treatment. The ion-exchange phenomenon entails some non-trivial physical chemistry. This section therefore introduces the basic concept of those mechanisms involved whilst keeping the description to the specific case of Ag^+/K^+ ion-exchange on the surface-modified polyimide substrate containing the carboxylic acid functional group within the amorphous surface layer.

3.4.1 Ion-exchange resins

Ion-exchange resins are widely used in industrial applications due to their effectiveness to exchange ions. The resins are usually in the form of beads or chelated resins that contain different chemical functional groups on their surface. Commonly used resins are made from cross-linked polystyrene. The functional groups can be classified into four different types: strongly basic, strongly acidic, weakly basic and weakly acidic. These functional groups contain electric charge by which the adsorption phenomenon occurs when a free ion is immobilised by electrostatic forces. The acidic groups carry a negative charge therefore attract cations whereas the positive charge of the basic groups attracts anions. The most common functional groups found in acidic resins for metal cations ion-exchange are $R\text{-}SO_3^-$ deprotonated from sulfonic acid $R\text{-}SO_2\text{-}OH$ for strongly acidic resins and $R\text{-}COO^-$ deprotonated from carboxylic acid R-COOH for weakly acidic resins. Depending upon the type of ions and other conditions in the system, each resin exhibits different affinities towards different ions. Table 3.1 shows a general order of ion selectivity for each example of function groups for the four types of resins. For example, sodium ions are adsorbed to the carboxylic acid groups in a weakly acidic resin. When this resin is then placed in a solution containing another type of cation with a higher affinity for carboxylic acid, the sodium will be displaced by the new cations. The factors that influence the ion affinities to a resin are described in more detail in the next Section.

Table 3.1: Ion-exchange functional group affinities [112], [113].

Resin Type	Example of Functional Group	Order of Selectivity
Strongly basic	$R\text{-}CH_2N^+(CH_3)_3$	$I>NO_3>Br>CN>Cl>HCO_3>OH>F$

Resin Type	Example of Functional Group	Order of Selectivity
Strongly acidic	$R\text{-}SO_3^-$	Pb>Ca>Mg>Ag>Rb>Cs>K>Na>H>Li
Weakly basic	$R\text{-}NH_3^+$	H_3PO_4>HNO_3>HI>HBr>HCl>HF>HCOO
Weakly acidic	$R\text{-}COO^-$	H>>Ag>K>Na>Li

Through the alkaline hydrolysis of polyimide, the imide ring opening by KOH exposes the carboxylic group $R\text{-}COO^-$ and thus this surface modified polymer layer effectively becomes a weakly acidic ion-exchange resin. Consequently the potassium ions K^+ are electrostatically adsorbed into the polymer phase forming $R\text{-}COO^-K^+$. The result is a surface layer of polyamate potassium salt in the polymer phase.

Since $Ag^+ > K^+$ for selectivity affinity to $R\text{-}COO^-$, when $R\text{-}COO^-K^+$ is immersed into a silver salt electrolyte solution, Ag^+ displaces K^+ resulting in an adsorbed layer of $R\text{-}COO^-Ag^+$ in the polymer phase (Figure 3.8). Some of the mechanisms in this ion-exchange are described in more detail in the next Section.

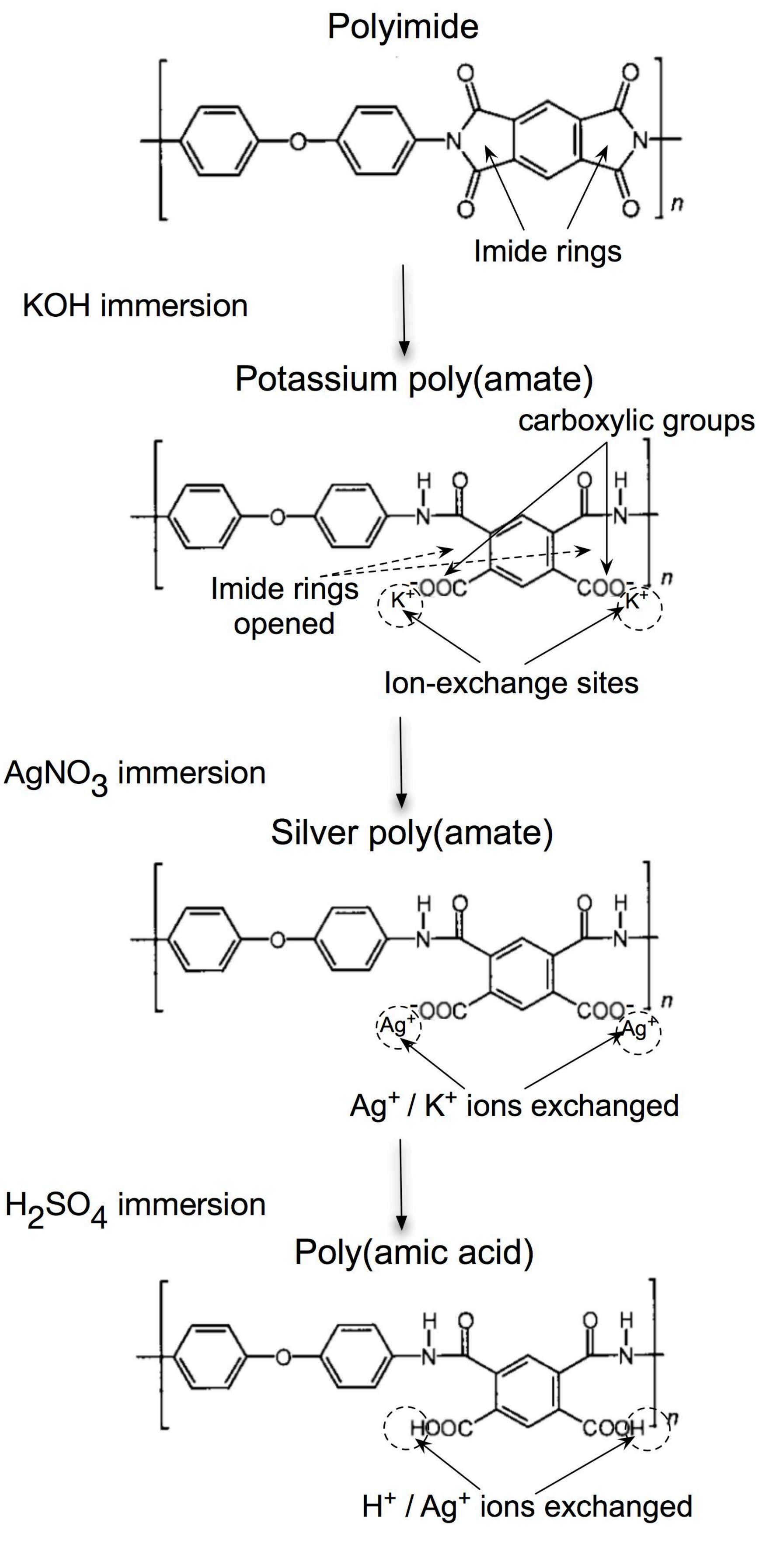

Figure 3.8: Scheme of Ag^+ / K^+ and H^+ / Ag^+ ion-exchange used in this thesis.

3.4.2 Ion-exchange mechanisms

For a given ion-exchange resin, the ion selectivity as described in the last Section is also a function of the ionic charge, the hydrated radius of the ion (Table 3.2), and the ion / functional group chemical interactions. The movement of cations within the solution and the polymer phase, and across the interface is governed by a combination of factors [114]. Figure 3.9 illustrates some of the key factors; each is complemented with the description as follows:

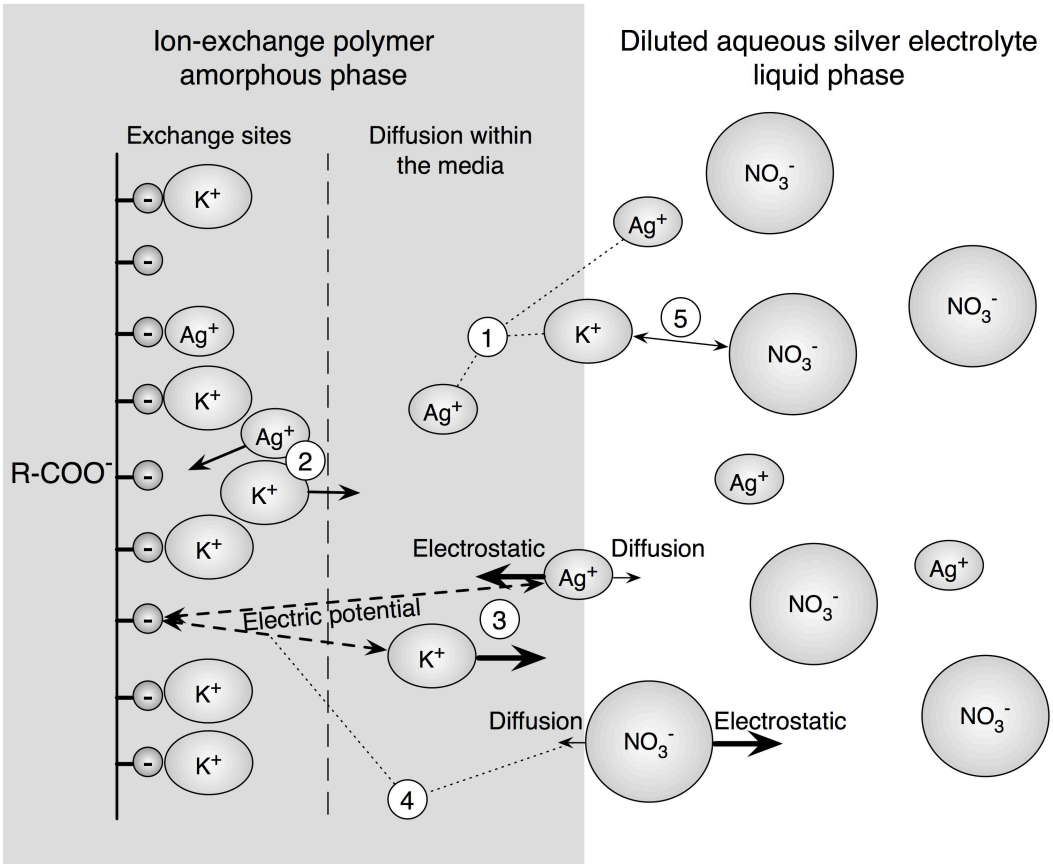

1. Chemical potential equilibrium between the liquid phase and the polymer phase.
2. Ion-exchange on the functional group according to its affinity to different cations.
3. Electroneutrality, any Ag^+ entering is accompanied by a K^+ leaving the polymer phase.
4. Anions exclusion, any anions to enter the cation loaded polymer will disturb the electroneutrality principle.
5. Association of K^+ to NO_3^- in the aqueous solution.

Figure 3.9: Key factors influencing ion-exchange between a liquid electrolyte and an ion-exchange resin.

(1) *Chemical potential equilibrium*

When the substrate is immersed into the silver electrolyte solution, cations are able to cross the boundary between the amorphous polymer phase and the solution phase. The polymer substrate and the electrolyte solution form a thermodynamically closed system. The chemical potential of Ag^+ ions in the ion-exchanger phase and the solution phase will reach equilibrium. That is, the energy per mole of Ag^+ ions in the solution will be equal to the energy per mole of Ag^+ ions contained in the media. In order to achieve this, some Ag^+ ions will distribute into the polymer phase. Likewise, the mobile K^+ ions within the media can diffuse into the solution.

(2) *Ion-exchange on the functional group*

The preference of a functional group to have higher affinity towards a specific ion can be reasonably attributed to the hydrated radius α of the ion [115]. Firstly, according to Coulomb's Law,

$$F = \frac{q_1 q_2}{4\pi\varepsilon_0 r^2} \tag{3.1}$$

which states that the electrostatic force, *F,* between the carboxylic group R-COO^- and a cation is inversely proportional to the square of the distance r between them, with q_1 and q_2 representing the charge on R-COO^- and on the cation, when treating them as point charges. ε_0 is the permittivity of free space. The closest approach r between a cation and an R-COO^- site is thus the hydrated radius α of the cation. Since K^+ and Ag^+ carry the same charge, therefore the smaller the hydrated radius, the greater the force of attraction for adsorption onto R-COO^-. The hydrated radii of some ions often involved in microfabrication are listed in Table 3.2. Ag^+ has a smaller hydrated radius than K^+ and thus can be adsorbed more strongly.

Secondly, the macro-reticular pore spaces in the amorphous polymer phase have limited volume which is determined by the percentage of cross-linkage of the polymer. As this polymer phase is relatively deformable, the hydrated ions coming in from the solution phase can cause swelling of the amorphous layer. As a consequence, a cation with a smaller hydrated radius has a higher preference to stay in the polymer phase due to less pressure caused by the swelling.

(3) *Electroneutrality*

The contributions from the chemical potential equilibrium and the difference in the hydrated radius sizes between Ag^+ and K^+, as described above, can reasonably dictate that Ag^+ ions are present in the polymer phase. So when these Ag^+ ions transport into the polymer phase from solution, another driving force for Ag^+/K^+ ion-exchange arises from the electroneutrality principle. In order to maintain the neutrality of electric charges in the polymer phase, a K^+ ion must move out of the phase as an Ag^+ ion moves in. Once the Ag^+ ion is inside the media, it is attracted by the electrostatic force from the R-COO^-. Although the concentration of Ag^+ ions in the polymer phase would be higher than that in the electrolyte solution, the electrostatic force is much stronger than any diffusion force due to the concentration gradient to drive the Ag^+ ion back into the solution.

(4) *Anions exclusion*

Following from the electroneutrality principle, a polymer substrate loaded with K^+ ions after KOH immersion would have equal amount of R-COO^- sites and K^+ ions. When this substrate is then immersed in a silver salt solution for Ag^+ ion-exchange, the anions in the solution e.g. NO_3^- should diffuse into the polymer phase according to the concentration gradient. However, this would disturb the electroneutrality in the polymer phase and the electrostatic force is much greater to exclude the anions in the polymer phase. Likewise, the only possibility for a K^+ ion to diffuse out is to exchange with an Ag^+ ion from the solution to maintain electroneutrality.

(5) *Association of K^+ to NO_3^-*

When K^+ leaves the polymer phase, weak metal-to-ligand bonds are formed with electron donors called ligands such as H_2O and NO_3^- in the solution phase. Although KNO_3 solids are not formed in the solution, the favourable attraction between K^+ and NO_3^- which further assists the Ag^+/K^+ ion-exchange in the system can be supported by the qualitative observation that $AgNO_3$ has a considerably higher solubility than KNO_3 in water [116]. This may indicate that K^+ has a higher affinity towards NO_3^- compared to Ag^+, and, as a consequence, favouring K^+ transport from the polymer phase into the solution phase.

Table 3.2: Hydrated radius of ions commonly involved in fabrication processes of microelectronics for comparison purpose. [115]

Ion	Hydrated Radius α (nm) [Rounded Values]
H^+	9
Li^+	6
Ag^+	2.5
K^+, Cl^-, I^-, CN^-, NO_3^-,	3
OH^-, F^-	3.5
Na^+	4 - 4.5
Pb^{2+}	4.5
Hg^{2+}, S^{2-}	5
Ca^{2+}, Cu^{2+}, Zn^{2+}, Sn^{2+}, Fe^{2+}, Ni^{2+}, Co^{2+}	6
Al^{3+}, Fe^{3+}, Cr^{3+}, Y^{3+}	9

All of the above hold for a limited range of concentration of a diluted electrolyte solution. Increased concentration of the electrolyte solution does not necessarily enhance the rate of ion-exchange. A paper published in 2009 studied the chemistry involved during the ion-exchange process into PAA [117]. It was reported that the metal ions in the PAA can induce structural variations in the polymeric molecular structure which results in the generation of diversified silver chemical entities. Furthermore, the presence of the metal ions can induce cross-linking of the PAA, whilst some of these metal ions within the PAA matrix could be self-reduced to metal particles. Detailed investigations regarding the mechanism of metal ions and PAA interaction are still required. This again shows that the phenomenon occurring in the ion-exchange process is non-trivial. In addition, water swelling and osmotic pressure can also influence the ion-exchange rate. The detailed characterisation of ion-exchange isotherm, ion-exchange capacity of the ion-exchange resins and further selectivity characteristics involve the computation of the equilibrium, selectivity and activity coefficients of the ions involved as well as the thermodynamic constant, etc. [114]. These studies are beyond the scope of this thesis.

Regarding the second ion-exchange step using dilute sulfuric acid solution to displace the unreacted Ag^+ ions, one unique property of the hydrogen ion is that it has a particularly strong affinity with the carboxylic group R-COO- to form carboxylic acid R-COOH due to the strong hydrogen bond which overrides the electrostatic force and hence consideration of hydrated ion radius (as shown in Table 3.2, the hydrated hydrogen ion radius is one of the largest). This fact is especially convenient when selective photoreduction of Ag^+ ions is carried out; the remaining Ag^+ in the unexposed region in the polymer can be easily removed by exchanging with H^+ ions when immersed in a dilute H_2SO_4 acid solution.

3.5 Reduction of the metal ions incorporated in the polymer substrates

After incorporation of Ag^+ ions into the surface modified polyimide substrates by ion-exchange, various reduction strategies can be applied to these ions as illustrated in the schemes of metalisation in Figure 2.20. This Section first introduces some basic principles of reduction of metal ions. Then the mechanism of silver nanoparticles formation within the polymer substrate is described.

3.5.1 Reduction of metal ions

Neutral silver has one electron in its highest energy level (the outer most shell), whilst the total number of electrons is equal to the total number of protons at the nucleus. A positively charged silver ion, Ag^+, is formed when this electron in the outer most shell is donated to other substances. This is referred to as oxidation. The Ag^+ is said to have an oxidation state of +1. When Ag^+ gains one electron, the oxidation state is then reduced to 0, i.e. an electrically neutral silver atom Ag^0 is formed. This is referred to as reduction. Reduction potential is a measure of the tendency of a chemical species to acquire electrons. So for instance the reduction potential for ($Ag^+ + e^- \rightarrow Ag$) is +0.79 V (vs Standard Hydrogen Electrode or SHE). A more positive reduction potential means the species has a greater affinity for electrons. Table 3.3 lists some common metals used in microsystems in descending order of tendency to gain electrons.

Table 3.3: Reduction potential of common metals used in microsystems in descending order of electron affinity. Hydrogen and potassium are included for comparison purposes. [118]

Metal	Reduction Reaction	Reduction Potential E^0 (V) (vs SHE)
Gold	$Au^{3+} + 3e^- \rightarrow Au$	+1.50
Platinum	$Pt^{2+} + 2e^- \rightarrow Pt$	+1.20
Palladium	$Pd^{2+} + 2e^- \rightarrow Pd$	+0.83
Silver	$Ag^+ + e^- \rightarrow Ag$	+0.79
Platinum	$PtCl_4^{2-} + 2e^- \rightarrow Pt + 4Cl^-$	+0.73
Copper	$Cu^+ + e^- \rightarrow Cu$	+0.52
Copper	$Cu^{2+} + 2e^- \rightarrow Cu$	+0.34
Hydrogen	$2H^+ + 2e^- \rightarrow H_2$	0.00
Iron	$Fe^{3+} + 3e^- \rightarrow Fe$	-0.04
Nickel	$Ni^{2+} + 2e^- \rightarrow Ni$	-0.25
Potassium	$K^+ + e^- \rightarrow K$	-2.92

The values in Table 3.3 refer to the pure reduction of the metal ions without influence of any other factors considered in the reaction system. For example in a plating bath, the reduction potential can be adjusted by other chemical additives in the bath. For nanoparticle growth, the reduction potential values can vary significantly for metal ions to be reduced to a single standalone silver atom in solution phase, to a small silver nanoparticle surface, a larger silver cluster, or a very large silver surface. Such size effects are discussed in references [61], [63].

The most common reduction methods applied in industrial fabrication are through electrochemical, chemical and thermal reactions. Electrochemical reduction occurs during the deposition of metal films in an electroplating cell. An applied voltage on a metal electrode with a value greater than the required reduction potential of the metal ions in the chemical electrolyte solution drives the deposition onto the surface of the electrode.

Chemical reduction of metal ions is achieved by the release of electrons from chemical reducing agents which are usually dissolved in the liquid phase. Common reducing agents are formaldehyde, hydrazine, dimethylaminoborane (DMAB), sodium borohydride, to name but a few. This reaction is the foundation of electroless deposition which is described in detail in Chapter 8.

Simple thermal reduction of metal ions can be carried out in a hydrogen atmosphere (also known as hydrogen reduction) at various temperature, some reducing agents can be employed which could lower the metalisation temperature and time required.

Photoreduction of metal ions generally refers to the reactions driven by the electrons which are excited by the incident photon energy and donated by substances in the vicinity of the metal ions. This can be facilitated by semiconductor materials as described before in Section 2.4.2. Photo-excitable chemical reducing agents, or photoreducing agents, can also be used. Irrespective of the mechanisms involved in the photoexcitation, this category of reducing agents is a broad subject and a deeper understanding is still required for researchers to characterise a photoreduction process with a particular photoreducing agent. The pioneering work described in Section 2.4.1 mostly used high energy photons at 254 nm wavelength which is in the deep UV region. At this wavelength, oxidation of water molecules can be initiated which, in turn, results in electron transfer for the reduction of nearby metal ions [119]:

$$Ag^{+} + H_2O \xrightarrow{h\nu} Ag^{0} + H^{+} + OH^{\bullet} \tag{3.2}$$

The photolysis of water using a short UV wavelength of light source as depicted in Equation 3.2 may not apply in the two photoreducing agents under studies in this thesis. Not only they both employed ethanol as a solvent instead of water, much longer wavelengths in the near UV region were also used. Some of the different pathways of radicals and electrons transfer involved are discussed in Sections 3.7 and 3.8. Since the reduction of metal ions is mediated by photoexcitation of other chemical molecules in the system, this type of reaction is also referred to as photochemical reduction or photoinitiated reduction.

3.5.2 Electron transfer for the reduction of the doped metal ions

The key feature of the proposed photoreduction route pursued in this thesis is the reliance of electrons generated from the rigid coating on top of the substrate which are transported into the substrate crossing the coating / substrate boundary. This differs to the one-pot solution matrix process where the photoreducing agents and the metals ions are mixed homogeneously in the liquid phase in which the excited electrons are only required to travel a short distance to reach the target metal ions. Whilst the consideration of electron transfer mechanisms is beyond the scope of this thesis, it is recognised that the experimental results herein provide evidence that such photoinitiated electron transfer is possible.

3.6 Development of polyimide metalisation based on ion-exchange

Research in the ion-exchange process on polyimide has been revitalised by the group at Konan University, Japan, between 2001 and 2007. Their development entailed intensive studies in doping and metalisation of noble metal ions such as Cu^{2+} [120-124], Ag^{+} [53], Ni^{2+} [123], [125-127], and Pt^{2+} [123] onto polyimide resin. Their aim was to study metal nanoparticle/polyimide composites and to develop direct metallisation methods that are easy to implement, and do not require complex or expensive chemical compounds. The group continued research activity in this field up to 2010. Following the initial publications from the group at Konan University, other groups also began characterisations of ion-doped polyimide substrates [128], [129] and extended research in other types of doping ions such as tin [130], whilst, later on, some other groups, most notably from Beijing University of Chemical Technology, Beijing, China, and from Shanghai Jiao Tong University, Shanghai, China, focused on the investigation of various reduction techniques to apply on the metal ions within these ion-doped substrates. As already mentioned in Section 2.3.4, three types of reduction are usually carried out, namely photoreduction, chemical reduction and thermal reduction. Chemical or thermal reductions have been applied most frequently whereas the main focus of this thesis is development of photoreduction methods. Selective metalisation has been achieved by either masking at the ion-exchange stage or at the reduction stage. Five examples are selected to illustrate the versatility in micropatterning of metal tracks based on ion-exchanged, surface modified polyimides in the following subsections.

3.6.1 Selective photoreduction of doped copper ions using TiO_2 photocatalyst

This report was published in 2001 by Ikeda *et al* [120] from Konan University, Japan. The metalisation scheme utilising a layer of TiO_2 nanoparticles coated on top of the copper ion-doped polyimide substrate is shown in Figure 3.10.

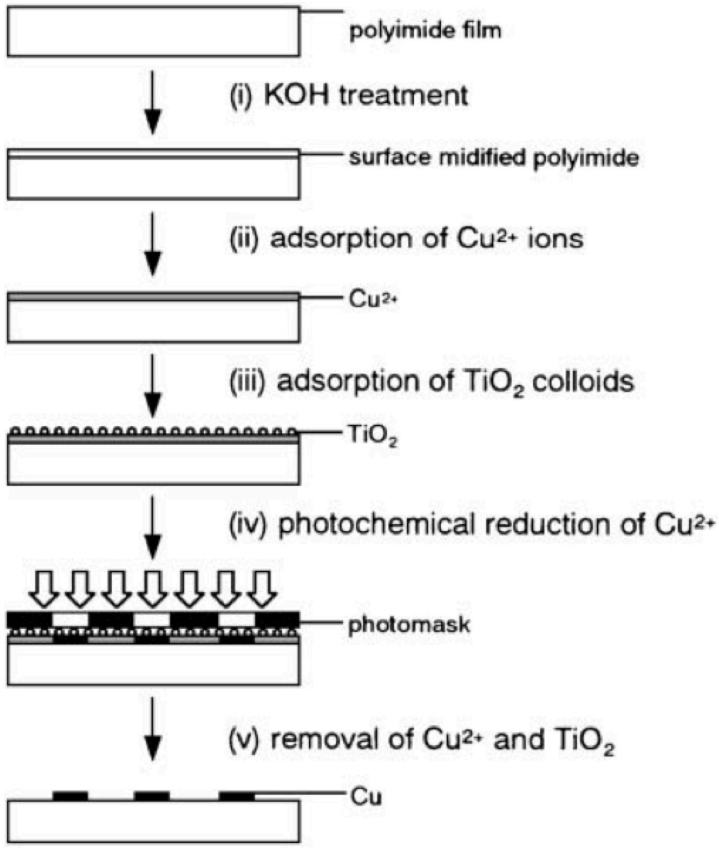

Figure 3.10: Schematic diagram of the process steps employing selective TiO_2-assisted photoreduction on copper ion-doped polyimide [120].

Substrate preparation

50 μm thick PMDA-ODA type polyimide film (Kapton 200-H, Du-Pont) was immersed in 5 M KOH solution at 50 ^oC for 5 minutes for hydrolysis. Cu^{2+} ion-exchange was carried out by immersion in a 0.005 M $CuSO_4$ solution for 1 minute. Afterwards, TiO_2 colloids containing 20 nm diameter particles (Ishihara Techno. Ltd. anatase TiO_2 sol) were coated as a top layer onto the substrate. The coating method and thickness of the TiO_2 layer was not disclosed.

Reduction method

The mechanisms of TiO_2-assisted photoreduction and a different example using glass substrates have been described in Section 2.4.2. UV irradiation (intensity not disclosed) was carried out through a quartz photomask for 2 hours.

Anneal and re-imidization

No anneal or re-imidization was carried out.

Results

After removal of TiO_2 and the unreacted Cu^{2+} ions by washing in dilute H_2SO_4 solution, the photoreduced copper thin film exhibited a surface conductivity of 1.12 x 10^{-5} S and is suitable to act as a seed layer for subsequent electroplating. The micropatterns created through the photomask exposure contained copper lines of 5 μm width as shown in Figure 3.11.

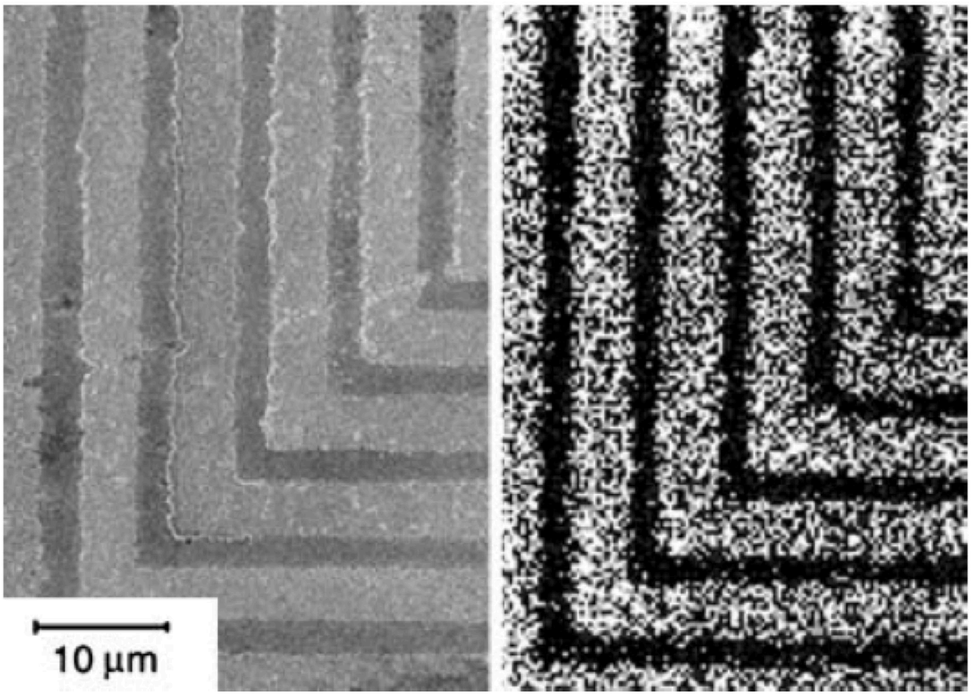

Figure 3.11: FEGSEM micrograph (left) and corresponding elemental mapping image (right) of the copper patterns formed on the polyimide substrate [120].

Remarks

The mechanisms involved in TiO_2 photocatalysts for generating electrons for metalisation is a wide subject requiring much further research. The variable parameters include the crystalline structure of the semiconductor, the size effect of the nanoparticles, and the size distribution of the nanoparticles during synthesis etc, all can arise during the preparation of the TiO_2 layer. Therefore, it is preferable to use a photocatalytic material that is easier to be prepared and subjected to less critical variations.

3.6.2 Selective photoreduction of doped silver ions using water acceleration

This paper, also from Konan University, Japan, was published in 2003 by Akamatsu *et al* [53]. Similar to the experimental configuration above, a thin layer of water was applied as the photocatalyst layer on top of a silver ion-doped polyimide substrate for UV photopatterning of micro silver tracks through a photomask, as illustrated in Figure 3.12.

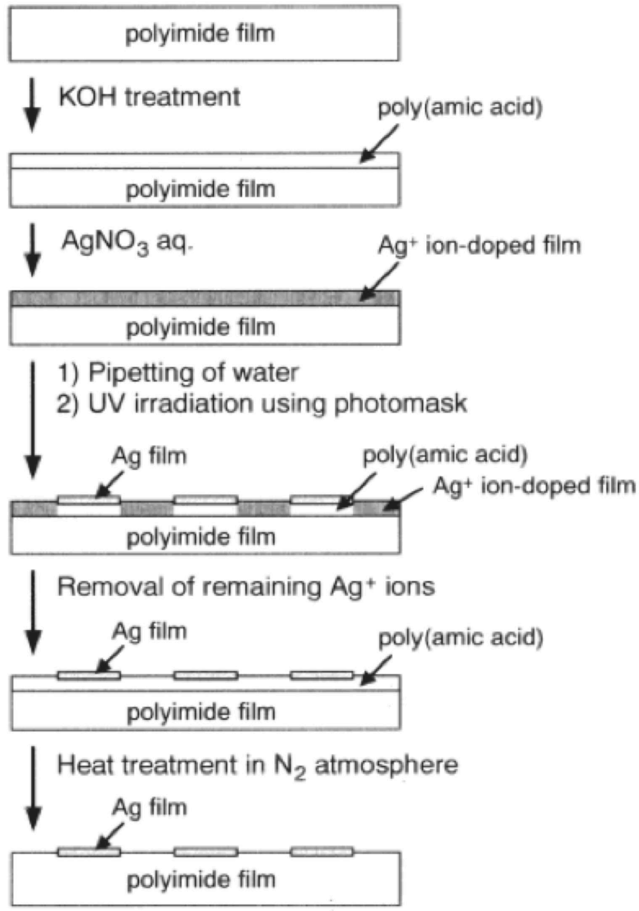

Figure 3.12: Schematic diagram of the process steps employing selective water-assisted photoreduction on silver ion-doped polyimide [53].

Substrate preparation

50 µm thick PMDA-ODA type polyimide film (Kapton 200-H, Du-Pont) was immersed in a 5 M KOH solution at 50 ºC for 5 minutes for hydrolysis. Ag^+ ion-exchange was carried out by immersion in a 0.05 M $AgNO_3$ solution at room temperature for 5 minutes. A few drops of distilled water was pipetted onto the substrate surface in order to form a thin water layer between the photomask and the substrate.

Reduction method

A 315 nm fluorescent lamp with an intensity of 260 mW cm^{-2} was used as the UV light source. Irradiation was carried out for 60 minutes through a metal-on-quartz photomask. The water layer between the substrate and the photomask plays an essential role in the growth of the silver thin films. It was reported that in the photoreduction experiments carried out in vacuum (i.e. in the absence of a water layer), only small silver islands were formed. Without water, the UV light can induce reduction of silver ions by charge transfer from the carboxylate ions $–COO^-$ to silver ions, resulting in the formation of carboxyl radicals $–COO^•$ and silver atoms:

$$-\mathrm{COO}^{-}\ \mathrm{Ag}^{+} \xrightarrow{h\nu} -\mathrm{COO}^{\bullet} + \mathrm{Ag}^{0} \tag{3.3}$$

When a top layer of water is present on the surface of the substrate, protonation of the carboxyl radicals from the water molecules results in the formation of carboxylic acid –COOH and hydroxyl radicals $OH^•$:

$$-\mathrm{COO}^{\bullet} + \mathrm{H_2O} \longrightarrow -\mathrm{COOH} + \mathrm{OH}^{\bullet} \tag{3.4}$$

The paper postulated that the carboxylic acid –COOH thus formed at the top surface of the substrate can accelerate the silver ions bound in the deeper side of the modified layer ($–COO^-$ Ag^+) to transport towards the top surface by Ag^+/H^+ ion-exchange. Therefore, more silver atoms are photoreduced in the presence of water on top of the substrate.

Anneal and re-imidization

After UV irradiation, the samples were washed in 1 wt% H_2SO_4 solution and subsequently annealed at 250 ^oC in a N_2 atmosphere for 30 minutes to achieve re-imidization.

Results

The dimensions of the photoreduced silver patterns were in good agreement with the photomask specifications. Anneal did not cause distinct change of pattern structure. Figure 3.13 shows that 500 nm line width and spacing was achieved, and the silver film generated was crack free, composed of small particles. The film has an electrical conductivity of 7.0×10^{-1} S cm^{-1}.

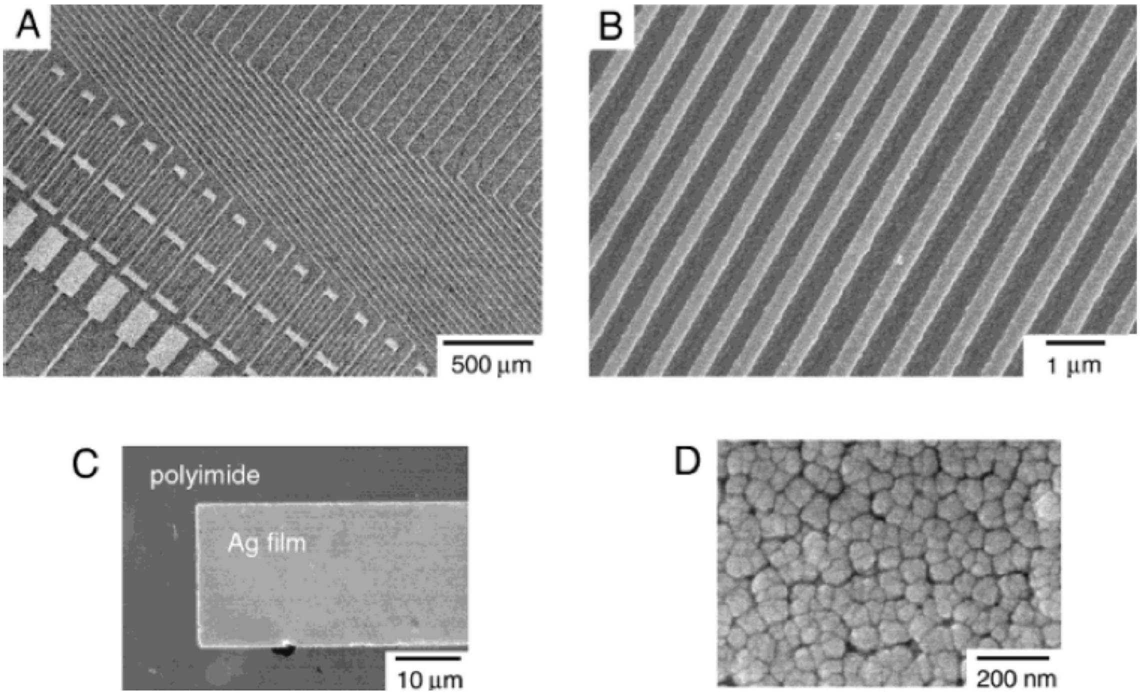

Figure 3.13: FEGSEM images of silver circuit patterns formed by UV irradiation for 60 minutes using a metal-on-quartz photomask. (C) & (D) are enlargements of (A) & (B). [53]

Remark

The pipetting of water to form a layer that assists photoreduction is much simpler compared to the synthesis of TiO_2 nanoparticle colloids. Combined with the easy immersion procedures of KOH hydrolysis and ion-exchange using $AgNO_3$, this direct metalisation method is very attractive to pursue. However, processing of a liquid-coated substrate would also be difficult when combined with the photomask or laser writing setting. This has motivated an objective of this thesis in searching for a rigid assisting coating for photoreduction that is simple enough to use. This is detailed in Chapters 6 and 7.

3.6.3 Ink-jet printing KOH solution for polyimide hydrolysis

This report was published in 2004 also by Akamatsu *et al* [122]. Instead of photopatterning which involved the use of a photoreduction-assisting material such as

TiO_2 or water, the patterning was realised by ink-jet printing KOH solution so that the polyimide surface was selectively modified. Thereafter, ion-exchange and chemical reduction was carried out by immersion of the whole substrate and copper tracks were formed only on the KOH printed regions. Figure 3.14 illustrates the scheme of processing.

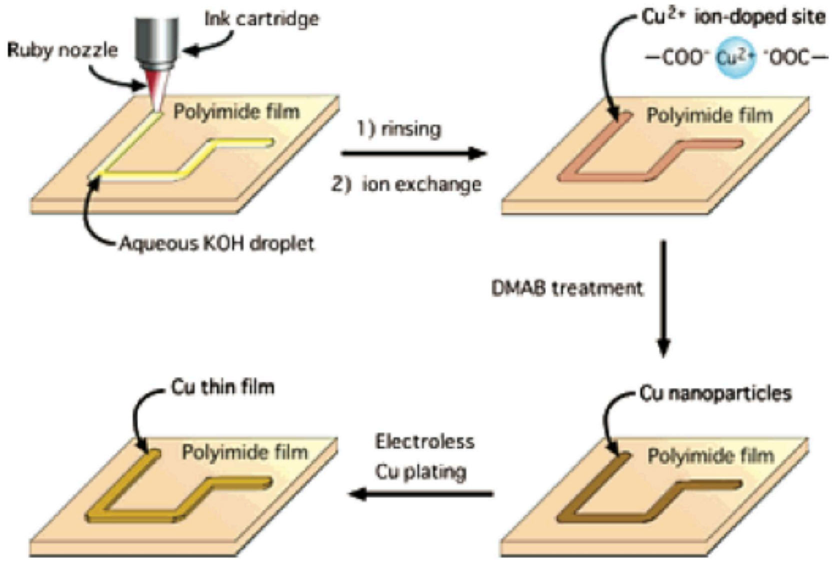

Figure 3.14: Schematic diagram of the processing steps for ink-jet printing KOH solution, copper ion-exchange, chemical reduction using a DMAB solution and electroless plating [122].

Substrate preparation

A 125 µm thick PMDA-ODA type polyimide film (Kapton 500-H, Du-Pont) was placed under a customised, fine-precision dispenser equipped with temperature-controlled X-Y stage and ink cartridge (Musashi Engineering, SMP-III, ruby nozzle diameter: 40 µm). A solution of KOH in a water/ethylene glycol mixture (3/1 by volume, final KOH concentration: 5 M) was printed on the polyimide surface as a circuit pattern using CAD software. The printing was performed at 30 ºC for both substrate and cartridge and at a relative humidity of 33%. Addition of ethylene glycol effectively lowers the evaporation rate and improves the wettability of the solution to the hydrophobic polyimide surface. After printing and standing for 5 minutes followed by copious rinsing with distilled water, the resulting modified surface can be readily differentiated from the bare (unmodified) polyimide by optical microscopy as shown in Figure 3.15(a).

Ion-exchange on the printed circuit pattern was then carried out by immersion of the whole printed film into a 0.05 M $CuSO_4$ solution for 5 minutes.

Reduction method

Chemical reduction was applied by immersion of the ion-exchanged film into a 0.1 M DMAB solution for certain time (not disclosed by the paper).

Anneal and re-imidization

No anneal or re-imidization was carried out since the regions of the polyimide film not printed with KOH solution was not chemically modified.

Results

The paper reported that the printed feature size could be controlled from 50 µm to many centimetres depending on the resolution of the X-Y translation stages and nozzle diameter. Figure 3.15(b) shows 200 µm line width of copper pattern formed after chemical reduction. Figure 3.15(c) shows a cross-sectional image of the chemically reduced copper thin film which acts as a seed layer and the subsequently deposited electroless copper top layer. The electroless copper layer passed the Scotch-tape adhesion test.

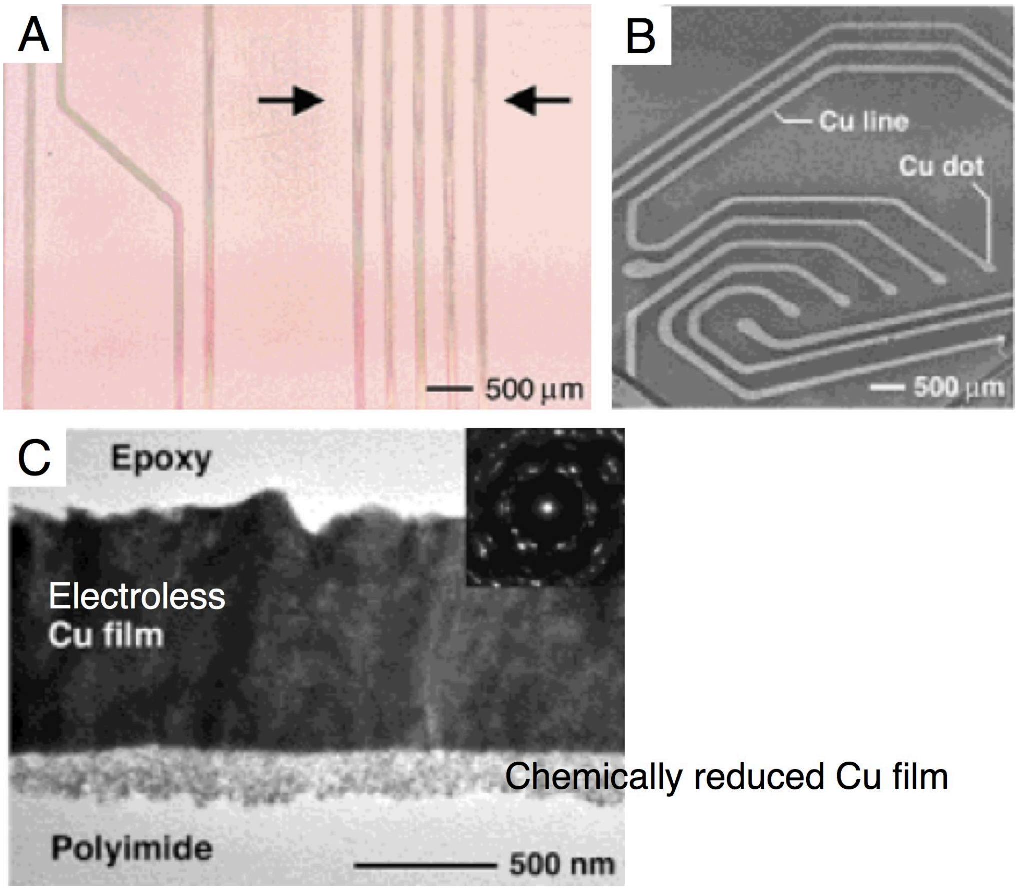

Figure 3.15: (a) Optical microscope image of selectively modified polyimide film. The pattern was generated by printing at a scan rate of 5 mm/s and an ink dispensation rate of 5 mL/min at 30 °C (relative humidity: 33%), and the printed film stood for 10 minutes at 30 °C. (b) FEGSEM image of chemically reduced copper circuit by DMAB solution consisting of 200 µm line width and 300 µm dot diameter. (c) Cross-sectional TEM image of the chemically reduced copper film from the doped ions and the electroless copper film deposited on top. [122]

Remark

Ink-jet printing is a convenient process for micropatterning and the printed KOH solution required only a short drying time of 10 minutes. The subsequent ion-exchange and chemical reduction can be applied to the whole substrate easily since only the KOH modified regions would allow binding of metal ions and thus selective metalisation. By this method, the need and difficulties in patterning during either the ion-exchange or the reduction step are eliminated. However further improvement of the printed feature resolution depends on the ability to reduce the droplet size as well as its correct deposition on the surface of the substrate.

3.6.4 Pulsed laser induced silver seeding for electroless plating

This study employed a nanosecond pulsed laser at 266 nm wavelength to reduce the silver ions in the surface modified polyimide [131]. Figure 3.16 shows the scheme of the processing steps.

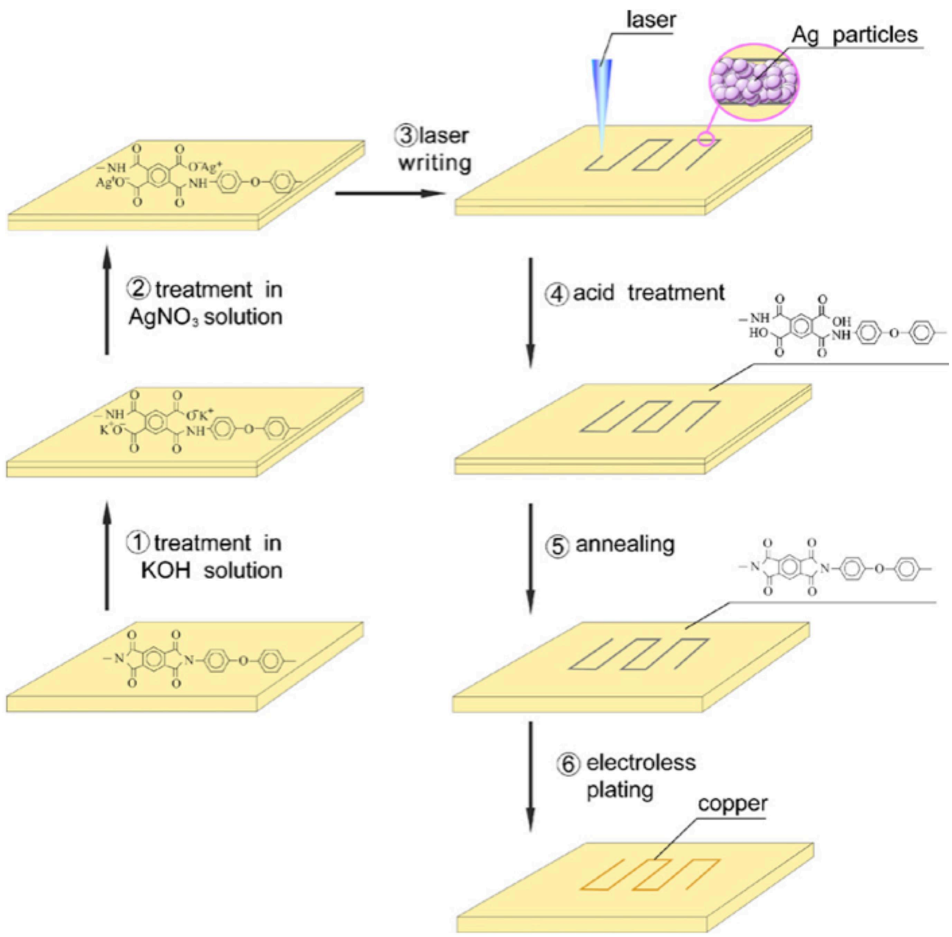

Figure 3.16: Schematic diagram of the pulsed laser induced silver seeding process [131].

Substrate preparation

50 μm thick PMDA-ODA type polyimide film (Kapton 200-H, DuPont) was immersed in a 0.5 M KOH solution at 50 ºC for 20 minutes for hydrolysis. Ag^+ ion-exchange was carried out by immersion in a 0.1 M $AgNO_3$ solution at room temperature for 30 minutes. No additional layer of material was applied on the surface of the substrate to assist the reduction of metal ions.

Reduction method

A pulsed Nd:YAG laser (λ = 266 nm) in TEM_{00} mode with Q-factor modulation was used as irradiation source. The repetition rate and pulse duration of the laser were 10 Hz and 5 ns, respectively. The laser fluence was adjusted to 3.5 mJ/cm^2 after achieving focus. Different laser scanning velocities ranging from 0.10 - 0.55 mm/s were tested.

Anneal and re-imidization

After washing with a 1 wt% H_2SO_4 solution for 10 minutes to exchange unreacted Ag^+ ions with H^+ ions, the films were then annealed in a furnace at 200 ºC for 2 hours for re-imidization. Finally, the films were immersed in an electroless copper bath at room temperature for 30 minutes for deposition of a top copper layer on the laser scanned patterns.

Results

Figure 3.17 shows the SEM images of the deposited electroless copper patterns on the activated surface by laser scanning at: (a) 0.10 mm/s; (b) 0.15 mm/s; (c) 0.20 mm/s; (d) 0.25 mm/s; (e) 0.3 mm/s; (f) 0.35 mm/s; (g) 0.4 mm/s; (h) 0.55 mm/s. Uniform continuous lines were formed at velocities below 0.20 mm/s.

Remark

Ablation, which caused damage on the flexible substrate, was reportedly observed although metallic silver was produced. The mechanisms of the Ag^+ reduction using the pulsed laser for the given peak power, pulse width as well as wavelength, were also not clearly explained. Nonlinear effects caused by such a pulsed laser including absorption of laser energy, electron–ion energy coupling, the breakdown threshold in terms of the laser pulse width, and so on, made the material processing far more complex. The subsequent electroless Cu plating could in fact be initiated by bond breaking on the etched polyimide and not necessarily on the intended silver particle sites only. The reported quality of the electroless Cu deposit appeared poor. In addition, the slow laser scan velocities (<0.20 mm/s) which enabled continuous tracks are not attractive for manufacturing purposes.

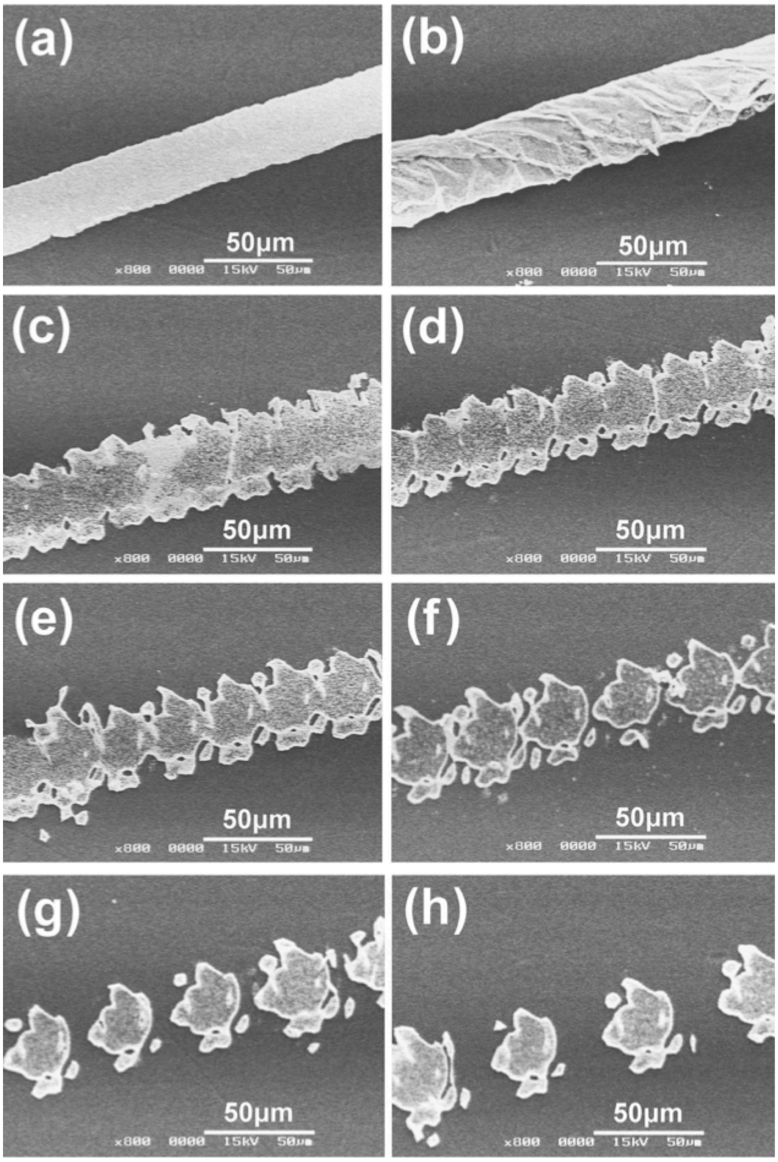

Figure 3.17: Effect of laser scanning velocity on the deposited copper pattern: (a)0.10 mm/s; (b) 0.15 mm/s; (c) 0.20 mm/s; (d) 0.25 mm/s; (e) 0.3 mm/s; (f) 0.35 mm/s; (g) 0.4 mm/s; (h) 0.55 mm/s. [131]

3.6.5 Polyimide as interlayer ink-jet printed on glass substrate

Although ion-exchange is a substrate-material specific process, a way to apply the immobilisation technique of metal ions onto other types of substrates was reported in 2008 by the group at Konan University using polyimide from its resin precursor as adhesive interlayers [132]. Figure 3.18 illustrates this scheme of direct metalisation process.

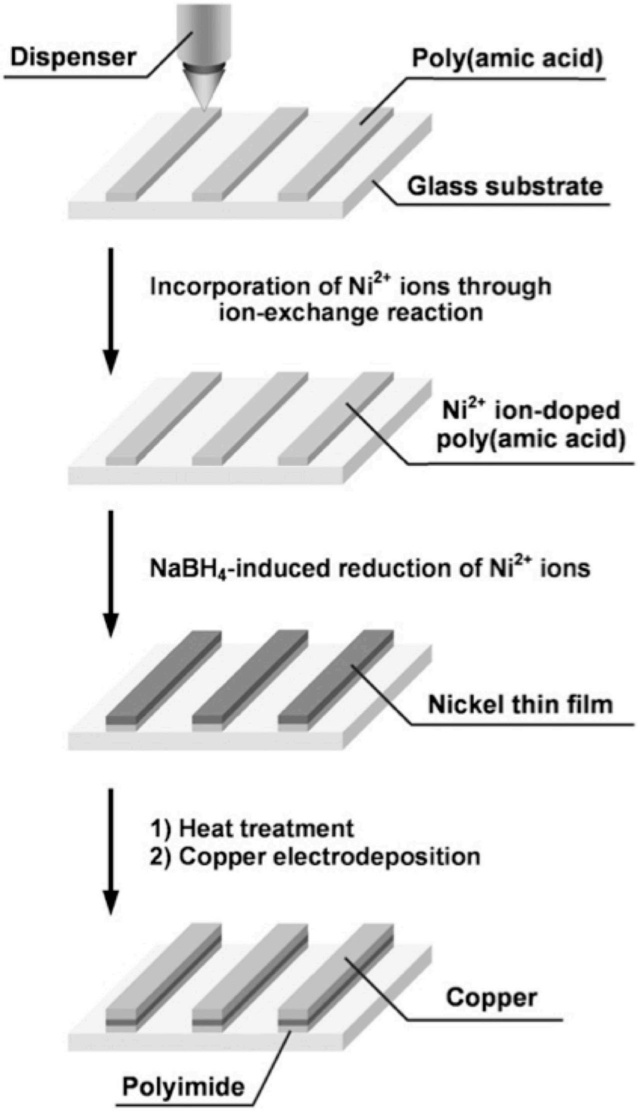

Figure 3.18: Schematic diagram of direct metalisation on glass substrates using PAA as interlayers [132].

Substrate preparation

The precursor, PMDA-ODA poly(amic acid) resin was dispensed by a fine-precision inkjet printer equipped with a temperature-controlled X-Y stage. After patterning the PAA on an amino functionalised glass substrate, the solvent was evaporated at 130 ºC for 20 minutes, producing dry PAA film patterns on the glass substrate.

Reduction method

Subsequent ion-exchange was carried out by immersion into a 0.1 M nickel(II) acetate solution or a (0.6 M) ammonical - 0.1 M nickel(II) acetate solution at 25 ºC. After rinsing, the doped Ni^{2+} ions were reduced by chemical reduction using a 0.01 M $NaBH_4$

solution. After chemical reduction, the remaining unreacted metal ions were extracted by immersion into a 1 wt% citric acid solution for 3 minutes.

Anneal and imidization

After rinsing, the nickel/PAA film was stepwise annealed at 150 ºC for 30 minutes, 200 ºC for 30 minutes, 250 ºC for 30 minutes and 300 ºC for 10 minutes. After anneal, the PAA film was imidized into polyimide and the top nickel thin films were highly adhesive to the polyimide/glass substrate. The metalised nickel film patterns can then be used as the seed layer for copper electrodeposition.

Results

Typical resolution of printed straight and bent lines of 300 μm width and dots of 400 μm diameter were produced. Resistivity of the copper film subsequently electrodeposited onto the chemically reduced nickel thin film was 1.87 μΩ cm (bulk copper: 1.67 μΩ cm). Optical micrographs of the printed patterns and cross-sectional image of the electrodeposited copper and the nickel/polyimide heterojunction are shown in Figure 3.19.

Remarks

The nickel thin film to be suitable as a seed layer for subsequent electrodeposition needs to possess good continuity and uniformity not only at the microscale, i.e. the quality of the ink-jet printed PAA adherent base layer, but also at the nanoscale as the chemically reduced nickel particles need to be connected together to provide good conductivity rather than forming small islands of clusters.

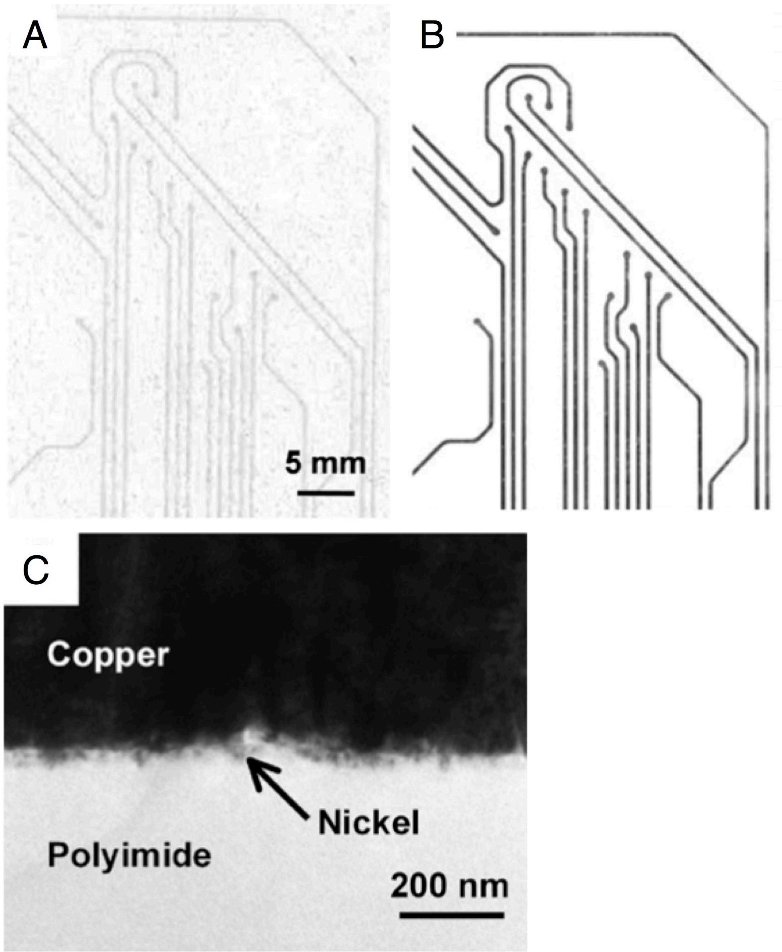

Figure 3.19: Optical microscope images of (a) poly(amic acid) patterns ink-jet printed on glass substrates, and (b) Copper electrodeposited on the nickel thin film seed layer produced based on ion-exchange on the printed poly(amic acid) patterns. [132]

3.7 Photoreduction using methoxy poly(ethylene glycol)

Amongst the above, optically induced deposition techniques are the most attractive because of the better control of the line width and the finer features that can be achieved compared to localised heat or ink-jet printing. Based on the initial work of Akamatsu *et al* on the UV-metalisation of silver ions on polyimide using water for acceleration of the photoreduction [53], further process development has been carried out in this thesis to overcome the reliance on this water layer. A polymer, methoxy polyethylene glycol (MPEG), was coated onto the substrate as a thin film for the first time which serves as a reducing agent upon UV irradiation.

Methoxy poly(ethylene glycol) (MPEG) is a derivative of the very commonly used polymer poly(ethylene glycol) (PEG). Both are low-cost polymers widely used in attachment to drugs, tissues and implants or as a lubricant in biopharmaceutical systems due to their high solubility in polar solvents, chemical stability and non-toxicity.

As mentioned in Section 2.4.1, MPEG was first used by Mallick *et al*. in the solution synthesis of silver and gold particles between 2005 and 2006. This is often referred to as one-pot chemistry synthesis where all reactants, reagents and products are in the same beaker. For metal nanoparticle synthesis, the particles could be obtained from the solution by centrifuge, filtering and evaporation of the residue solution. The simple setup and the gold nanoparticles formed by UV photoreduction by Mallick *et al* [60] is shown in Figure 3.20.

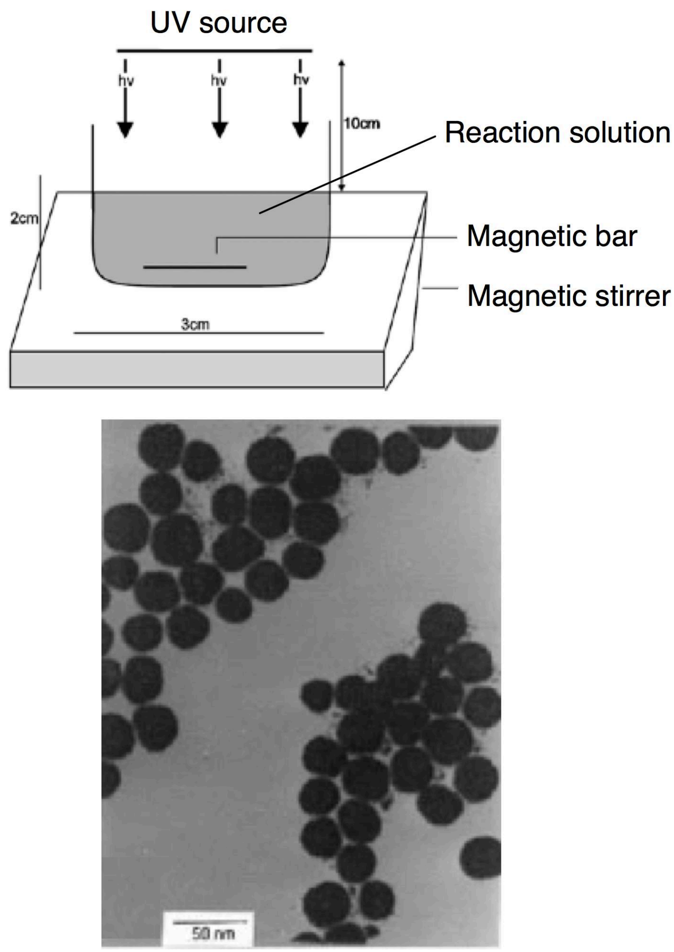

Figure 3.20: (Top) Schematic diagram of the experimental setup for the solution synthesis of metal nanoparticles. (Bottom) TEM image of colloidal gold particles formed by UV irradiation of the reaction solution containing 20 g/l MPEG-5000 and 0.01 M $HAuCl_4$. [60]

Unlike the sparse nanoparticle formation in solution in Mallick's work, formation of a metallic thin film on the surface of a substrate is required for the purpose in this thesis. Experiments carried out in this thesis have demonstrated that it is possible to reduce the metal ions within the surface modified polyimide by electrons released from photoexcitation of the photoreducing agent in the external coating of the substrate. The chemical pathway for MPEG to act as a reducing agent upon UV irradiation is described in the following sub-section. Experiments using MPEG are presented in Chapter 6.

3.7.1 Mechanisms

The chemical formula of MPEG is:

$$\mathrm{CH_3 - O - (OCH_2CH_2)}_n \mathrm{- H}$$

where *n* indicates the average number of oxyethylene groups. Methoxy refers to the functional group CH_3–O. In the demonstration of the photochemical reduction of Ag^+ and Au^{3+} ions from their salts to metal nanoparticles using a one-pot MPEG in water matrix solution in which metal salts were dissolved, Mallick *et al* suggested a reaction pathway as follows [58], [60-63].

When the chemical formula of MPEG is rewritten as

$$\mathrm{CH_3 - O - (OCH_2CH_2)}_{n-1}\mathrm{CH_2CH_2 - OH}$$

the group –CH_2CH_2–OH can react with the $H^\bullet$ and $OH^\bullet$ radicals generated from photolysis of water under irradiation at 254 nm wavelength:

$$\mathrm{H_2O} \xrightarrow{h\nu} \mathrm{H^\bullet + OH^\bullet} \tag{3.5}$$

giving the two reactions:

$$-CH_2CH_2 - OH \xrightarrow{H^\bullet} -CH_2CH^\bullet - OH + H_2 \tag{3.6}$$

$$-CH_2CH_2 - OH \xrightarrow{OH^\bullet} -CH_2CH^\bullet - OH + H_2O \tag{3.7}$$

Where, in both cases, the radical $–CH_2CH^\bullet–OH$ is created which can then serve as a powerful reducing agent with a large potential value of -1.9 V (vs SHE) for the redox couple ($–CH_2CHO/–CH_2CH^\bullet–OH$) [58], [60-63]. According to the reduction potential values listed in Table 3.3 for (Au^+/Au^0) and (Ag^+/Ag^0) which are +1.50 V and +0.79 V (vs SHE) respectively for reduction onto a large metal surface, the much more negative potential value for oxidising $–CH_2CH^\bullet–OH$ should be capable of reducing both gold and silver ions. Although Mallick *et al* also suggested this method for the reduction of these metal ions into standalone atoms in aqueous solution (the very early stage of particle formation) instead of a large metal surface, these potential values are significantly lower at -1.40 V and -1.80 V (vs SHE) for (Au^+/Au^0_{atom}) and (Ag^+/Ag^0_{atom}) respectively [61], [63]. Nevertheless, $–CH_2CH^\bullet–OH$ with potential value of -1.9 V (vs SHE) can still serve as a suitable reducing agent.

As already described in Section 3.5.2, the electrons are required to transport from the external coating across the interface into the amorphous phase of the substrate to reach the metal ions, therefore the efficiencies in electron transport within these mediums also need to be taken into account as well as the reduction potential values. The other key difference between the experiments carried out by Mallick *et al* and those in this thesis is that ethanol is used as the solvent for MPEG instead of water in order to make it possible for spin-coating of a thin film on top of the ion-doped polyimide substrates. No H_2O can then be accounted for, so the reaction pathways described earlier involving $H^\bullet$ and $OH^\bullet$ radicals for generation of $–CH_2CH^\bullet–OH$. Photodissociation of ethanol ($CH_2CH_3–OH$) occurs at around 193 nm [133], a much lower wavelength than that for water therefore a direct generation of $H^\bullet$ and $OH^\bullet$ radicals is unlikely using the light sources employed in this thesis which emit mainly in the near-UV region. There might well be other mechanisms involved for providing radical reaction pathways in the system.

Polymer-reducing agents such as poly(vinyl pyrrolidone) (PVP) have been widely used recently for synthesis of metal nanoparticles [134], [135]. The hydroxyl (–OH) end groups in the polymer were found to be responsible for the reduction of various noble metal ions under mild heat treatment. The mild reducing power of the hydroxyl end groups has been utilised for a long time as reducing agents for metal colloids synthesis in alcohol [135], which comprises a simple molecular structure of inactive hydrocarbon chains with hydroxyl end groups. Both the molecules of MPEG and ethanol are hydroxyl terminated. It could therefore be suggested that the hydroxyl in the MPEG-ethanol system played a role as a reductant for noble metal ions analogous to PVP.

While the origins of the generation of the photoreducing functional groups from the MPEG molecules in the MPEG-ethanol matrix upon near-UV irradiation requires further studies in the fundamental chemistry aspect, experiments have shown that this configuration of wavelength and by replacing ethanol with water with MPEG, electron release and transfer from the MPEG coating into the amorphous substrate is achieved, thereby reaching the goal of reduction of the incorporated mobile metal ions.

3.8 Photoreduction using photosystem I

Besides MPEG, another photocatalyst discovered in this thesis for metal ions reduction and consequently producing micro-scale metallic patterns is the most abundant biological light-harvesting material available on earth, photosystem I (PS-I). PS-I comprises of light harvesting pigment proteins, amongst which, chlorophyll is being most commonly referred to for photosynthesis. Several modifications of chlorophyll occur among plants and other photosynthetic organisms. All photosynthetic organisms (plants, certain protistans, prochlorobacteria, and cyanobacteria) have *chlorophyll a* which absorbs its energy from the violet-blue and reddish orange-red wavelengths, and little from the intermediate (green-yellow-orange) wavelengths. Accessory pigments also present in PS-I absorb energy from some other regions of wavelength that *chlorophyll a* does not absorb. Accessory pigments include *chlorophyll b* (also c, d, and e in algae and protistans), xanthophylls (such as lutein and zeaxanthin in spinach, sweet corn and potato), and carotenoids (such as beta-carotene and lycopene in carrots and tomatoes). The light absorption spectra of these pigments [136] are shown in Figure 3.21.

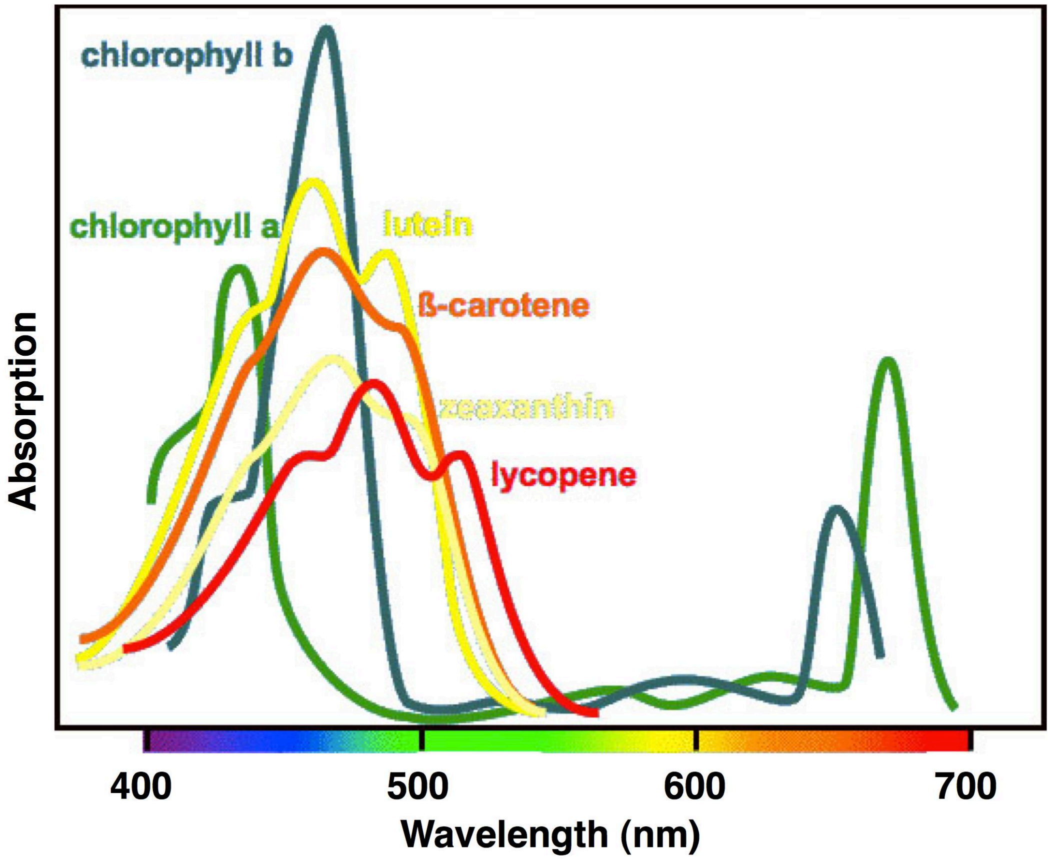

Figure 3.21: Absorption spectra of chlorophyll a and b and some other accessory pigments [136].

The absorbed energy excites electrons from the pigment molecules into a higher energy state. The excited electrons can then be quenched by neighbouring electron recipients, whereby the excited charge is separated from the pigment molecules. This electron transfer process occurs within a very short time of up to picoseconds and at a very short length scale of up to about 1 nanometre [137]. Strikingly, this thesis has demonstrated that photoexcited electrons can be successfully transferred from a coating of this visible light-activated photocatalyst over a considerably long distance to the target metal ions within the surface-modified polyimide. This is explained in further detail in Chapter 8.

Only UV light was used in all of the photoreduction type processes described in Chapter 2. No other prior literature on utilising chlorophyll or the accessory pigments for producing metal nanoparticles in a suspension or for metal thin films by visible light irradiation have been found. There are suggested uses of photoexcited electrons from chlorophyll pigments in electrical engineering for assisting electricity generation in solar cells in conjunction with semiconductor materials [138].

This Section will first describe the basic background of PS-I in plants, then introduce briefly the photoexcitation mechanisms that take place in PS-I followed by the absorption spectrum characterisation using photospectroscopy. Experiments using PS-I are presented in Chapter 8.

3.8.1 Chloroplast and chemical structures of chlorophyll

PS-I is housed within the chloroplast of a plant cell. Chloroplast is the specialised subunit within a plant cell that is directly responsible for photosynthesis and is separately enclosed within its own lipid membrane. Within a chloroplast, the thylakoid is the structural unit of photosynthesis and has a flat disc shape. They are stacked on top of each other into columns of different lengths in order to increase the surface area of the thylakoid membrane exposed to sunlight. PS-I are found in the thylakoid membrane. Figure 3.22 shows a schematic structure of thylakoid stacks in a chloroplast. During PS-I extraction (see Chapter 4), the membranes of the chloroplast and thylakoid are mechanically broken apart so that the PS-I within the thylakoid's membrane can be dissolved in the ethanol solvent.

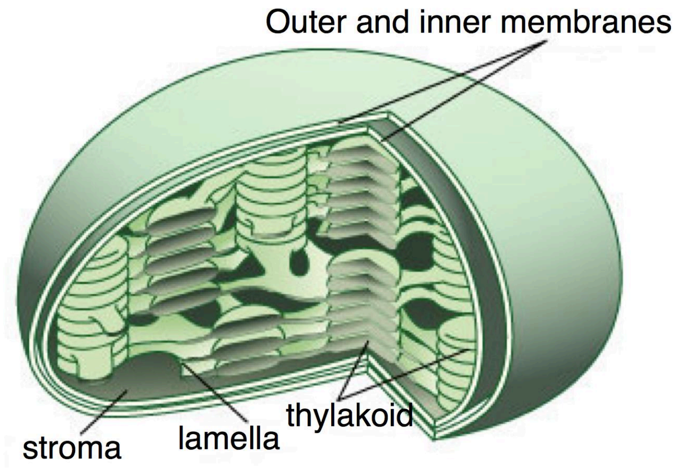

Figure 3.22: A chloroplast consisting of outer and inner membranes, stacks of thylakoids each connected by lamella, the skeleton unit structure, and stroma, the area where sugar production takes place. The ellipsoidal chloroplast is about 2.5 μm thick and 5 μm long. [139]

The mechanism of absorption of light by the chlorophyll molecules in the PS-I can be seen from its chemical structure as shown in Figure 3.23. The chlorophyll molecule consists of a hydrophilic head and a long hydrophobic tail. The magnesium ion in the head can gain or lose electrons resulting in a charge change. The magnesium ion is chelated by four structures called pyrrole ring, therefore the whole system is called a tetrapyrrole ring. The whole system is rich in conjugated double bonds, that is, the single and double bonds in the molecule alternate. This structure enables the electrons to be delocalised over the whole system and so be shared by many atoms, meaning they may move around the whole system. When these bonds are excited by light, the resonance of the conjugated bonds can expand the electron cloud of the magnesium ion.

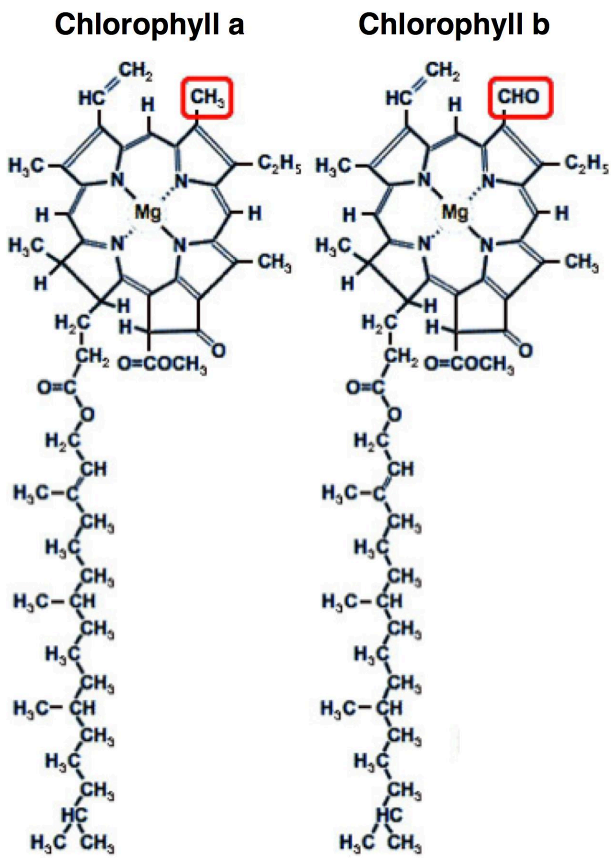

Figure 3.23: Chemical structures of chlorophyll a and b, with the only difference that distinguishes between the two molecules highlighted by the red lines [136].

3.8.2 Photoexcitation, transfer and efficiency

Excitation transfer

When light is absorbed by a chlorophyll molecule, the photon energy excites an electron from its ground energy level to an excited energy level. The extraction of this excited electron from the pigment molecule is referred to as photo-induced charge separation. The excited molecule transfers this electron to a nearby acceptor molecule, thereby producing an ion pair state consisting of the oxidized chlorophyll and reduced acceptor. After the initial electron transfer event, in order to transfer the excitation further over a length of distance, a series of electron transfer reactions take place through a chain of redox relays between various acceptors such as accessory pigments, various proteins in the membrane and enzyme. The collection of chlorophyll and the accessory pigments is often referred to as the antenna system.

Excitation transfer must be fast enough to deliver excitations to the photochemical reaction centre, where sugar is produced, and have them trapped in a time relatively short compared to the relaxation time where the electrons relax from an excited state to the ground state. The relaxation time of isolated antenna complexs, where the reaction centres have been removed, are typically in the 1 to 5 nanoseconds range. Observed excited state lifetimes of systems where antennas are connected to reaction centres are generally of the order of a few tens of picoseconds. It means that, in the presence of electron trapping by the photochemistry in the reaction centres, almost all the excitation energy is transferred [140].

Quantum efficiency

The quantum efficiency of the chlorophyll pigments is different to that of the complete photosynthesis process. The energy conversion percentage figures for chlorophyll is usually measured by experiments such as CO_2 conversion to O_2 or sugar production for a given amount of incident light energy, usually from the full white light spectrum. These products of photosynthesis are produced through complex pathways in the photochemical reaction centres after excitation transfer through a redox relay from the initial pigments which absorbed light. Therefore, the direct estimation of the percentage of photons producing an electron-hole pair by photosynthetic pigments has been carried out by fluorescence measurements and computational methods, with a report describing a well above 96% quantum yield for chlorophyll b pigments [137]. Another recent report demonstrated that chlorophyll derivatives, i.e. the natural dyes in different types of plants, can achieve monochromatic photon to current conversion yields exceeding 60% [141].

3.9 Re-imidization

As the final step of the metalisation process, the reformation of the imide ring and hence the polyimide chemical structure from PAA by the second ion-exchange step as shown in Figure 3.8 in dilute sulfuric acid solution is known as re-imidization. The conditions for this process to occur is similar to curing of the poly(amic acid) precursor. Since such a thin layer and small quantity of PAA is being re-imidized, heat treatment at 250 ºC for 30 minutes after the second ion-exchange in 1 wt% H_2SO_4 solution is generally sufficient as evidenced in the literature. Silver nanoparticles aggregation within the surface-modified layer occurs concurrently with the re-imidization process and higher temperature and longer heat treatment times have been investigated in this thesis. This is described in details in Chapter 9.

3.10 Conclusion

This chapter has presented the backgrounds and necessary knowledge of each of the process step of the direct metalisation methodology proposed in this thesis. The science of ion-exchange on the surface of polyimide was described in detail. Several techniques for the reduction of the ion-exchanged metal ions incorporated in the surface modified polyimide system were reviewed and compared, before presentation of the photoreduction mechanisms of the two novel photoreducing agents selected for the studies in this thesis.

Chapter 4

Preparation of the surface modified polyimide and photoreducing agents

4.1 Introduction

This Chapter describes the preparation procedures of the standard Ag^+ ion-exchanged polyimide substrate used throughout this thesis. After that, the preparation of the two photoreducing agents, MPEG and PS-I extract from spinach leaves is described.

4.2 Ion-doped polyimide preparation

Kapton HN type 50 μm thickness polyimide films (PI) was used throughout this thesis. The cleaning procedures of all Kapton PI films were as follows:

(i) Rinsing in acetone.
(ii) Rinsing in isopropyl alcohol (IPA).
(iii) Washing in deionized water (DI) with DECON 90 detergent in an ultrasonic bath for 5 minutes.

After further rinsing with DI, the films are ready for the surface modification steps. Surface modification starts with the alkaline hydrolysis of polyimide by KOH immersion whereby cleavage of the imide ring takes place. Subsequently, the ion-exchange is carried out by immersion of the substrate into a $AgNO_3$ solution.

4.2.1 KOH immersion and post-process re-imidization

Cleaned PI films were immersed in a KOH aqueous solution with concentrations of 0.5 to 5 M at 50ºC for durations ranging from 5 to 30 minutes. These conditions determine the depth of the surface modified layer on the polyimide substrate. The substrates were immersed vertically in a large beaker containing the KOH solution, on a magnetic stirrer hot plate. The deeper the modified layer, the more Ag^+ ions can be subsequently exchanged into the substrate. It is however not desirable to have a high degree of modification for the following two reasons:

(i) The mechanical rigidity of the polyimide film deteriorates with the degree of modification.

(ii) A lower degree of modification makes it easier and quicker to recover the polyimide structure by re-imidization.

Mechanical degradation can be readily observed as the polyimide, weakened by alkaline attack, has a jelly-like appearance and eventually dissolved. Table 4.1 lists the qualitative film rigidity observed. Since a shorter immersion time is preferred and a lower degree of surface modification could potentially minimise any defects in re-imidization, therefore 1 M KOH solution concentration and 5 minutes immersion time were selected as the best process conditions. To confirm that these conditions do indeed achieve hydrolysis of polyimide, Fourier transform infrared (FTIR) spectroscopy was used to observe the changes in the molecular structure using the Thermo Nicolet IN10 FT-IR. The attenuated total reflection mode (ATR-FTIR) was used to obtain the reflected signals from the substrate. The set up of the measurements is shown in Figure 4.1

Table 4.1: Mechanical degradation of polyimide films of 50 μm thickness as a function of various KOH immersion conditions at 50ºC.

KOH Concentration (M)	Immersion Time (minutes)	Film Rigidity
0.5	5	Good
0.5	15	Good
0.5	30	Good
1	5	Good
1	15	Moderate
1	30	Deteriorated
2	5	Deteriorated
2	15	Weak
2	30	Weak
5	5	Some dissolution
5	15	Severe dissolution
5	30	Severe dissolution

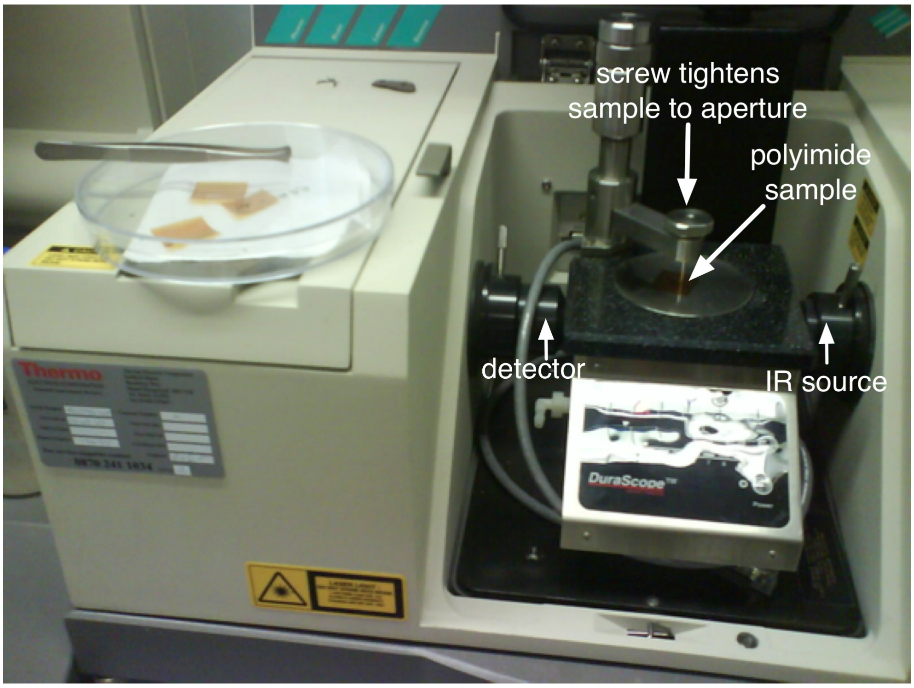

Figure 4.1: Thermo Nicolet IN10 ATR-FTIR apparatus.

The important indicators from these spectra are the presence or absence of the characteristic absorption peaks of imides, which correspond to the specific vibration frequencies of certain chemical bonds. The peaks at ~1780, 1710, 1370 cm^{-1} correspond to the double bond C=O asymmetric stretching, the C=O symmetric stretching, and the imide ring C–N–C stretching, respectively [142]. It can be seen in Figure 4.2(a) that the sample treated by the 0.5 M KOH solution for 5 minutes shows the presence of all three characteristic peaks. In fact this spectrum is very similar to that of a non-treated polyimide film. It means that the immersion under these conditions has not been sufficient for a significant depth of the polyimide substrate to be modified.

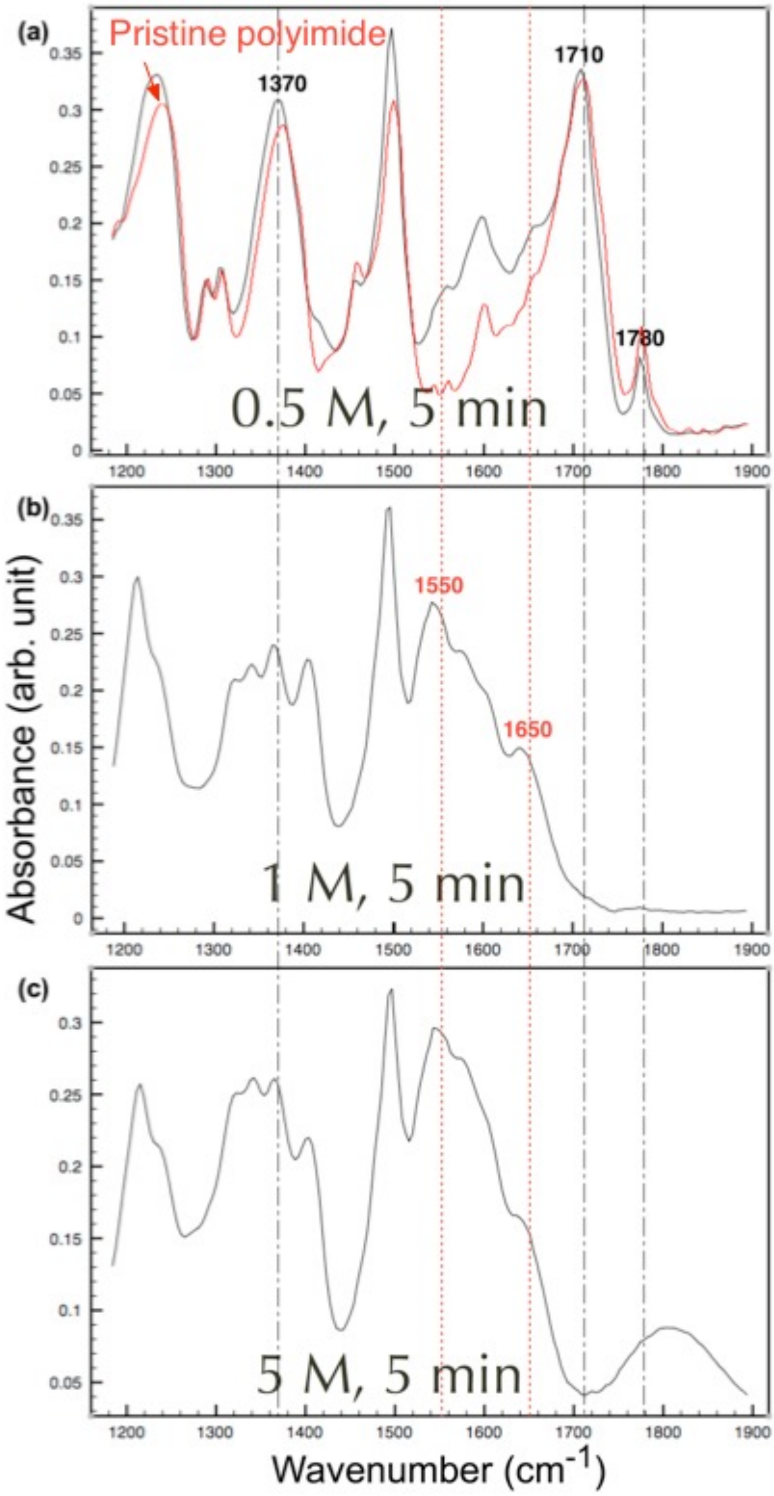

Figure 4.2: ATR-FTIR spectra of the polyimide films after immersion in

KOH solution of concentration: (a) [black] 0.5 M in comparison with [red] pristine polyimide without KOH treatment; (b) 1 M; (c) 5 M, for 5 minutes.

In contrast, the spectra for the samples treated by the 1 M and 5 M KOH solution for 5 minutes also shown in Figure 4.2(b) and (c) clearly indicate the hydrolysis of the imide rings. In these spectra, the peak at 1370 cm^{-1} is reduced whilst the peaks at 1710 and 1780 almost diminished, showing the absence of the imide characteristics. The subsequent formation of the potassium polyamate amide by KOH hydrolysis is further supported by the appearance of the characteristic peaks of the amides I and II vibrations near 1650 and 1550 cm^{-1}, respectively [142].

These two spectra (5 M and 1 M KOH solution) look very similar despite the very obvious differences in the resultant film rigidity. The peak heights between the two samples cannot be used for direct comparison because of the arbitrary amplitude created when the screw tightens each sample onto the aperture on the ATR-FTIR apparatus. Therefore the spectra here can only indicate the existence of changes in the surface molecular structure but cannot characterise the relative degree of modification between samples.

Using ATR-FTIR, evidence of the re-imidization of the modified layer where the C-N-C imide rings reform was also detected. Figure 4.3 shows that the peaks at ~1780, 1710, 1370 cm^{-1} reappeared after a surface-modified sample was re-imidized. Re-imidization is performed when the metalisation step is completed and after the unreacted Ag^+ ions are removed from the substrate using a second ion-exchange step by immersion in a 1wt% H_2SO_4 solution for 30 minutes. Re-imidization is typically achieved at 250ºC for 30 minutes [53].

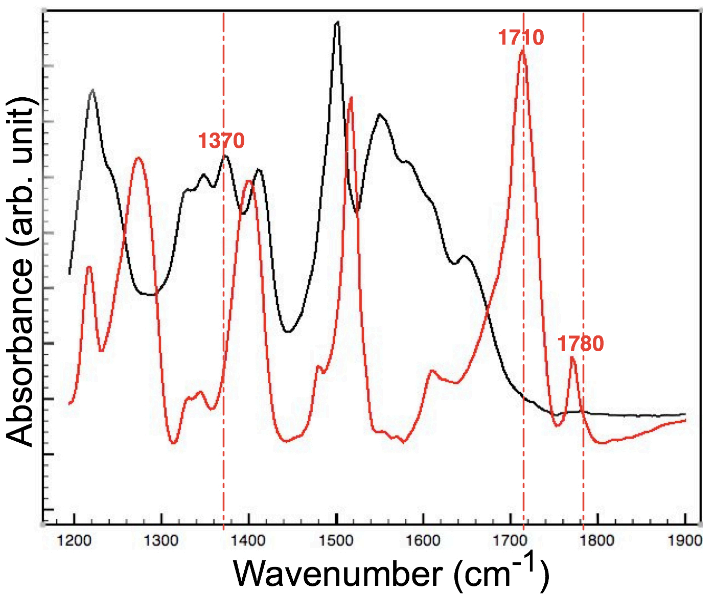

Figure 4.3: ATR-FTIR spectra of a KOH hydrolysed polyimide film (black line) and a re-imidized

polyimide film (red line).

4.2.2 Ag^+ ion-exchange

For each of the KOH immersion conditions, two different $AgNO_3$ immersion times of 15 and 30 minutes were applied. No noticeable differences were observed under an optical microscope about the appearance of the resultant photoreduction of silver tracks by UV-photomask exposure or laser writing. Also no noticeable differences in the subsequent electroless Cu deposition were observed as the incubation time varied. This time is defined as the time between the substrate being immersed into the plating bath and the copper deposit being visibly observed. Therefore the silver ion-exchange condition of 0.1 M $AgNO_3$ solution and 15 minutes at room temperature have been used throughout this thesis. As the goal for this ion-exchange step is to exchange all the K^+ ions already in the substrate with the Ag^+ ions from the solution, the concentration of the $AgNO_3$ solution and immersion time can be chosen beyond their optimum values. Further investigation using analytical surface profiling is needed to determine the minimum required concentration of $AgNO_3$ and the shortest possible immersion time.

4.3 Photoreducing agents

4.3.1 MPEG preparation

The MPEG-5000 (Aldrich) concentration was 100 g/l, using ethanol as the solvent. The polymer solution was heated to 50ºC until the MPEG was completely dissolved. After that, the coating was carried out by spin-coating at 4000 rpm for 30 s, resulting in a transparent thin film of approximately 1 μm thickness when dried as shown in the height measurement in Figure 4.4. Figure 4.5 shows a UV-vis spectrum of the MPEG in ethanol solution measured by a Shimadzu UV-1601 spectrophotometer.

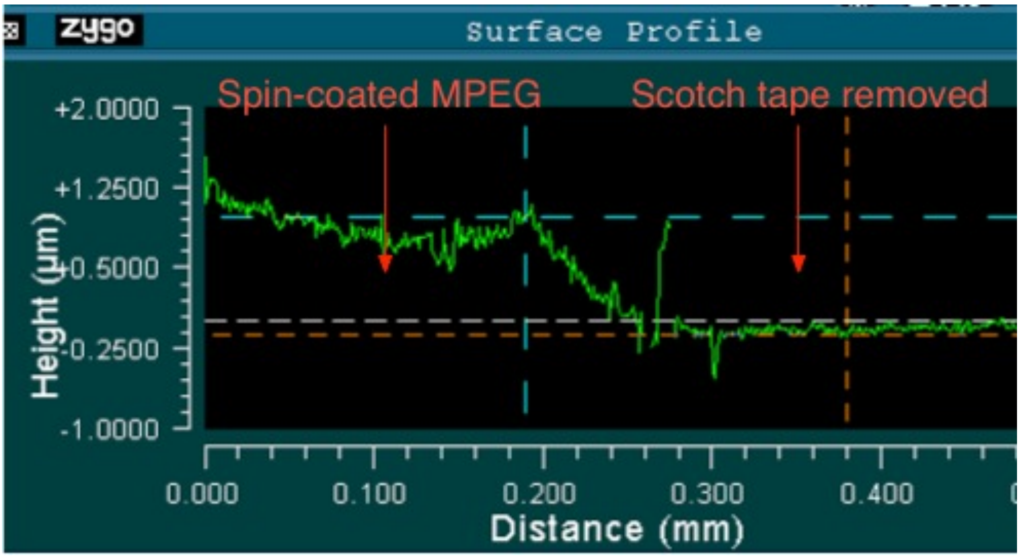

Figure 4.4: Zygo white light interferometry of a step height created by spin-coating MPEG onto a polyimide substrate with Scotch tape on one side.

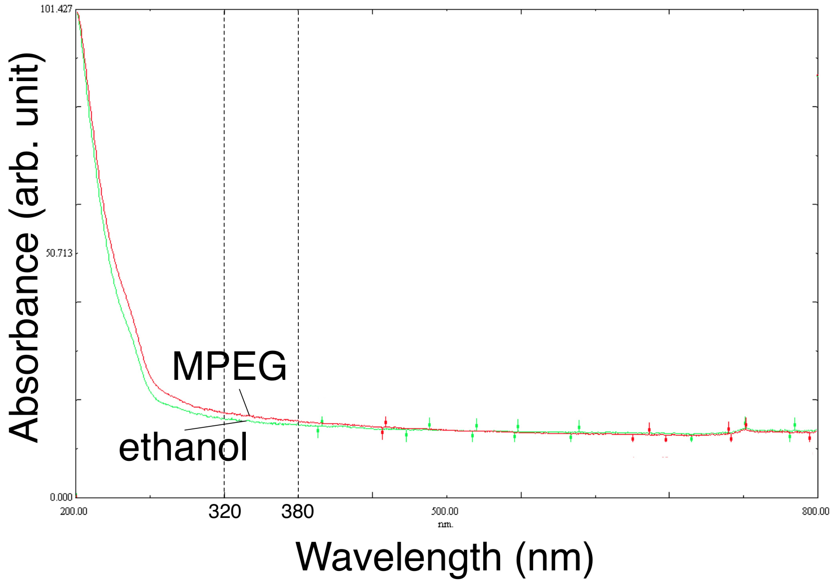

Figure 4.5: UV-vis spectroscopy of 100 g/l MPEG in ethanol solution.

4.3.2 PS-I preparation

The PS-I was extracted from 25 g of spinach leaves in a blender with 250 ml of ethanol. The PS-I solution was then filtered through a 11 µm Whatman filter paper. The filtered solution was left to stand for 10 minutes to allow the fine debris from the broken cells to settle on the bottom of the conical flask by sedimentation [143]. 90% of the liquid was then poured into a second conical flask and left to stand for a few hours. After that, 90% of the liquid from the second conical flask was poured into a third conical flask to obtain a clean PS-I solution after the sedimentation. Figure 4.6 shows a UV-vis spectrum of the clean PS-I solution measured by the same spectrophotometer. The absorption peak positions in this spectrum were expected as they are in good agreement with the absorption spectra of chlorophyll a and b and the convolution of some other accessory pigments in the PS-I as shown in Figure 3.21 from the literature.

The PS-I solution was typically deposited in 1 ml volume on the substrates for the experiments described in Chapter 8 by a pipette drop-wise and left to dry.

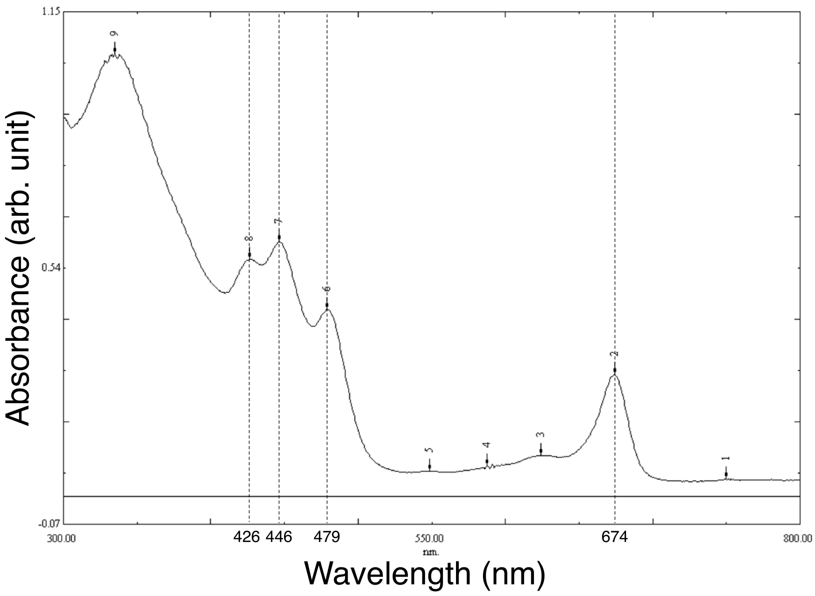

Figure 4.6: UV-vis spectroscopy of the clean PS-I solution.

4.4 Summary of process steps

The process steps for the preparation of the Ag^+ ion-doped polyimide substrate used throughout this thesis are as follows:

(i) Cleaning of the polyimide sheet as described in Section 4.2.

(ii) Immersion in 1 M KOH solution for 5 minutes at 50ºC. Rinse with DI water.

(iii) Immersion in 0.1 M $AgNO_3$ solution for 15 minutes at room temperature. Rinse with DI water.

After the Ag^+ ion-doped polyimide substrate is prepared, the photoreducing agent, either MPEG or PS-I can be applied on top as described in Section 4.3. Photoreduction can then be carried out using the exposure apparatus described in Chapter 5. Subsequently, the substrate would be immersed into a 1 wt% H_2SO_4 solution for 30 minutes at room temperature to achieve a second ion-exchange where the unreacted Ag^+

ions in the substrate are replaced by H^+ ions in the dilute acid solution. Finally, the substrate containing the photoreduced silver particles are heat treated for re-imidization typically at 250ºC for 30 minutes in air, and at various other conditions as described in Chapter 7.

Chapter 5

Exposure apparatus and sample characterisation techniques

5.1 Introduction

Photoreduction was carried out on the Ag^+ ion-doped polyimide substrates coated with either MPEG or PS-I by several different UV or blue light sources. The apparatus setup of each exposure system is described in this Chapter. These include UV lasers with outputs from a very low optical power of less than 1 mW up to 12 mW, which is considered a high power in terms of the UV-polymer interaction, as will be described by the results in Chapter 6. A UV flood exposure system was also used for a more in-depth investigation of the reactions that occurred during the photoreduction in Chapter 7. Light emitting diodes (LED) were used as blue light sources for the photoreduction experiments using PS-I as the catalyst as described in Chapter 8. The scanning electron microscopy, elemental analysis and the mechanical profiling characterisation techniques used in this thesis are also described.

5.2 Exposure apparatus

5.2.1 Laser systems

Laser system 1

This setup was used for the experiments in Chapter 6.3. As illustrated in Figure 5.1, a GaN diode pumped continuous wave (CW) laser with an output wavelength of 375 nm and an optical output power of 15 mW was used. A variable neutral density filter wheel was used to attenuate the laser beam. A beam splitter was used to split the laser input into two parts so that the substrate could be observed by a CCD camera. A beam expander was used to adapt the beam diameter to the objective lens in order to achieve a circular focused spot size down to around 1 μm onto a small computer-controlled XY translation stage. The laser beam spot diameter was defined as the boundary of the beam as observed by the CCD camera. A mechanical computer-controlled shutter was interfaced to the laser scanning software. The maximum resultant optical power is 0.6 mW after focus.

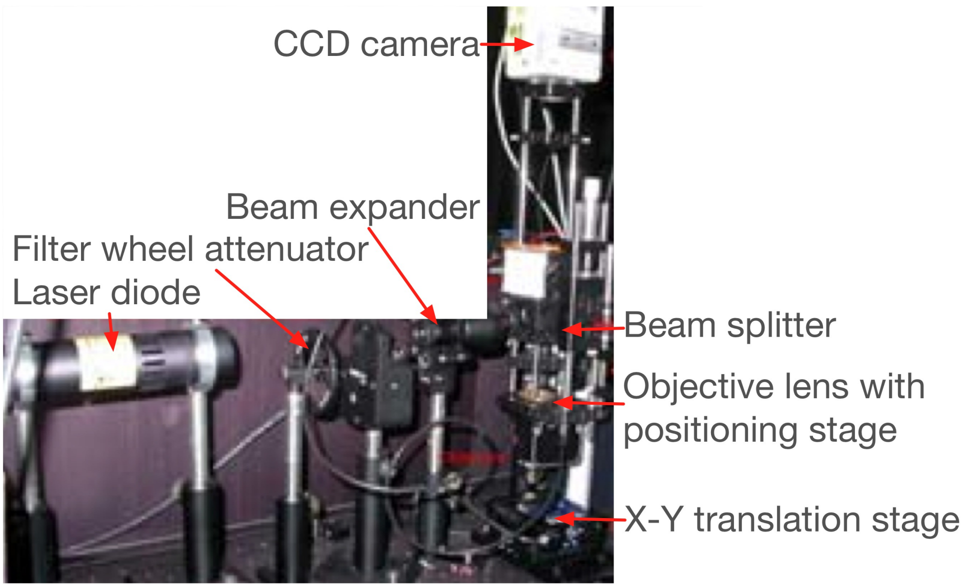

Figure 5.1: Laser system 1 setup – GaN diode pumped laser.

Laser system 2

Since laser system 1 provided a very low optical power of less than 1 mW, a second setup was used for the experiments described in Chapter 6.4.1. The CW diode laser chosen (Koheras, LGT laser system) has an output wavelength of 375 nm for an optical output power of 15 mW. It is a "pigtailed" laser diode with a single mode fibre coupled for beam delivery. The fibre core diameter is about 2 μm for a length of 1.5 metre and

40% coupling efficiency. At the end of the fibre is a collimator with an aspheric lens of focal length f of 6.2 mm. The optical power is typically 6 mW when focused to a spot size of 20 µm.

Two translation setups were used. Figure 5.2 shows the end of the fibre with the focusing lens mounted onto the bread board with a computer-controlled XY translation stage (Aerotech) underneath. Figure 5.3 shows the end of the fibre with the focusing lens mounted onto a translation robot prototype, the Equator Concept, provided by the Company Renishaw plc.

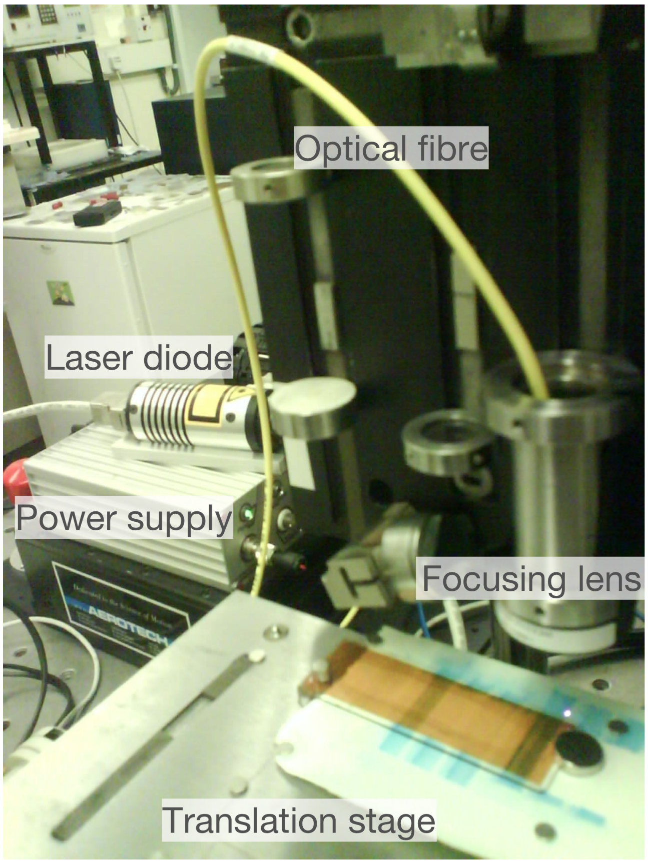

Figure 5.2: Laser system 2 setup with translation stage.

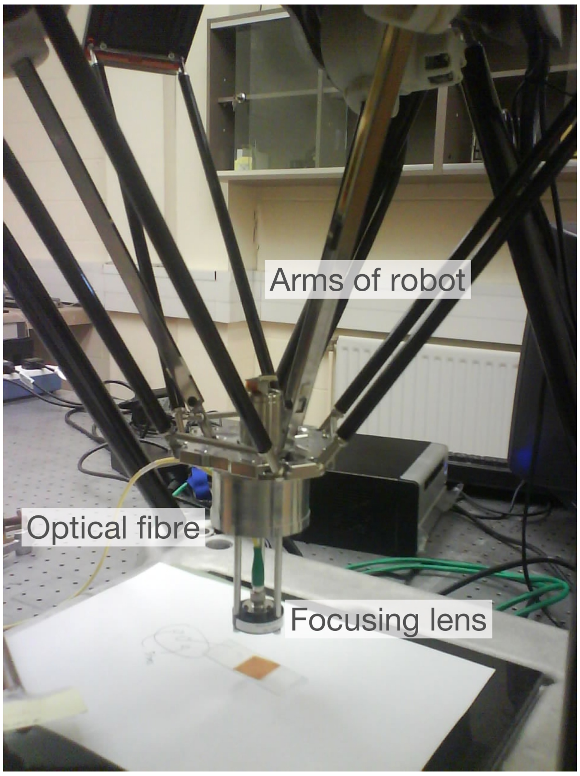

Figure 5.3: Laser system 2 setup with translation robot.

Laser system 3

The third laser system used in Chapter 6.4.2 is a CW HeCd laser (KIMMON Koha Co. Ltd Model IK3201R-F) with an output wavelength of 325 nm with a Gaussian TEM_{00} beam profile. The optical output power available at the writing plane is between 6-12 mW focused to a spot size of 15 µm. Figure 5.4 shows the apparatus for this set up which includes a filter wheel attenuator, beam splitter and focusing lens on a bread board, computer-controlled mechanical shutter, a XY translation stage and a manual Z-axis stage for focusing.

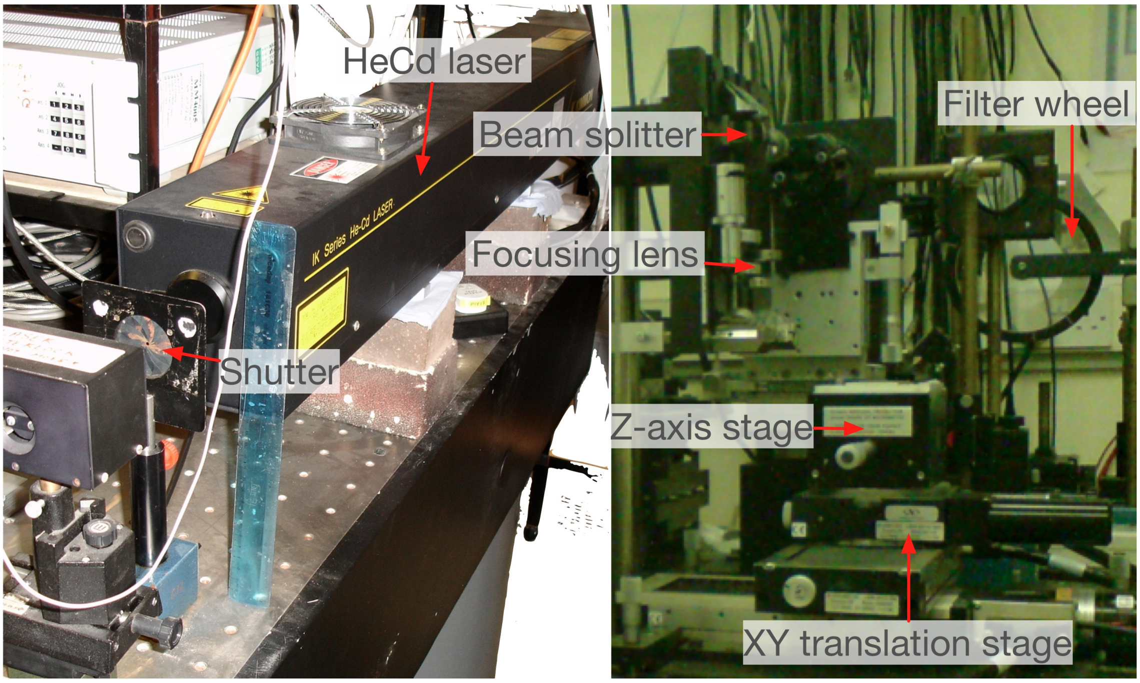

Figure 5.4: Laser system 3 apparatus.

5.2.2 UV lamp exposure

UV lamp 1

The UV light source LQ UV 1000 from Linos Photonics, as shown in Figure 5.5, was used in the initial proof of concept experiments in Chapter 6.2. The UV light (250 nm – 450 nm) was coupled out of the enclosure of the light source using a fibre delivery cable. A collimator lens was connected to the far end of the cable, producing a uniform beam with a diameter of 2 cm. The output power at a distance of 5 cm from the collimator lens was measured to be 750 mW/cm^2.

Figure 5.5: UV light source used for the proof of concept experiments.

UV lamp 2

A collimated UV exposure system (Tamarack Model 152) as shown in Figure 5.6 was used in the experiments described in Chapter 7. The system provides a 12”x12” exposure area, suitable for producing a large batch of samples using the direct metalisation process described in this thesis.

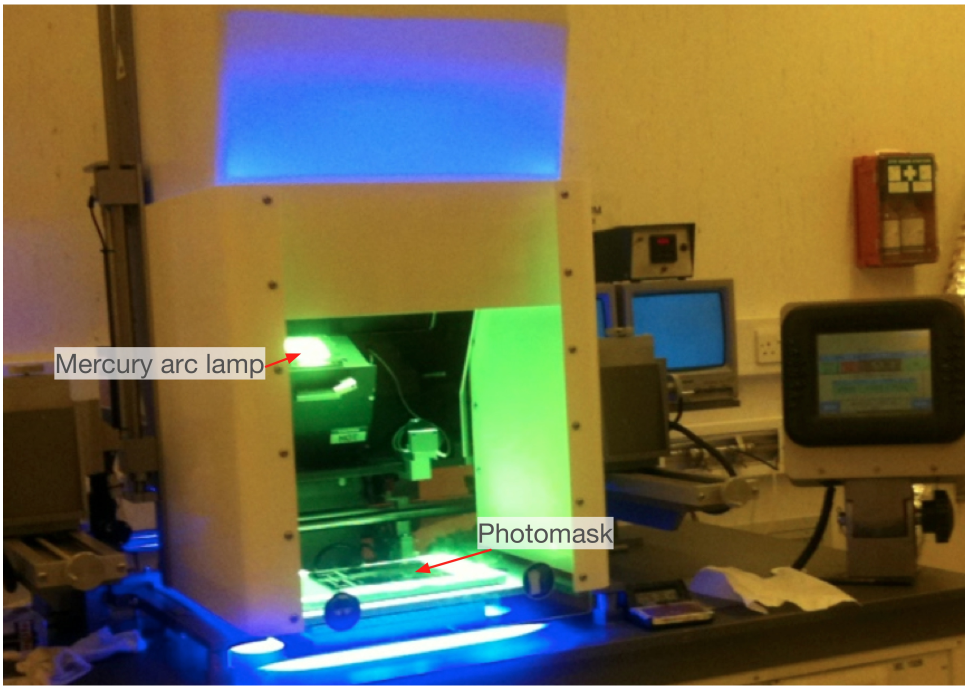

Figure 5.6: *Tamarack collimated UV exposure system.*

5.2.3 Blue light exposure

Blue LED system 1

A mounted blue LED (Thorlabs - MBLED) containing 16 emitters as shown in Figure 5.7 emitting uncollimated light at 470 nm (spectral half width = 25 nm) was used without any additional optics. The light source was placed directly on top of the sample substrates. A resultant optical power between 25 – 55 mW was measured on the substrate over an area of approximately 1 cm^2.

Figure 5.7: LEDs mounted on a heat sink.

Blue LED system 2

This system provides a much higher optical power than that from the Blue LED system 1 above. A maximum power of 1270 mW/cm^2 was delivered by an optical fibre, which was coupled to a high power LED (Prizmatix – UHP-Mic-LED-460) as shown in Figure 5.8.

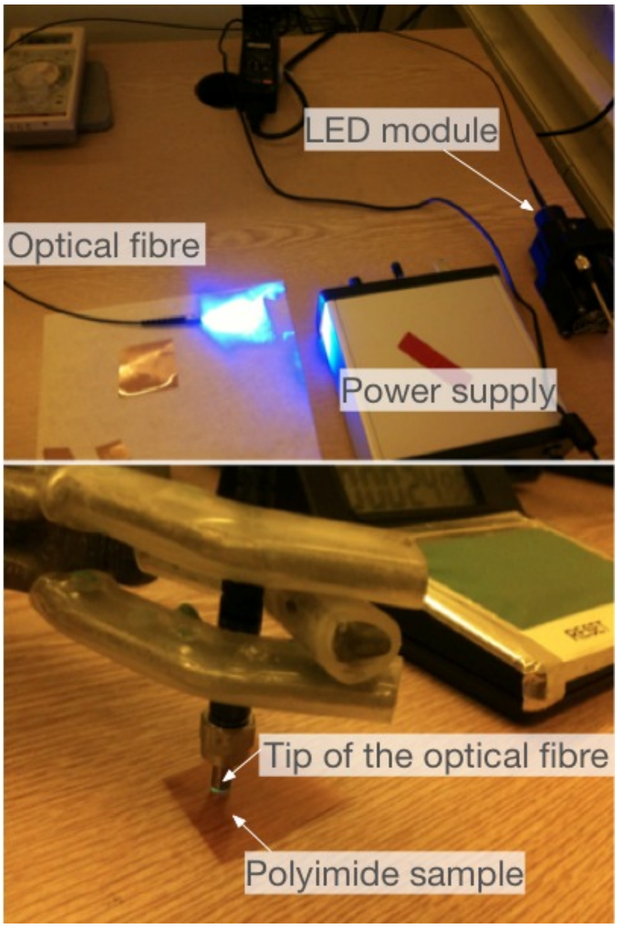

Figure 5.8: Blue LED system 2.

Both systems were used in the experiments described in Chapter 8.2.

5.3 Characterisation techniques

5.3.1 Electron microscopes and element analysis

In scanning electron microscopy, an electron gun generates electrons and accelerates them to energy in the range of 0.1 – 30 keV towards the sample. Through a series of focusing lenses, the electron beam interacts with the sample to a penetrating depth of approximately 1 µm. The incident electrons knock off some low-energy (<50 eV) electrons from the k-orbitals out of the the specimen atoms, known as secondary electrons, which are then detected to generate an image of the sample after scanning of an area.

Images were also generated in these studies by another type of imaging technique known as backscattered electrons microscopy. For this technique electrons are scattered at large angles (from 0º to 180º) when the impinging electrons interact with the positively charged nucleus on the sample. In the backscattering mode, the metal (silver nanoparticles) and the non-metal (polyimide) regions can be clearly distinguished by the brightness of the images, albeit at the expense of the image feature resolution. These results are presented and discussed together in Figure 6.14.

Three scanning electron microscopes were used in this thesis. An environmental scanning electron microscope (ESEM), XL30 LaB_6 ESEM, was used to examine the samples without any form of preparation of the samples. Since electron charges build up readily on the insulating polyimide samples, the ESEM works at low vacuum (typically 2 – 6 Torr) and utilizes a chamber gas (H_2O) to supress the charges. Field-emission electron microscopes were used to obtain higher resolution imaging of the nanoparticles. A field-emission cathode in the electron gun provides narrower probing beams, resulting in both improved spatial resolution and minimised sample charging and damage. A Leo 1530 VP field emission gun scanning electron microscope (FEGSEM) at Loughborough University, U.K., was used for the results presented in Chapter 6 and 7. A field emission scanning electron microscope (FESEM), Quanta 3D FEG, at Heriot-Watt University, U.K. was used for the results presented in Chapter 8.

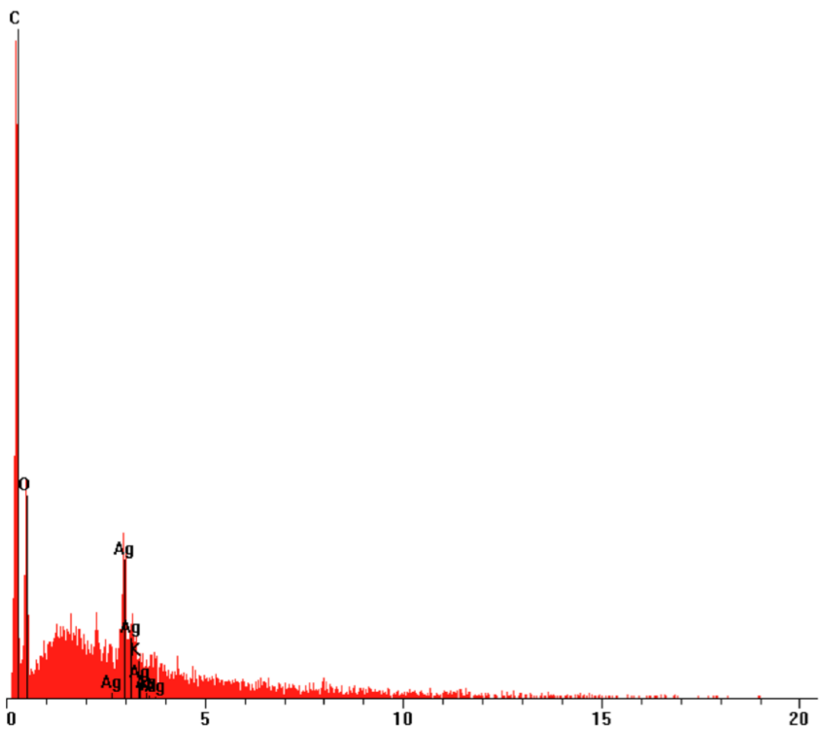

Figure 5.9: A typical EDX spectrum for a silver nanoparticles coated polyimide produced by the photoreduction methodologies under study.

Energy dispersive X-ray spectroscopy (EDX) identifies the elemental composition of materials imaged in a scanning electron microscope by the characteristic X-ray fluorescence generated from the atoms impinged by the incident electron beam. A typical measurement on the silver nanoparticles coated polyimide sample produced by the photoreduction methodologies under study in this thesis is shown in Figure 5.9.

An electron probe micro-analyser (EPMA) was used in the early stage of laser direct writing studies as discussed alongside Figure 6.10. It works on the same principle as EDX, with the additional capability of constructing a geometric map of the intensity count of the element (silver) being analysed.

5.3.2 Mechanical surface profiling

Atomic force microscope (AFM)

The AFM (Veeco – Model Explorer) as shown in Figure 5.10 is capable of producing nano-scale images of a surface profile by the deflection of the scanning tip. This deflection is registered on a photo-detector, as a change in the position of a laser beam projected onto the surface of the tip. The scanning was operated using a constant force and in contact mode. The control and data analysis software was Thermomicroscopes SPMLab V.5.01.

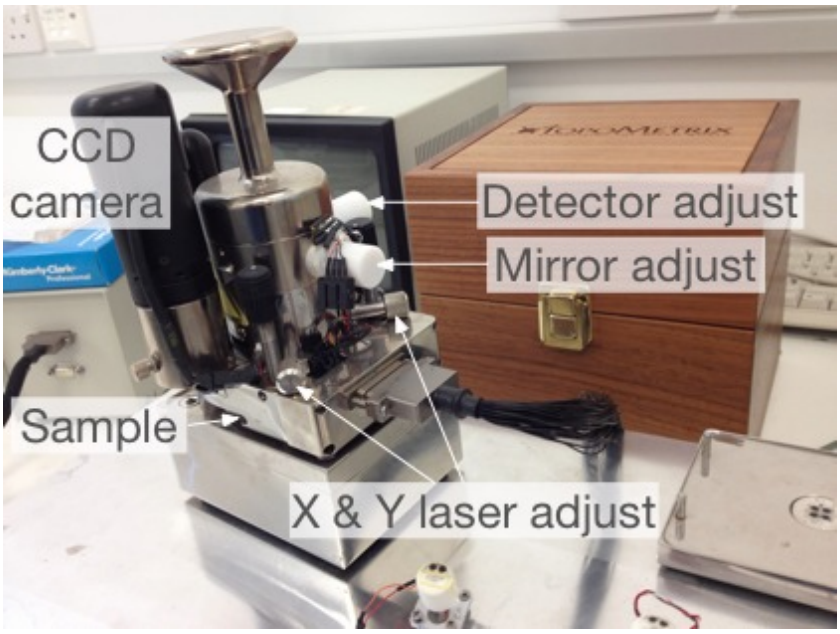

Figure 5.10: Atomic force microscope.

Dektak

The Dektak (Sloan, now Veeco) profilometer as shown in Fig. 5.11 was used for measuring step heights or trench depths on a surface. This is a surface contact measurement technique where a very low force stylus is dragged across a surface. The display range of the data is 200 Å to 65.5 μm with a vertical resolution of around 5 Å. The lateral resolution is limited by the tip shape.

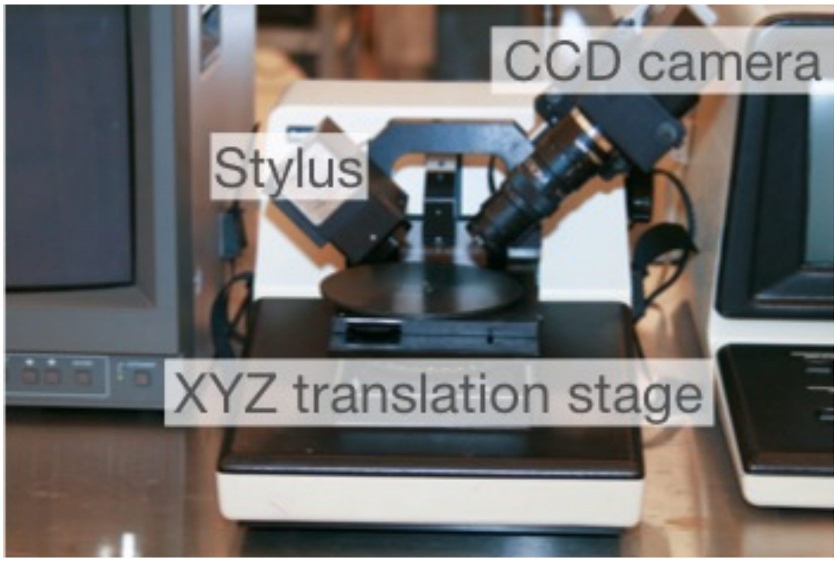

Figure 5.11: Dektak profilometer.

In summary, this Chapter aimed to present the optical exposure systems and characterisation techniques used in Chapters 6 to 8. Different exposure systems were necessary depending on the various types of electron donor coatings used.

Chapter 6

UV laser induced formation of silver nanoparticles

6.1 Introduction

This chapter first presents the initial experiments which demonstrated successful photoreduction of the doped silver ions catalysed by a water layer and a MPEG coating using a mercury arc lamp. In order to realise resist-less and maskless photolithography, laser experiments were then carried out systematically to investigate the formation process of silver nanoparticles using slow and fast scans and different laser power intensities. Continuous-wave (CW) lasers were employed to minimise the number of variables involved in the process characterisation. The use of pulsed lasers would involve too high a peak power which could cause undesirable substrate surface damage. A laser write speed in the range of tens of centimetre per second, preferably metres per second would also be required for a printable electronic manufacturing process to be practical and up-scaleable [144]. Therefore the experiments here investigated reactions in that region of scan speed using variable laser power. The spot sizes were fixed for each of the measurements using the laser systems described in Chapter 5.

6.2 Proof of concept using water and MPEG coatings by UV lamp exposure

In order to validate the photoreduction reaction in the proposed system, two initial experiments were carried out using a water coating and a MPEG coating using a mercury UV lamp. The water coating experiment proved that the concept of metal patterning without photoresist works only on the exposed regions as previously described by Akamatsu *et al* [53].

6.2.1 Water coating

The UV lamp described in Chapter 5.2.2 was set up with a photomask in the configuration shown in Figure 6.1. The power intensity of the UV light output from the collimating lens was measured to be 440 mW/cm^2, providing a circular spot size of about 1 cm in diameter. A fixed UV exposure time of 30 minutes was used providing an energy density of 792 J/cm^2. The water coating as the catalyst for the photoreduction was applied by first pipetting a few drops of DI water and then spreading by using two microscope coverslips of 0.8 mm thickness on two sides of the droplet as spacers and another coverslip covering the top of the droplet in between the two spacers. In the spectral range >350 nm, the transmission coefficient of the glass coverslips is over 90% as specified by the supplier Thermo Fisher. The effective energy density applied to the sample is therefore around 710 J/cm^2.

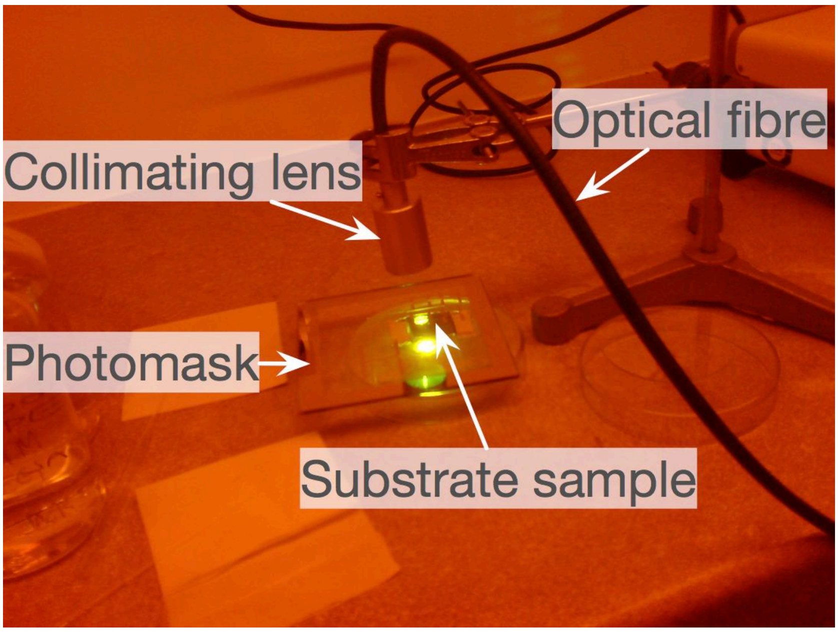

Figure 6.1: Initial photoreduction experiments setup using water coating.

Photoreduction of the doped silver ions assisted by the water coating was successful as shown in Figure 6.2. A silver layer with an area close to the light spot size was produced as shown in Figure 6.2(a). Using a photomask with a design line width of 125 µm, metallic patterns with line width close to that value were formed using water coating as shown in Figure 6.2(b) proving thereby that the concept of direct selective metalisation at the micro scale is possible without the use of photoresist materials. Although spacers were used in between the photomask and the substrate, the water layer thickness was still not controlled reliably. Gas bubbles were observed through the photomask during UV irradiation, indicating hydrogen evolution reaction at the silver nanoparticle surfaces [145]. The colour of the silver spots produced varied from each experiment, indicating that the silver nanoparticles formed were nucleated differently with different densities and sizes. This effect can be attributed to some uncontrollable factors such as movement of the water underneath the coverslip due to capillary force.

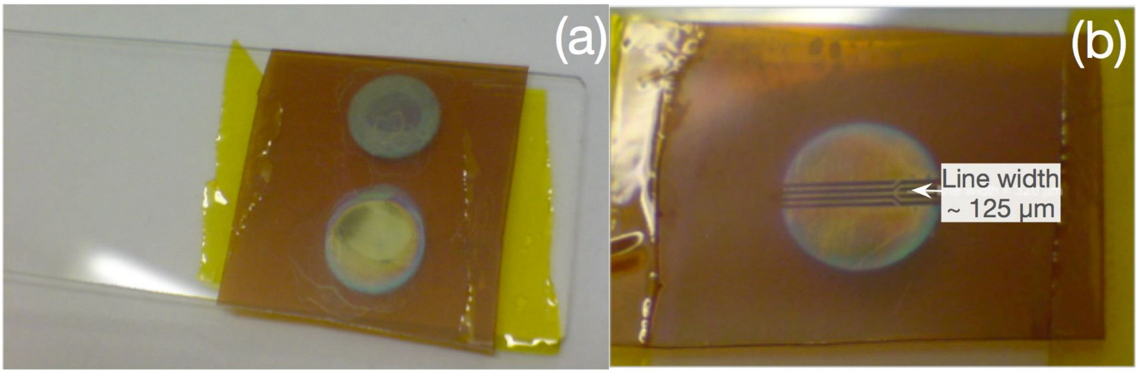

Without any water coating, no visible silver layer was produced.

Figure 6.2: Results of photoreduction experiments using water coating (a) without and (b) with a photomask.

6.2.2 MPEG coating

Instead of water, a large area coating of MPEG was applied by spin coating and patterned with a photomask in the mask aligner Tamarack system as described in Chapter 4.3.1. The power intensity was measured at about 48 mW/cm^2 and exposure times ranging between 30 minutes to over 4 hours were tested. At 30 minutes (86 J/cm^2), no pattern could be visibly observed. At 90 minutes (259 J/cm^2), orange patterns were seen in the exposed areas as shown in Figure 6.3(a) indicating formation of nanoparticle of a certain size. At 4 hours (691 J/cm^2), reflective purple or green tinted silver colour was displayed by the photoreduced silver particles as shown in Figure 6.3(b) which matches the appearance obtained with the water coating example. The colours on both of these samples shown were prior to re-imidization without any heat treatment applied. The effects of high UV dose and heat treatment are discussed together in Chapter 7 with high resolution imaging of the silver nanoparticles.

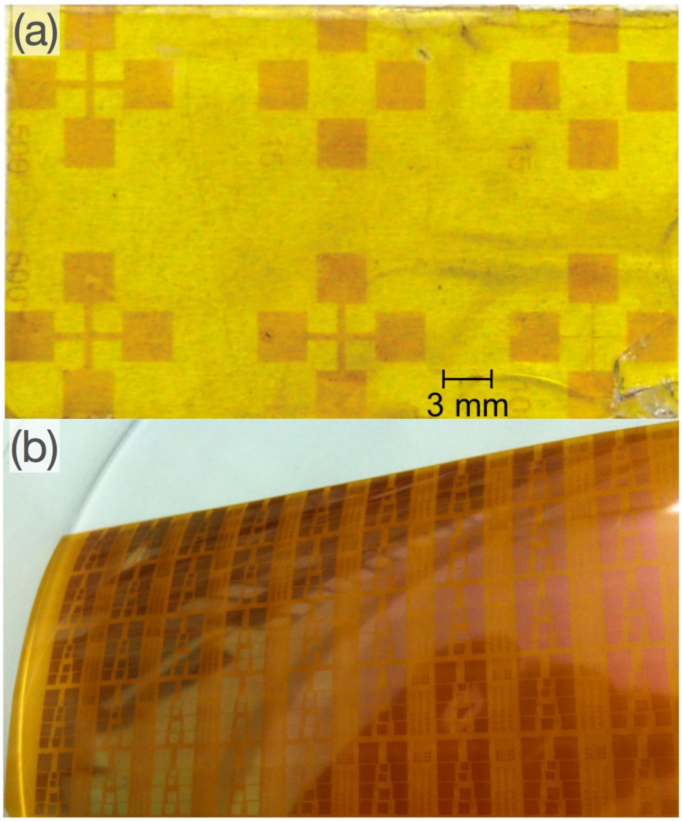

Figure 6.3: Optical micrographs of Ag patterns exposed by (a) 259 J/cm^2 and (b) 691 J/cm^2 UV energy dose.

6.3 UV laser scanning at low intensities

As no similar laser induced photoreduction systems could be found for process benchmarking, low laser intensities were first applied in order to gain insights into the formation process of silver nanoparticles using spot exposure and slow laser scan rates with an MPEG coating. The experiments in this section were carried out using a diode pumped 375 nm wavelength laser as described in Chapter 4.3.2. The maximum power measured after the focusing optics was 0.6 mW. The spot diameters used were roughly 35, 15 and 5 μm defined by the boundary of the circumference as observed by the CCD camera.

6.3.1 Stationary laser exposure

For a fixed exposure time of 60 seconds, a minimum of 0.3 mW was required to produce a pattern. The silver pattern generated was close to the 35 μm diameter of the laser spot as shown in Figure 6.4.

The variation of the laser beam intensity across its Gaussian beam profile can be witnessed by the red ring at the edge of the pattern indicating a change in the density of silver nanoparticles formed at the surface of the polyimide. Beyond the edge of the ring the intensity of the laser beam is not large enough to produce substantial silver particles. Doubling the laser power from 0.3 mW to 0.6 mW produced similar densities of silver particles as measured by EDX. It is noted that the electron beam in the SEM/EDX machine used a small spot size of 5.2 μm. Therefore as seen in the magnified image in the bottom of Figure 6.4, the non-uniform distribution of silver deposits is likely to give rise to variation in the measurement of silver content depending on the particular location of the electron beam on the pattern. Nevertheless the variations in the results obtained by the 0.3, 0.4 and 0.6 mW laser powers are not largely different, so increasing the laser power in this scale does not accelerate the photoreduction process.

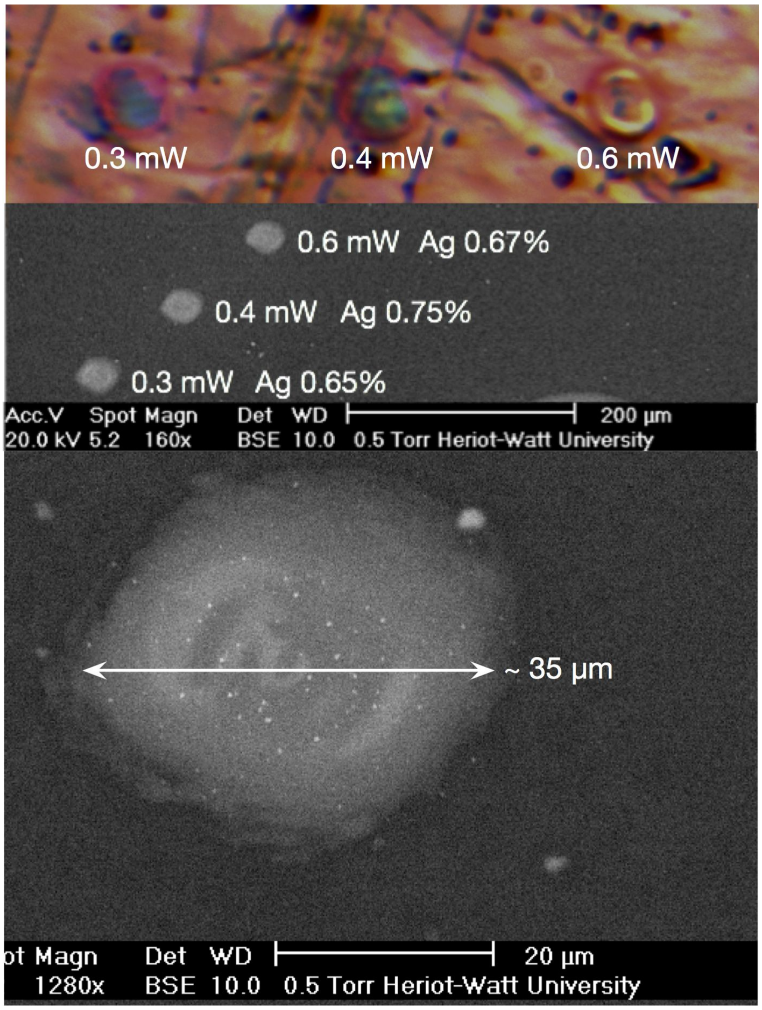

Figure 6.4: (Top) Optical micrograph of Ag patterns using attenuated laser powers and a constant exposure time of 60 seconds after rinsing in 1 wt% H_2SO_4 solution without any heat treatment; (middle) SEM micrographs of the same set of samples with relative Ag atomic % values as measured by EDX; (bottom) magnified image of the 0.6 mW exposed pattern.

Further measurements explained in the next Section demonstrate an increase of silver concentration with time for a given power intensity, confirming therefore that not all silver ions have been depleted in the ion-exchanged polyimide matrix. These two observations indicate therefore the photoreduction process may be diffusion limited, and that even with a surplus of light energy from the laser beam, the Ag^+ ions require a minimum amount of time to transport to the reaction sites. With a 60 seconds exposure time, all silver ions do not have sufficient time to reach the surface and therefore the densities of silver content in the laser exposed spots are barely altered by the increase of laser intensity.

The effect of exposure time for a constant laser power of 0.6 mW is shown in Figure 6.5. In that figure, the 2 seconds exposure spot is barely visible with a very faint blue/purple colour. Since the 2 and 4 seconds spots were too faint to produce sensical results, the relative concentration as a percentage of silver as measured by the EDX in the range of 7 seconds up to 10 minutes exposure spots. The Ag atomic percentage increases with exposure time. The Ag content for the 10 minutes exposure is nearly double that of the 5 minutes exposure as shown in Figure 6.5. However the increase in Ag content was slower between 1 minute and 5 minutes exposure. The unusual spike for the 30 seconds exposure spots is likely due to the large pin hole in the spots as can be seen from the optical microscope picture in Figure 6.5, therefore altering the volume of material being probed. No significant difference in the spot diameter between the 1 minute and the 10 minutes exposure was observed in the SEM image despite the spots appearing brighter with increasing exposure times as the Ag atomic percentage increases. This indicates that the photoreduction process is predominantly a photochemical process, as a thermal effect would have led to the spreading of the silver at such a prolonged exposure time. Below 1 minute exposure time, a decrease in spot diameter was observed, indicating that the energy in the outer region of the laser beam, i.e. beyond the shoulders of the Gaussian intensity profile, is insufficient for the photoreduction process.

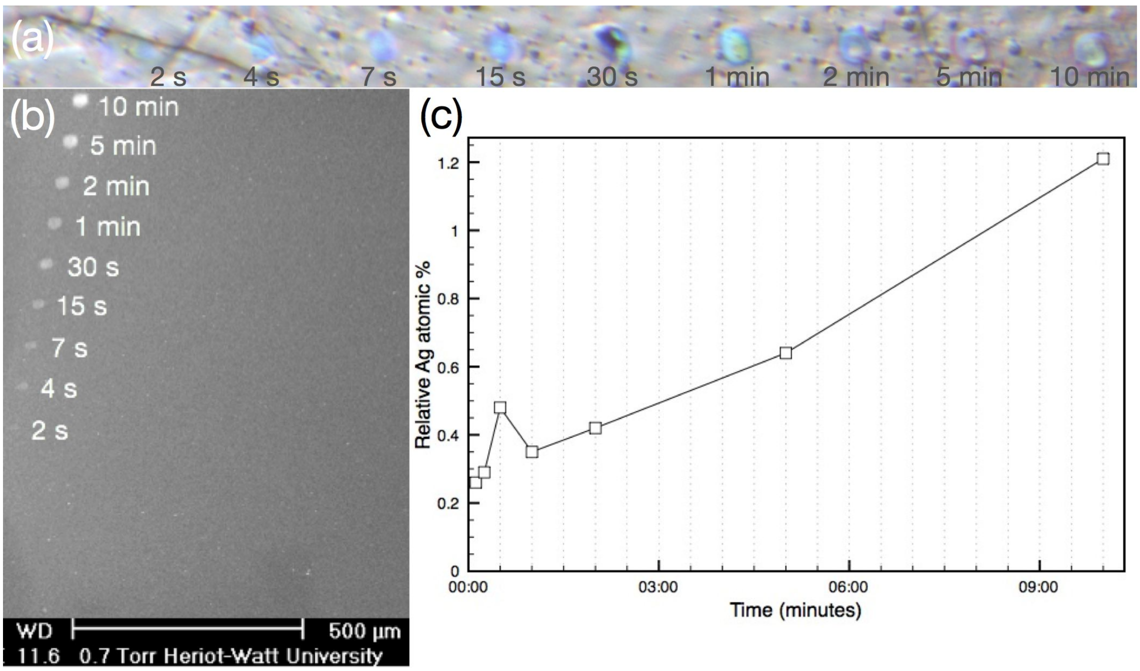

Figure 6.5: (a) Optical microscopy and (b) SEM images of spots produced by a stationary 0.6 mW laser with different exposure times; (c) the corresponding Ag atomic percentage concentration detected by EDX.

It is noted that the numerical values of the EDX Ag atomic % results contain a significant level of error due to noise generated from the volume of the material being probed. As can be seen in the cross section images (Figure 6.11 and 6.13) examined in the later section, the maximum depth of silver content within the substrate surface do not exceed 1 µm with laser scanning under higher intensities. The silver spots produced using the low laser intensities here certainly have much thinner depths. This means that the penetration depth of the X-ray probe, generally exceeding 1 µm and up to several microns depending on the accelerating voltage, contributed errors to the data points in Figure 6.5(c) resulting in the linear extrapolation of the plot not going through the origin. Nevertheless, it can be deduced qualitatively that exposure time seems to be the dominant factor here. In addition, as a thin absorbing film of silver nanoparticles with increasing thickness is being formed on the surface, the light energy getting transported is increasingly decaying over time.

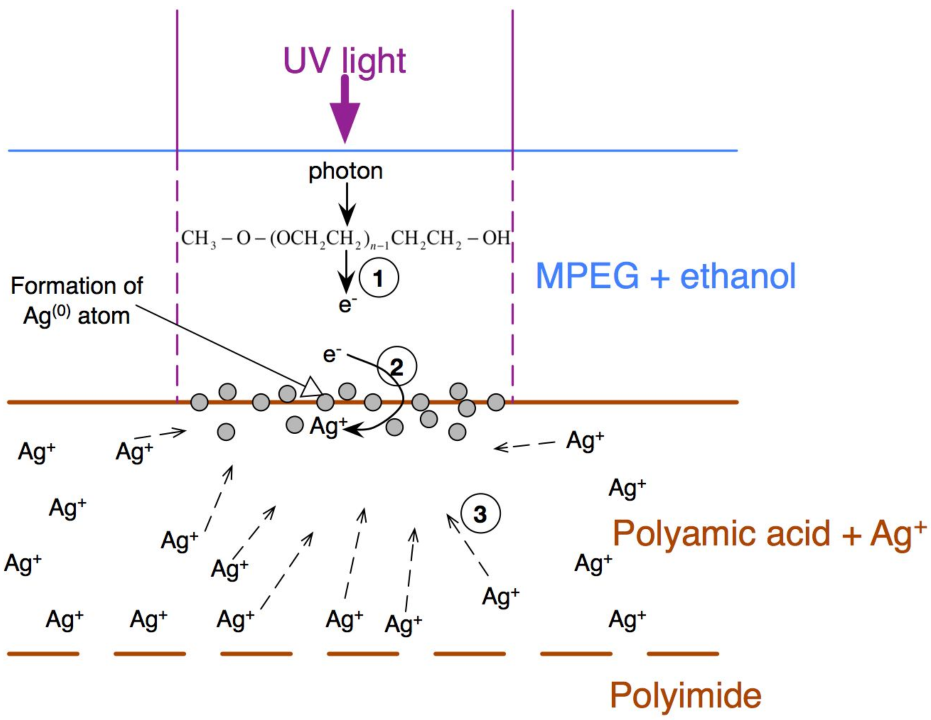

Figure 6.6: The mass transport limited mechanisms of the photoreduction system. (1) Electron release from the MPEG molecules; (2) Electron migration to the Ag^+ rich region, crossing the MPEG coating / substrate interface; (3) Diffusion of Ag^+ ions to the depleted region where some Ag^+ ions have been used for photoreduction.

The results in this section indicate that the time for photoreduction is a stronger influencing factor than the laser power or the energy dose. Another qualitative indication is that the 15 seconds exposure pattern with energy density of ~950 J/cm^2 does not show a prominent reflective silver colour, in comparison to the appearance of the patterns from the UV lamp exposure with a lower energy density of 691 J/cm^2

(4 hours exposure) as shown in Figure 6.3. Laser exposure time as long as 10 minutes still caused an increase in silver concentration. It can be deduced that the photoreduction in the current system is a mass transport diffusion limited process. Based on that process, there are two possible rate limiting mechanisms: (i) the electrons release and migration from the MPEG coating into the substrate, or/and (ii) the diffusion of Ag^+ ions within the substrate to the photoreduction reaction region. This is illustrated in the schematic diagram below shown in Figure 6.6.

6.3.2 Varying scan rates, multiple passes and small laser spot diameter

In order to determine the range of scan rates that allows the photoreduction process to occur, the scanning of a laser beam with a spot size of about 15 μm at a constant laser power intensity of 0.6 mW was carried out at speed ranging from 1 to 800 μm/s. AFM characterisation showed that the 1 and 5 μm/s scanned tracks were found to be composed of nanoparticles. The 10 μm/s scanned area was barely distinguishable and no nanoparticle morphology could be detected. The AFM micrograph for the 5 μm/s scanned track is shown in Figure 6.7. The biggest silver particle size is in the range of a few hundreds of nanometers. The sample was annealed at 250ºC for 30 minutes after laser scanning and dilute acid washing. The line width of the track was just under 17 μm which is close to the laser spot diameter, indicating again no signifiant photo-thermal effects as far as the formation of silver particles is concerned. Under the optical microscope, only the 1, 5 and 10 μm/s scanned tracks were visible with the 25 μm/s track faintly distinguishable as shown in Figure 6.8.

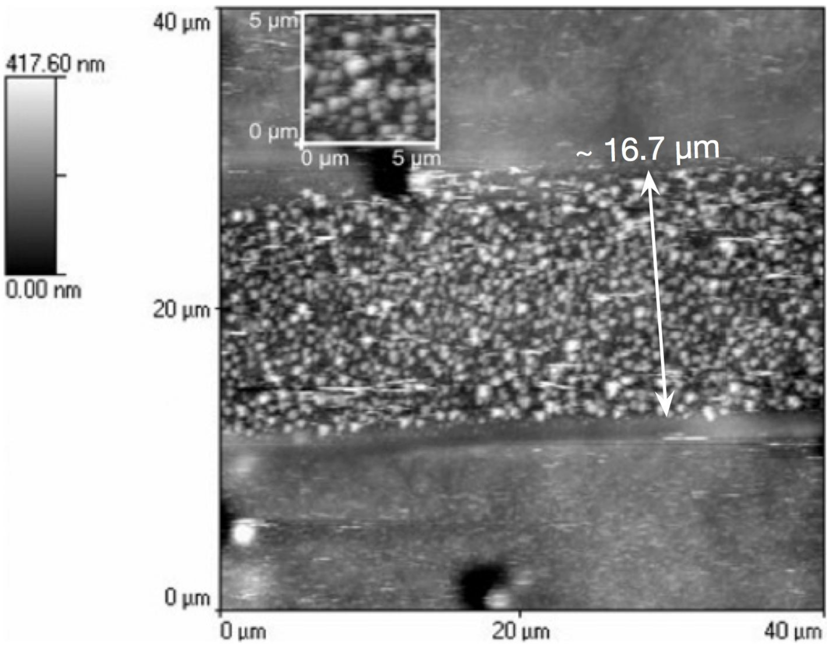

Figure 6.7: AFM measurement of a 0.6 mW laser scanned track at 5 µm/s.

The SEM image in Figure 6.8 reveals that some marking in the faster scanned tracks (> 50 µm/s) were detected, although very faintly. These silver particles were not observable by AFM or optical microscope, which means that the density of silver produced was low.

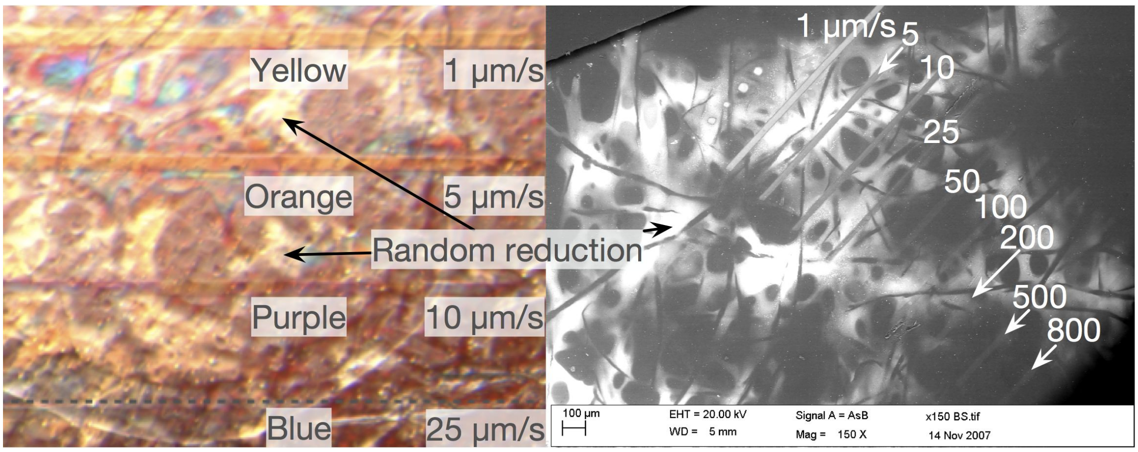

Figure 6.8: (Left) optical micrograph of Ag tracks by 1, 5, 10 and 25 µm/s laser scanning; (right) SEM micrograph of Ag tracks by laser scanning in the range of 1 to 800 µm/s.

Both the optical micrograph and the SEM micrograph images showed that some silver ions in the background of the substrate were randomly reduced. This was an example of the incomplete second ion-exchange using 1 wt% H_2SO_4 solution due to insufficient immersion time (less than 15 minutes). After this observation, all the samples in the rest of this thesis were immersed longer than 15 minutes and no such random reduction of silver ions occurred again.

Multiple passes of 10 μm/s laser scan show that the Ag content increases with increasing number of scans as evidenced in Figure 6.9. The Ag content as detected by EDX is however not directly proportional to the number of scans. For example, the 5 and 9 passes track does not contain 5 and 9 times the Ag content of the single pass track. This further confirms results explained in the previous section. The illuminated regions are depleted of Ag^+ ions and are being replenished by the diffusion of nearby Ag^+ ions between each pass of laser scanning. The silver particles formed by each pass of the laser scanning are however likely to scatter or reflect some of the incident light from the next pass preventing thereby further photoreduction of metal ions.

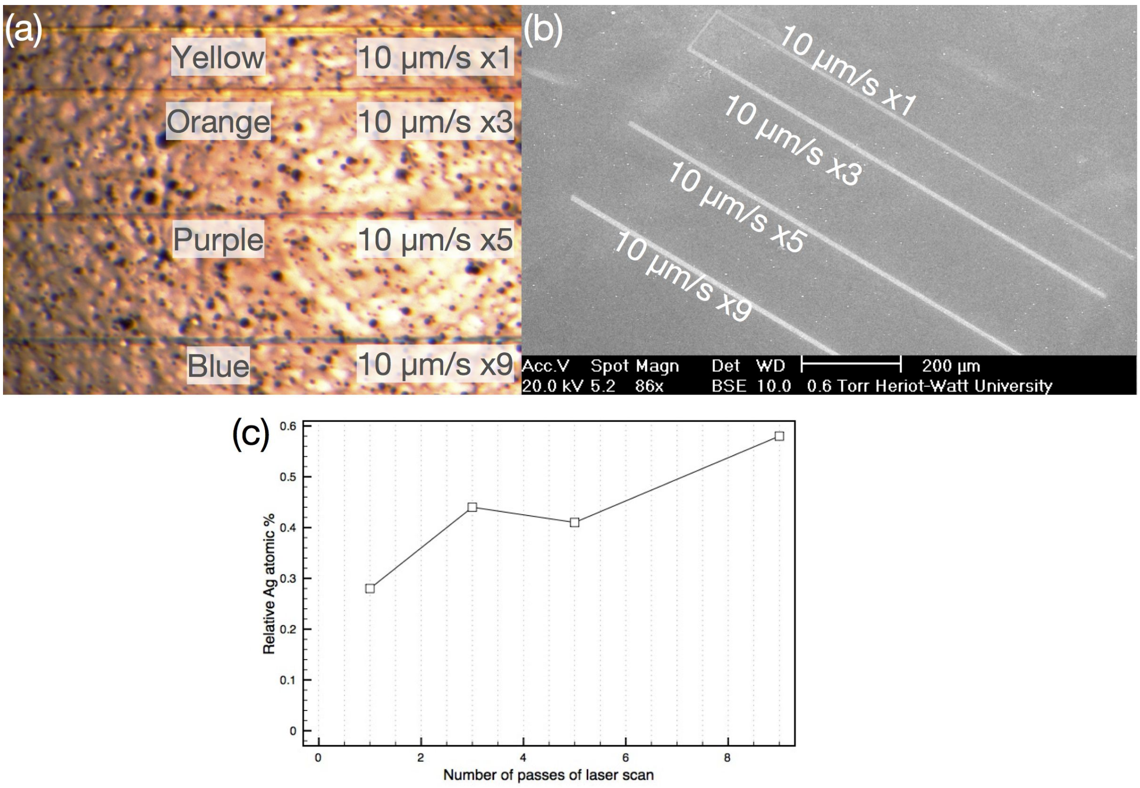

Figure 6.9: (a) Optical micrograph of Ag tracks written by increasing number of passes of laser scan at 10 μm/s at 600 μW after focus; (b) SEM micrographs of the same set of samples; (c) Graph of relative Ag atomic % as measured by EDX for each track.

The laser spot diameter was reduced to around 5 μm from around 15 μm using a different focusing lens in order to test the smallest line width achievable. Figure 6.10(a) shows that the line width of the 25 μm/s scanned tracks are also close to 5 μm, indicating that any spreading effects due to thermal conduction is minimal. Figure

6.10(b) shows the electron probe microanalysis (EPMA) that indicated the distribution of trace elements confirming the laser scanned tracks consist of silver. The bright white silver particles scattered across the substrate are ejected from the laser scanned tracks. This phenomenon is due to UV laser degradation of the polymer substrate and ejection of materials and is further discussed in detail in Section 6.4.3. The effect of the profile of the intensity of the Gaussian beam can be observed in Figure 6.10(c).

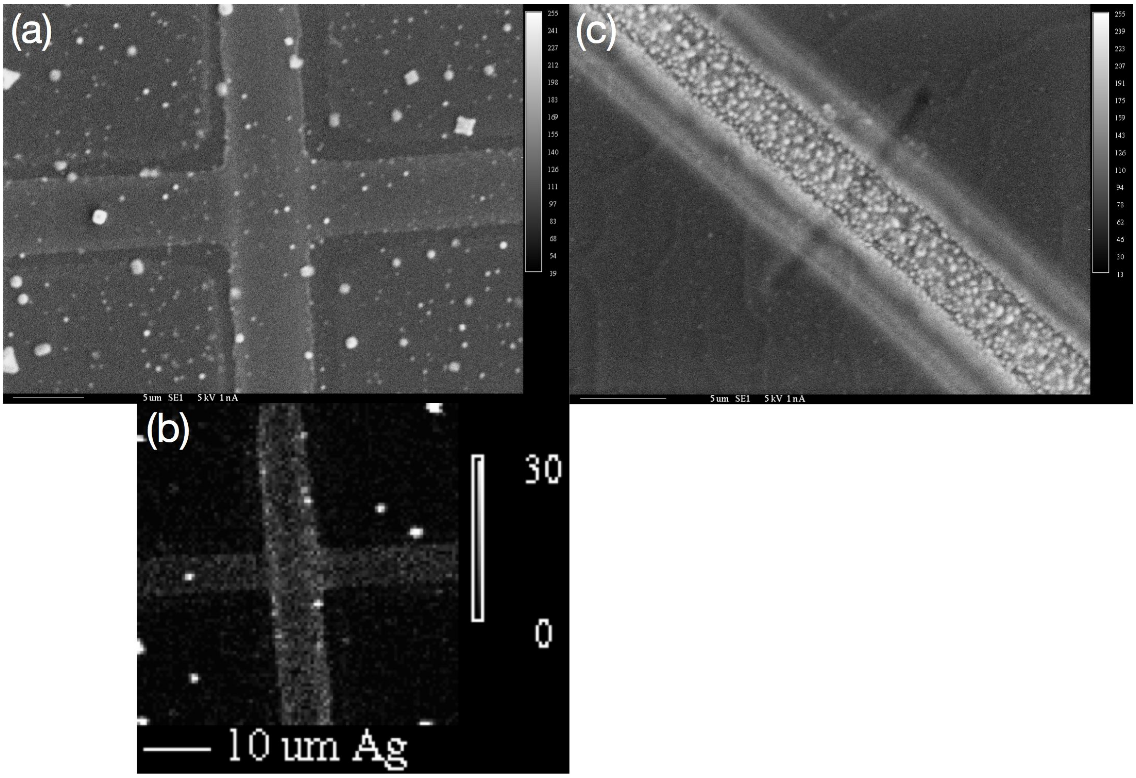

Figure 6.10: (a) SEM showing two laser scanned tracks crossing each other; (b) Electron probe micro analysis (EPMA) showing a map of the silver element; (c) Magnified SEM image revealing the morphology of the silver nanoparticles in the centre of the track.

6.4 UV laser scanning with high intensities

To investigate whether the silver seed layer formation could be achieved by using higher laser scan speed with higher laser intensities, the laser systems 2 and 3 as described in Chapter 4.3.2 were employed. Two types of reactions responsible for groove formation and swelling were found when laser power above 6 mW was used whilst the spot size and scan speeds were also varied. Section 6.4.1 describes the results obtained by laser system 2 with a power of 6 mW after focus. In Section 6.4.2 laser system 3 that was used provided a power between 6 and 12 mW after focus and the translation system was also capable of higher speeds. Consequently the results showed more distinguishable differences allowing separate regimes to be identified. Energy dose and the time available for the light-material interaction decrease with increasing laser scan speeds.

6.4.1 Laser power at 6 mW

The setup of laser system 2 produced a continuous-wave focused beam with a power of 6 mW and a spot diameter of 20 μm at 375 nm wavelength. Scan speeds ranging from 0.25 mm/s up to 80 mm/s were used. For the 0.25 - 1.5 mm/s scans, the height profile of the tracks obtained from the Zygo (Figure 6.11) shows that grooves are formed with a depth of up to 200 nm recessed into the substrate. At 1.5 mm/s, some residue deposit was found distributed along the groove formed by the laser scanning. At 2 mm/s, a deposit with a height of over 1.37 μm was measured by the Zygo at the centre of the track. Therefore at this point, the reactions responsible for the deposit behaviour prevail over the reactions for groove formation behaviour. Essentially, they are two types of competing reactions which involve polymer restructuring and movement of photoreduced silver particles. The deposit height versus laser scan rate plotted in Figure 6.12 shows that the deposit formation regime is distinguishable, starting at 3 mm/s where the deposit height is significantly higher than that at 2 mm/s. As the scan rate increases from 3 mm/s to 10 mm/s, the deposit height gradually decreases due to decreasing energy and reaction time available for the photoreduction of the silver ions and for the other reactions occurring in the polymer substrate contributing to polymer restructuring which is discussed along with Figure 6.13 later on. The line width plot in Figure 6.12 shows that there is a sharp decrease in line width with increasing laser scan rates. A possible explanation is that the energy dose provided by the laser beam is only large enough to drive the photoreduction reaction but not the polymer structuring.

An 80 mm/s laser scan was performed using the laser system 2 setup in order to test if any photoreduction would occur at all. The system was not calibrated for such a high speed movement which resulted in non-uniform motion. It was interesting to find that a raised track with a line width of about 3 μm was formed, although the line width was not uniform along the track due to the unoptimised motion of the robotic arms at this fast scan rate. However, this result encouraged experiments using the laser system setup 3 to allow for scan rates above 100 mm/s. These experiments are presented in the following Section.

A comparison between the optical microscopy images of the 3 and 10 mm/s scanned tracks in Figure 6.11 demonstrated also that a faster scan rate produced a more continuous track. The 3 mm/s scanned track indeed consists of large grains.

The cross section images of the silver tracks were prepared by first potting the polyimide specimen in an epoxy, followed by cross-sectioning using a focused ion beam (FIB) which was equipped in the FEGSEM at Loughborough University. This procedure allows cross-sectioning of soft materials which would otherwise be challenging to polish.

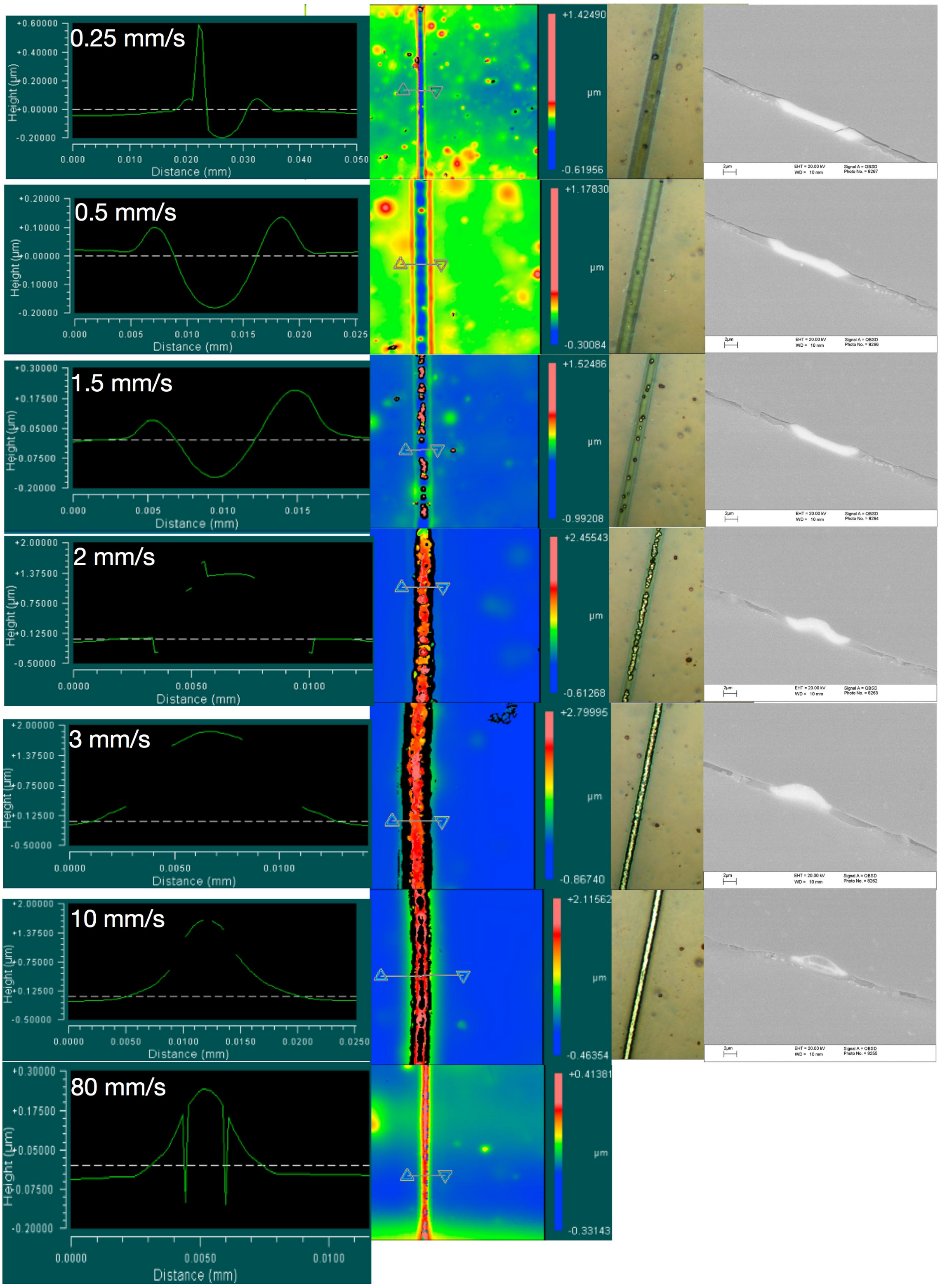

Figure 6.11: (Left to right) Zygo, optical micrograph, cross section by FEGSEM of the silver tracks obtained with increased scanning rates. The samples were washed in 1 wt% H_2SO_4 solution without no heat treatment / re-imidization.

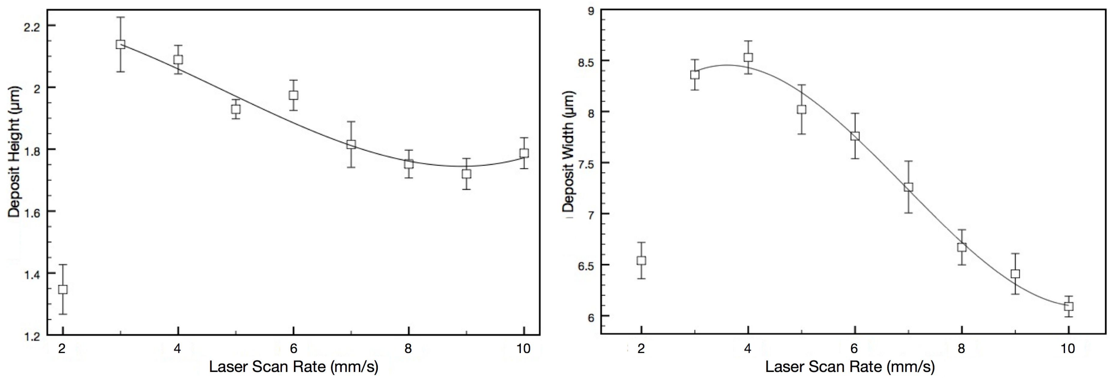

Figure 6.12: Graphs of deposit height and line width versus laser scan rate. 10 measurements were taken from the Zygo measurements from Figure 6.11 for each data point.

The cross-section images obtained from the FEGSEM shows the presence of a silver layer produced by the photoreduction for all laser scan rates as shown in Figure 6.11. These results include the 0.25 - 1.5 mm/s scanned tracks which are recessed slightly into the substrate. The bright white colour detected by the FEGSEM represents a high density of charges, i.e. the silver particles. The silver layer, composed of the photoreduced silver particles dispersed in a polymer phase, is about 1 μm deep from the surface of the substrate. This layer, in essence, the surface modified layer of the polyimide substrate, can be observed more clearly in Figure 6.13(a). The bottom edge of this bright white layer terminates uniformly within the substrate. This reflects the depth of the modification by KOH hydrolysis which was driven purely by diffusion.

The cross sectional FEGSEM images prompt for an explanation on how a "hill shape" deposit of over 2 μm high such as that observed for the 3 mm/s track in Figure 6.11 was produced. Firstly, there should not be enough supply of silver ions within the 1 μm thickness of the surface modified layer to build up such a large amount of silver particle deposit. Any diffusion of the Ag^+ ions in the regions not illuminated by light into the photoreduction region would take place at both sides of the track, as illustrated by the schematic diagram in Figure 6.13. The centre region of the track is likely to be depleted of Ag^+ ions. This will more likely create a "valley shape" silver layer rather than a "hill shape". Secondly, it is reasonable to conclude that the Ag^+ ions within the polymer matrix have been photoreduced, resulting in a segment of the surface modified layer containing silver *in* the substrate as shown in Figure 6.13(a). However it is rather peculiar that a large "hill shape" volume such as the example of a 50 mm/s scanned track shown in Figure 6.13(b) was created on *top* of the substrate, whilst the supply of

Ag^+ ions came from within the substrate. It appeared as though some material had been pushed upwards from the substrate.

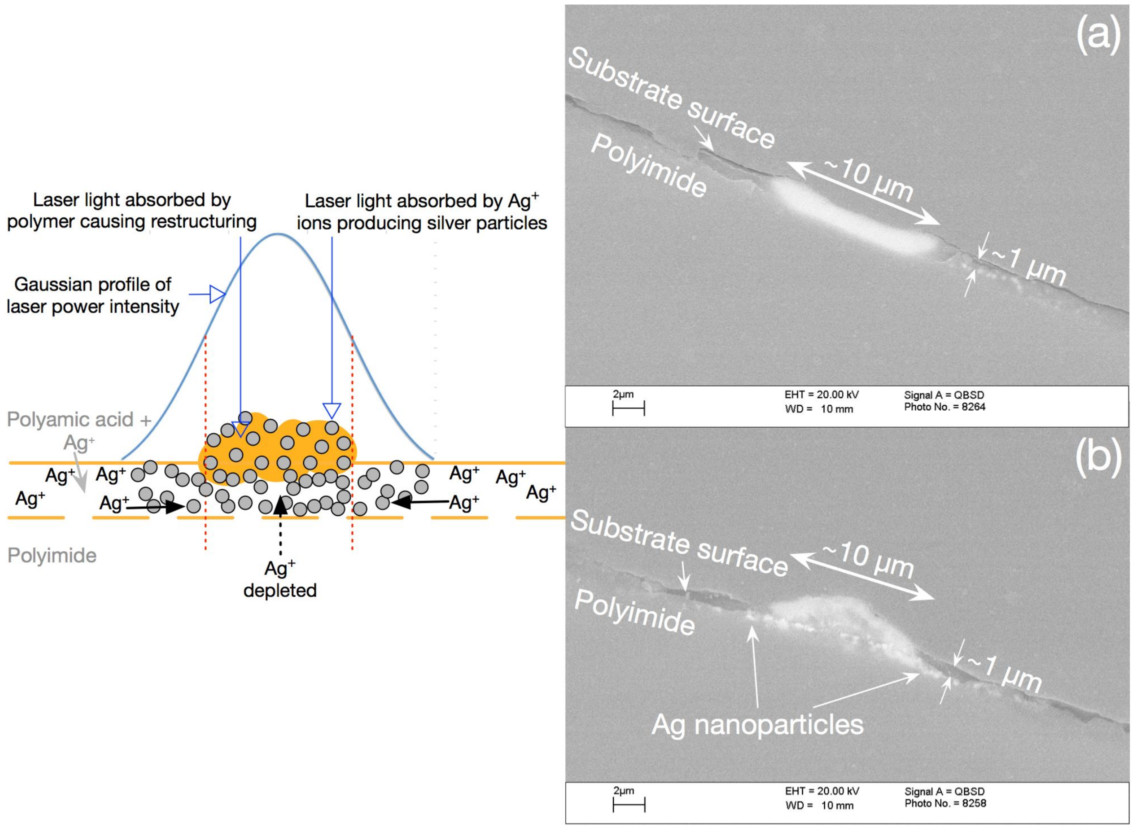

Figure 6.13: (Left) Schematic diagram of the proposed mechanisms responsible for the height observed for some of the laser scanned tracks; (right) cross sectional FEGSEM images of (a) a 1.5 mm/s scanned track, and (b) a 50 mm/s scanned track.

The incident laser light not only reacted with the Ag^+ ions, but also the polymer in the substrate. The "hill shape" structure of the laser scanned track is in fact the direct response of the polymer to the Gaussian intensity profile of the laser beam as illustrated in Figure 6.13. Polymer swelling occurred above a certain level of power intensity, at the centre of the beam. The swollen polymer and the silver particles produced by laser irradiation concomitantly formed a silver-polymer nanocomposite. This observation is further supported by the results in the following Section.

6.4.2 Laser power from 6 to 12 mW

The setup of laser system 3 provided a continuous-wave focused beam with a power range from 6 to 12 mW and a spot diameter of 15 μm at 325 nm wavelength. Scan rates in the range of 0.25 mm/s up to 500 mm/s were used. Using electron backscattering, the silver regions can be clearly seen on both sides of the laser scanned tracks as shown in Figure 6.14. EDX also confirmed the presence of silver on the bright white regions and also in the grey region at the centre of the 500 mm/s scanned track. A width of just over 6 µm between the outer edges of the silver regions was formed at 50 mm/s scan rate. With ten times faster scan rate at 500 mm/s, this width is reduced to just over 4 µm. The Zygo images show that the centre of the 50 - 250 mm/s laser scanned tracks are raised (in red) above the substrate, resembling the "hill shape" cross section result shown in Figure 6.13(b). Fine details could not be obtained for these images due to the limitations of the ESEM used for the electron backscattering imaging. Using the high resolution FEGSEM, the 12 mW, 50 mm/s scanned track (the first track in Figure 6.14) was imaged at a 45 degree tilt as shown in Figure 6.15. The polymer swelling and degradation can be clearly observed at the centre of the track. The magnified image shows some remaining silver nanoparticles along the edge of the track.

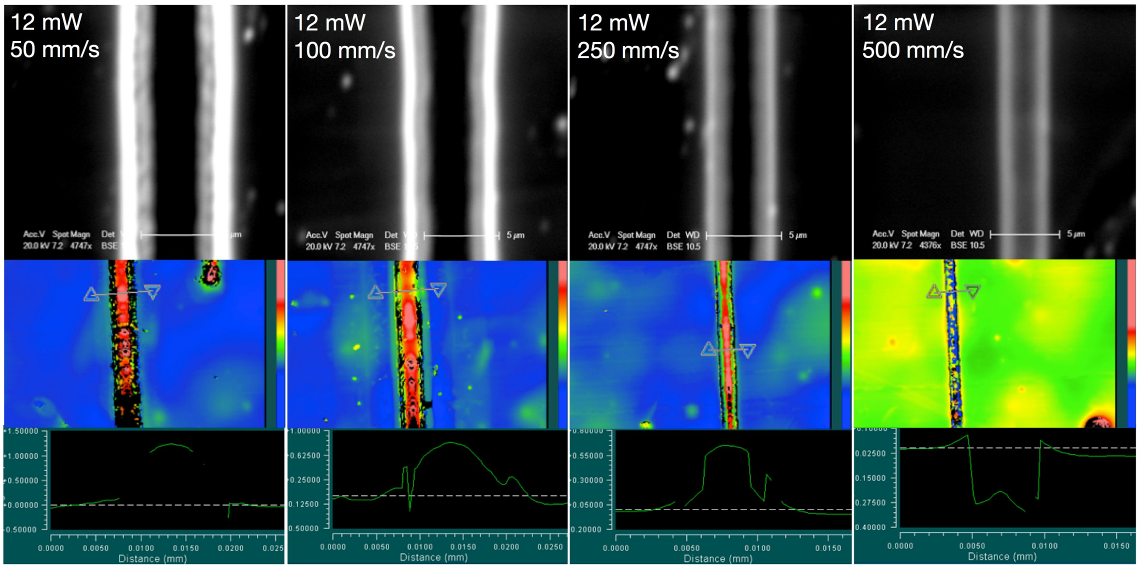

Figure 6.14: (Top) Electron backscattering images; (Bottom) Zygo pictures (top view and interpreted cross-section).

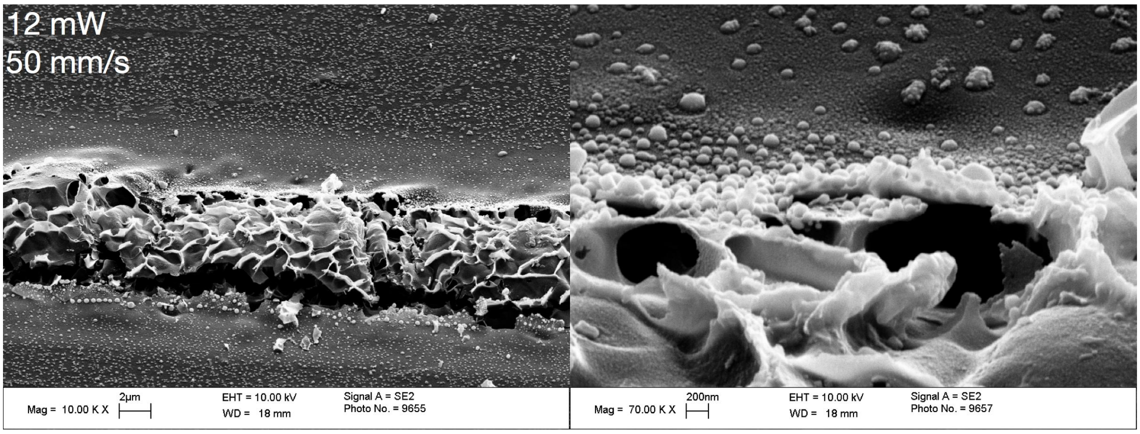

Figure 6.15: FEGSEM with a 45 degree tilt showing polymer swelling and silver nanoparticles along the edge of the 12 mW, 50 mm/s scanned track.

Following the above observations, the parameter space of power between 6 to 12 mW and scan rates between 0.25 to 50 mm/s was investigated systematically. Three main behaviours were identified and highlighted in yellow, orange and green in Table 6.1. The yellow coded pictures showed spectacular explosion of the polymer with silver particles scattered all over the nearby areas as a result. The orange coded pictures show the interplay between the two competing reactions: polymer restructuring occurs at the centre of the track, and the two silver ridges along both sides of the track indicate no polymer restructuring while the laser light induced photoreduction of the silver ions takes place. The green coded pictures show polymer swelling and the pictures with no colour codes are intervening regions between these three main behaviours.

Table 6.1: Laser scanning using different power and equivalent energy densities. The scan speed decreased correspondingly from 12 mW to 6 mW to achieve the constant energy densities in each column.

	1202 J/cm^2	616 J/cm^2	120 J/cm^2	12 J/cm^2
12 mW	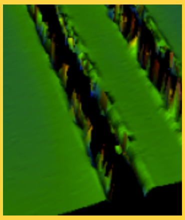 0.5 mm/s	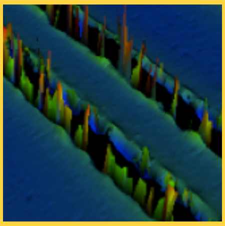 1 mm/s	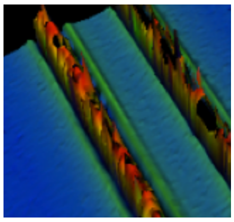 5 mm/s	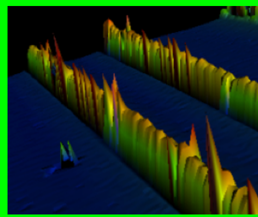 50 mm/s
11.5 mW	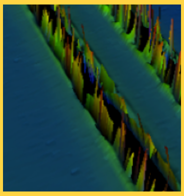	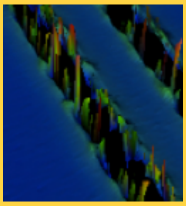	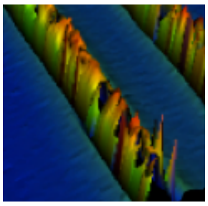	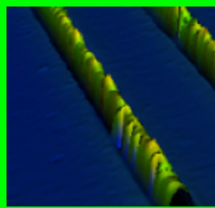
11 mW	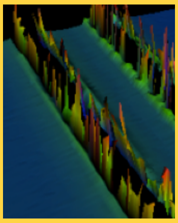	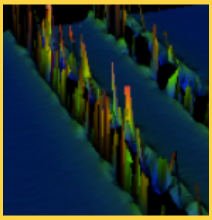	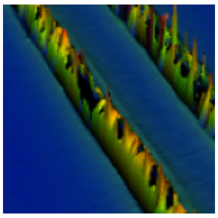	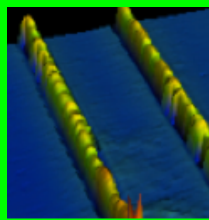
10.5 mW	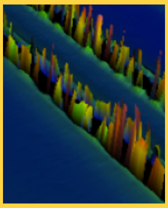	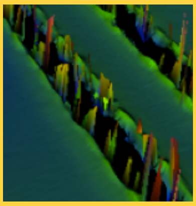	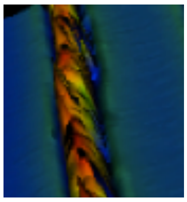	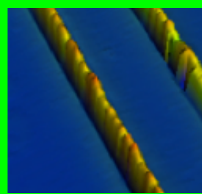
10 mW	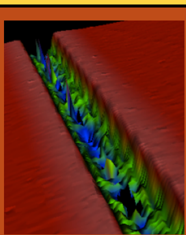	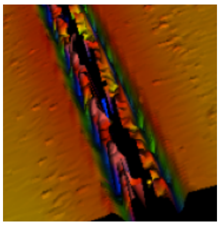	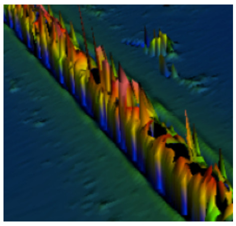	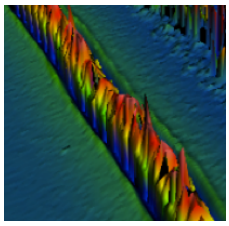
8 mW	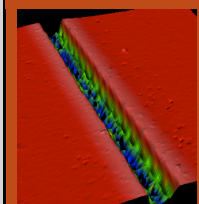	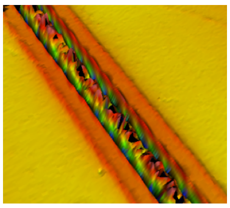	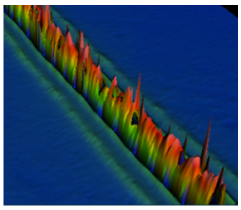	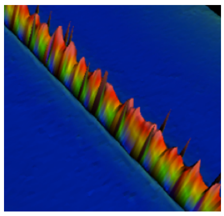
6 mW	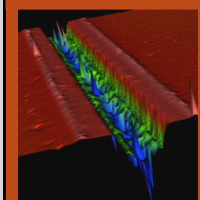 0.25 mm/s	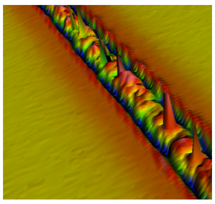 0.5 mm/s	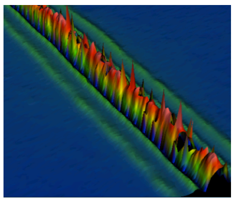 2.5 mm/s	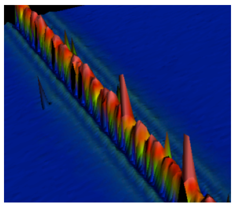 25 mm/s

6.4.3 Tuning the laser writing parameters

From Table 6.1, samples were selected for FEGSEM imaging. Figure 6.16 shows that, starting at the maximum power available, 12 mW, at relatively slow scan speed of 4 mm/s (near to the yellow region where spectacular ejection of materials akin to an explosion was identified), severe polymer damage can be clearly seen where the laser scanned area displayed a honeycomb like structure. Increasing the laser scan rate by 25 times, therefore reducing the energy dose, at 100 mm/s (faster speed beyond the green region), the laser scanned polymer exhibited a leaf like appearance which would likely be swollen similar to those samples observed by the Zygo in the green region in Table 6.1. Also a lot of silver residues were found on both sides of the scanned track. These silver particles look as if they were once formed on the laser scanned areas and were expelled away from the track. Increasing the laser scan rate by another 2.5 times at 250 mm/s, the silver nanoparticles grown on the surface of the laser scanned polymer were clearly seen. The presence of two large silver clusters there indicate fast particle aggregation that took place during the laser induced photoreduction. Formation of silver atoms, immediate coalescence of nanoparticles, and subsequent aggregation of clusters occurred within the short duration of time the laser light spent on the substrate. Some holes were seen on the laser scanned area and the surface looks as if it is close to a threshold of being completely peeled away like the 100 mm/s and the 4 mm/s scanned tracks. With the translation stages used for the experiments, it was difficult to increase the scan rate further. Therefore the laser power was reduced to decrease the energy dose in an attempt to minimise the polymer damage by the laser energy. As shown in Figure 6.17, the tracks either exploded, degraded, or there was just not enough energy or reaction time to form a track such as the 6 mW, 4 mm/s scanned track.

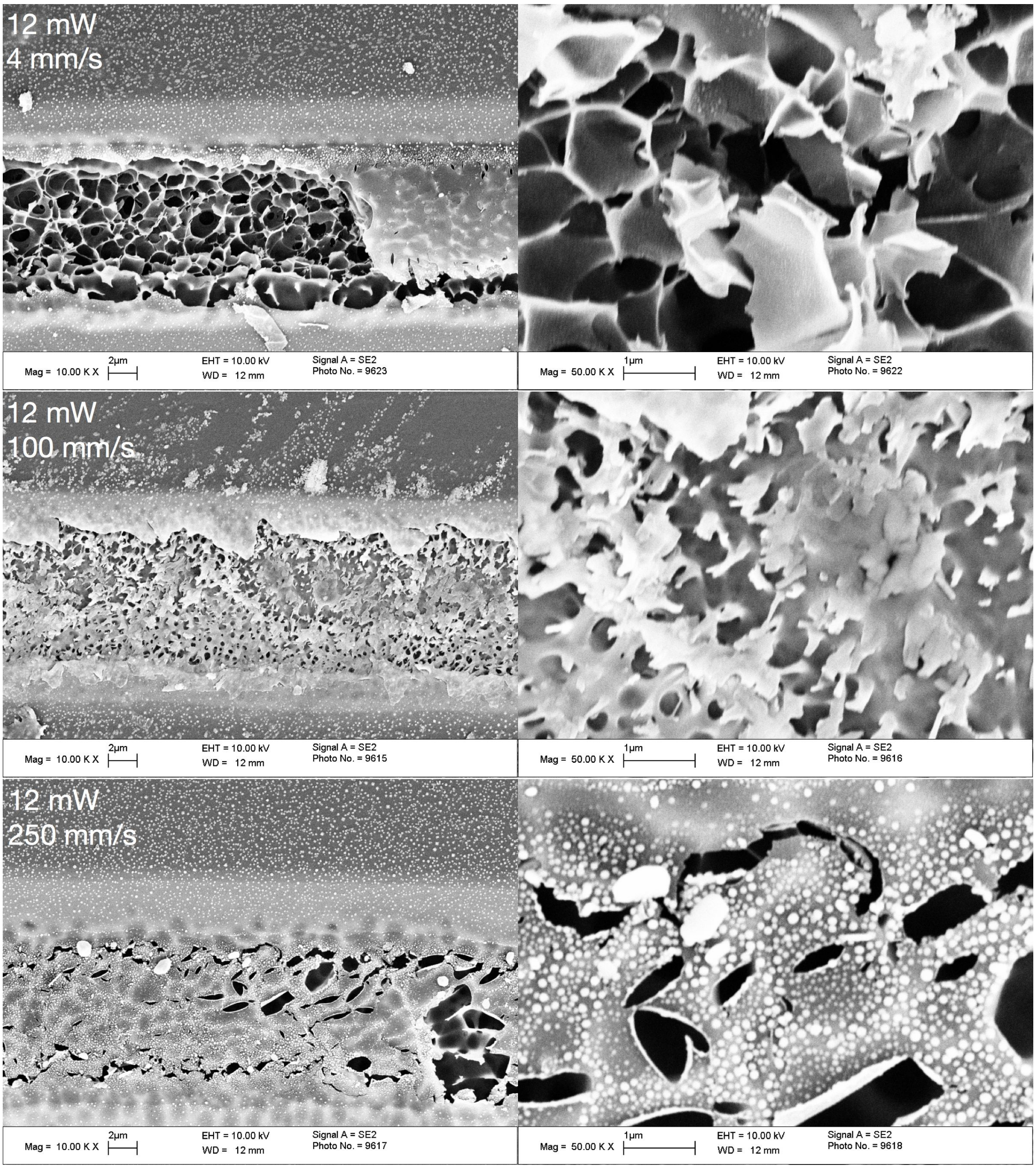

Figure 6.16: FEGSEM images of samples written at 12 mW laser power with high scan rates up to 250 mm/s showing polymer degradation on the substrate.

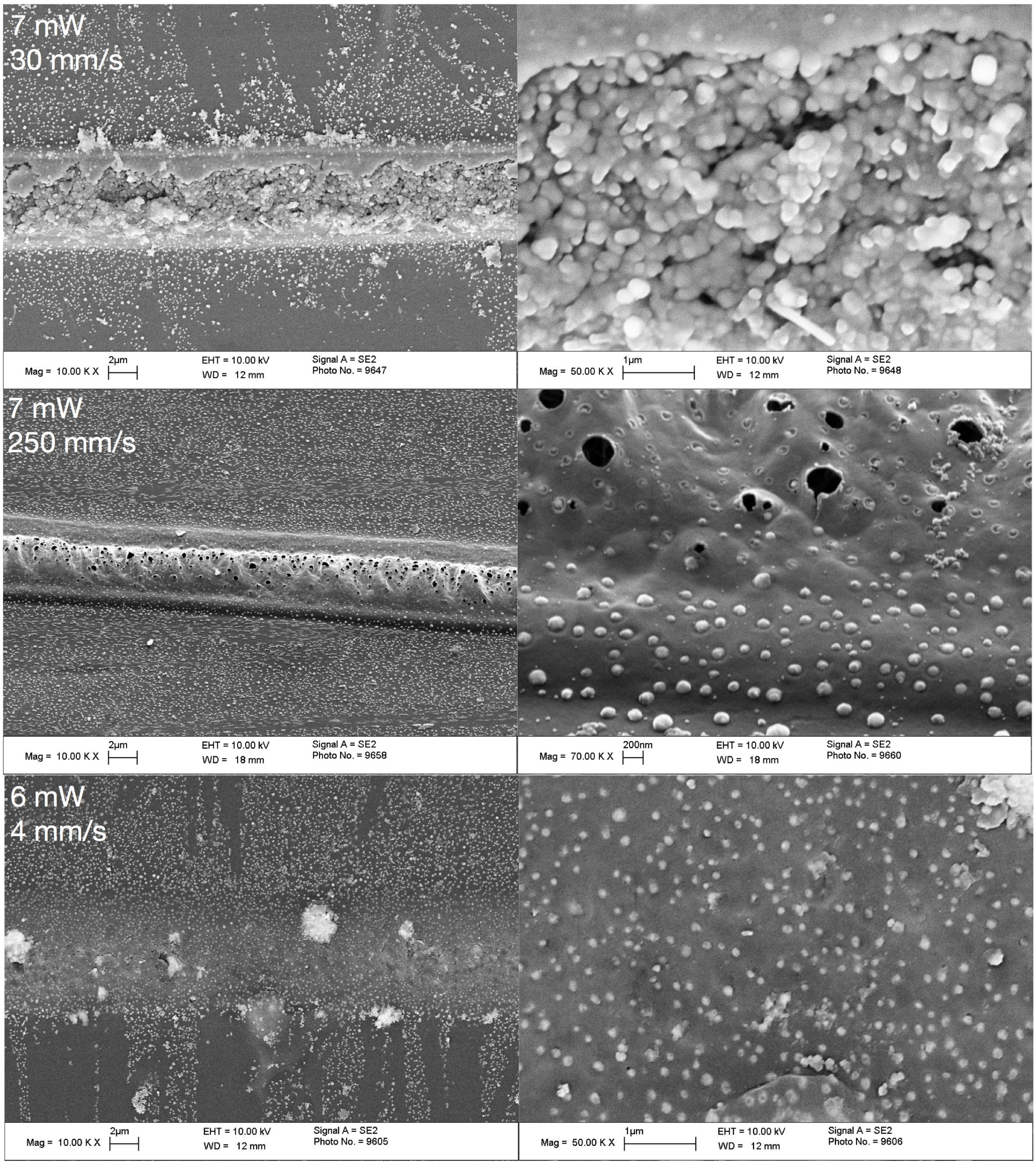

Figure 6.17: FEGSEM images of samples written at reduced laser power at 6 and 7 mW with scan rates between 4 - 250 mm/s.

Quite a different observation to the 12 mW samples was found on the 7 mW power, 30 mm/s scanned track (top figure in Figure 6.17) where densely packed silver nanoparticles and aggregated clusters are found within the laser scanned track. However, it is evident that the laser energy still caused the explosion of materials. Reducing the energy dose by increasing the scan rate to 250 mm/s, the swollen polymer surface can be seen without being completely ruptured like the previous cases. The small circular holes on the surface appeared as if they had been punctured by materials from within the substrate. The silver nanoparticles distributed on the surface are sparse, which is a stark contrast compared to the 30 mm/s scanned track when the energy dose was more than 8 times higher. Reducing the energy dose further by using 6 mW power and 4 mm/s scan rate, the polymer substrate was less swollen and no holes were seen on the laser scanned surface. Again only sparse distribution of silver nanoparticles was produced at this energy dose.

In summary, the 7 mW power and 30 mm/s scanned track produced high density silver nanoparticles in the laser scanned area although undesirable ejection of materials still occurred. By adjusting the power and the scan rate for higher or lower energy dose, either severe polymer damage and ejection of materials was induced or only sparse distribution of particles were produced on the substrate surface due to insufficient photon dosage. The groove or marking produced did not grow significantly beyond the laser spot diameter, so the main reactions for the above observations are not attributed to thermal effect. Photolytic dissociation of molecules could be caused by photon energy in the UV wavelength. Clearly, further understanding of the physical and chemical mechanisms that took place is still required. However it was decided at this stage of the investigation to proceed further to the next processing steps in the process flow (Figure 3.1) in order to gain some understanding of the relationships between electroless plating and the UV exposed surface containing the silver seed particles. Electroless plating was tested on some laser scanned tracks and also the patterns formed by UV-photomask exposure, which are described in Chapter 7.

6.5 3-dimensional laser writing

The methodology pursued in this thesis principally enables the patterning and metalisation not only on planar surfaces but also 3-dimensional surfaces owing to the convenience of not requiring any photoresist coating. In addition, the patterning process by photoreduction can take place in air without requiring any inert gas or pressurised environment, making manoeuvre of the contour surfaces for the light exposure more convenient. To demonstrate this novel concept, the MPEG coating was first drop-coated and dried onto a cylindrical silver ion-doped polyimide substrate prepared by taping a thin polyimide sheet onto the surface of a glass pipette which has a diameter of 6 mm. The ion-exchange was performed by dipping the polyimide tubes into the KOH solution and then the $AgNO_3$ solution using the standard parameters. After that, the cylindrical sample was placed in the laser writing set up as illustrated in Figure 6.18 using the laser system 2 with a spot size of 15 µm and a power of 6 mW after focus. The sample was rotated at a speed of 9 rpm (equating to approximately 31.4 mm/minute across the surface) and translation speed of 3.6 mm/minute, allowing writing along the whole longitudinal length of the tube of 25 mm.

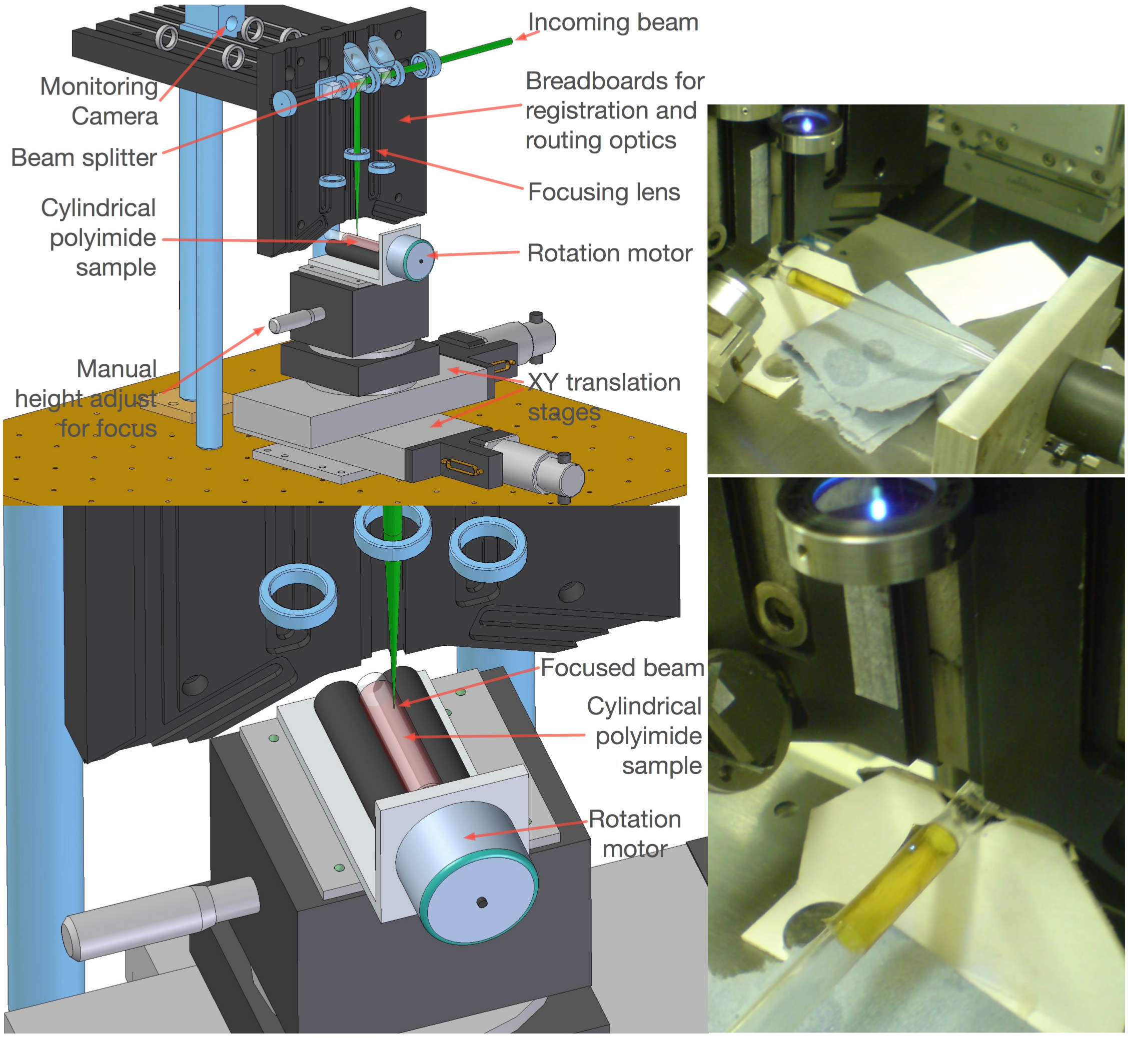

Figure 6.18: Schematic diagram and photographs of the 3-dimensional laser writing on a cylindrical polyimide tube.

Figure 6.19 shows photographs and SEM images of the laser written silver and electroless gold plated helixes on the cylindrical polyimide surface. Silver nanoparticles were formed on the contour surface directly. The resultant line width of both the silver track and the electroless gold plated track are both close to the laser spot size. The results demonstrate the possibility for a 3-dimensional manufacturing process by utilising the combination of a dry catalyst coating and isotropic electroless plating on a contour surface. However, it was not possible to measure the conductivity of the track due to discontinuity at various locations of the helix track. This breakage was likely due to dust in the non-cleanroom environment and the polymer damage by the laser energy as described above.

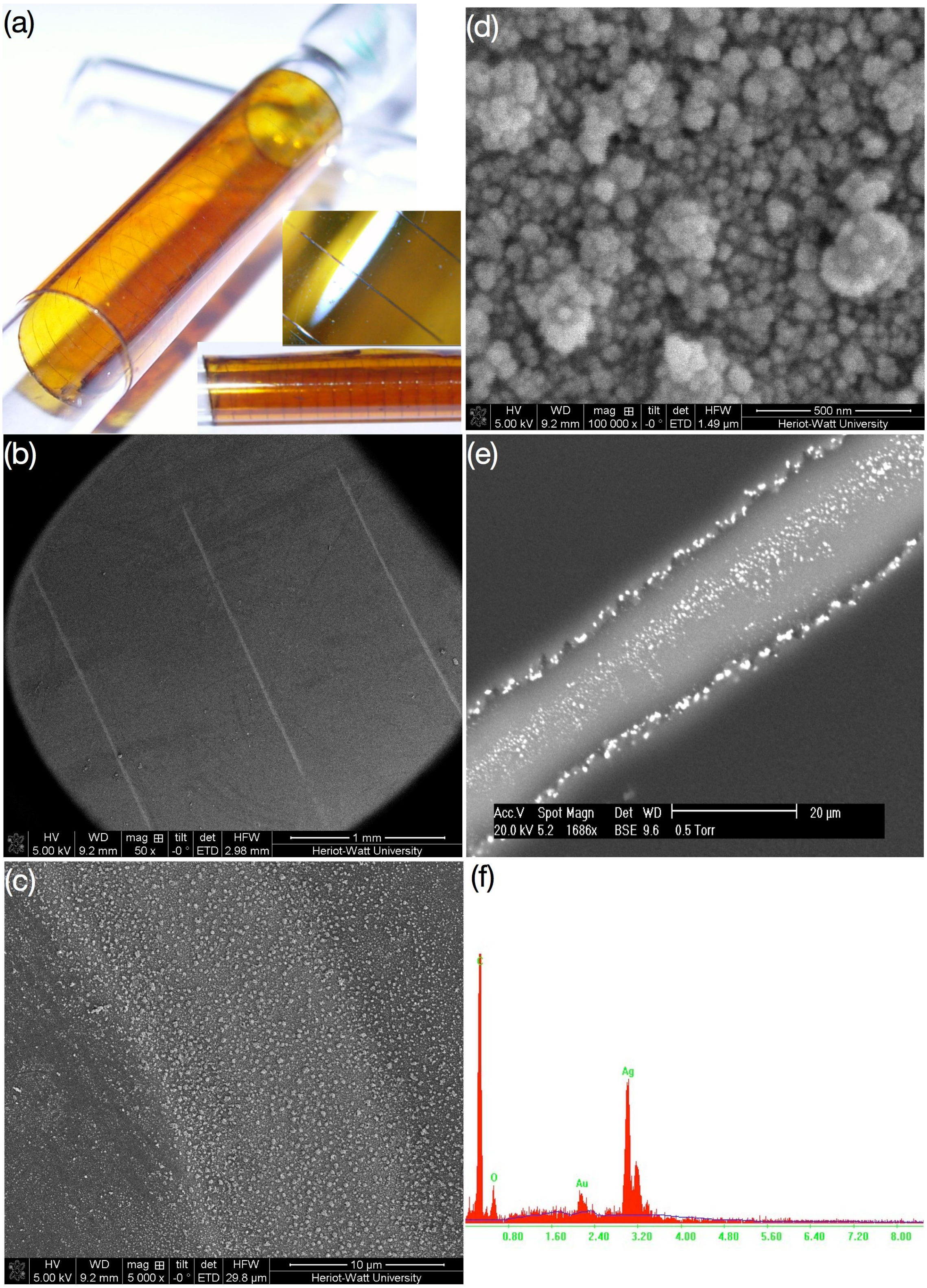

Figure 6.19: 3-dimensional laser writing (a) photographs of the polyimide tube with a helical silver track; (b) & (c) FEGSEM images of the contour surface on which the silver track was produced by laser direct writing, washed in 1 wt% H_2SO_4 solution, without heat treatment; (d) magnified image showing the morphology of the silver nanoparticles after heat treatment at 250ºC for 30 minutes; (e) part of the helical track plated with electroless gold; (f) EDX elemental analysis indicating a thin layer of gold plated on top of the silver seed layer.

6.6 Conclusion

This chapter has examined the use of the UV laser and MPEG coating system in lieu of the UV lamp and water coating system as reported by Akamatsu *et al* on the silver ion-exchanged polyimide substrates [53]. The two factors most likely to affect the yield and quality of the silver particles produced by photoreduction namely: laser power intensity and scan rate, were studied. At a low power of 0.6 mW and small spot diameter from 15 µm down to 5 µm, very slow scan rates much less than 100 µm/s and as slow as 5 µm/s were used, by which, tracks containing silver nanoparticle were produced without much observable material ejection. Since the results here indicated that the photoreduction process in the current system is a diffusion limited process, such slow scan rates would also allow ample diffusion time for the Ag^+ ions to transport into the depleted reaction sites. However this range of laser scan rates is not practical for large scale manufacturing.

Increasing the laser power allows for much faster laser scan rates to produce visible silver nanoparticle tracks. In the 6 - 12 mW laser power regime with a spot diameter of 20 µm, laser scanned results from 0.25 - 500 mm/s scan rates were examined. Despite the interferometry and cross-sectioned FEGSEM results first appearing to indicate that a hill-shaped deposit composed of silver was formed in the laser scanned volume for 6 mW power and up to 10 mm/s scan rate, the peculiarly large height "deposit" in the scale of well over 1 µm was later concluded to be in fact a volume of swollen polymer containing scattered silver nanoparticles. The top view high resolution FEGSEM imaging later showed that 7 mW power and 30 mm/s scan rate showed dense silver nanoparticles and aggregates within the laser scanned track whilst energy dose above or below this level either induced severe damage to the polymer substrate and ejection of material or did not provide sufficient energy to induce photoreduction for a high density of silver particles.

Ultimately, the polymer substrate was inherently subjected to damage by the high energy photons of the laser at 375 nm wavelength. Photothermal damage is regarded as not significant since no heat conduction was evident on the substrate in the range of the laser powers, spot sizes and scan rates used in these studies. On the other hand, dissociation or alteration of chemical bonds in the molecular structure is possible by photon energy in the UV wavelength. The results in Chapter 7 will further prove that to be the case through the use of a UV lamp thereby decreasing the number of causative factors such as the laser power intensity and the time spent on the substrate during laser scanning. The material behaviour can then be more clearly attributed to UV photolysis with changes on the surface of the substrate occurring slowly. As a consequence of the material damage observed in this chapter, it was decided to change the working wavelength from UV to above 400 nm in the visible spectrum.

Chapter 7

Influence of UV energy and heat treatment time on substrate integrity

7.1 Introduction

Following the production of the silver seed nanoparticles, the next step in the direct metalisation process is electroless plating. Electroless plating is a chemically driven redox process, which involves many influencing factors from the participating chemical constituents and the conditions of the substrate itself. In search for a suitable plating process for the silver seed nanoparticles generated on the substrate, this Chapter first compares several copper and silver bath compositions with regard to their plating performance. As shown in the previous Chapter, the laser-induced photoreduction process resulted in damage to the polyimide substrate. It was decided therefore that the silver seed layer would be produced by a UV lamp instead of a laser. This Chapter will show that the initiation of electroless plating and its adhesion are influenced more prominently by the density of the silver nanoparticles than the composition of the plating baths. The UV dosage and heat treatment were both increased to change the nanoparticles density. By analysis of the results, the origin of the polymer degradation has been revealed.

7.2 Electroless plating

In electroless plating, the properties of the final metal deposits depend strongly on the bath formulation and the particular type of chemical reaction driving the electroless process in the bath. Formaldehyde acting as an electron-releasing reducing agent and is commonly found in electroless copper baths, which are widely used in the Printed Circuit Board (PCB) manufacturing industry. The formaldehyde-copper bath can be prepared using two main kinds of formulations: one based on a tartrate-based recipe or one on an ethylene-diamine-tetra-acetic acid (EDTA) based recipe [146], [147]. Due to the difference in the reaction rates of the electroless plating mechanisms, that include the release of metal ions from the protecting molecules and the electrons transfer, the plating rates, morphology and conductivity of the copper deposits can be drastically different.

When a substrate with a catalytic surface is first immersed into an electroless bath, there is usually an incubation period during which the first complete atomic layer of the electroless metal nucleates onto the catalytic site [148]. Thereafter, subsequent layers of copper can be plated auto-catalytically onto previous layers of copper. The thicker metal deposit then becomes visible. In order to test the plating baths, the silver nanoparticles, used as the catalytic surface, were produced by UV lamp-photomask exposure through a MPEG coating for 90 minutes at optical intensity of ~50 mW/cm^2 for the electroless copper testing baths (I), (II), (III) and (IV) described hereafter. Subsequently, bath (V), an electroless silver bath, was chosen to test the conditions that influence the silver nanoparticles catalytic activity.

7.2.1 Bath (I): highly concentrated tartrate-based copper bath

The bath [146] contains 30 g/l $CuSO_4$, 40 g/l NaOH, 140 g/l NaK-tartrate and 100 ml/l HCOH concentration. The pH was 11. At such a high concentration for each of the chemical components in the bath, the reaction rates are so rapid that some other controlling factors such as temperature and agitation become insignificant. Therefore, room temperature operation can be used and it is not necessary to apply agitation. The plating solution can be dropped by pipette onto the substrate with catalytic micro-patterns. The lifetime of the bath is very short (less than 10 minutes), therefore only a very thin layer can be achieved with this bath by pipetting the plating bath onto the substrate. Figure 7.1 shows a sample, which was first patterned with the direct silver seeding technique via UV-photomask exposure. The electroless Cu layer plated on top was so thin that the metal does not fill up the native pinholes on the polyimide substrate.

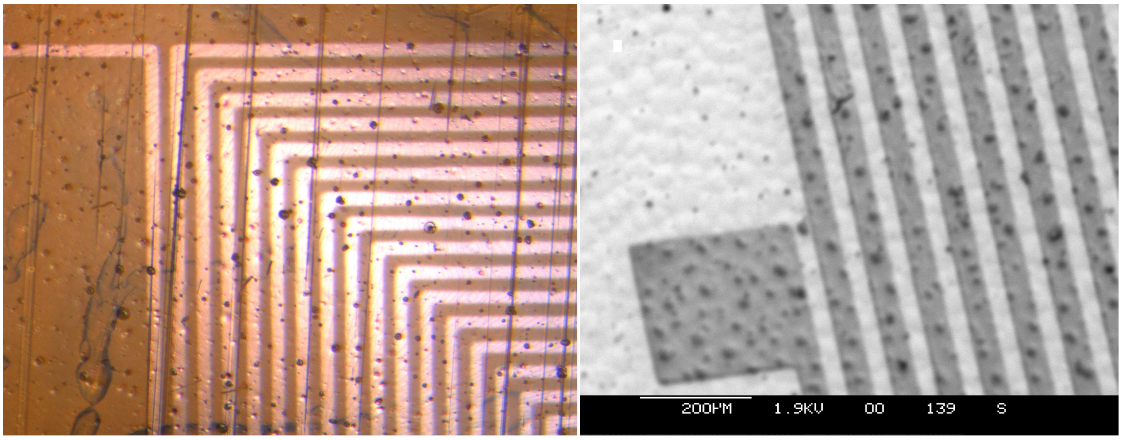

Figure 7.1: (Left) Optical microscopy and (right) SEM micrograph of a micro coil patterned by UV lamp-photomask exposure, followed by electroless plating using Bath (I). The line width of the tracks is ~50 µm.

7.2.2 Bath (II): tartrate-based copper bath

The bath [147] contains 5 g/l $CuSO_4$, 5-10 g/l NaOH, 25 g/l K-Na tartrate, and 10 ml/l HCOH. The pH was adjusted to 13 by controlling the NaOH concentration. This recipe has been widely used for some of the deposition techniques presented in Chapter 2. Slight variations in the concentration of some chemical components can be found in various papers, but the typical characteristics of this bath are low temperature operation (30°C) and low plating rate (a few microns per hour). The incubation time is between 10 to 15 minutes. A sample plated using this bath is shown in Figure 7.2. The pinholes on the polyimide have been filled with electroless copper. However, the stability of the plating bath was found to be problematic. Although the bath has not decomposed, some undesired plating on the polyimide substrate without silver seed was observed.

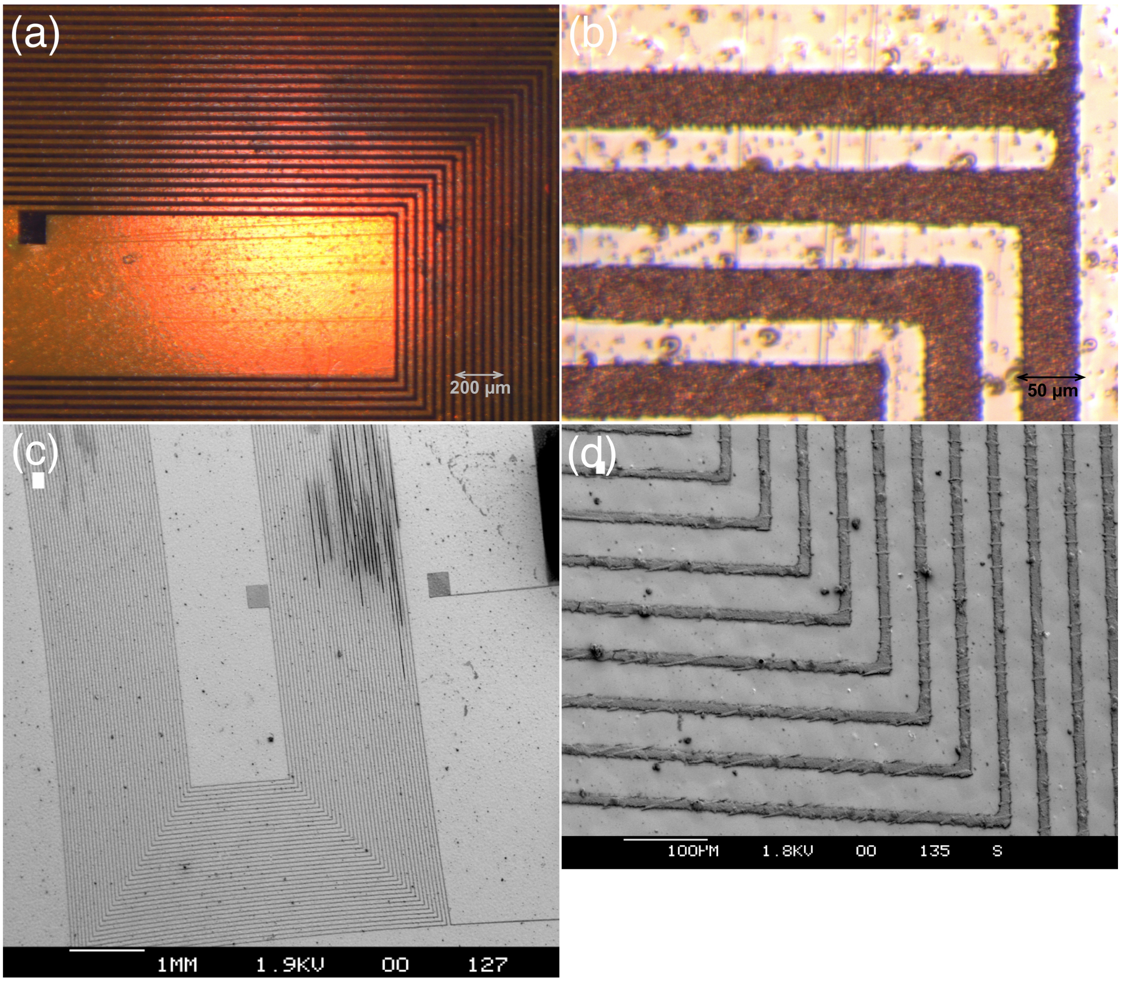

Figure 7.2: (a) & (b) Optical microscopy and (c) & (d) SEM micrograph of a micro coil patterned by UV lamp-photomask exposure, followed by electroless plating using Bath (II).

The line width and height profile of the electroless copper deposits which form part of the micro coil windings were characterised by a ZYGO Viewmeter 5200 white light phase shifting interferometer. A photomask with 50 µm linewidth was used for the UV exposure. Two samples, one fabricated with the present direct-write approach followed by electroless Cu plating and one with the conventional UV-LIGA process [149] followed by Au electroplating were compared as shown in Figure 7.3. The average height of the copper tracks was about 4.5 µm after 45 minutes of electroless plating time whereas the height of the gold tracks was about 8.3 µm after 60 minutes of electroplating time.

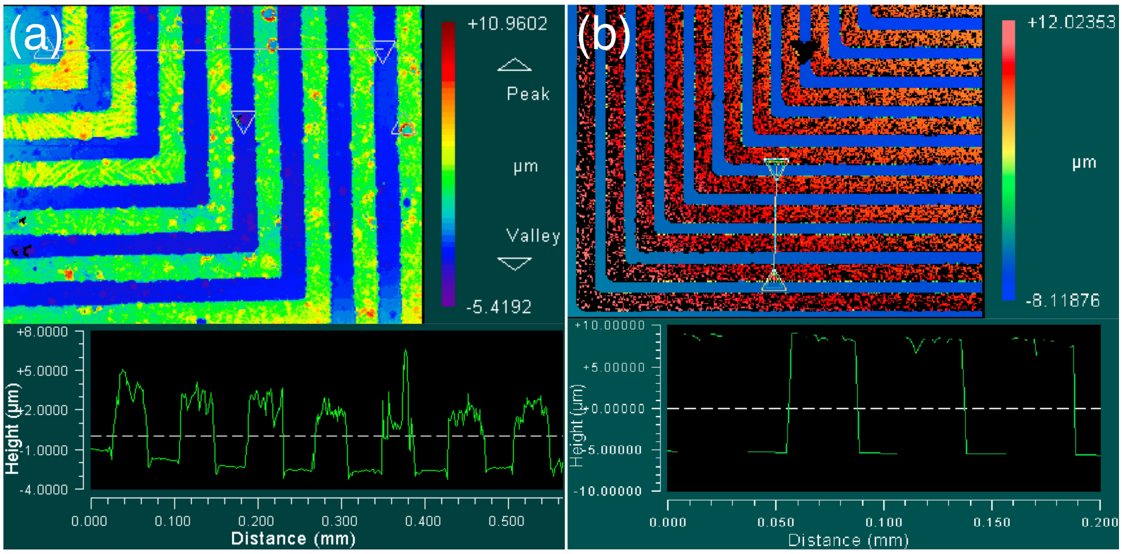

Figure 7.3: Zygo profile of metal tracks fabricated from (a) the direct metalisation approach using UV lamp-photomask exposure and (b) the conventional UV-LIGA process.

The sloping effects on the sidewalls of the tracks were not significant for both samples, even in the case of electroless plating where no photoresist mold is present to condition the shape of the metal deposits. The electroless plated sample exhibited a rougher top surface morphology. The spacing between the tracks on the direct-write sample was found to be as regular as the one fabricated from the UV-LIGA process, indicating that the electroless copper deposited only onto the silver seed patterns.

The average deposited line widths from both samples were found to be over 40 µm, which is smaller than the designed 50 µm line width on the photomask. The origin of this shrinkage could be due to some accumulative effects: the effect of the mask and the distance between the mask and the substrate. Any irregularities in the glass mask construction may result in a slight convergence of the light entering the mask. In addition, if there is an imperfect contact between the mask and the substrate then the converging effect will become more pronounced. In the present direct-write patterning technique, a relatively large dose of energy was needed. As a consequence, the difference in energy density which could occur between the outer regions (edge) of the track and the centre region of the tracks due to the above reasons might be significantly amplified resulting in shrinkage of the line width. Further investigation is needed to verify this possible shrinkage mechanism.

A laser scanned micro-coil was also tested using this electroless bath. Laser system 3, as described in Chapter 5.2.1, was used with 6 mW power, a scan speed of 0.5 mm/s and a defocus of the light beam to a spot diameter of about 50 µm. Despite the polymer restructuring that took place in similar laser writing conditions as shown in Chapter 6.4.1, the electroless copper plating took place. As can be seen in Fig. 7.4(a), some copper delaminated in various parts of the coil winding. Figure 7.4(b) shows that the line width of the electroless copper plated tracks are about 70 µm. The widening is believed to be due to the much wider gap of 300 µm in between the windings compared to the photomask design above, therefore allowing a higher rate of fluid flow and thus higher rate of the electroless plating growth on both sides of the tracks.

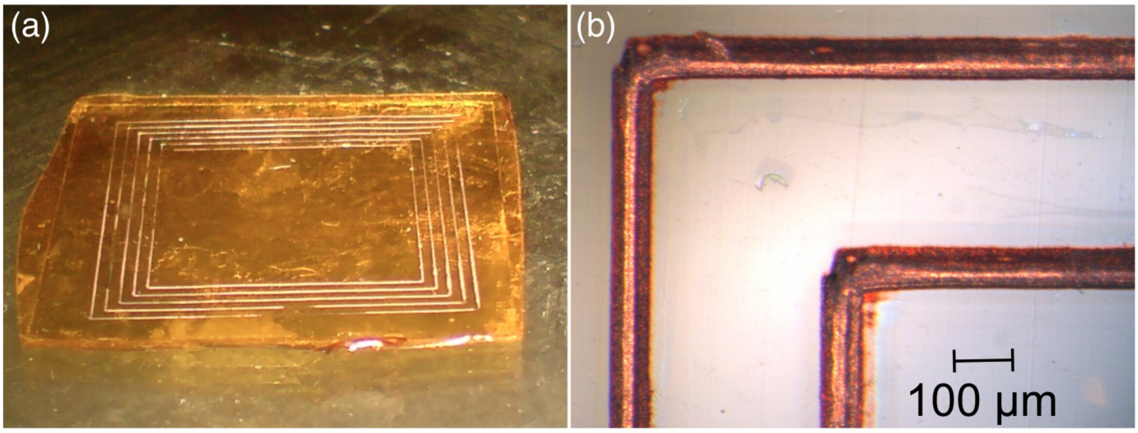

Figure 7.4: (a) Photograph of an electroless copper plated micro-coil with its seed layer fabricated by laser direct-writing; (b) optical microscope image of (a).

7.2.3 Bath (III): EDTA-based copper bath

This bath [147] contains 5 g/l $CuSO_4$, 10-15 g/l NaOH, 30 g/l EDTA, and 15 ml/l HCOH. The pH was adjusted to 13 by adjusting the NaOH concentration. This bath shows excellent stability and hence good selectivity of plating could be achieved. The general characteristics of an EDTA-based bath are higher operation temperature (50 to 60°C) and high plating rate (~10 to 20 µm/hr). The incubation time is less than 10 minutes. In almost all cases, the deposited copper patterns delaminated from the substrate during plating, as shown in Figure 7.5.

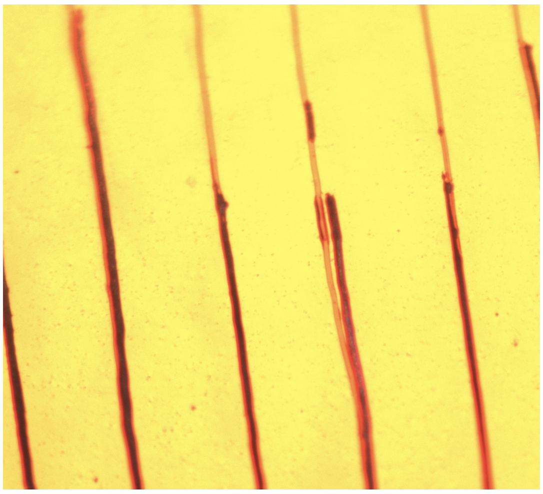

Figure 7.5: Optical micrograph of a sample with tracks first fabricated by laser direct-writing followed by electroless plating using Bath (III). Delamination of the copper deposit can be clearly observed.

7.2.4 Bath (IV): Rohm & Haas Circuposit 4750 EDTA-based copper bath

This commercial bath was tested at 52°C. Air agitation and mild magnetic stirring were applied. The surface of the substrate was observed *in situ* during the plating process by shinning light through the plating solution from the side of the water-jacketed glass container. Within 15 minutes, the seed patterns dissolved together with the top surface of the polyimide before any plating proceeded. When the sample was taken out of the plating bath, no seed pattern remained.

Temperature and pH are the two most prominent influencing factors in electroless plating. All electroless Cu baths tested here have been driven by formaldehyde which requires pH near 13 to operate sufficiently as a reducing agent. Delamination of either the silver seed layer or the subsequent Cu plated patterns were observed due to the nature of the electroless plating solution. It is indeed well known that polymers, especially polyimide, are particularly sensitive to an alkaline environment. Blistering of the copper deposits due to other side reactions from the formaldehyde driven mechanisms can also develop, resulting in higher probability for defects appearance.

Although similar recipes have been commonly employed by many research groups for metalisation of ion-exchanged polyimide, few have demonstrated upscale manufacturing of prototypes or complete working circuits on the modified polyimide substrate. In order to achieve this goal, a lower pH operation must be employed; this requires the substitution of formaldehyde as the reducing agent. One such bath [150], first developed by IBM in 1993 operates at pH 9 and uses dimethylaminoborane (DMAB) as the reducing agent. However, a commercial bath is recommended for its more reliable repeatability, which is particularly important for upscale manufacturing.

7.2.5 Bath (V): PK Plating Technology ESM 100 silver bath

This commercial autocatalytic silver bath (PK Plating Technology AB, Sweden) uses cyanide as the complexing agent, and is extremely stable over a long running time. The bath uses DMAB as the reducing agent. The deposited silver layer acts as the catalyst itself for further plating, so that high thickness can be achieved. The key parameters for controlling this bath are the cyanide to silver ion ratio (CN:Ag), pH and temperature. These parameters can be tuned to suit the catalytic activity of the silver nanoparticles. Cyanide is a ligand which prohibits the release of the silver ions in the bath and therefore, if the CN:Ag ratio is too high, no plating occurs while if it is too low, overplating occurs and the rapidly plated layer detaches itself easily from the substrate. Moreover the substrate areas without any catalysts can nucleate a plated area during overplating. CN:Ag ratios of 0.79–1.1 were tested. The optimum operating temperature of the bath was 67^{o}C but temperatures as low as 55^{o}C were tested, and it was found that when the temperature is too low the plating will not occur. Similarly, variations of pH between 9.8 and 10.3 were also tested and the optimum pH was 10 for the electroless plating to proceed.

Compared to the electroless copper baths (I) to (IV), this bath was found to be the most controllable. However within the upper and lower limits of the CN:Ag ratio, pH and temperature of this bath tested, with the same silver seed layer produced by UV lamp exposure of 90 minutes, the incubation time prior to the start of visible silver plating was unusually long, up to more than 10 minutes. The plated top silver layer still suffered from very poor adhesion. For normal operation of this bath, plating on a plain sheet of silver or a micro-etched copper surface, autocatalytic plating would be visible within a minute. This led to the conclusion that the catalytic activity of the silver nanoparticle seed layer needs to be increased.

To achieve this, the UV lamp exposure dose was increased to investigate the exposure time when all the Ag^{+} ions in the substrate were exhausted. The heat treatment time was also increased to allow further coalescence. Evidence of the transformation of the silver nanoparticles during these extended conditions are presented in the following section, which also uncovers a connection between the poor electroless metal adhesion and the polymer substrate degradation.

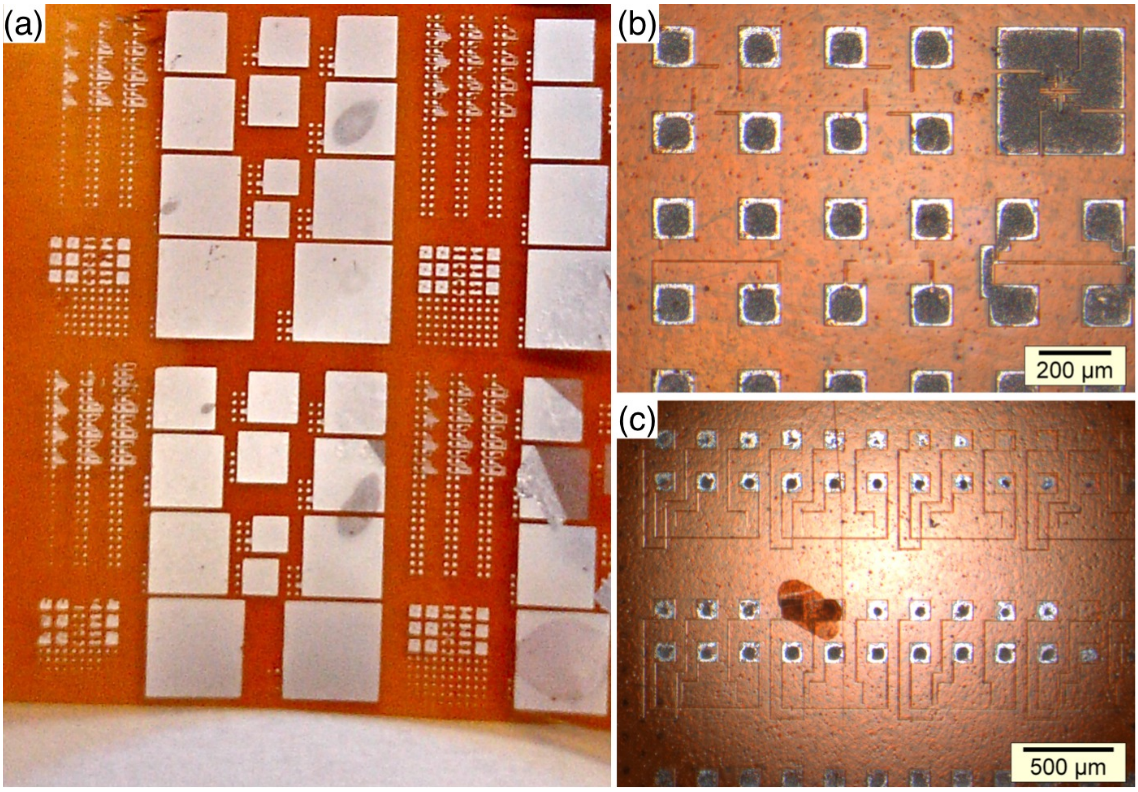

Figure 7.6: Optical microscope images of electroless silver plated micro-patterns fabricated by UV-MPEG direct metalisation (a) zoom-out image showing the overall design of the photomask; (b) Greek-cross and line width test structures, (c) fine line circuits with contact pads.

Figure 7.6 shows the best electroless plated result obtained with the silver nanoparticles seed layer produced by UV exposure dose of 690 J/cm^2 (equivalent to 4 hours of UV lamp exposure) and 4 hours heat treatment. The deposited electroless silver has a rough white appearance. Small features still suffered from delamination. The minimum feature size that allowed the deposited electroless silver layer to remain on the sample was about 30 µm. The tracks with line width between 10 and 20 µm appeared to have been attacked by the plating bath. Not only was no plated layer found on those patterns, but the original silver nanoparticle seed layer had also disappeared. It is believed that with such narrow line width the plating solution could more readily attack any degraded polymer underneath the silver nanoparticle layer, resulting in the detachment of the seed layer. Figure 7.6(c) shows that, when the sample was immersed in the plating bath for a longer period, the electroless silver layer deposited on the bigger feature patterns also starts to disappear. The detachment was not between the electroless silver layer and the silver nanoparticle seed layer as no silver nanoparticles seed layer could be seen remaining. The silver nanoparticles had an exceptionally strong adhesion to the modified polyimide substrate since they are mechanically interlocked with the polymer chains within the substrate. They cannot be scratched off by a scalpel nor dissolved in deionized water. This interlocking mechanism was breached in the electroless bath environment indicating that the reimidized polymer substrate does not exhibit the same chemically inert properties as in the pristine polyimide.

7.3 Effects of UV exposure dose on the silver nanoparticles

The photo-reduction of silver ions results in the formation of silver atoms within the polymer matrix at the surface of the substrate, which can then immediately nucleate into bigger particles. The applied optimum light dose should therefore be high enough so that all silver ions in the exposed areas can be used for photo-reduction. With no heat treatment and at a relatively low UV energy dose of approximately 260 J/cm^2 through a MPEG coating, faint patterns in the exposed areas are observed while above 345 J/cm^2, a more prominent silver colour is produced. The silver nanoparticles generally display a silvery colour tinged with green or purple as already shown in Figure 6.3.

Using high resolution FEGSEM microscopy, the samples after 1 wt% H_2SO_4 solution washing without heat treatment in Figure 7.7 show that increasing energy doses increased the density of silver particles formed as expected. Without annealing, the silver particles have a narrow distribution of particle size. However, at UV energy doses above 690 J/cm^2, the polymer substrate becomes degraded and small holes appear on the substrate amongst the silver nanoparticles. The particle density is found to peak at a UV dose of 865 J/cm^2 although some polymer degradation on the substrate has already occurred by this stage. No clear differences in the particle density can be observed, when the UV dose is increased up to 1210 J/cm^2, the polymer substrate becomes increasingly degraded with prominent pores appearing. This plateau in particle density indicates that the silver ion source incorporated in the polymer substrate has been depleted. At a dose of 1380 J/cm^2, the polymer is noticeably degraded with a rough surface containing fewer silver nanoparticles than with doses in the range from 865 to 1210 J/cm^2.

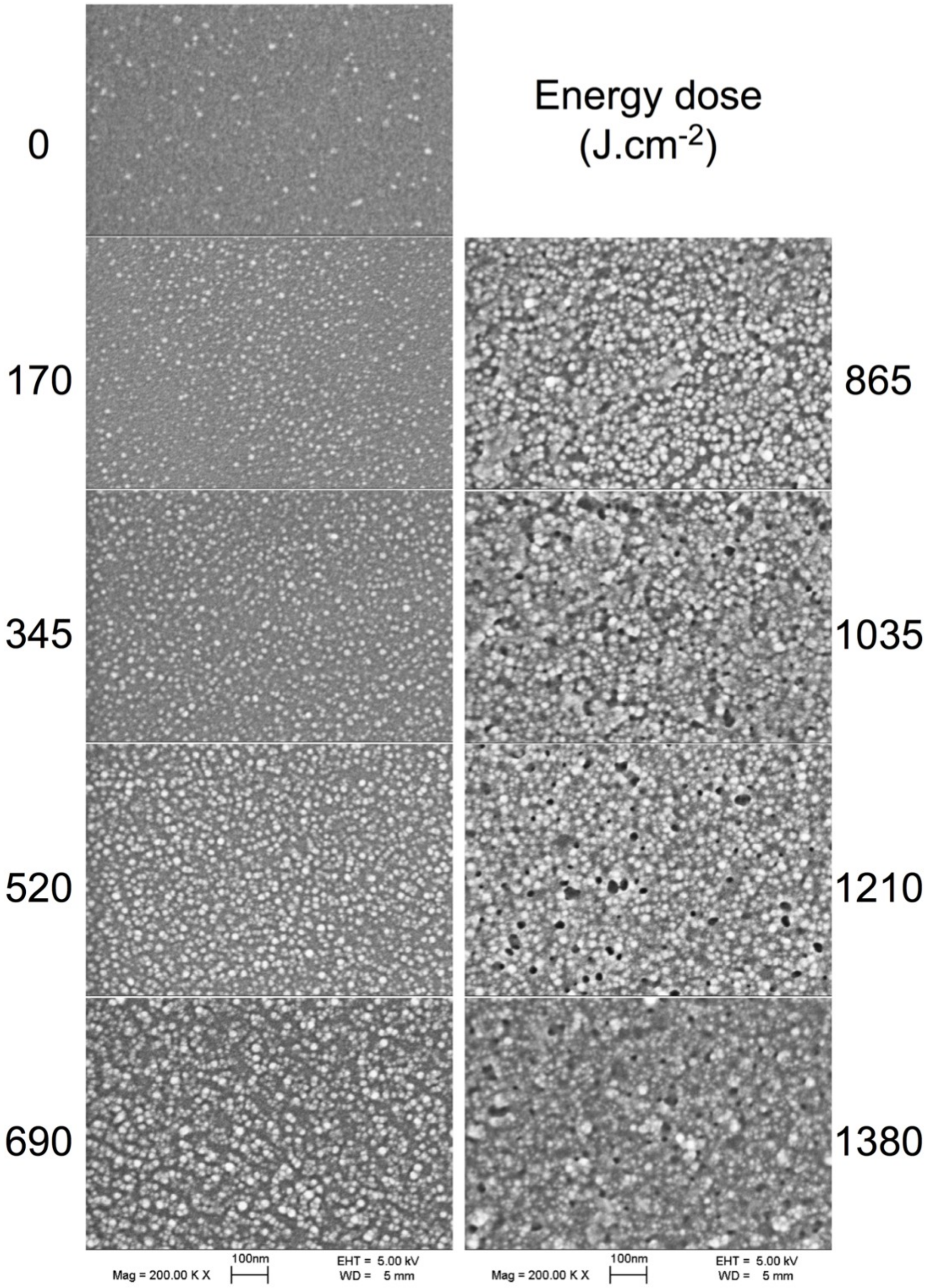

Figure 7.7: FEGSEM images of a silver ion-exchanged sample subjected to UV irradiation with different energy dose and washing in a 1 wt% H_2SO_4 solution afterwards. No heat treatment was applied.

7.4 Effect of heat treatment

To produce a silver layer with high surface catalytic activity suitable for subsequent electroless plating, a combination of sufficient dose of light energy and duration of heat treatment at 250ºC is required. The thermal energy allows the coalescence of the silver particles within the polymer matrix. As a consequence, the silver layer develops a bright silver appearance after heat treatment for 4 hours as shown in Figure 7.8(a). Figure 7.9 shows a reflectivity measurement of the samples prepared with a fixed UV exposure dose of 690 J/cm^2 and annealing times varying from 2 to 5 hours. The measurements have been carried out at different incident angles with a laser light source of 632.8 nm wavelength with maximum power of 0.95 mW. The reflectivity of the samples increases as the heat treatment time is increased at a constant temperature of 250ºC, especially for samples heated for more than 1 hour. The reflectivity decreases however beyond 4 hours of annealing time. With 5 hours of heat treatment, the exposed areas where silver nanoparticles/polymer composite should be, have turned into a brown colour as shown in Figure 7.8(b). It can be clearly seen that the polymer regions surrounding the degraded brown patterns also exhibit some changes. This indicates that a thermal effect certainly plays a role in the degradation of the areas that have been exposed to UV radiation. The brown patterns have a roughened surface, which shows an even poorer reflectivity than the sample without heat treatment.

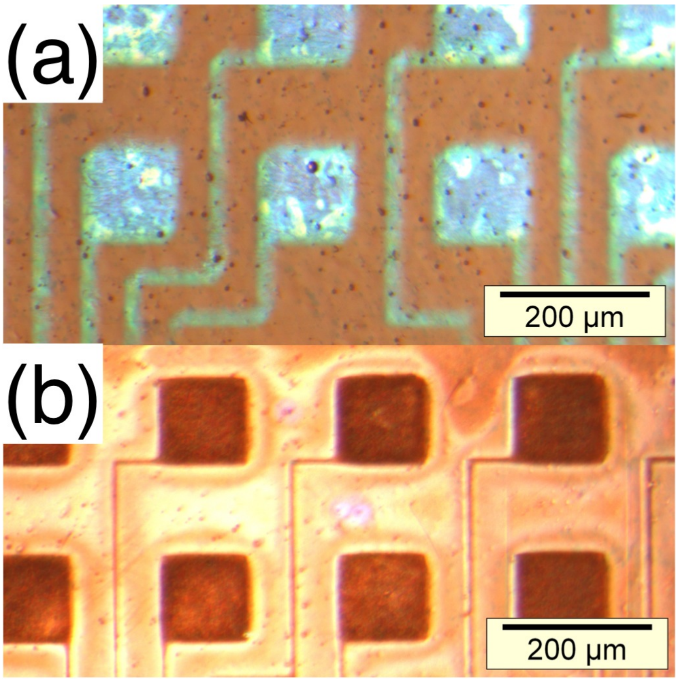

Figure 7.8: Optical microscopy images of a sample after photo-reduction with 690 J/cm^2 and (a) 4 hours and (b) 5 hours heat treatment at 250ºC.

Although it is advantageous to choose as short a heat treatment time as possible, the most desirable treatment conditions for these samples are those that result in silver nanoparticles with high catalytic activity for the initiation of subsequent electroless plating.

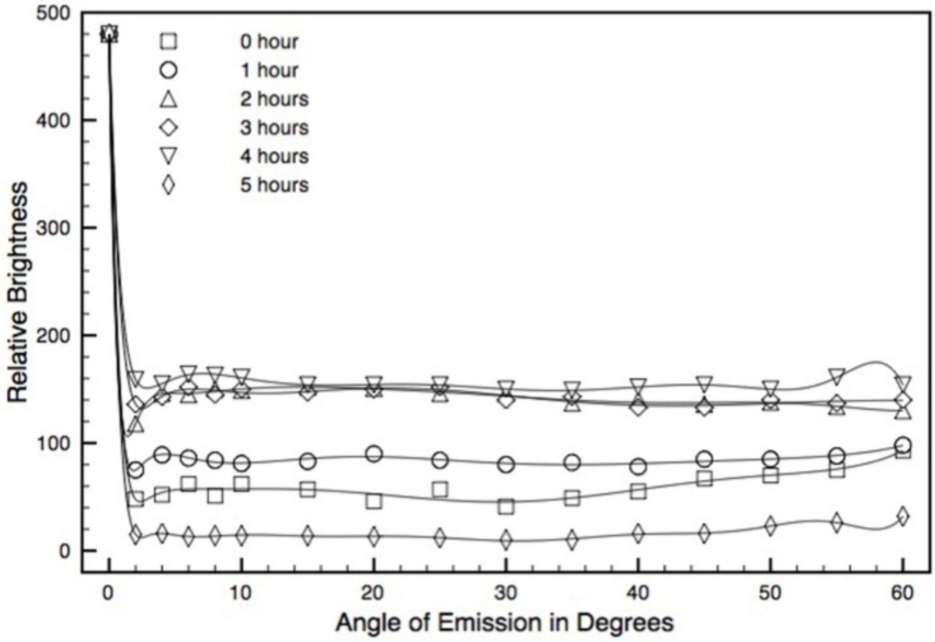

Figure 7.9: Reflectivity measurements of a set of samples with fixed UV dose of energy of 690 J/cm^2 and varying heat treatment times at a constant temperature of 250ºC.

The coalescence of the silver particles and degradation of the surface of the substrate occur concomitantly. The evolution of the morphology of the silver nanoparticles can be observed in Figure 7.10 from the FEGSEM images of samples with approximately 690 J/cm^2 UV exposure energy dose and varying heat treatment times at 250ºC. A pristine polyimide control sample with no chemical pretreatment is also used to isolate any contribution to the substrate of the UV exposure and subsequent annealing. As the duration of the heat treatment increases, the silver treated sample (sample (iii)) displays silver particles with increasing average particle size. When no heat treatment is applied, there is a reasonably regular distribution of silver particles formed by photo-reduction on top of the substrate.

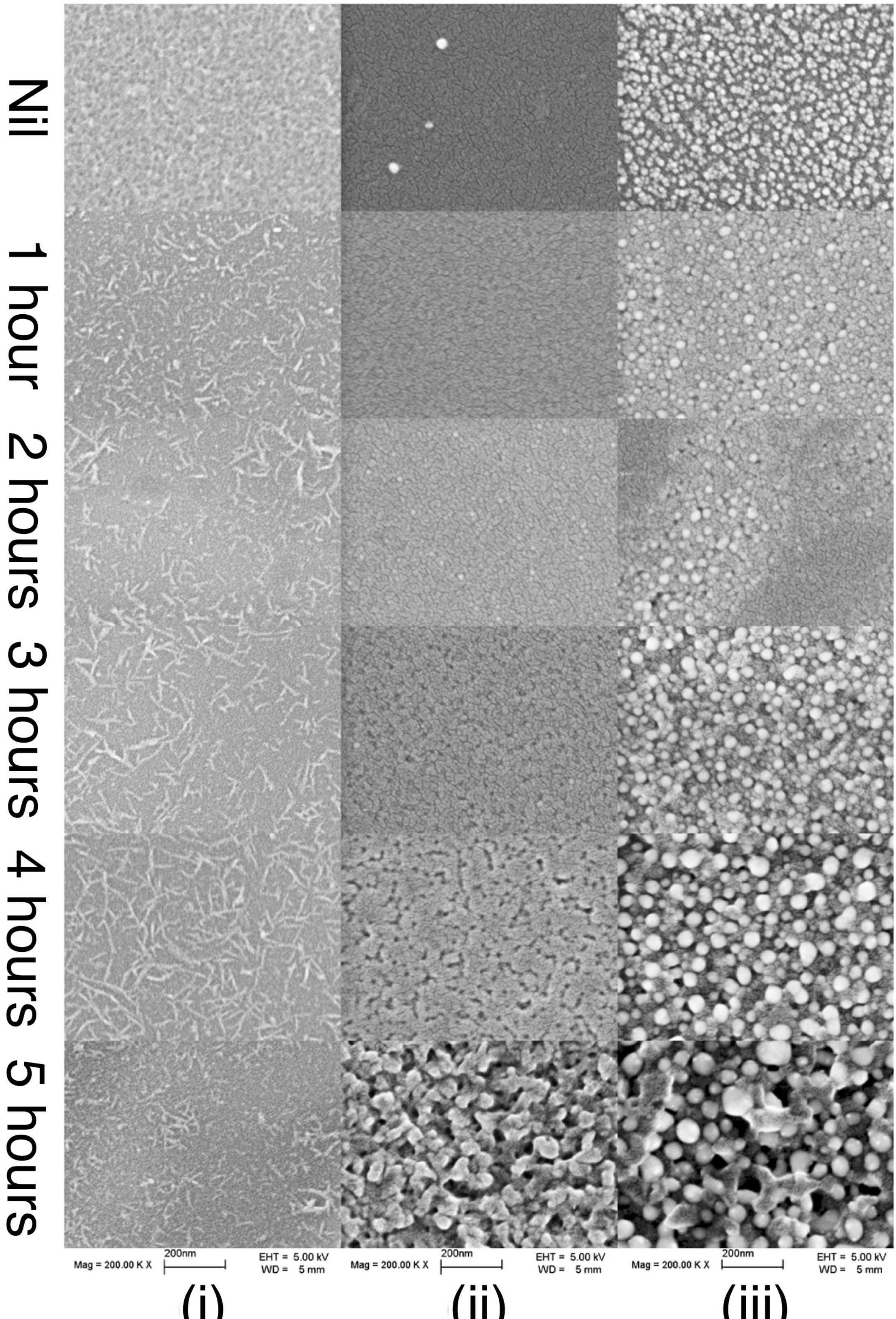

Figure 7.10: FEGSEM images of the surface degradation and silver particle coalescence of the samples submitted to different process conditions under varying heat treatment times at 250ºC. Samples: (i) KOH surface modified polyimide with UV exposure, (ii) silver ion-exchanged polyimide, and (iii) silver ion-exchanged polyimide with UV exposure. A constant UV energy dose of approximately 690 J/cm^2 is employed for the exposed samples.

To determine whether the UV exposure or the annealing step is responsible for the degradation of the substrate, samples annealed for different lengths of time and various treatment conditions and their levels of degradation are shown in Table 7.1. A control sample with no chemical pretreatment on the polyimide substrate is also used to isolate any contribution to the substrate of the UV exposure and subsequent annealing. These samples, denoted as (a – f) are as follows: (a) polyimide with no subsequent chemical processing, (b) polyimide with UV exposure and no subsequent chemical processing, (c) KOH surface modified polyimide with no UV exposure, (d) KOH surface modified polyimide with UV exposure, (e) silver ion-exchanged polyimide with no UV exposure, (f) silver ion-exchanged polyimide with UV exposure. All samples subjected to UV exposure (samples b, d and f) have been coated with the MPEG polymer. FEGSEM images of these samples can be seen in Figure 7.10. As expected, samples (a – c) did not exhibit any significant change in appearance and are therefore not shown here. Columns (d – f) in Table 7.1 correspond to columns (i – iii), respectively. A constant UV energy dose of approximately 690 J/cm^2 was used. All samples with surface modification (samples c – f) have been washed with 1 wt% H_2SO_4 solution prior to anneal. The two polyimide samples with only MPEG coating, no subsequent chemical processing (samples a, b), either with or without UV irradiation, both also show no degradation at 5 hours heat treatment.

Table 7.1: Levels of degradation of the surface of the substrate based on FEGSEM images. Samples: (a) unmodified polyimide, (b) unmodified polyimide with UV exposure, (c) KOH surface modified polyimide, (d) KOH surface modified polyimide with UV exposure, (e) silver ion-exchanged polyimide, and (f) silver ion-exchanged polyimide with UV exposure. A constant UV energy dose of around 690 J/cm^2 was employed for the exposed samples.

Heat treatment time	(a) PI	(b) PI + UV	(c) KOH/PI	(d) KOH/PI + UV	(e) Ag^+/PI	(f) Ag^+/PI + UV
None	no	no	no	textured	no	no
1 hour	no	no	no	textured	some	some
2 hours	no	no	no	textured	some	some
3 hours	no	no	no	textured	moderate	moderate
4 hours	no	no	no	textured	moderate	moderate
5 hours	no	no	no	textured	severe	severe

Without UV irradiation, the KOH surface modified sample (sample c) does not exhibit any morphology changes upon heat treatment up to 5 hours. This sample has a similar appearance as the control sample (sample a).

With UV exposure, the same hydrolyzed surface (sample d) shows a "nest-like" texture when no heat treatment is applied, providing thereby a clear indication that the UV irradiation produces the morphology of the surface. When heat treatment is applied, the sample does not exhibit any degradation as observed for samples d and e, but maintains a similar texture throughout the 1 to 5 hours heat treatment.

Without UV exposure, the silver ion-exchanged sample (sample e) starts exhibiting some surface morphological changes at 3 hours annealing time and after 5 hours, significant degradation of the polymer substrate is observed. Therefore, without UV irradiation the silver ion-exchange and subsequent dilute acid washing must play a role in inducing the thermal degradation of the polymer substrate.

The silver ion-exchanged sample with UV irradiation (sample f) is the only sample that produces silver nanoparticles. The coalescence of the silver particles and degradation of the surface of the substrate occur concomitantly. The evolution of the morphology of the silver nanoparticles can be observed as the duration of the heat treatment increases. When no heat treatment is applied, there is a reasonably regular distribution of silver particles formed by photo-reduction on top of the substrate without any coalescence taking place. At 1 and 2 hours heat treatment, the coalescence of the silver nanoparticles is not very pronounced. After 3, 4 and 5 hours of annealing times, the average particle size increases with heat treatment times.

At the same time, the polymer substrate develops leaf-like structures for annealing times above 3 hours. Since no morphology changes are observed for the control sample, which underwent the same UV exposure and thermal annealing (sample b), the transformation of the polymer substrate must be due to the chemical treatments. The level of polymer degradation can be seen to be increasing for annealing times between 3–5 hours. After 5 hours of heat treatment, the degraded polymer shows a leaf-like structure. The silver particles are found on the surface or in the gaps of the fragmented polymer substrate.

The degradation of the surface of the substrate can be explained in terms of oxidative degradation due to UV irradiation and heat treatment in air.

The surface of the substrate is an amorphous polymer containing mobile metal ions, namely potassium polyamate and silver polyamate for the KOH surface modified samples and silver ion-exchanged samples, respectively. After washing in dilute H_2SO_4, hydrogen ions are exchanged with the potassium or silver ions in these samples, forming polyamic acid. These amorphous polymer layers do not exhibit the same good thermal stability of the unmodified polyimide as seen in the samples at 5 hours anneal without UV irradiation. The extent of degradation is also dependent on the UV energy dose when UV irradiation is applied.

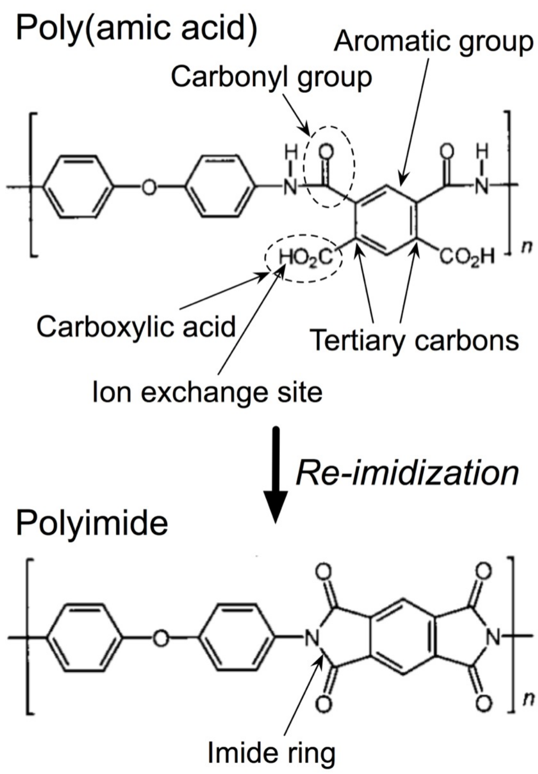

Figure 7.11: Structural formulae of poly(amic acid) and polyimide of the type pyromellic dianhydride - oxydianiline (PMDA-ODA).

Based on the mechanism suggested by Srinivasan et al. [151], during the heat treatment, oxygen attacks the amorphous layer, which contains tertiary carbon atoms and carboxylic acid, as illustrated by Figure 7.11. At elevated temperatures, free radicals formed at tertiary carbon atoms are more stable and longer lasting, making them more susceptible to attack by oxygen. Consequently, there is a possibility that the following two reactions can take place together: (1) carbonyl groups can be formed from the oxidation of the tertiary carbon which can then be further oxidized, (2) the neighboring carboxylic acid, composed of a carbonyl group and a hydroxyl group, is already in a high oxidation state and further oxidation removes the carboxyl carbon as carbon dioxide. As a result, some carbon atoms are lost and/or some polymer chains are broken thereby weakening the poly(amic acid) structure.

When continuous UV irradiation is applied, the presence of aromatic groups in the poly(amic acid) molecule can act as a good UV absorbing agent. More free radicals can be formed by the interactions of UV photons with the aromatic groups or the tertiary carbon bonds. The generated free radicals then again react further with oxygen in the atmosphere, inducing more oxidative attacks. Therefore, more severe damage is observed on the surface modified, UV irradiated samples after heat treatment compared to those not submitted to UV irradiation.

The reaction of poly(amic acid) reforming the C-N-C imide rings upon heat treatment, known as re-imidization, also takes place. Some of the imide rings are indeed reformed after 30 minutes of heat treatment as described in Chapter 4. However, the completeness of this re-imidization process has not been quantified. Whilst re-imidization is taking place, some oxidative degradation effects have already occurred, i.e. some carbon atoms are already removed or the polymer chains are already shortened, especially in the UV irradiated regions of the samples. This could affect the crosslinking of the reformed polyimide molecules and hence the layer of polyimide recovered from the modified material may not possess the same physical properties as those of the unmodified polyimide in the bulk of the substrate.

7.5 Further degradation effects on the UV irradiated and heat treated areas

The silver patterns on the UV exposed and annealed samples were found to be recessed into the substrate as shown in the Zygo white light interferometer height profile in Figure 7.12. This phenomenon may be attributed to polymer deterioration due to the oxidative degradation described in the previous section. The depth of the recession is quite uniform across the whole microstructure exposed to UV light. The Dektak stylus profiler measurements across a UV exposed pattern, shown in Figure 7.13, confirms that the recessed areas are up to a few hundred nanometers deep with silver nanoparticles residing at the bottom of the recessed patterns.

As discussed earlier, the oxidative degradation on the substrate is believed to be due to a combination of heat treatment and UV irradiation. To obtain further evidence for this hypothesis, the influence of the annealing time and UV energy dose on the size of the recess has been investigated.

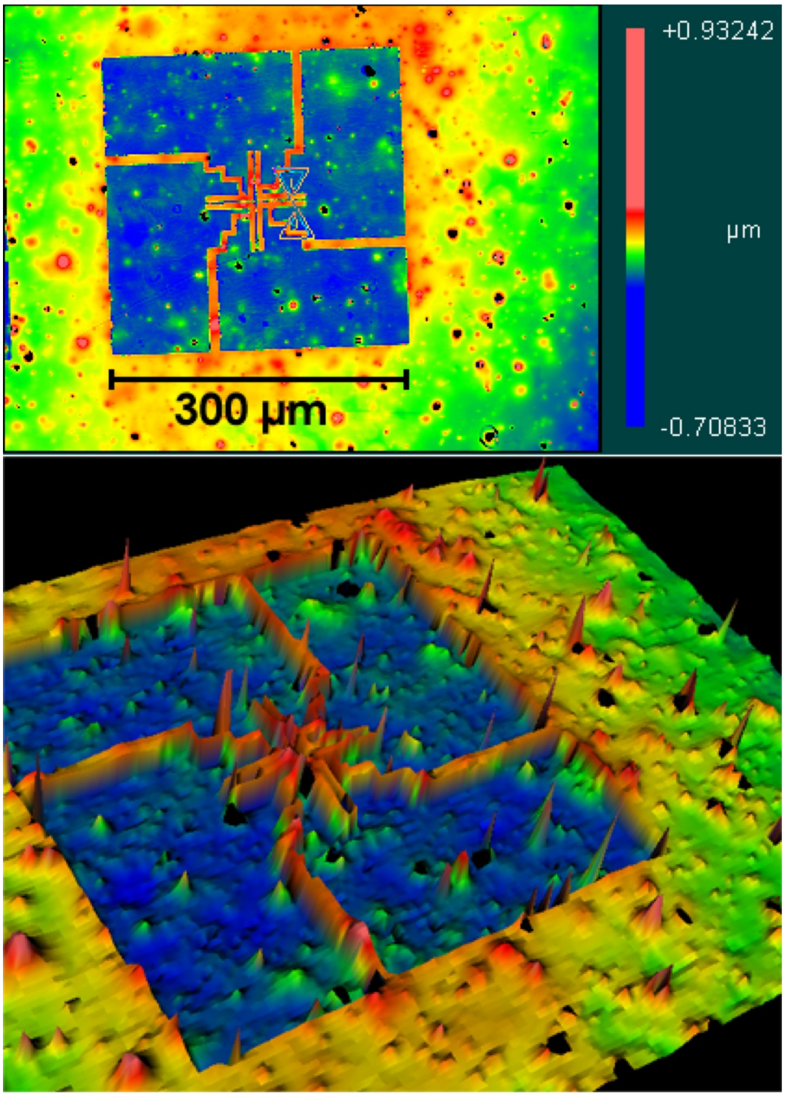

Figure 7.12: Height profiles measured by Zygo.

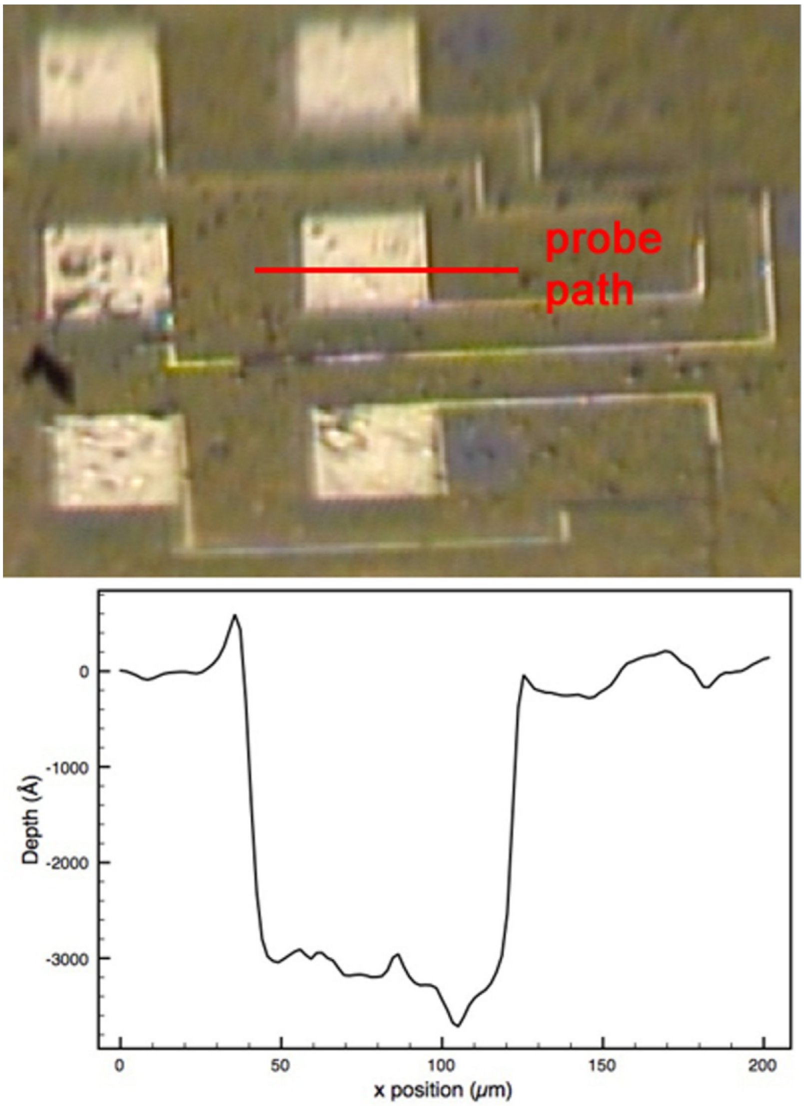

Figure 7.13: Dektak stylus profiler measurement across an 80 x 80 μm^2 contact pad with silver seed layer fabricated by 690 J/cm^2 UV dose and 4 hours anneal time.

The graph in Figure 7.14 shows that the depth of recess increases with annealing time for a range of different UV exposure times. Clearly the longer a sample is annealed for, the greater the recess depth. However it appears that no further degradation occurs after between approximately 4 to 6 hours, depending on the previous UV energy exposure time, where a plateau is reached. The shorter UV exposure times, i.e. the samples with the lower energy doses before annealing, take longer to reach a plateau than those given a higher UV energy dose. It is also evident from Figure 7.14 that the UV exposure plays a part in the degradation, with recess depth from an 8-hour UV exposure being approximately 50% greater than a 2-hour exposure. These results clearly indicate that the polymer shrinkage can be attributed to a combination of both photo- and thermal effects.

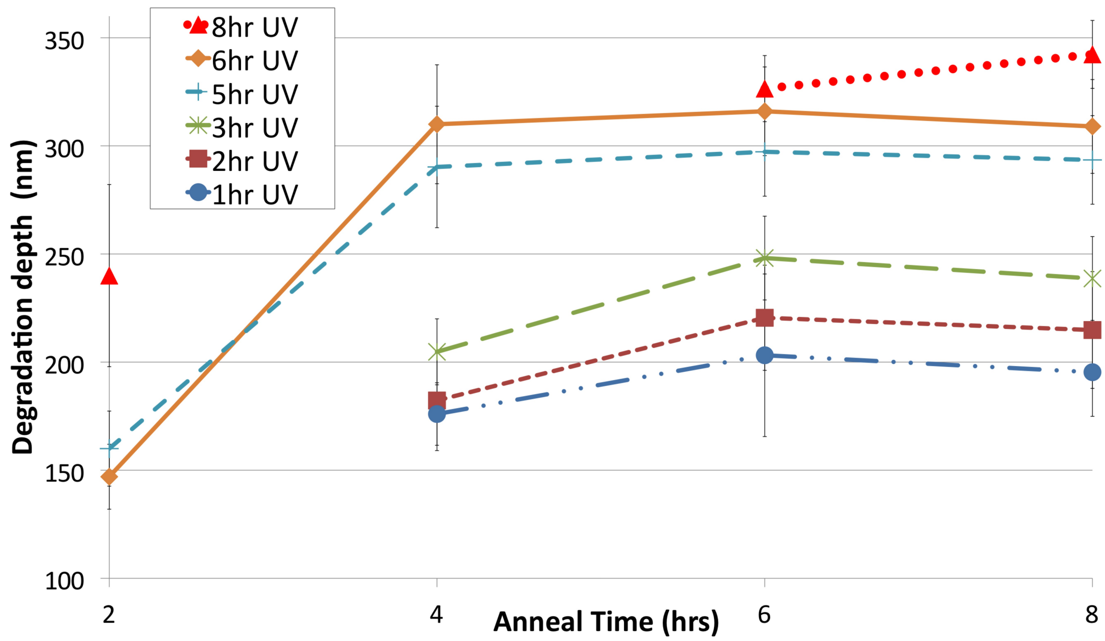

Figure 7.14: Effect of annealing time on depth of substrate degradation for selected UV exposure times.

To articulate how these effects combine to produce this phenomenon, we present a tentative hypothesis of the physical mechanisms at molecular level. The longer the UV exposure time, the more silver nanoparticles will coalesce [53]. Also, it has been shown that incompletely imidised polyimide is liable to break down into smaller molecules, mainly in the form of carbon monoxide and carbon dioxide [151-154]. Furthermore, it has been reported that the presence of silver on a polyamic acid interface can inhibit re-imidization [155]. It is possible that this effect, combined with the silver particles acting as thermal radiators, during both the photochemical and thermal steps of the process, will accelerate the decomposition of the Kapton substrate. Attenuated total reflection Fourier Transform Infra-Red spectroscopy (ATR-FTIR) has been measured on the recessed areas of the re-imidized samples. The spectra (results not shown) were found to be almost identical to pristine polyimide. The degraded polymer top layer is believed to be too thin such that the surrounding unmodified polyimide molecules contribute to the FTIR signals collected.

Since the samples with heat treatment only and without UV irradiation patterning to produce a step height difference, whether this recession effect took place on those samples was not investigated and will need to be the study of further research.

7.6 Conclusion

This chapter first examined the suitability of electroless plating onto a bed of silver nanoparticles as seed layer produced by UV lamp-photomask exposure through MPEG, so that the severe polymer restructuring caused by laser scanning could be avoided. The constituents in the electroless baths and especially the high pH nature of copper baths were originally believed to be the cause of the copper detachment and the dissolution of the silver nanoparticles layer due to the re-imidized polymer substrate being more susceptible to such an alkaline environment. The commercial autocatalytic electroless silver bath, which has some flexibility in its operating parameters, was subsequently selected to benchmark the catalytic activity of the silver nanoparticles seed layer when they were prepared by increasing UV exposure dose and heat treatment.

The applications of various UV energy doses and heat treatment times have been presented in the context of the surface modification of the polyimide substrate. Increasing the UV energy dose increases the amount of silver nanoparticles formed. When a critical UV energy dose is employed, all the silver ions available in the exposed areas of the substrate are used for photo-reduction. At energy dose above 690 J/cm^2, degradation of the surface modified polymer substrate is observed. UV irradiation was also shown to cause morphology changes to the sample with KOH surface modification only without incorporation of silver ions. This change remained constant upon increasing heat treatment times. Heat treatment of silver nanoparticles induced two antagonistic effects: particle growth and polymer degradation. Possible causes of the oxidative degradation of the polymer substrate have been suggested. The catalytic activity of the silver nanoparticles for the initiation of electroless plating has been shown to increase with increased heat treatment time.

Adhesion of the electroless metal deposits has been shown to be affected by the degradation of the polymer substrate and also the insufficient density of the silver nanoparticles as a seed layer. It can be concluded from the FEGSEM microscopy observations that the silver nanoparticles are not closely packed together in any of the samples. In fact, the silver nanoparticles only occupied no more than 50% of the substrate with areas of polymer gaps in between them. The low density of the silver nanoparticles would provide a weak adhesion strength to any electroless layer plated on top and it also exposes more of the degraded polymer to the attack of the plating solution.

The maximum density of the silver nanoparticles on the substrate produced by the photo-reduction, can only be increased by increasing the loading of silver ions in the substrate. This can be achieved by increasing the degree of KOH surface modification initially and thus a larger volume of silver ions can be exchanged into the substrate. However, a high degree of surface modification on polyimide using high concentration of KOH solution has been shown in Chapter 4 to cause severe degradation to the rigidity of the polyimide film.

From the analysis in this Chapter, the use of UV exposure for the optical power intensity and dosage required for the proposed metalisation process in this thesis is concluded to be a major stumbling block. As a consequence, a drastic change of operating wavelength in the visible spectrum is proposed in the next Chapter.

Chapter 8

Photosystem I as a photoreducing agent for the formation of thin metal film patterns

8.1 Introduction

Results from the previous Chapter demonstrated that UV irradiation caused the photo-dissociation of molecular bonds of the polyimide resulting in uneven formation of metal tracks onto the substrate. An alternative photoreducing agent to MPEG needs therefore to be found that works similarly at a wavelength that does not belong to the UV spectrum. A key requirement for such a photoreducing agent is its efficiency in releasing electrons, since large energy dosage irradiating onto the substrate is not desirable as demonstrated previously.

Harvesting visible light for electron generation has been the subject of active research over many years in solar cell technologies. Light absorbing dyes such as nanostructured TiO_2 [66], [156] have been added to enhance the photoelectron generation in semiconductor panels. However a low cost dye requiring the simplest preparation is desirable here since one of the aims of this thesis is to reduce processing time and cost whilst allowing mass manufacturability. In addition, the photoreducing agent coating should be used only once for each silver photoreduction exposure and then gets washed away. Employing semiconductor dyes with bandgap energy customised to match the visible light photons for photoelectron generation would create an additional processing step and would be expensive. On the other hand biomaterials are abundant. Using the light harvesting system in plants, which works perfectly in the visible spectrum, is a natural step to follow as evidenced by some exploratory research in solar cells over three decades ago. In this work, chlorophyll extracted from spinach leaves was used to boost the generation of electrons [157]. Construction of such an artificial light harvesting system incorporating chlorophyll met however with challenges such as quenching of the photoexcited electrons across the chlorophyll proteins/semiconductor interface, electron-hole recombination making electron transfer over a long distance difficult, and stabilization of the protein activity when the chlorophyll molecules were removed from their natural environment [158], [159].

Using the photosystem I proteins in plants, referred to as PS-I, as a photoinitiator for circuit manufacturing is a completely new concept. The Chapter of this thesis describes preliminary work using PS-I for photolithographic fabrication of metal thin film patterns. Such a work has led to a patent filing [160]. The exploratory experimental results presented in this chapter provide evidence that, contrary to the previous challenges encountered in solar cell panels, the ternary system of PS-I/Ag-NPs(nanoparticles)/Ag^+ ions formed on the surface of the polyimide creates a unique scenario whereby exceptional increase in the generation of electrons and transfer in this artificial light harvesting system are allowed. This Chapter proposes also discussion on possible mechanisms responsible for these phenomena.

8.2 Blue light and PS-I catalysed silver nanoparticles growth

The PS-I protein containing chlorophyll was extracted, filtered and drop-coated onto the silver ion-doped polyimide substrate as described in Section 4.3. The blue light exposure apparatus, blue LED systems 1 and 2 were set up as described in Chapter 5. Table 8.1 presents the exposure dosage range at 470 nm wavelength using blue LED system 1 in the initial experiments that allowed the photoreduction to take place. A typical sample produced is shown in Figure 8.1. An approximately 0.8 cm^2 circular area of a silver seed layer was produced. The circular shape is due to the light being enclosed by the casing of the LED arrays. The sample was cut into halves so that one half of the samples could be tested for electroless plating. The electroless silver bath as described in Chapter 5 was used and 2 minutes of plating time was performed.

Table 8.1: Photoreduction experiments carried out using a blue (470 nm) light source impinging onto an area of around 0.8 cm^2 with MPEG in ethanol and PS-I coatings and control samples with no coating. Yes = visible silver layer with prominent bright reflective appearance. No = no visible pattern observable.

Power and time	Energy dose	MPEG in ethanol	PS-I in ethanol	No coating
25 mW 30 minutes	45 J	No	Yes	No
25 mW 60 minutes	90 J	No	Yes	No
43 mW 10 minutes	25.8 J	No	Yes	No
43 mW 30 minutes	77.4 J	No	Yes	No
55 mW 10 minutes	33 J	No	Yes	No
55 mW 20 minutes	66 J	No	Yes	No
55 mW 30 minutes	99 J	No	Yes	No

Qualitatively, an improvement in the adhesion of the plated silver was immediately seen compared to the plating described in Chapter 7. Pushing the deposit from the side by tweezers confirmed some level of adhesion, whereas in the previous case of the seed layer formed by the UV-MPEG process, the plated silver had very poor adhesion and usually delamination occurred whilst the sample was still in the plating bath. The exposure time required for the photoreduction by PS-I is also notably shorter, tens of minutes, than the MPEG process, which was in the region of hours to produce an appreciable amount of visible silver.

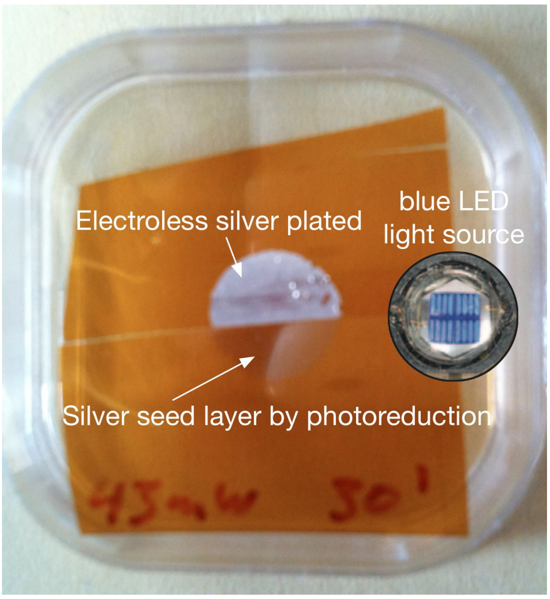

Figure 8.1: Photograph of a blue light exposed sample resulting in a circular shape seed layer. The top half of the sample was subsequently immersed in an electroless silver bath resulting in a white layer of silver deposit.

To explore further the photo-reducing power of PS-I with the silver ion-doped substrates, the blue LED system 2 with a fibre delivered output power intensity of 1270 mW/cm^2 was used and resulted in the generation of a circle of 3 mm diameter when the fibre end was placed 5 mm away from the substrate. Figures. 8.2 and 8.3 show photographs and FESEM micrographs of the samples exposed by the tip of the optical fibre for 30 – 600 seconds. The growth of silver nanoparticles can be clearly observed on the silver/polymer composite at 30 seconds exposure time where silver nanoparticles as small as 15 nm can be easily identified across the illuminated area. Some particles aggregated to about 70-80 nm sizes. Within 60 seconds exposure time, the whole illuminated area was compactly covered with silver nanoparticles. The smaller particles have an average size of about 30 nm and the larger aggregated particles about 70 nm. At 180 seconds exposure time, a large amount of particles had aggregated to 40 nm or bigger, where, noticeably, some particles as large as 120 nm can be seen. In this case the silver nanoparticles are not compactly connected as in the case of the 1 minute exposed sample. This indicates that the silver ion source in the substrate supplying the photochemical reduction has been depleted thus leaving a void behind when the smaller particles aggregated to grow bigger particles. At a prolonged exposure of 600 seconds, a dark mark can be clearly seen at the centre of the exposed spot in the photograph in Figure 8.2. The prolonged exposure of the substrate at a power intensity 2 orders of magnitude higher than that of the blue LED system 1 has probably generated some thermally induced effects. The corresponding FESEM micrograph shown in Figure 8.3(e) also suggests that a reaction, as yet not explained, seemed to have taken place, which removed the larger particles seen in Figure 8.3(d).

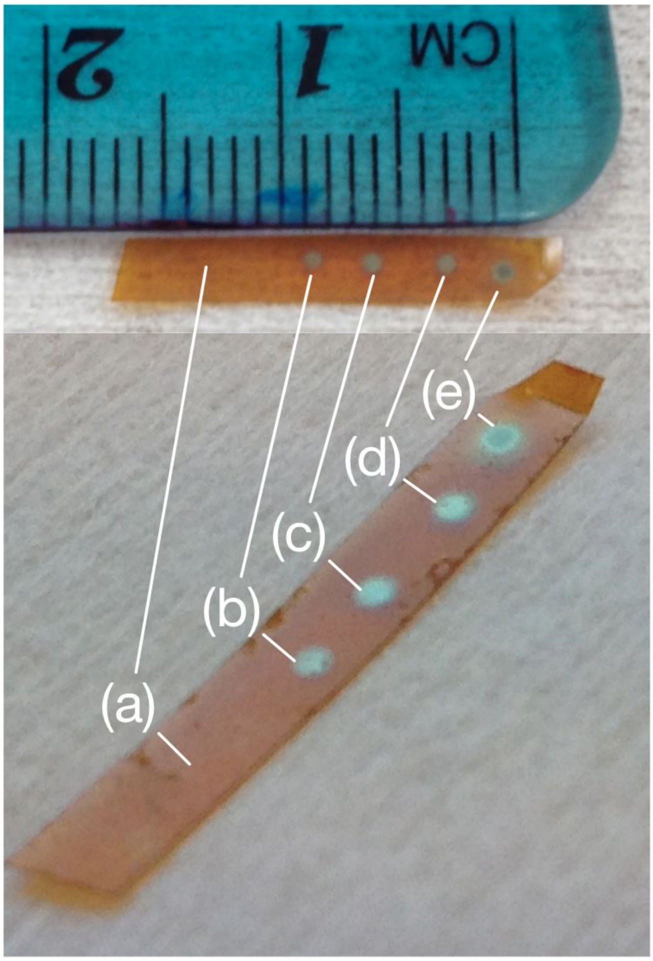

Figure 8.2: Photographs of the results of photoreduction using a fiber delivered blue LED light source, indicating (a) control background, (b) 30, (c) 60, (d) 180, (e) 600 seconds exposure times. (a) - (e) corresponds to the FEGSEM micrographs in Figure 8.3.

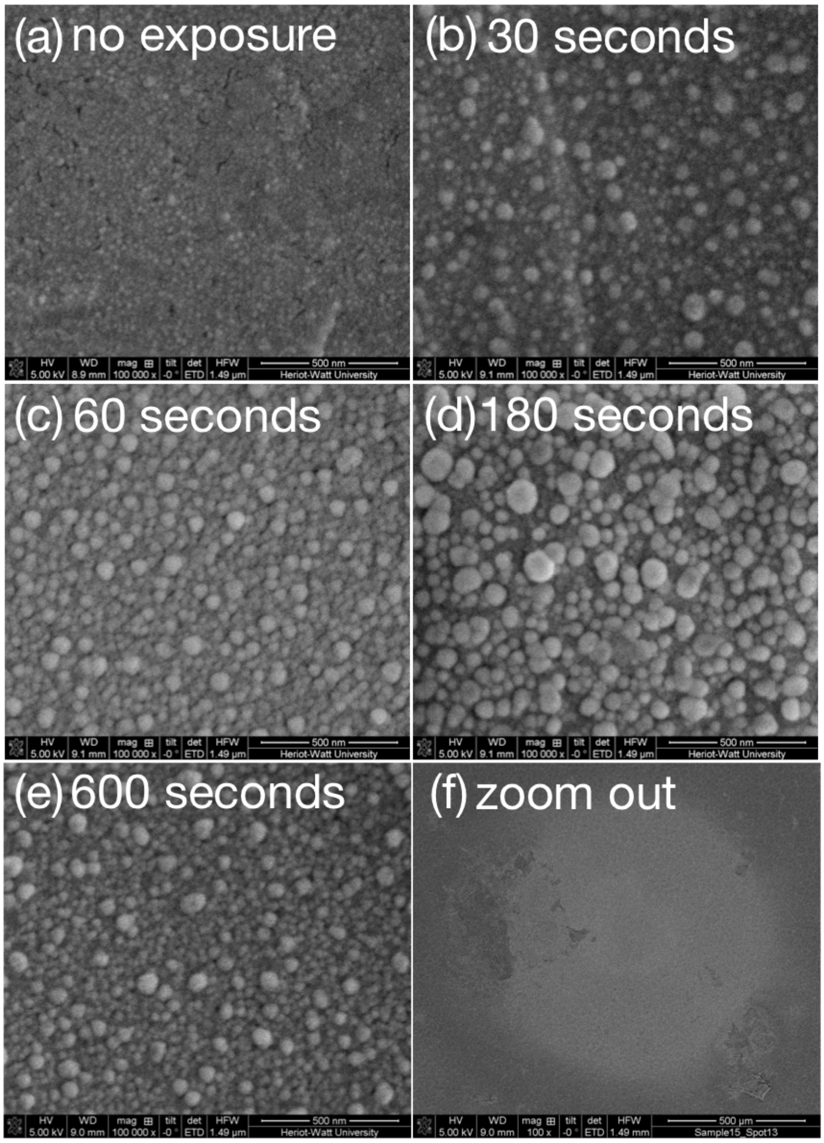

Figure 8.3: FESEM micrographs corresponding to the photoreduction results shown in Figure 8.2: (a) control background, (b) 30, (c) 60, (d) 180, (e) 600 seconds exposure times.

8.3 Height measurements

To study whether the blue light PS-I system degraded the substrate in the same way as that described in previous chapters, profilometry measurements were carried out to study the height of the illuminated samples. Figure 8.4 shows a Zygo white light phase shifting interferometer surface profile measurement of a 60 seconds exposed sample (as in Figure 8.3(c) above) after washing in a 1 wt% H_2SO_4 solution and heat treated at 250ºC for 30 minutes for re-imidization. The result shows that no height difference between the silver region and the polyimide could be detected. The curvature of the flexible polyimide substrate is evident on the Zygo pictures.

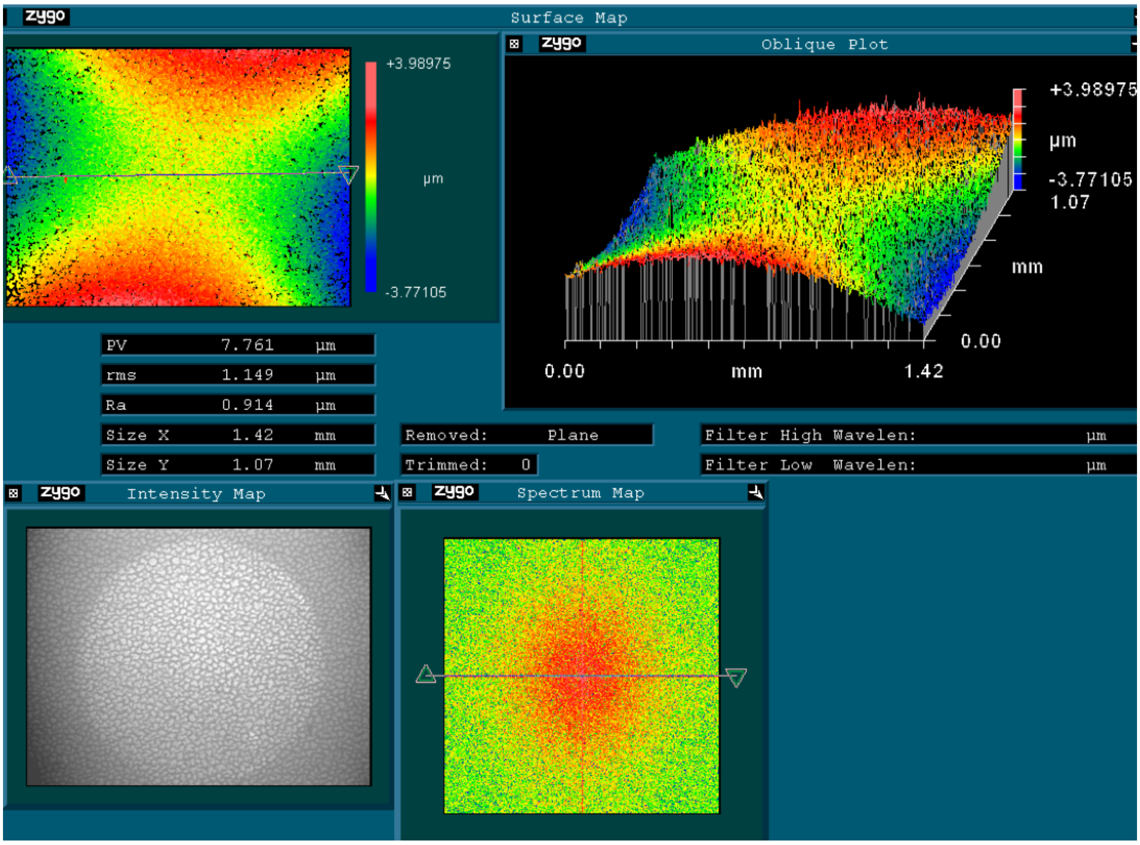

Figure 8.4: Zygo measurement of a silver spot exposed through PS-I coating for 60 seconds and heat treated at 250ºC for 30 minutes.

Similar observation was made using the Dektak stylus profilometer to scan across the silver spot as shown in Figure 8.5. The roughness and the irregularities of the flexible polyimide substrate are clearly seen but no definition of the boundaries of the silver region can be identified in the surface profile. This again indicates that the events that occurred during the UV-MPEG process resulting in a clear recession of the polymer substrate in the silver regions did not happen in the blue light PS-I system here.

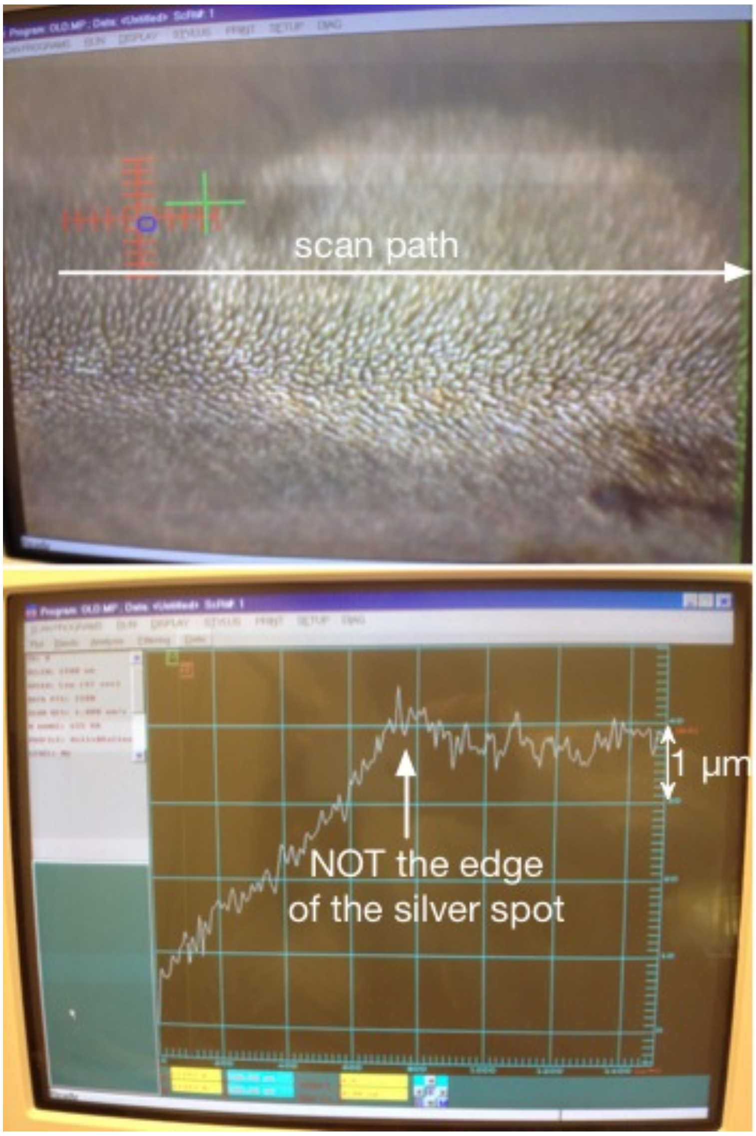

Figure 8.5: Dektak stylus measurement of the same sample as in Figure 8.4. The rising curve is an artifact due to the stylus and the flexible substrate which does not reflect the height of the silver deposition.

8.4 Discussion

PS-I was found to be a remarkable photo-reducing agent for metal ions in the current simple experimental setup. Table 8.2 compares the properties of the PS-I and the MPEG photoreduction systems, demonstrating the novelty and advantages of silver production using PS-1.

Usually, photoreduction of metal ions is carried out with an ultra-violet light source using higher energy photons [161], [162]. A few articles have been published which describe the use of visible wavelength photons assisted by uncommon organic agents [163] or inorganic photoconductive material [164] to initiate the reduction of silver ions.

Recently a paper on the production of nanoscale silver plates in a suspension was published but it required a very large amount of light energy dose; as much as 90 hours of exposure time were necessary [156].

Table 8.2: Comparison between the photoreduction systems using water, MPEG and PS-I as the photoreducing agents.

	Akamatsu	**MPEG**	**PS-I extract + ethanol**
Assisting coating	Water	MPEG	Spinach extract
Wavelength	315 nm (main)	250 - 450 nm	470 nm
Incident light intensity	260 mW/cm^2	~50 mW/cm^2	43 mW/cm^2
Minimum exposure time	60 minutes	90 to 240 minutes	10 minutes

Traditional metal nanoparticle formation by irradiation methods usually produces sparse particles in a dispersion in the liquid phase [165]. Those methods are not suitable to produce compactly packed particles in a large area solid thin film. The molecular clusters of PS-I protein simply drop-coated without using any additional binding agents onto the amorphous phase of the plastic surface containing Ag^+ ions convincingly form an efficient donor-acceptor system. The reason seems to be the following. When the molecular chains of the PS-I protein are dried on top of the high surface roughness amorphous polymer substrate, a molecular conjugate is formed as illustrated in Figure 8.6. It has been reported recently that Ag^+ ions can be bound directly to multiple sites on the PS-I protein [166], [167]. Therefore the Ag^+ ions located at the surface of the substrate are exposed to the PS-I molecular conjugate and can be easily photoreduced, when they are in the proximity of the light-harvesting and redox cofactors amongst the PS-I protein. As a result, Ag atoms are produced at the PS-I/substrate interface and quickly nucleate into a first layer of small Ag-NPs.

The ternary system of PS-I/Ag-NPs/Ag^+ ions thus formed on the surface of the plastic surface creates a unique setting which allows exceptional increase of electron generation and transfer in this artificial light harvesting system. During the course of both the small and large sizes of Ag-NPs growth as illustrated in Figure 8.6, the PS-I proteins are confined into the nanocavities amongst the Ag aggregates. The surface plasmon, which can be described as an oscillation of free electron density with respect to the stationary positive ions in the Ag-NPs, will reflect light of frequency below the plasma frequency. The confined PS-I in the nanocavities then interact again with those reflected photons, and, in turn, generate more electrons [168], [169].

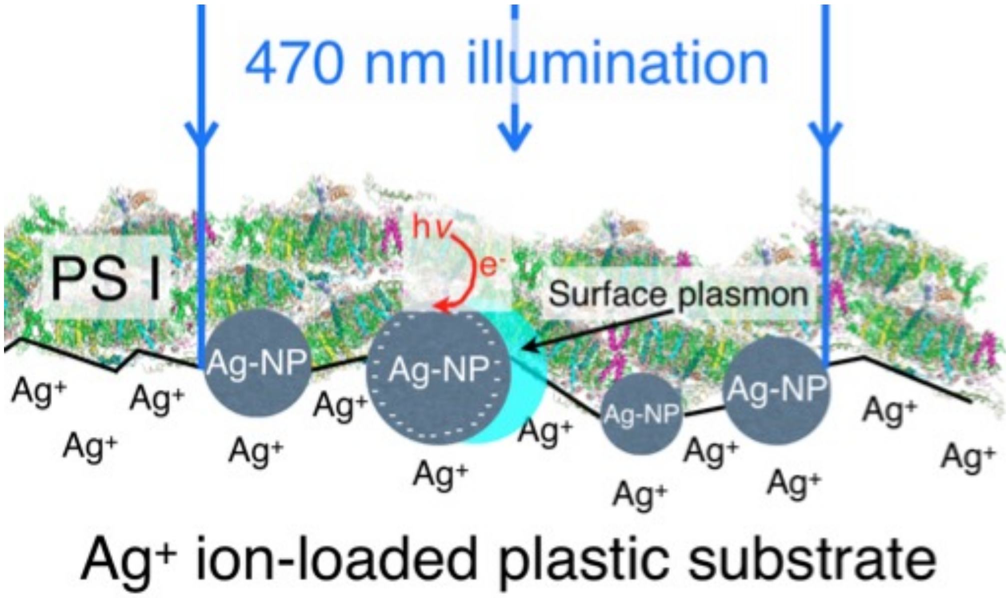

Figure 8.6: Schematic diagram of possible mechanisms during the blue light PS-I photoreduction.

In addition, the Ag-NPs produced *in situ* during the photoreduction process act as ultra large surface area nanostructured electrodes for immediate storage of the excited electrons released from the PS-I as charges on the Ag-NPs surfaces [170]. This significantly improves the lifetime and travel range of the excited electrons within the (PS-I + small growing Ag-NPs) aggregates, allowing them to reach the Ag^+ acceptors on the substrate.

8.5 Conclusion

For the first time, the concept of using PS-I as a photocatalyst for visible light photolithography of metal thin films was demonstrated in this thesis. Significant improvements from using the UV-MPEG system have been made in terms of energy dose or exposure time required. An improvement of the polymer degradation problem was indicated by an initial electroless silver plating test and the absence of prominent recession of the polymer substrate in the light exposed and annealed areas.

The production of large scale Ag-NP thin films by the blue light PS-I photoreduction is a proof that the lifetime and the transfer distances of the excited state electrons are extended within the PS-I/Ag-NPs/Ag^+ ions ternary system. The pioneering results presented in this chapter are supported by some recently established phenomena, which encourage wider fundamental studies on such an interesting and unique ternary photoreduction system. The discovery of this exciting application of PS-I under the present system opens up a wide scope of future research, which is suggested in the next Chapter.

Chapter 9

Conclusions and future work

9.1 Introduction

This thesis has described a new light-directed patterning process based on resist-free and vapour-free direct metalisation and micropatterning. After reviewing the progress in the metalisation and patterning processes used in microfabrication, ion-exchanged polyimide loaded with Ag^+ ions was chosen as the starting procedure for this research due to the ease of substrate preparation compared to the other routes, the process versatility and up-scalability, as well as the wide range of polyimide based applications in flexible circuits and inter-layers present in the electronic packaging industry. The thesis successfully demonstrated the direct metalisation of metal thin films from the loaded Ag^+ ions using two novel photoreducing agents, MPEG and PS-I.

These findings have the following significance:

i. A compact layer of silver nanoparticles can be produced in a pattern selectively on a substrate as directed by light. This ability to place nanoparticles conveniently and precisely covering a designated location is a novelty and can find applications ranging from molded interconnects to sensor technology such as Surface Enhanced Raman Scattering (SERS).

ii. The photoreduction of metal ions was carried out in air and at atmospheric pressure. This is a novelty because other previous methods relied either on a liquid (water) coating to catalyse the reduction or on the use of a colloidal solution where the production of metal particles takes place. As a consequence, the equipment in the production line can be simplified in upscale manufacturing allowing even the possibility of reel-to-reel manufacturing. It also makes the photoreduction process suitable to be carried out on contoured surfaces on objects.

iii. Hazardous chemicals normally used for metal synthesis can be replaced. Both MPEG and PS-I are completely non-toxic, and have no waste disposal requirements., PS-I i.e. chlorophyll is arguably one of the most environment friendly materials.

iv. Using a simple, abundant and very low cost biomaterial, PS-I, for the first time in manufacturing of metal thin films provided a huge improvement in photoreduction rate compared to MPEG or other photoreducing agents in the literature.

v. Using PS-I, the visible part of the optical spectrum can be used for the photolithography. This is not only beneficial for the construction of a production line with less expensive light sources compared to using UV light, it also minimizes the polymer degradation caused by the UV photon dosage required for the photoreduction of metal ions.

It was demonstrated that, although silver nanoparticles were generated by the photoreduction using various photon energy densities, degradation of the ion-exchanged polyimide substrates occurred during the direct writing by UV lasers, which was observable starting from 6 mW. This was attributed to dissociation or alteration of chemical bonds in the molecular structure of the modified substrate by UV photons. The degradation process was in fact initiated already using a UV lamp with energy doses several orders of magnitude lower than that provided by the lasers. The degradation was accelerated by heat treatment after UV lamp exposure. The ion-exchanged surface layer of the polyimide substrate did not exhibit the same superior physical properties of the unmodified polyimide. UV irradiation was believed to induce free radical formation at reactive sites such as the aromatic groups or the tertiary carbon bonds in the modified layer of the substrate, causing oxidative degradation. In addition, carbon atoms are lost and/or some polymer chains are broken during the heat treatment for re-imidization. The polymer restructuring of the substrate caused by laser irradiation appeared to be an amplified version of these UV photolytic mechanisms.

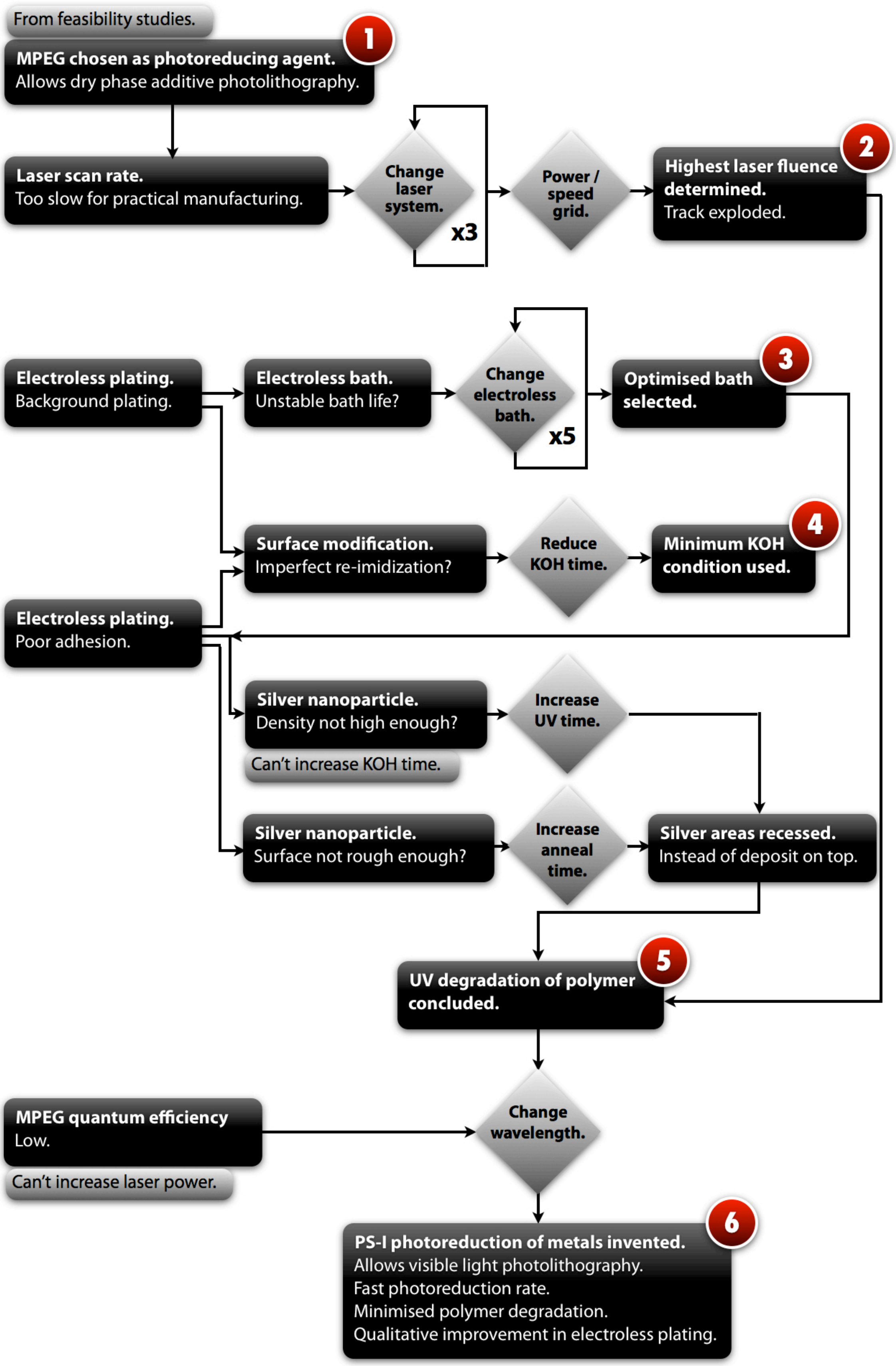

Figure 9.1: Map of the observations, hypothesis and decision nodes leading to the research outcomes of this thesis.

This thesis has concluded that it is unworkable to continue the process development further using UV wavelengths to realise the proposed innovative photolithography. The challenges encountered in these studies have led to the discovery of PS-I catalysed visible light photolithography. A map of the observations, hypothesis and decision nodes leading to the milestones of research outcomes in this thesis is illustrated in the chart in Figure 9.1. The 6 milestones highlighted are summarised as follows:

1. Successful production of a metal thin film on a solid substrate using MPEG as a standalone coating to catalyse the photoreduction, without mixing the Ag^+ ions together into a colloidal solution.

2. Laser direct-writing at less than 1 mW laser (375 nm) power; lines of silver nanoparticles were produced at low scan rates in the range of µm/s. Increasing the scan rates to the range of mm/s in conjunction with varying the laser energy densities, damage to the substrate was found to be unavoidable.

3. Electroless plating occurred uncontrollably on the areas of the re-imidized polyimide substrate without silver nanoparticles. Various plating bath compositions and operating conditions were tested against the surface modified samples. A cyanide based electroless silver bath within a certain range of pH and temperature operation was found to eliminate the problem of plating selectivity.

4. On one hand the degree of surface modification was desired to be minimal in order to improve plating selectivity, on the other hand a low level of KOH hydrolysis would in turn result in less silver nanoparticles available for the initiation of electroless plating. 1 M KOH solution for 5 minutes at 50ºC was selected as a result of the experiments undertaken with electroless plating.

5. The unsatisfactory initiation time for electroless plating and the poor top metal adhesion led to the investigation into the grain size and density of silver nanoparticles produced. These two qualities of the nanoparticles are influenced by the UV energy dose – the amount of the available Ag^+ ions within the ion-exchanged substrate being converted, and the heat treatment – the coalescence of the silver nanoparticles. Consequently degradation of the surface-modified polyimide substrate was attributed to the problems inherited

in the electroless plating, and concluded to be unavoidable.

6. To overcome the photolytic damage of the surface-modified polyimide, the proposed photolithography process needs to work in the visible wavelengths instead. Inspired by nature's greatest visible light harvesting dyes, PS-I, for electron generation, this thesis has successfully demonstrated a standalone coating of PS-I as a photo-reducing agent to replace the role of MPEG. No prior work has been found using PS-I to directly produce metal nanoparticles or metal thin films. The photoreduction rate observed was a huge improvement from using MPEG. Qualitatively, the previous degradation caused by using UV light was not found.

9.2 Future work

The continuation of research to increase the technology readiness level for the new photolithography process demonstrated in this thesis is suggested in the following three areas:

- Optimisation of the surface-modified polyimide substrate and silver seed layer for electroless plating.

- Optimisation of PS-I catalysed photoreduction.

- Laser direct-writing experiments to be carried out on the PS-I catalysed patterning process.

9.2.1 Optimisation for top metal plating

The re-imidized polyimide, the silver nanoparticles seed layer and the electroless plating bath are the determining factors for the adhesion of the top plated layer. The relationships between these and their optimal parameters can be determined by design of experiments (DoE). The adhesion of the top metal from electroless plating should be only influenced by the nucleation of the electroless metal to the silver nanoparticles seed layer, if no degradation takes place in the surface-modified substrate during any of the steps in the photolithography process. Using PS-I to catalyse the photoreduction instead of MPEG, all the available Ag^+ ions in the ion-exchanged substrate can be reduced by a smaller energy dose in the visible wavelengths, minimising the possibilities of substrate degradation as well as opening up opportunities for introducing a higher loading of Ag^+ ions in order to increase the density of the silver nanoparticles seed layer. The following actions for substrate and seed layer preparation are suggested for DoE optimisations:

i. Increasing Ag^+ ions loading in order to produce a higher density of silver nanoparticles and hence nucleation sites for electroless plating. The ion-exchange parameters used in this thesis were not characterised to provide the optimal catalytic surface. Increasing the level of KOH hydrolysis by the concentration of the KOH solution and the immersion time, would provide a deeper modification depth on the polyimide surface, and thus increase the ion-exchange capacity. The concern, as described in this thesis is that, with a high degree of hydrolysis even after re-imidization, the surface properties might not be the same as the pristine polyimide. Using the stable electroless silver bath identified in this thesis as a benchmark with fixed operating conditions, any influence on the selectivity of plating by KOH hydrolysis can be determined. The plated metal adhesion can be characterised against the amount of silver nanoparticles in the seed layer.

ii. A high level of KOH hydrolysis can degrade the integrity of the polyimide substrate. Other grades of polyimide, which are subject to proprietary additives or surface treatments, can be characterised by the level of hydrolysis each could sustain, in order to determine the maximum level applicable. Indeed, other electronic substrates in the polyimide family such as poly(ether imide) and photosensitive polyimides can be explored too.

iii. Heat treatment optimisation. Without the UV photolytic damage triggering the oxidative degradation during re-imidization by using visible light and PS-I, the heat treatment temperature and time would have direct influence on the catalytic activity of the silver nanoparticles when coalescence takes place. The grain size of the nanoparticles aggregates, surface roughness, and surface area can be characterised. A more catalytically active surface would almost instantly initiate electroless plating, without minutes of incubation time when the sample was immersed in the bath as observed in this thesis. Again adhesion is also an output factor to be characterised here. Moreover, vacuum or inert atmosphere could be used, if some level of oxidative degradation still occurred.

9.2.2 Optimisation of PS-I catalysed photoreduction

This thesis has demonstrated that PS-I can catalyse the photoreduction of the metal ions in the surface-modified polyimide a lot faster than with MPEG. The efficiency of employing such innovative bio-material in inorganic engineering needs to be quantified for upscale manufacturing in a production line, for example in a large area photomask-exposure system. In particular, the optimal values for the following parameters need to be determined by a DoE for complete photoreduction of all available Ag^+ ions loaded within the ion-exchanged substrate:

i. Exposure time – materials conditions for which the shortest time is possible.

ii. Optical power density at blue wavelengths (e.g. 455-475 nm) – to determine whether it is a linear relationship with the amount of Ag^+ ions photoreduced. Maximum power density before causing substrate damage can be determined.

iii. Concentration of PS-I during extraction and amount applied on the substrate – to determine the relationship with optical power density against the amount of Ag^+ ions photoreduced.

The know-how of implementing PS-I in upscale manufacturing will need to be developed. The lifetime of PS-I after extraction from plant leaves, where its photoreducing power still remains strong, during storage and during illumination needs to be determined. Since the PS-I is extracted by ethanol, the low viscosity of the resultant solution makes it difficult to be applied as a coating. A coating technique that would work with a reel-to-reel production line is required. A gelating agent maybe added to the extracted solution. Finally, a protocol needs to be put in place for handling of PS-I, especially in equipment cleaning and maintenance to prevent build up of residues, spoiled protein or biofilm.

9.2.3 PS-I catalysed laser direct-writing

In changing the working wavelength to the visible spectrum from UV using PS-I, much higher power lasers are available and are affordable. With the optical power intensity not being the limiting factor, the photochemical process, and in turn, the laser scan rate operable, is limited by the diffusion of Ag^+ ions within the surface-modified layer to the reaction region as discussed in this thesis. Therefore, the amount of solid silver produced should be characterized against the laser scan rates and powers employed.

Although photochemical damage to the polymer substrate is minimized when using a visible wavelength, when increasing the power of the laser, polymer restructuring will occur due to photothermal effects. A DoE characterisation is required to determine conditions where the polymer restructuring is minimal, the silver nanoparticles may be embossed, or the substrate integrity is degraded. Importantly, the laser writing parameters, which provide the optimal surface condition for electroless plating with good adhesion need to be identified. This condition maybe a combination of restructured laser scanned track covered with a certain morphology of silver nanoparticles. A certain beam shape profile such as a top hat maybe used.

Ultimately, the proposed laser direct-writing process using PS-I on ion-exchanged polyimide needs to fulfil customers specifications: line width, metal thickness and adhesion. The variation of laser spot size to the resultant electroless plated line width needs to be characterised. The autocatalytic electroless silver bath selected can achieve a very high thickness in the range of several tens of microns to over 100 microns. However without using photoresist as a mold, the line width can be expected to widen for high thickness plating. The adhesion of the electroless metal is not only influenced by the morphology of the substrate and seed particles as mentioned above, but secondarily by the plating bath operating parameters – pH, temperature and ligand release speed (cyanide to silver ratio). This would require a DoE to optimize the process, so that it can be transferred to industry.

References

[1] E. Beyne, "Interconnect and Packaging Technologies for Realizing Miniaturized Smart Devices," in *Amlware Hardware Technology Drivers of Ambient Intelligence*, vol. 5, no. 3, S. Mukherjee, R. M. Aarts, R. Roovers, F. Widdershoven, and M. Ouwerkerk, Eds. Springer Netherlands, 2006, pp. 107–123.

[2] R. Gutfeld, E. Tynan, R. Melcher, and S. Blum, "Laser enhanced electroplating and maskless pattern generation," *Appl. Phys. Lett.*, vol. 35, no. 9, pp. 651–653, 1979.

[3] R. von Gutfeld, "Laser-enhanced patterning using photothermal effects: maskless plating and etching," *J. Opt. Soc. Am. B*, vol. 4, no. 2, pp. 272–279, 1987.

[4] L. Wee and L. Li, "Multiple-layer laser direct writing metal deposition in electrolyte solution," *Appl. Surf. Sci.*, vol. 247, no. 1, pp. 285–293, 2005.

[5] S.-H. Chen and J. Lin, "The formation of micro/nanoparticles in laser-enhanced electroplating with continuous-wave and pulsed Nd-YAG laser interactions," *Opt. Laser Technol.*, vol. 44, no. 1, pp. 169–176, 2012.

[6] M. Wehner, F. Legewie, B. Theisen, and E. Beyer, "Direct writing of gold and copper lines from solutions," *Appl. Surf. Sci.*, vol. 106, pp. 406–411, 1996.

[7] K. Kordás, J. Békési, R. Vajtai, L. Nánai, S. Leppävuori, A. Uusimaki, K. Bali, T. George, G. Galbacs, F. Ignacz, and P. Moilanen, "Laser-assisted metal deposition from liquid-phase precursors on polymers," *Appl. Surf. Sci.*, vol. 172, no. 1, pp. 178–189, 2001.

[8] K. Kordás, J. Remes, S. Leppävuori, and L. Nánai, "Laser-assisted selective deposition of nickel patterns on porous silicon substrates," *Appl. Surf. Sci.*, vol. 178, no. 1, pp. 93–97, 2001.

[9] A. Manshina, A. Povolotskiy, T. Ivanova, Y. Tver'Yanovich, S. Tunik, D. Kim, M. Kim, and S. Kwon, "Effect of salt precursor on laser-assisted copper deposition," *Appl. Phys. A: Mater. Sci. Process.*, vol. 89, no. 3, pp. 755–759, 2007.

[10] K. Kordás, S. Leppävuori, A. Uusimaki, T. George, L. Nánai, R. Vajtai, K. Bali, and J. Békési, "Palladium thin film deposition on polyimide by CWAr+ laser radiation for electroless copper plating," *Thin Solid Films*, vol. 384, no. 2, pp. 185–188, 2001.

[11] J. H. Kim, B. Shin, J. S. Ko, J. Go, K. Kim, and Y. Jeong, "Direct micro fabrication of flexible copper clad laminate using 355 nm UV laser," *Jpn. J. Appl. Phys.*, vol. 47, no. 8, pp. 6883–6886, 2008.

[12] A. Watanabe and T. Miyashita, "Formation of copper micro-wiring by laser direct writing," *J. Photopolym. Sci. Technol.*, vol. 20, no. 1, pp. 115–116, 2007.

[13] M. Aminuzzaman, A. Watanabe, and T. Miyashita, "Direct writing of conductive silver micropatterns on flexible polyimide film by laser-induced pyrolysis of silver nanoparticle-dispersed film," *J. Nanopart. Res.*, vol. 12, no. 3, pp. 931–938, 2010.

[14] P. Buffat and J. Borel, "Size effect on melting temperature of gold particles," *Phys. Rev. A: At., Mol., Opt. Phys.*, vol. 13, no. 6, pp. 2287–2298, 1976.

[15] G. Shafeev, "Laser-assisted activation of dielectrics for electroless metal plating," *Appl. Phys. A: Mater. Sci. Process.*, vol. 67, no. 3, pp. 303–311, 1998.

[16] X. Wang, H. Zheng, and G. Lim, "Laser induced copper electroless plating

on polyimide with Q-switch Nd : YAG laser," *Appl. Surf. Sci.*, vol. 200, no. 1, pp. 165–171, 2002.

[17] K. Kordás, A. Pap, J. Saavalainen, H. Jantunen, P. Moilanen, E. Haapaniemi, and S. Leppävuori, "Laser-induced surface activation of LTCC materials for chemical metallization," *IEEE Trans. Adv. Pack.*, vol. 28, no. 2, pp. 259–263, 2005.

[18] J. Xu, Y. Liao, H. Zeng, Y. Cheng, Z. Xu, and K. Sugioka, *Mechanism study of femtosecond laser induced selective metallization (FLISM) on glass surfaces*. 2008.

[19] Q. Zhou, H. Chen, and Y. Wang, "Region-selective electroless gold plating on polycarbonate sheets by UV-patterning in combination with silver activating," *Electrochim. Acta*, 2009.

[20] G. Decher and J. B. Schlenoff, *Multilayer Thin Films: Sequential Assembly of Nanocomposite Materials*. Weinheim, Germany: Wiley-VCH, 2003.

[21] J. Schlenoff, "Retrospective on the Future of Polyelectrolyte Multilayers†," *Langmuir*, vol. 25, no. 24, pp. 14007–14010, 2009.

[22] Y. Guo, W. Geng, and J. Sun, "Layer-by-Layer Deposition of Polyelectrolyte- Polyelectrolyte Complexes for Multilayer Film ...," *Langmuir*, vol. 25, no. 2, pp. 1004–1010, 2009.

[23] P. Fischer and A. Laschewsky, "Layer-by-layer adsorption of identically charged polyelectrolytes," *Macromolecules*, vol. 33, no. 3, pp. 1100–1102, 2000.

[24] T. Wang, M. Rubner, and R. Cohen, "Manipulating nanoparticle size within polyelectrolyte multilayers via electroless nickel deposition," *Chem. Mater.*, vol. 15, no. 1, pp. 299–304, 2003.

[25] H. Chen and S. Dong, "A method to construct polyelectrolyte multilayers film containing gold nanoparticles," *Talanta*, vol. 71, pp. 1752–1756, 2007.

[26] D. Zabetakis and W. Dressick, "Selective electroless metallization of patterned polymeric films for lithography applications.," *ACS Appl. Mater. Interfaces*, vol. 1, no. 1, pp. 4–25, Jan. 2009.

[27] Y. Fujiwara, Y. Kobayashi, T. Sugaya, A. Koishikawa, Y. Hoshiyama, and H. Miyake, "Adsorption Promotion of Ag Nanoparticle Using Cationic Surfactants and Polyelectrolytes for Electroless Cu Plating Catalysts," *J. Electrochem. Soc.*, vol. 157, pp. D211–D216, 2010.

[28] J. Y. Chen, G. B. Luo, and W. X. Cao, "The study of layer-by-layer ultrathin films by the dynamic contact angle method," *J. Colloid Interface Sci.*, vol. 238, no. 1, pp. 62–69, 2001.

[29] S. Sukhishvili, E. Kharlampieva, and V. Izumrudov, "Where polyelectrolyte multilayers and polyelectrolyte complexes meet," *Macromolecules*, vol. 39, no. 26, pp. 8873–8881, 2006.

[30] I. Lee, P. Hammond, and M. Rubner, "Selective Electroless Nickel Plating of Particle Arrays on Polyelectrolyte Multilayers," *Chem. Mater.*, vol. 15, no. 24, pp. 4583–4589, 2003.

[31] Azzaroni O, Zheng Z, Z. Yang, and W. Huck, "Polyelectrolyte brushes as efficient ultrathin platforms for site-selective copper electroless deposition," *Langmuir*, vol. 22, no. 16, pp. 6730–6733, 2006.

[32] S. Huang, T. Tsao, and L. Chen, "Selective Electroless Copper Plating on Poly(ethylene terephthalate) Surfaces by Microcontact Printing," *J. Electrochem. Soc.*, vol. 157, no. 4, pp. D222–D227, 2010.

[33] B. Michel, A. Bernard, A. D. E. G. M. Bietsch, D. Juncker, H. Kind, J.-P. R. H. Renault, H. Schmid, P. S. R. Schmidt-Winkel, and H. Wolf, "Printing meets lithography: Soft approaches to high-resolution patterning," *IBM J. Res. Dev.*, vol. 45, no. 5, pp. 697–719, 2001.

[34] Azzaroni O, Moya SE, Brown AA, Zheng Z, Donath E, and H. WTS,

"Polyelectrolyte brushes as ink nanoreservoirs for microcontact printing of ionic species with poly(dimethyl siloxane) stamps," *Adv. Funct. Mater.*, vol. 16, no. 8, pp. 1037–1042, 2006.

[35] K. Cheng, M. Yang, W. Chiu, C. Huang, J. Chang, T. Ying, and Y. Yang, "Ink-jet printing, self-assembled polyelectrolytes, and electroless plating: Low cost fabrication of circuits on a flexible substrate at room temperature," *Macromol. Rapid Commun.*, vol. 26, no. 4, pp. 247–264, 2005.

[36] S. J. Ebbens, D. A. Hutt, and C. Liu, "Patterning Copper using Ink Jet Printing of Self Assembled Monolayers," *Electronics Packaging Technology Conference*, 2007.

[37] P. Shah, Y. Kevrekidis, and J. Benziger, "Ink-jet printing of catalyst patterns for electroless metal deposition," *Langmuir*, vol. 15, no. 4, pp. 1584–1587, 1999.

[38] K. Murata, J. Matsumoto, A. Tezuka, Y. Matsuba, and H. Yokoyama, "Super-fine ink-jet printing: toward the minimal manufacturing system," *Microsys. Technol.*, vol. 12, no. 1, pp. 2–7, 2005.

[39] Andreas Brose, Thomas Leneke, Soeren Hirsch, and B. Schmidt, "Aerosol Deposition of Catalytic Ink to Fabricate Fine Pitch Metallizations for Moulded Interconnect Devices (MID)," presented at the Electronics System Integration Technology Conference ESTC 2010, Berlin, 2010.

[40] U. Partsch, S. Mosch, and M. Ihle, "Aerosol printed conductors for miniaturized LTCC packaging," presented at the Electronics System Integration Technology Conference ESTC 2010, Berlin, 2010.

[41] T. van Osch, J. Perelaer, A. de Laat, and U. Schubert, "Inkjet printing of narrow conductive tracks on untreated polymeric substrates," *Adv. Mater.*, vol. 20, no. 2, pp. 343–345, 2008.

[42] B. Kang and J. Oh, "Geometrical characterization of inkjet-printed conductive lines of nanosilver suspensions on a polymer substrate," *Thin Solid Films*, 2009.

[43] D. Mager, A. Peter, L. Tin, E. Fischer, P. Smith, J. Hennig, and J. Korvink, "An MRI receiver coil produced by inkjet printing directly on to a flexible substrate.," *IEEE Trans. Med. Imaging*, vol. 29, no. 2, pp. 482–487, Feb. 2010.

[44] J. Perelaer, B. de Gans, and U. Schubert, "Ink-jet printing and microwave sintering of conductive silver tracks," *Adv. Mater.*, vol. 18, no. 16, pp. 2101–2104, 2006.

[45] K. Yung, S. Wu, and H. Liem, "Synthesis of submicron sized silver powder for metal deposition via laser sintered inkjet printing," *J. Mater. Sci.*, vol. 44, no. 1, pp. 154–159, 2009.

[46] J. Valeton, K. Hermans, C. Bastiaansen, D. Broer, J. Perelaer, U. Schubert, G. Crawford, and P. Smith, "Room temperature preparation of conductive silver features using spin-coating and inkjet printing," *J. Mater. Chem.*, vol. 20, no. 3, pp. 543–546, 2010.

[47] M. Allen, M. Aronniemi, T. Mattila, A. Alastalo, K. Ojanperä, M. Suhonen, and H. Seppä, "Electrical sintering of nanoparticle structures," *Nanotechnology*, vol. 19, p. 175201, 2008.

[48] A. Alastalo, T. Mattila, M. Allen, M. Aronniemi, J. Leppäniemi, K. Ojanperä, M. Suhonen, and H. Seppä, "Rapid Electrical Sintering of Nanoparticle Stuctures," presented at the Low-Cost Solution-Based Deposition of Inorganic Films for Electronic/Photonic Devices, Warrendale, PA, 2009, vol. 1113, pp. 1113–F02–07.

[49] I. Reinhold, C. Hendriks, R. Eckardt, J. Kranenburg, J. Perelaer, R. Baumann, and U. Schubert, "Argon plasma sintering of inkjet printed silver

tracks on polymer substrates," *J. Mater. Chem.*, vol. 19, no. 21, pp. 3384–3388, 2009.

[50] J. Szczech, C. Megaridis, D. Gamota, and J. Zhang, "Fine-line conductor manufacturing using drop-on-demand PZT printing technology," *IEEE Trans. Electron. Pack. Manuf.*, vol. 25, no. 1, 2002.

[51] S. Jahn, T. Blaudeck, R. Baumann, A. Jakob, P. Ecorchard, T. Rüffer, H. Lang, and P. Schmidt, "Inkjet Printing of Conductive Silver Patterns by Using the First Aqueous Particle-Free MOD Ink without Additional Stabilizing Ligands†," *Chem. Mater.*, vol. 22, no. 10, pp. 3067–3071, 2010.

[52] J. Wu, S. Hsu, M. Tsai, and W. Hwang, "Direct Inkjet Printing of Silver Nitrate/Poly (N-vinyl-2-pyrrolidone) Inks To Fabricate Silver Conductive Lines," *J. Phys. Chem. C*, vol. 114, no. 10, pp. 4659–4662, 2010.

[53] K. Akamatsu, S. Ikeda, and H. Nawafune, "Site-Selective Direct Silver Metallization on Surface-Modified Polyimide Layers," *Langmuir*, vol. 19, no. 24, pp. 10366–10371, 2003.

[54] A. Roucoux, J. Schulz, and H. Patin, "Reduced transition metal colloids: a novel family of reusable catalysts?," *Chem. Rev.*, vol. 102, no. 10, pp. 3757–3778, 2002.

[55] B. Cushing, V. Kolesnichenko, and C. O'Connor, "Recent advances in the liquid-phase syntheses of inorganic nanoparticles.," *Chem. Rev.*, vol. 104, no. 9, pp. 3893–3946, Sep. 2004.

[56] T. Sau, A. Pal, N. Jana, Z. Wang, and T. Pal, "Size controlled synthesis of gold nanoparticles using photochemically prepared seed particles," *J. Nanopart. Res.*, vol. 3, no. 4, pp. 257–261, 2001.

[57] Y. Zhou, C. Wang, Y. Zhu, and Z. Chen, "A novel ultraviolet irradiation technique for shape-controlled synthesis of gold nanoparticles at room temperature," *Chem. Mater.*, vol. 11, no. 9, pp. 2310–2312, 1999.

[58] K. Mallick, M. Witcomb, and M. Scurrell, "Self-assembly of silver nanoparticles: Formation of a thin silver film in a polymer matrix," *Mater. Sci. Eng., C*, vol. 26, no. 1, pp. 87–91, 2006.

[59] K. Mallick, Z. Wang, and T. Pal, "Seed-mediated successive growth of gold particles accomplished by UV irradiation: a photochemical approach for size-controlled synthesis," *J. Photochem. Photobiol., A*, vol. 140, no. 1, pp. 75–80, 2001.

[60] K. Mallick, M. Witcomb, and M. Scurrell, "Polymer-stabilized colloidal gold: a convenient method for the synthesis of nanoparticles by a UV-irradiation approach," *Appl. Phys. A: Mater. Sci. Process.*, vol. 80, no. 2, pp. 395–398, 2005.

[61] K. Mallick, M. Witcomb, and M. Scurrell, "Redox catalytic property of gold nanoclusters: evidence of an electron-relay effect," *Appl. Phys. A: Mater. Sci. Process.*, vol. 80, no. 4, pp. 797–801, 2005.

[62] K. Mallick, M. Witcomb, and M. Scurrell, "Self-assembly of silver nanoparticles in a polymer solvent: formation of a nanochain through nanoscale soldering," *Mater. Chem. Phys.*, vol. 90, no. 2, pp. 221–224, 2005.

[63] K. Mallick, M. Witcomb, and M. Scurrell, "Silver nanoparticle catalysed redox reaction: An electron relay effect," *Mater. Chem. Phys.*, vol. 97, no. 2, pp. 283–287, 2006.

[64] W. Huang and Y. Chen, "Photochemical synthesis of polygonal gold nanoparticles," *J. Nanopart. Res.*, vol. 10, no. 4, pp. 697–702, 2008.

[65] T. Thompson and J. J. Yates, "Surface science studies of the photoactivation of TiO2--new photochemical processes.," *Chem. Rev.*, vol. 106, no. 10, pp. 4428–4453, Oct. 2006.

[66] U. Diebold, "The surface science of titanium dioxide," *Surf. Sci. Rep.*, vol.

48, no. 5, pp. 53–229, 2003.
[67] R. Janisch, P. Gopal, and N. Spaldin, “Transition metal-doped TiO2 and ZnO—present status of the field,” *J. Phys.: Condens. Matter.*, vol. 17, p. R657, 2005.
[68] J. Wang, J. Yu, Z. Liu, Z. He, and R. Cai, “A simple new way to prepare anatase TiO2 hydrosol with high photocatalytic activity,” *Semicond. Sci. Tech.*, vol. 20, p. L36, 2005.
[69] A. Zuruzi and N. MacDonald, “Facile fabrication and integration of patterned nanostructured TiO2 for microsystems applications,” *Adv. Funct. Mater.*, vol. 15, no. 3, pp. 396–402, 2005.
[70] D. Zhang, J. Downing, F. Knorr, and J. McHale, “Room-temperature preparation of nanocrystalline TiO2 films and the influence of surface properties on dye-sensitized solar energy conversion.,” *J. Phys. Chem. B*, vol. 110, no. 43, pp. 21890–21898, Nov. 2006.
[71] S. Buzby and S. I. Shah, “Titania nanoparticles: Photocatalytic properties,” in *Titania nanoparticles: Photocatalytic properties*, 2009.
[72] C. Noh, H. Son, J. Kim, O. Hwang, K. Song, T. Byk, V. Sokolov, and J. Kim, “A novel patterning method of low-resistivity metals,” *Chem. Lett.*, vol. 34, no. 1, pp. 82–83, 2005.
[73] C. Noh, J. Kim, O. Hwang, S. Cho, K. Song, and T. Byk, “Photochemical Patterning of Pd with Amorphous TiO2 Layer and Selective Electroless Deposition of Ni,” *Electrochem. Solid-State Lett.*, 2005.
[74] K. Song, O. Hwang, J. Kim, S. Cho, T. Byk, C. Noh, and H. Lee, “Photodefinable metal deposition on an amorphous TiO2 layer for electromagnetic interference filters,” *Electrochem. Solid-State Lett.*, vol. 8, no. 11, pp. D40–D42, 2005.
[75] J. Kim, C. Noh, K. Song, H. Son, E. Hwang, S. Cho, T. Byk, H. Kim, J. Kim, B. Kong, N. Lee, and Y. Woo, “Fabrication of patterned catalyst films for carbon nanotube by selective electroless deposition,” *Carbon*, vol. 44, pp. 1862–1866, 2006.
[76] T. Byk, V. Sokolov, T. Gaevskaya, D. Sviridov, C. Noh, K. Song, and S. Cho, “Photochemical deposition of Ni-Cu patterns onto conducting substrates employing TiO2-Pd2+ layers,” *Electrochem. Solid-State Lett.*, vol. 10, no. 6, pp. D63–D66, 2007.
[77] T. Byk, V. Sokolov, T. Gaevskaya, E. Skorb, D. Sviridov, C. Noh, K. Song, Y. Kwon, and S. Cho, “Photochemical selective deposition of nickel using a TiO2-Pd2+ layer,” *J. Photochem. Photobiol., A*, vol. 193, no. 1, pp. 56–64, 2008.
[78] C. Noh, K. Song, J. Kim, T. Byk, V. Sokolov, TV, “Method of forming metal pattern having low resistivity,” U.S. Patent US Patent App 10/9592004.
[79] J. Kim, S. Cho, K. Song, C. Noh, and E. Hwang, “Method for forming highly conductive metal pattern on flexible substrate and EMI filter using metal ...,” U.S. Patent US Patent App 11/0142004.
[80] K. Song, J. Kim, C. Noh, S. Cho, E. Hwang, and H. Lee, “Optical filter for image display devices and manufacturing method thereof,” U.S. Patent US Patent App 11/2832005.
[81] E. Hwang, C. Noh, J. Kim, K. Song, and S. Cho, “Black matrix, method for preparing the same, and flat panel display and electromagnetic interference filter using the same,” U.S. Patent US Patent App 72559802005.
[82] S. Cho, E. Hwang, J. Kim, C. Noh, K. Song, and H. Lee, “Method for manufacturing high-transmittance optical filter for image display devices,”

U.S. Patent US Patent App 11/2802005.
[83] S. Cho, K. Song, C. Noh, and J. Kim, "Transparent electrode for solar cells, manufacturing method thereof, and semiconductor electrode ...," U.S. Patent US Patent App 11/4542006.
[84] C. Noh, T. Byk, S. Cho, K. Song, T. Gaevskaya, and V. Sokolov, "Method for forming metal pattern flat panel display using metal pattern formed by the method," 2007.
[85] K. Kordás, S. Leppävuori, J. Békési, L. Nánai, J. Remes, R. Vajtai, and S. Szatmári, "Nickel deposition on porous silicon utilizing lasers," *Appl. Surf. Sci.*, vol. 186, no. 1, pp. 232–236, 2002.
[86] A. Pap, K. Kordás, R. Peura, and S. Leppävuori, "Simultaneous chemical silver and palladium deposition on porous silicon; FESEM, TEM, EDX and XRD investigation," *Appl. Surf. Sci.*, vol. 201, no. 1, pp. 56–60, 2002.
[87] G. Tóth, K. Kordás, J. Vähäkangas, and A. Uusimaki, "Laser-Induced Gold Deposition on p-Si from Liquid Precursors: A Study on the Reduction of Gold Ions ...," *J. Phys. Chem. B*, vol. 109, no. 15, pp. 6925–6928, 2005.
[88] H. Sakata, S. Chakraborty, E. Yokoyama, M. Wakaki, and D. Chakravorty, "Laser-induced forward transfer of TiO_2–Aunanocomposite films for maskless patterning," *Appl. Phys. Lett.*, vol. 86, p. 114104, 2005.
[89] C. Arnold, P. Serra, and A. Piqué, "Laser direct write of complex materials," *MRS Bull.*, vol. 32, pp. 23–31, 2007.
[90] A. Ouchi, Z. Bastl, J. Bohacek, J. Subrt, and J. Pola, "Laser-induced chemical liquid deposition of discontinuous and continuous copper films," *Surf. Coat. Technol.*, vol. 201, no. 8, pp. 4728–4733, 2007.
[91] N. Smirnova, T. Boitsova, V. Gorbunova, L. Alekseeva, V. Pronin, and G. Kon'uhov, "Nickel films: Nonselective and selective photochemical deposition and properties," *Thin Solid Films*, vol. 513, no. 1, pp. 25–30, 2006.
[92] Y. Byun, E. Hwang, S. Lee, Y. Lyu, J. Yim, J. Kim, S. Chang, L. Pu, and J. Kim, "Highly efficient silver patterning without photo-resist using simple silver precursors," *Mater. Sci. Eng., B*, vol. 117, no. 1, pp. 11–16, 2005.
[93] A. Kumaran, T. Miyawaki, and M. Ichimura, "Photochemical deposition of patterned gold thin films," *Jpn. J. Appl. Phys. 2*, vol. 45, no. 46, pp. L1283–L1285, 2006.
[94] C. Allmond, A. Sellinger, K. Gogick, and J. Fitz-Gerald, "Photo-chemical synthesis and deposition of noble metal nanoparticles," *Appl. Phys. A: Mater. Sci. Process.*, vol. 86, no. 4, pp. 477–480, 2007.
[95] M. Dicks, G. Broxton, J. Thomson, J. Lobban, J. Stevenson, and A. Walton, "Characterization of platinum films produced by UV exposure of a novel photosensitive organometallic material," *IEEE Trans. Semiconduct. Manuf.*, vol. 17, no. 2, pp. 91–97, 2004.
[96] T. Baum, E. Marinero, and C. Jones, "Projection printing of gold micropatterns by photochemical decomposition," *Appl. Phys. Lett.*, vol. 49, no. 18, pp. 1213–1215, 1986.
[97] G. Condorelli, L. Costanzo, I. Fragala, S. Giuffrida, and G. Ventimiglia, "A single photochemical route for the formation of both copper nanoparticles and patterned nanostructured films," *J. Mater. Chem.*, vol. 13, no. 10, pp. 2409–2411, 2003.
[98] A. Narayan, L. Landstrom, and M. Boman, "Laser-assisted synthesis of ultra small metal nanoparticles," *Appl. Surf. Sci.*, vol. 208, pp. 137–141, 2003.
[99] H. Park, H. Park, and R. Hill, "Direct-patterning of SnO_2 thin film by photochemical metal-organic deposition," *Sensor Actuat. A-Phys.*, vol. 132,

no. 2, pp. 429–433, 2006.
[100] N. Mirchin, A. Peled, I. Baal-Zedaka, R. Margolin, M. Zagon, I. Lapsker, A. Verdyan, and J. Azoulay, "Photodeposited diffractive optical elements of computer generated masks," *Appl. Surf. Sci.*, vol. 248, no. 1, pp. 509–513, 2005.
[101] E. Hugonnot, M. Delville, and J. Delville, "Universal behavior of photochemical deposition in liquid solutions driven by a one-photon transition," *Phys. Rev. E: Stat., Nonlinear, Soft Matter Phys.*, vol. 75, no. 6, p. 61602, 2007.
[102] A. Avey and R. Hill, "Solid state photochemistry of Cu-2(OH2)(2)(O2C(CH2)(4)CH3)(4) in thin films: The photochemical formation of high-quality films of copper and copper(I) oxide. Demonstration of a novel lithographic technique for the patterning of copper," *J. Am. Chem. Soc.*, vol. 118, no. 1, pp. 237–238, 1996.
[103] R. Klassen and T. Baum, "Mechanistic studies on the thermal and photochemical decomposition of dimethy(2,4-pentanedionato)gold(III) in solution," *Organometallics*, vol. 8, no. 10, pp. 2477–2482, 1989.
[104] T. Deng, F. Arias, R. Ismagilov, P. Kenis, and G. Whitesides, "Fabrication of metallic microstructures using exposed, developed silver halide-based photographic film," *Anal. Chem.*, vol. 72, no. 4, pp. 645–651, 2000.
[105] *Conductive Inkjet Technology*. [Online]. Available: http://www.conductiveinkjet.com. [Accessed: 25-Feb.-2013].
[106] "TEKNOflex Interconnect Solutions," *flexiblecircuits.co.uk*, 2010. [Online]. Available: http://www.flexiblecircuits.co.uk/products/reel_to_reel.asp. [Accessed: 12-Apr.-2011].
[107] "ManTech Materials - Advanced Polymer Materials for High-Tech Applications," *mantechmaterials.com*. [Online]. Available: http://www.mantechmaterials.com/products.asp. [Accessed: 11-Apr.-2011].
[108] K. L. Mittal, "Synthesis of polyimides," in *Polyimides: Fundamentals and Applications*, M. K. Ghosh and K. L. Mittal, Eds. New York: Marcel Dekker, 1996.
[109] K. W. Lee, S. P. Kowalczyk, and J. M. Shaw, "Surface modification of pmda-oda polyimide - surface-structure adhesion relationship," *Macromolecules*, vol. 23, no. 7, pp. 2097–2100, 1990.
[110] L. E. Stephans, A. Myles, and R. R. Thomas, "Kinetics of alkaline hydrolysis of a polyimide surface," *Langmuir*, vol. 16, no. 10, pp. 4706–4710, 2000.
[111] M. M. Plechaty and R. R. Thomas, "Chemical Surface-Modification of a Polyimide: Characterization and a Kinetic Study on the Diffusion of ions in a modified polymer," *J. Electrochem. Soc.*, vol. 139, no. 3, pp. 810–821, 1992.
[112] H. Strathmann, *Ion-exchange membrane separation processes*, 1st ed. vol. 9. Elsevier Science, 2004, pp. 76–80.
[113] G. M. Scott, "The virucidal properties of silver ion-exchange resins and metal-based nanoparticles and their potential use in water purification," Kansas State University, Manhattan, Kansas, 2010.
[114] A. A. Zagorodni, *Ion Exchange Materials Properties and Applications*. Amsterdam, The Netherlands: Elsevier, 2007.
[115] J. Kielland, "Individual activity coefficients of ions in aqueous solutions," *J. Am. Chem. Soc.*, vol. 59, no. 9, pp. 1675–1678, 1937.
[116] P. Wang, A. Anderko, and R. D. Young, "A speciation-based model for mixed-solvent electrolyte systems," *Fluid Phase Equilibria*, vol. 203, no. 1, pp. 141–176, 2002.

[117] S. Qi, Z. Wu, D. Wu, W. Yang, and R. Jin, “The chemistry involved in the loading of silver(I) into poly(amic acid) via ion exchange: A metal-ion-induced crosslinking behavior,” *Polymer*, vol. 50, no. 3, pp. 845–854, 2009.

[118] C. R. Nave, “HyperPhysics,” *Electrochemistry*, 2010. [Online]. Available: http://hyperphysics.phy-astr.gsu.edu/hbase/hframe.html. [Accessed: 06-Nov.-2012].

[119] T. Sato, T. Ito, H. Iwabuchi, and Y. Yonezawa, “Photochemical deposition of noble metal ultrafine particles onto liposomes,” *J. Mater. Chem.*, vol. 7, no. 9, pp. 1837–1840, 1997.

[120] S. Ikeda, K. Akamatsu, and H. Nawafune, “Direct photochemical formation of cu patterns on surface modified polyimide resin,” *J. Mater. Chem.*, vol. 11, no. 12, pp. 2919–2921, 2001.

[121] S. Ikeda, K. Akamatsu, H. Nawafune, T. Nishino, and S. Deki, “Formation and growth of copper nanoparticles from ion-doped precursor polyimide layers,” *J. Phys. Chem. B*, vol. 108, pp. 15599–15607, 2004.

[122] K. Akamatsu, S. Ikeda, H. Nawafune, and H. Yanagimoto, “Direct patterning of copper on polyimide using ion exchangeable surface templates generated by site-selective surface modification,” *J. Am. Chem. Soc.*, vol. 126, no. 35, pp. 10822–10823, 2004.

[123] K. Akamatsu, H. Shinkai, S. Ikeda, S. Adachi, H. Nawafune, and S. Tomita, “Controlling interparticle spacing among metal nanoparticles through metal-catalyzed decomposition of surrounding polymer matrix,” *J. Am. Chem. Soc.*, vol. 127, no. 22, pp. 7980–7981, 2005.

[124] S. Ikeda, H. Yanagimoto, K. Akamatsu, and H. Nawafune, “Copper/polyimide heterojunctions: Controlling interfacial structures through an additive-based, all-wet chemical process using ion-doped precursors,” *Adv. Funct. Mater.*, vol. 17, no. 6, p. 889, 2007.

[125] K. Akamatsu, K. Nakahashi, S. Ikeda, and H. Nawafune, “Fabrication and structural characterization of nanocomposites consisting of ni nanoparticles dispersed in polyimide films,” *The European Physical Journal D-atomic, Molecular and Optical Physics*, vol. 24, no. 1, pp. 377–380, 2003.

[126] S. Tomita, K. Akamatsu, H. Shinkai, S. Ikeda, H. Nawafune, C. Mitsumata, T. Kashiwagi, and M. Hagiwara, “Tuning magnetic interactions in ferromagnetic-metal nanoparticle systems,” *Physical Review B*, vol. 71, no. 18, p. 180414, 2005.

[127] S. Tomita, P. E. Jönsson, K. Akamatsu, H. Nawafune, and H. Takayama, “Controlled magnetic properties of ni nanoparticles embedded in polyimide films,” *Physical Review B*, vol. 76, no. 17, p. 174432, 2007.

[128] W. Yu and T. M. Ko, “Surface characterizations of potassium-hydroxide-modified upilex-s® polyimide at an elevated temperature,” *European Polymer Journal*, vol. 37, no. 9, pp. 1791–1799, 2001.

[129] H. Okumura, T. Takahagi, N. Nagai, and S. Shingubara, “Depth profile analysis of polyimide film treated by potassium hydroxide,” *Journal of Polymer Science Part B: Polymer Physics*, vol. 41, no. 17, pp. 2071–2078, 2003.

[130] J. Y. Kim, T. V. Byk, S. H. Cho, C. H. Noh, K. Y. Song, J. M. Kim, and T. V. Gaevskaya, “Selective Electroless Deposition Using Photoinduced Oxidation of Sn (II) Compounds on Surface-Modified Polyimide Layers,” *Electrochem. Solid-State Lett.*, vol. 9, p. H118, 2006.

[131] D. Chen, Q. Lu, and Y. Zhao, “Laser-induced site-selective silver seeding on polyimide for electroless copper plating,” *Appl. Surf. Sci.*, vol. 253, no. 3, pp. 1573–1580, 2006.

[132] Y. Matsumura, Y. Enomoto, M. Sugiyama, K. Akamatsu, and H. Nawafune, “Direct metallization of nickel on polymeric template patterns

for fabrication of copper circuits on glass substrates," *J. Mater. Chem.*, vol. 18, no. 42, pp. 5078–5082, 2008.

[133] K. Xu, G. Amaral, and J. Zhang, "Photodissociation dynamics of ethanol at 193.3 Nm: The h-atom channel and ethoxy vibrational distribution," *Journal of Chemical Physics*, vol. 111, no. 14, pp. 6271–6282, 1999.

[134] I. Washio, Y. J. Xiong, Y. D. Yin, and Y. N. Xia, "Reduction by the end groups of poly(vinyl pyrrolidone): A new and versatile route to the kinetically controlled synthesis of Ag triangular nanoplates," *Adv. Mater.*, vol. 18, no. 13, p. 1745, 2006.

[135] Y. Xiong, I. Washio, J. Chen, H. Cai, Z. Y. Li, and Y. Xia, "Poly(vinyl pyrrolidone): A dual functional reductant and stabilizer for the facile synthesis of noble metal nanoplates in aqueous solutions.," *Langmuir*, vol. 22, no. 20, pp. 8563–8570, Sep. 2006.

[136] R. E. Koning, "Home Page for Ross Koning, Plant Physiology Information," *plantphys.info*, 1994. [Online]. Available: http://plantphys.info/index.html. [Accessed: 06-Nov.-2012].

[137] D. Noy, C. C. Moser, and P. L. Dutton, "Design and engineering of photosynthetic light-harvesting and electron transfer using length, time, and energy scales.," *Biochim Biophys Acta*, vol. 1757, no. 2, pp. 90–105, Feb. 2006.

[138] L. Sepunaru, I. Tsimberov, L. Forolov, C. Carmeli, I. Carmeli, and Y. Rosenwaks, "Picosecond electron transfer from photosynthetic reaction center protein to gaas.," *Nano Lett.*, vol. 9, no. 7, pp. 2751–2755, Jul. 2009.

[139] "Chloroplast," *Encyclopædia Britannica*, 2011. [Online]. Available: http://www.britannica.com/EBchecked/topic/113761/chloroplast. [Accessed: 06-Nov.-2012].

[140] J. DEISENHOFER and H. MICHEL, "The photosynthetic reaction center from the purple bacterium rhodopseudomonas-viridis (nobel lecture)," *Angewandte Chemie-international Edition in English*, vol. 28, no. 7, pp. 829–847, 1989.

[141] G. Calogero, G. Di Marco, S. Caramori, S. Cazzanti, R. Argazzi, and C. A. Bignozzi, "Natural dye senstizers for photoelectrochemical cells," *Energy Environ. Sci.*, vol. 2, no. 11, pp. 1162–1172, 2009.

[142] Z. Wu, D. WU, S. Qi, T. ZHANG, and R. JIN, "Preparation of surface conductive and highly reflective silvered polyimide films by surface modification and in situ self-metallization technique," *Thin Solid Films*, vol. 493, no. 1, pp. 179–184, 2005.

[143] E. L. Smith, "The chlorophyll-protein compound of the green leaf," *The Journal of general physiology*, vol. 24, no. 5, pp. 565–582, 1941.

[144] T. Taylor, "CPI Printable Electronics, The National Printed Electronics Centre," *Cambridge Integrated Knowledge Centre, December 2012*. pp. 1–18, 15-Dec.-2012.

[145] F. W. Campbell, S. R. Belding, R. Baron, L. Xiao, and R. G. Compton, "The Hydrogen Evolution Reaction at a Silver Nanoparticle Array and a Silver Macroelectrode Compared: Changed Electrode Kinetics between the Macro- and Nanoscales," *J. Phys. Chem. C*, vol. 113, no. 33, pp. 14852–14857, 2009.

[146] A. Tal, Y. S. Chen, H. E. Williams, R. C. Rumpf, and S. M. Kuebler, "Fabrication and characterization of three-dimensional copper metallodielectric photonic crystals," *Optics Express*, vol. 15, no. 26, pp. 18283–18293, 2007.

[147] F. Hanna, Z. A. Hamid, and A. A. Aal, "Controlling factors affecting the stability and rate of electroless copper plating," *Mater. Lett.*, vol. 58, no. 1,

pp. 104–109, Jan. 2004.
[148] X. Cui, D. A. Hutt, and P. P. Conway, "Evolution of microstructure and electrical conductivity of electroless copper deposits on a glass substrate," *Thin Solid Films*, vol. 520, no. 19, pp. 6095–6099.
[149] D. Flynn, A. Toon, and M. Desmulliez, "Manufacture and characterisation of micro-engineered DC-DC power converter using UV-LIGA process," *Electronics Letters*, 2005.
[150] R. Jagannathan and M. Krishnan, "Electroless plating of copper at a low pH level," *IBM J. Res. Dev.*, vol. 37, no. 2, pp. 117–124, 1993.
[151] R. Srinivasan, R. R. Hall, W. D. Loehle, W. D. Wilson, and D. C. Allbee, "Chemical transformations of the polyimide Kapton brought about by ultraviolet laser radiation," *Journal of applied physics*, vol. 78, no. 8, pp. 4881–4887, 1995.
[152] S. F. Dinetz, E. J. Bird, R. L. Wagner, and A. W. Fountain, "A comparative study of the gaseous products generated by thermal and ultraviolet laser pyrolyses of the polyimide PMDA-ODA," *Journal of analytical and applied pyrolysis*, vol. 63, no. 2, pp. 241–249, 2002.
[153] Y. N. Sazanov, A. V. Gribanov, and L. V. A, "The role of nitrogen atoms in forming the carbon structure in the carbonization of polymer composites," *Fibre Chemistry*, vol. 40, no. 4, pp. 355–364, Nov. 2008.
[154] E. E. Ortelli, F. Geiger, T. Lippert, J. Wei, and A. Wokaun, "UV-Laser-Induced Decomposition of Kapton Studied by Infrared Spectroscopy," *Macromolecules*, vol. 33, no. 14, pp. 5090–5097, Jul. 2000.
[155] J. T. Young, W. H. Tsai, and F. J. Boerio, "Characterization of the interface between pyromellitic dianhydride/oxydianiline polyimide and silver using surface-enhanced Raman scattering," *Macromolecules*, vol. 25, pp. 887–894, Nov. 1992.
[156] X. Tian, K. Chen, and G. Cao, "Seedless, surfactantless photoreduction synthesis of silver nanoplates," *Mater. Lett.*, vol. 60, no. 6, pp. 828–830, Mar. 2006.
[157] R. R. Hautala, R. B. King, and C. Kutal, "Solar energy: Chemical conversion and storage," *Solar Energy: Chemical …*, 1979.
[158] S. Barazzouk and S. Hotchandani, "Enhanced charge separation in chlorophyll a solar cell by gold nanoparticles," *Journal of applied physics*, 2004.
[159] G. Kumara, S. Kaneko, and M. Okuya, "Shiso leaf pigments for dye-sensitized solid-state solar cell," *Solar energy materials …*, 2006.
[160] J. H.-G. Ng, M. P. Y. Desmulliez, and D. E. G. Watson, "Additive metallisation process," U.S. Patent PCT/GB2012/000116.
[161] J. C. Scaiano, P. Billone, C. M. Gonzalez, L. Marett, M. L. Marin, K. L. McGilvray, and N. Yuan, "Photochemical routes to silver and gold nanoparticles," *Pure Appl. Chem.*, vol. 81, no. 4, pp. 635–647, 2009.
[162] C. Cheng, B. Lv, Y. Li, J. Wang, J. He, H. Yuan, and D. Xiao, "A facile photochemical route for the synthesis of gold nanoparticles," *Inorganic Materials*, vol. 47, no. 2, pp. 121–127, 2011.
[163] L. Balan and D.-J. Lougnot, "Photochemically Implemented Metal/Polymer Nanocomposite Materials for Advanced Optical Applications," in *Advances in Nanocomposites - Synthesis, Characterization and Industrial Applications*, B. Reddy, Ed. InTech, 2012, pp. 1–17.
[164] A. M. Schultz, Y. Zhang, P. A. Salvador, and G. S. Rohrer, "Effect of Crystal and Domain Orientation on the Visible-Light Photochemical Reduction of Ag on $BiFeO_3$," *ACS Appl. Mater. Interfaces*, vol. 3, no. 5, pp. 1562–1567, May 2011.
[165] L. Balan, R. Schneider, C. Turck, D. Lougnot, and F. Morlet-Savary,

"Photogenerating Silver Nanoparticles and Polymer Nanocomposites by Direct Activation in the Near Infrared," *Journal of Nanomaterials*, vol. 2012, pp. 1–6, 2012.

[166] L. M. Utschig and M. C. Thurnauer, "Metal Ion Modulated Electron Transfer in Photosynthetic Proteins," *Acc. Chem. Res.*, vol. 37, no. 7, pp. 439–447, Jul. 2004.

[167] L. M. Utschig, L. X. Chen, and O. G. Poluektov, "Discovery of Native Metal Ion Sites Located on the Ferredoxin Docking Side of Photosystem I †," *Biochemistry*, vol. 47, no. 12, pp. 3671–3676, Mar. 2008.

[168] A. O. Govorov and I. Carmeli, "Hybrid Structures Composed of Photosynthetic System and Metal Nanoparticles: Plasmon Enhancement Effect," *Nano Lett.*, vol. 7, no. 3, pp. 620–625, Mar. 2007.

[169] I. Carmeli, I. Lieberman, L. Kraversky, Z. Fan, A. O. Govorov, G. Markovich, and S. Richter, "Broad Band Enhancement of Light Absorption in Photosystem I by Metal Nanoparticle Antennas," *Nano Lett.*, vol. 10, no. 6, pp. 2069–2074, Jun. 2010.

[170] O. Lioubashevski, V. I. Chegel, F. Patolsky, E. Katz, and I. Willner, "Enzyme-Catalyzed Bio-Pumping of Electrons into Au-Nanoparticles: A Surface Plasmon Resonance and Electrochemical Study," *J. Am. Chem. Soc.*, vol. 126, no. 22, pp. 7133–7143, Jun. 2004.